CRANFIELD UNIVERSITY

Farhan Ashraf

Physics-Based Modelling of Cyclic Deformation and Microstructure-Sensitive Fatigue Crack Propagation from Shallow Scribes

School of Aerospace, Transport and Manufacturing
PhD in Manufacturing

PhD
Academic Year: 2020 - 2021

Supervisor: Dr. Gustavo M. Castelluccio
Associate Supervisor: Dr. Muhammad Ali Khan
December 2020

CRANFIELD UNIVERSITY

School of Aerospace, Transport and Manufacturing
PhD in Manufacturing

PhD

Academic Year 2020 - 2021

Farhan Ashraf

Physics-Based Modelling of Cyclic Deformation and Microstructure-Sensitive Fatigue Crack Propagation from Shallow Scribes

Supervisor: Dr. Gustavo M. Castelluccio
Associate Supervisor: Dr. Muhammad Ali Khan
December 2020

This thesis is submitted in partial fulfilment of the requirements for the degree of PhD
(NB. This section can be removed if the award of the degree is based solely on examination of the thesis)

Abstract

Face-centered cubic (FCC) metals with low to medium stacking fault energy (SFE) develop similar mesoscale substructures under cyclic loading. The formation of these substructures is controlled by dislocation interactions and loading conditions. For instance, cross slip facilitates cell formation and Hirth locks define the labyrinth structure. In the case of aluminium (high SFE metal), cross slip is easily activated and a cell structure is often observed. However, it is not always recognised that aluminium can also form PSBs at low temperatures. This highlights that the underlying mechanism controlling the cyclic response in aluminium is not different from other FCC metals.

This work proposes the role of mesoscale substructure as a material-invariant among FCC metals to predict the cyclic response of aluminium. The effect of number of cycles on modelling dislocation substructures is explored, which is found to trigger a change in dislocation structures in aluminium at 298K. A crystal plasticity framework based on mesoscale substructures is developed to study the cyclic response of aluminium under different crystal orientations, strain amplitudes, number of cycles, and temperatures.

Finally, this work implemented the crystal plasticity model to study the microstructure-sensitive crack propagation from shallow scribes in pure aluminium. The gradient of fatigue indicator parameters (FIPs) is estimated as crack extends inside a grain with explicit microstructure simulations, which followed the same decaying trend predicted by experiments. Thereby, an engineering solution is proposed to couple microstructural and geometric gradients at the crack tip independently. The model predicted the transgranular fatigue life with independently coupled gradients that agree well with experiments.

Keywords: Aluminium, Mesoscale substructures, Cyclic response, Scribe marks, Microstructure-sensitive fatigue cracks

Acknowledgements

All praise is due to Allah Almighty, the Lord of all worlds, the Greatest, the most Beneficent, the most Merciful, the ever providing, for his countless blessings and his everlasting inspiration. May the peace and blessing of Allah be upon his Prophet Muhammad, his family, and his companions.

I express my sincere and deepest gratitude to my supervisor Dr. Gustavo M. Castelluccio, for his valuable feedback, support, and time. I had a wonderful experience working with him as well as the privilege to be his first PhD student. I appreciate his patience and encouragement in improving my research and writing skills. His enthusiasm and insightful discussions have helped me to grow in the versatile field of mechanics of materials. I would also like to thank him for his financial support during hard times. His technical advice and feedback were essentials for the completion of this work. I would like to thank Dr. Muhammad Khan, Dr. Ali Mehmanparast, and Dr. Andrea Cini for reviewing this thesis and their valuable feedback.

I would also extend my gratitude to The Punjab Educational Endowment Fund (PEEF) for funding this work. Besides, I am also grateful for the financial support provided by the school. Without this financial support, I would never have been able to complete this work.

Many thanks to my colleagues and friends Dr. Ebiakpo Kakandar, Dr. Arijit Lodh, and Shahram Dindarlou for their help and insightful discussions. I would also like to thanks other colleagues in the TES centre for their help. Apart from my studies, I would like to mention many individuals who made my Cranfield stay a memorable one. I am indebted to Mr. Masood (Uncle) and Mrs. Masood (Khala) for their love and care during my stay at Cranfield. Thanks to Dr. Zaheer for his thoughtful discussions, care, and especially delicious food. I would also like to thanks the Pakistani community especially Iftikhar, Muntazir, Shoaib, Kamran, Ali, and Umair for their support and the memorable time we spent as a family. I would also like to mention other friends Dr. Sarhan, Dr. Abdul Qabeer, Dr. Faisal Asfand, Dr. Akram Afzal, and Dr. Abdullah Asmari for their help and support.

I am eternally indebted to my mother Sakina Ashraf and father Muhammad Ashraf, brothers, sisters, nieces, and nephews for their unconditional love and support without which I would not have reached this stage. Finally, I am heartedly grateful to my wife Maira, and children Maryam and Ibrahim for their love, support, and patience. They deserve my special gratitude for their understanding and encouragement.

Table of Contents

List of Figures

List of Tables

List of Equations

List of Abbreviations

FCC	Face Centred Cubic
SFE	Stacking Fault Energy
PSB	Persistent Slip Bands
Ni	Nickel
Cu	Copper
Ag	Silver
Al	Aluminium
R_ε	Strain Ratio
CSSC	Cyclic Stress-Strain Curve
$\Delta\gamma_p$	Plastic Shear Strain Range
SF	Schmid Factor
$\frac{T}{T_m}$	Homologous Temperature
T_m	Melting Point
MSC	Microstructure-Sensitive Small Fatigue Cracks
FM	Fracture Mechanics
FIP	Fatigue Indicator Parameter
FS	Fatemi-Socie
TST	Transition State Theory
N	Number of Cycles
N_c	Number of Computational Cycles
SC	Single Crystal
PC	Polycrystal
AA	Aluminium Alloy
SS	Stainless Steel
GEV	Generalised Extreme Value
Γ	Probability of a Dislocation to Overcome an Obstacle
T	Temperature
ΔG	Gibbs Free Activation Energy
k_B	Boltzmann Constant
F_0	Glide Activation Energy
s_0^t	Thermal Stress at 0K

p, q	Profile Parameters in Kock's Formulation
τ	Local Shear Stress
ΔV	Activation Volume
ΔF	Helmholtz Free Energy
F_0^*	Pinning Energy at Zero Stress
s_0^*	Taylor stress
C_f	Conversion Factor
σ_y^α	Yield Stress
FE	Finite Element
UMAT	User Material Subroutine
$\dot{\gamma}_0^\alpha$	Effective Shear Strain Rate
$\dot{\gamma^\alpha}$	Shear Strain Rate
μ	Shear Modulus
μ_o	Shear Modulus at 0K
τ_{eff}^α	Effective Shear Stress
τ^α	Local Resolved Shear Stress
S^α	Athermal Stress
B^α	Intragranular Back Stress
α_{LE}	Dislocation Line Energy Coefficient
A_{ii}	Self-Interaction Coefficient
ρ^α	Density of Mobile Dislocations
${\rho_o}^\alpha$	Initial Dislocation Density
$\Delta{\rho_y}^\alpha$	Dislocation Density upon Loading upto Yield
d	Fixed Dislocation Mean Free Path
d_{struc}	Dislocation Substructure Wall Spacing
$\boldsymbol{b}$	Burgers Vector
K_{struc}	Similitude Coefficient
K_{multi}	Constant Related to Dislocation Production
h	Planck's Constant
γ^α	Shear strain in α Slip System
l_v	Mean Spacing Between Point Obstacles
F_{oi}, a	Fitting Constants Correspond to F_o and SFE Relationship
l_{struc}	Mean Free Path in Mesoscale Substructures

v_G	Attempt Frequency
DSA	Dynamic Strain Aging
EV	Extreme Value
MLL	Maximum Log-Likelihood
$\boldsymbol{F}$	Deformation Gradient
$\boldsymbol{F^e}$	Elastic Component of the Deformation Gradient
$\boldsymbol{F^p}$	Plastic Component of the Deformation Gradient
$\boldsymbol{L^p}$	Plastic part of velocity gradient
$\boldsymbol{s^\alpha}$	Slip Direction of α Slip System
$\boldsymbol{n^\alpha}$	Normal Direction of α Slip System
$\dot{B^\alpha}$	Rate of Intragranular Back Stress
f_{Hill}^S	Macroscopic Plastic Deformation Tangent
S_{1212}, C_{12}	Eshelby Tensor Components for Prolate Spheroid Coordinate System
f_w	Wall Volume Fraction
η	Characteristic Spacing of Dislocation Substructure
ν	Poisson's ratio
v_p	Tangent elasto-plastic Poisson's ratio
$\dot{\rho}_m^{s\alpha}$	Rate of Mobile Dislocation Density
$\rho_m^{s\alpha}$	Density of Screw Dislocations in Primary Slip Plane (α)
$\rho_m^{s\xi}$	Density of Screw Dislocations in Cross Slip Plane (ξ)
y_s^{edge}	Edge Dislocation Annihilation Distance
y_s^{screw}	Screw Dislocation Annihilation Distance
V_{CS}^{α}	Cross Slip Activation Volume in Primary Slip Plane (α)
V_{CS}^{ξ}	Cross Slip Activation Volume in Cross Slip Plane (ξ)
d_o	Initial Structural Distance
ϕ_{cs}	Cross Slip Efficiency
γ_{cum}^{Cross}	Cumulative Plastic Shear Strain in Cross Slip Plane
$\Delta\gamma^{Cross}$	Range of Plastic Shear Strain in Cross Slip Plane
$d\gamma_{pl}^{\alpha}$	Plastic Shear Strain Increment in α Slip System
FIP_E^{α}	Energy Based FIP in α Slip System
γ_{max}	Maximum Shear Strain
σ_n^{max}	Maximum Normal Stress on γ_{max} Plane

k	Material's Constant in Fatemi-Socie FIP
FIP_{FS}	Fatemi-Socie Fatigue Indicator Parameter
$\Delta\gamma_{max}^{p}$	Maximum Plastic Shear Strain Range
FIP_{FS}^{α}	Fatemi-Socie FIP in α Slip System
FIP_{grain}	Grain Averaged FIP
FIP_{band}	Band Averaged FIP
$FIP_{element}$	Local FIP
FIP_{o}	Maximum Normalised Band Averaged FIP
FIP_{meso}	Normalised Band Averaged FIP
$FIP_{meso}^{\alpha,1}$	Normalised Band Averaged FIP in one plane
$FIP_{meso,net}$	Multislip Normalised Band Averaged FIP in one plane
MS	Microstructure Sensitive
$\Delta\gamma^{\alpha}$	Cyclic Plastic Shear Strain Range in Slip System α
σ_{n}^{α}	Peak Stress Normal to the Slip Plane α
σ_{y}	Cyclic Yield Strength
γ_{max}^{pl}	Maximum Plastic Shear Strain
γ_{max}^{el}	Maximum elastic Shear Strain
γ_{max}^{total}	Maximum total Shear Strain
σ_{1}	Maximum Principal Stress
σ_{2}	Minimum Principal Stress
ϵ_{1}	Maximum Principal Strain
ϵ_{2}	Minimum Principal Strain
n_{el}	Number of Elements
l_{el}	Length of an Element
MLB	Minimum Life Band
k_{1}, k_{2}	Fitting Constants Related to Geometric Gradient
P_{g}, m	Fitting Constants Related to Microstructural Gradient
d_{gr}^{ref}	Reference Grain Size
d_{gr}	Reference Band Size
γ_{max}	Maximum Total Shear Strain
LCF	Low Cycle Fatigue
ΔCTD	Crack Tip Displacement

ΔCTD_{th}	Threshold Crack Tip Displacement
$\frac{da}{dN}$	Crack Growth Rate
$\emptyset$	Proportionality Factor
$\gamma_{irr,local,pl}$	Irreversible Local Plastic Shear Strain
D	Grain Size
A, b	Scaling Constant that Relates FIP and ΔCTD
E	Modulus of Elasticity
σ	Normal Stress
ϵ	Normal Strain
h_c	Height of Extrusion
a_i	Crack Length in i^{th} Band
K_t	Stress Concentration Factor
$FIP_{o,ref}$	Reference Maximum Band Average FIP
$\Delta\epsilon_{ref}$	Reference Nominal Strain Range

1 Introduction

Fatigue refers to localised damage in structural materials under cyclic loading. Such a phenomenon can crack a structural component at relatively low engineering stresses or facilitate a surface defect to lead to fatigue failure [1]. Therefore, there is a keen interest in understanding the mechanical response of materials under cyclic loading to ensure safety and structural reliability.

High-performance computing along with numerical models improved our capabilities to redesign and advance better fatigue-resistant materials at low cost. However, efforts are still required to upgrade the models based on existing experiments. Here, this work leverages critical reviewing the existing experiments and models at different scales related to cyclic deformation of face-centered cubic (FCC) metals. The perceived information is used to construct a physics-based model that can predict the deformation response at different length scales and serve as an engineering tool.

1.1 Research motivation

This thesis studies aluminium, which is a widely used commercial aircraft material and a relatively high stacking fault energy FCC metal. Several studies [2–4] reported that the cyclic response of aluminium seems to differ substantially from other FCC metals at room temperature. For instance, a detailed review on cyclic deformation of FCC metals [5] demonstrated that Ni, Cu, and Ag evolve similar saturated dislocation substructures at mesoscale under cyclic loading at room temperature. However, they [5] did not include aluminium due to a lack of persistent slip bands (PSBs) at room temperature.

This research reviews experimental data related to the cyclic response of FCC metals to understand how aluminium differs from other FCC metals. Following on, this research mainly comprises of two main pillars,

1- Understanding aluminium mechanical response under cyclic loading compared to other FCC metals: Development of physics-based crystal

plasticity framework that can predict the cyclic response of aluminium under different loading conditions.

2- Effect of shallow notches on microstructure-sensitive fatigue crack propagation in pure aluminium.

The following sections describe the problem's background and explain the need for research in the respective areas.

1.1.1 Mesoscale substructure evolution during cyclic deformation

When an annealed FCC metal is subjected to fully reversed ($R_\varepsilon = -1$) strain-controlled loading, its microscopic examination shows complex dislocation arrangements: periodically ordered structure with dislocation rich and dislocation poor regions at mesoscale [6]. These dislocation arrangements are also termed as mesoscale dislocation substructures. The distinct stabilised substructures such as veins, persistent slip bands (PSBs), labyrinth, and cells were observed in Ni, Cu, and Ag single crystals subject to different crystal orientations and loading conditions. Figure 1-1 shows the effect of crystal orientation on saturated dislocation substructures evolved in FCC metals during cyclic deformation.

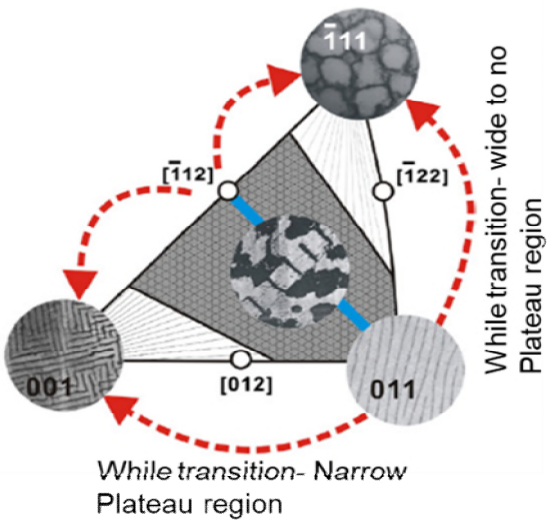

Figure 1-1 Explicit effect of crystal orientation on the evolution of dislocation substructure during cyclic deformation [5].

An important aspect of the mesoscale dislocation substructure is that they have a distinct effect on the cyclic stress-strain curve (CSSC) [5,7] as shown in Figure 1-2 [5]. These substructures accommodate plasticity during cyclic deformation and control hardening (mean stress response) of the material. Recent efforts [8] have proposed a crystal plasticity framework based on mesoscale substructure to predict the cyclic response of Ni single and polycrystal at room temperature. The substructures as shown in Figure 1-2 appear consistently in FCC metals under different loading conditions, which demonstrates that the underlying deformation mechanisms driving these substructures are important for predicting the mechanical response. This further shows that these substructures can be used as an invariant to model the cyclic response of FCC metals.

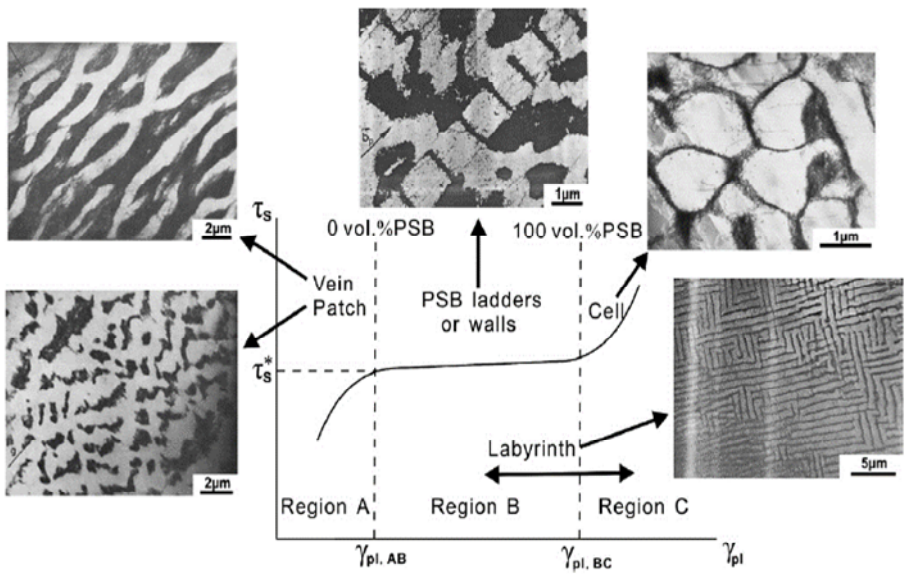

Figure 1-2 Evolution of dislocation substructures corresponds to different stages of CSSC in single slip oriented Cu single crystal [5].

Based on the experimental studies related to FCC single crystals (Ag, Cu, and Ni) by Li et al. [5] and references therein, the effect of loading condition on the dislocation substructure during cyclic deformation can be summarised as,

1. When single crystal oriented for single slip i.e. [123], [-149], and [153] is deformed under cyclic loading, dislocations start accumulating along the primary slip system during the first few initial cycles [9]. Repeated tension and compression cycles produce positive and negative dislocations. These opposite sign dislocations attract each other and become trapped, thereby form dislocation dipoles [10]. Note that only edge dislocations of opposite sign form dislocation dipoles because screw dislocations can annihilate easily by cross slipping if stacking fault energy is high.

   The process of trapping continues until dislocation arrangement within veins is full of dislocation dipoles [10]. These dislocation dipoles form dislocation walls surrounded by dislocation- poor matrix region as shown in Figure 1-2. Mughrabi [7] highlighted that veins can accommodate plasticity upto shear plastic strain amplitude ($\Delta\gamma_p$) of 6×10^{-5} (region A in Figure 1-2). Above $\Delta\gamma_p > 6 \times 10^{-5}$, ladder-type walls develop that lead to persistent slip bands (PSB) structure. These PSBs correspond to the plateau region in CSSC as shown in Figure 1-2. PSBs can accommodate much higher plastic deformation upto 7.5×10^{-3} (region B in Figure 1-2). Upon further loading, when the volume fraction occupied by PSBs reaches 100%, cell structure (region C in Figure 1-2) forms due to activity of secondary slip [11,12].

2. Crystals loaded along the [001] direction form a labyrinth structure due to activation of Hirth locks [5] as shown in Figure 1-2. At low strain amplitudes, vein-type structure forms, which transforms into a labyrinth structure with the increase in strain amplitude [5]. No saturation or plateau region was observed for this orientation [13]. Li et al. [5] demonstrated that critical slip systems play a major role in the formation of labyrinth structures. The (010) is the best plane to view the labyrinth structure, where two sets of PSB ladders form belonging to the primary and secondary critical slip systems.

3. Uniaxial loading along [011] direction typically forms a ladder-type wall structure [5]. The [011] crystals form a plateau region [14] in CSSC similar

to single slip crystals (region B in Figure 1-2). This plateau region becomes narrower, as we move towards [001] and vanishes at [001] as shown in Figure 1-1. The [001] and [011] activate multiple slip systems and have the same Schmid factor (SF), however, the latter does not evolve cross slip [8].

4. Crystals oriented along [111] loading direction has the lowest SF. These crystals also form a vein structure at lower strain amplitude, which directly transforms into cells skipping intermediate PSBs with increasing strain amplitude due to the activation of multiple slip systems and profuse cross slip [15]. The CSSC of [111] crystal also does not present any plateau region [14] similar to [001]. Li et. al. [5] mentioned that the activation of coplanar slip systems plays a primary role in the formation of cell structure.

5. High stacking fault FCC single crystals promote cross-slip and form cell structure earlier at low stresses.

6. The effect of crystal orientation is strongly affected by loading conditions i.e. if the peak stress or strain increases sharply then the cell structure will form irrespective of loading condition [16].

7. Deformation at higher homologous temperature ($\frac{T}{T_m}$) also promotes the formation of cell structure earlier due to the increase of cross slip. However, the upper temperature limit for the disappearance of plateau-region is different for different FCC crystals e.g. for Ni is ~750 K and Cu is ~523K [17,18].

Although not clearly stated, most studies [2–4,19] missed recognizing that aluminium also evolves the same dislocation-substructures [20], however at different absolute temperatures as shown in Figure 1-3.

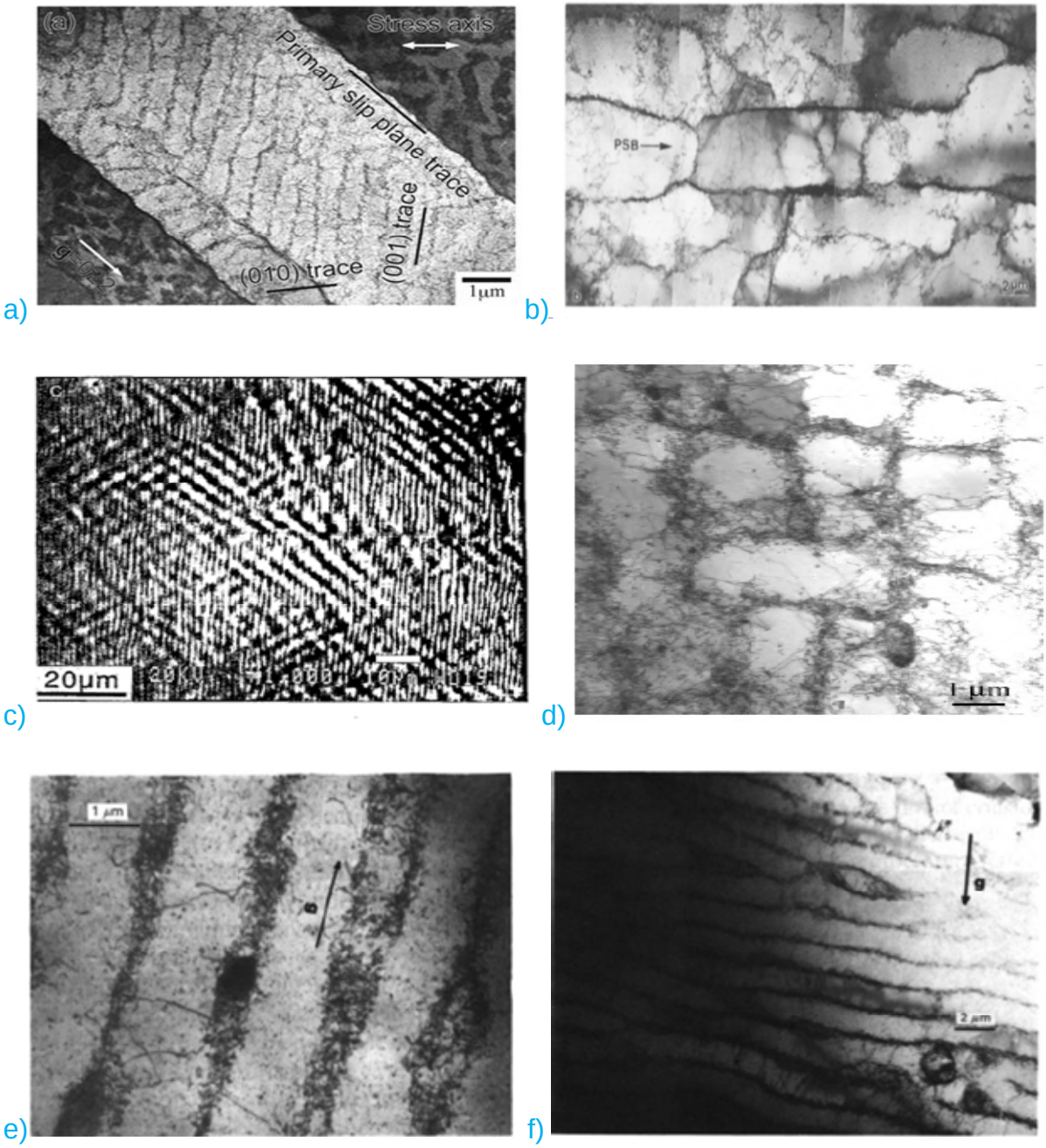

Figure 1-3 a) PSB in aluminium single crystals near ($2\overline{11}$) at $\gamma_{pl} = 3 \times 10^{-3}$, $\gamma_{cum} =$ 96 at 77K [21]**, and b) PSB in aluminium single crystals near ($2\overline{11}$) at $\tau_{res} = 4\ MPa$, $N = 5 \times 10^{6}$ at 298K** [22] **c) Labyrinth structure [001] aluminium single crystal at $\epsilon_{pl} = 3.2 \times 10^{-4}$, $N = 13000$** [23] **d) cell structure in pure aluminium at $\frac{\epsilon_{pl}}{2} = 6.25 \times 10^{-4}$** [24] **e) [100] dislocation walls in pure aluminium**[20] **at 77K, $\Delta\varepsilon = 1.4 \times 10^{-3}$, N = 5000 f) [201] dislocation walls in pure aluminium at 223 K , $\Delta\varepsilon = 6 \times 10^{-4}$, N = 23000** [20]**.**

It is evident from Figure 1-3 that aluminium evolves veins, labyrinth, and cell structures under room temperature and other loading conditions similar to other FCC metals. Besides, Figure 1-3(a) showed that aluminium also evolves ladder-type PSBs at 77K similar to Cu and Ni at 298K. The difference between the mesoscopic response of aluminium and other FCC metals argued in literature [2–4] is the temperature at which substructure develops.

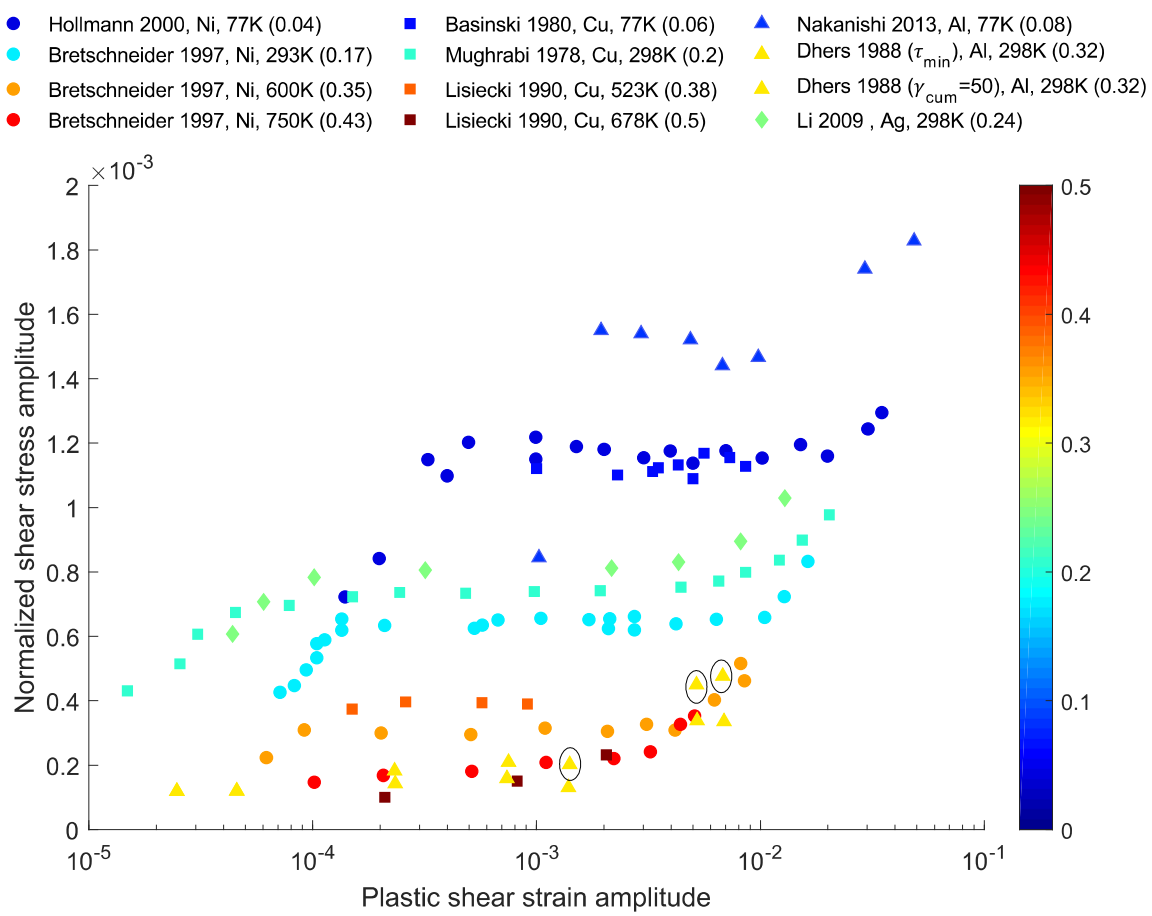

Figure 1-4 Comparison of cyclic response of FCC single crystals [7,17,19,21,25–28]**. Shear stress is normalised by shear modulus at the respective temperature. Colorbar represents homologous temperature ($\frac{T}{T_m}$).**

Figure 1-4 presents the existing experimental data for Ni, Cu, Ag, and aluminium single crystals, which demonstrates further that aluminium has a plateau region at lower number of cycles corresponding PSBs at room temperature. Following on, this work hypothesizes that aluminium evolves similar dislocation

substructures as other FCC metals at different temperatures. However, the detail of the underlying response is an open question. The challenge is determining the physics controlling and deviating the cyclic response of aluminium single crystal. Following on, this work focuses on,

1- Understanding the deformation mechanisms controlling the cyclic response of FCC metals using existing literature to predict the mechanical response,

2- Bridge the modelling gap between medium to high stacking energy FCC metals.

1.1.2 Scribe marks on aircraft fuselage skin

Scribe marks are micron-sized scratches introduced at fuselage joints using a sharp-edge tool during the sealant removal process prior to repainting [29]. These scratches [30,31] are not deeper than 200- 300μm in size, however, their location in a high stressed area close to the joints makes them a potential spot for a small fatigue crack nucleation site. Some investigations [30] showed that scribe marks of less than 200 μm depth can reduce fatigue live significantly under service loads. Following on, Cini A. [32] studied the effect of scribe geometry on nucleation and propagation of small fatigue cracks in cladded 2024- T351 aluminium alloy. The study [32] found that all the scribed samples showed microstructure-sensitive crack growth near the notch root and early growth was strongly influenced by the local microstructure.

Furthermore, the nucleation density of small cracks was found to be sensitive for 25 μm deep scribe inside the cladding (pure aluminium) [32]. Since we aim to develop a physics-based model to study the cyclic response of aluminium, this work further considered employing the crystal plasticity model to study the effect of shallow scribes on microstructure-sensitive fatigue crack growth in pure aluminium along with validating it with experiments [32].

1.2 Crystal plasticity modelling

Microstructure-sensitive small fatigue cracks (MSCs) from shallow scribes spend a major proportion of their fatigue lives growing inside a grain [33] and for entering into the next grain, they need to overcome the local crystal plasticity barrier [34]. Therefore, it is essential to consider the crystal plasticity response of individual grains while studying the growth of MSCs.

In general, there are two kinds of crystal plasticity models: rate-dependent and rate-independent. In the rate-independent crystal plasticity models, the lack of robust strategy to determine slip systems and shear rate on each slip system makes the numerical analysis of crystalline material difficult [35,36]. Alternatively, a rate-dependent crystal plasticity model was proposed by Asaro and Needleman [37] that relate shear rate with resolved shear stress on each slip system. In these models, the amount of shear that appears on certain slip systems depends on the resolved shear stress of that system. This work considered a rate-dependent crystal plasticity model to study the cyclic response of aluminium.

Several researchers [37–39] proposed a power law relation between shear rate and resolved shear stress to study the deformation in ductile single crystals. However, this phenomenological relation lacks physical interpretation such as activation energy required to overcome local barriers to glide etc. Furthermore, the power law relation also does not account for the effect of temperature unless exponent explicitly include it. On the other hand, Gibbs [40] noted that the probability of dislocation to overcome the barrier has Arrhenius temperature dependence on the barrier. He discussed two common formulations to quantify Gibbs free energy (ΔG). The choice of ΔG formulation is one of the differences in present thermally activated flow rules. This work considered both ΔG formulations to quantify dislocation glide activation energy and rationalise the difference.

Another difference in existing rate-dependent crystal plasticity models is the hardening mechanism. Several researchers [41–45] proposed a dislocation density-based hardening mechanism in which the shear rate in slip systems is primarily controlled by dislocation density. The models showed a good agreement with experimental trends. However, these models are much difficult to validate at

microscale due to the error in quantification of dislocation densities experimentally. Besides, these models are calibrated to study the deformation of polycrystals. However, some dislocation density-based models such as those proposed by Ma and Roters [44,46] and Dunne and co-workers [42,43,47,48] do not account for intragranular back stress, which is essential to study the cyclic response of FCC metals [49].

FCC metals at mesoscale evolve dislocation substructures that are composed of low dislocation density soft region and high dislocation density hard regions. These substructures induce back stress that represents kinematic hardening at the macroscopic scale. Some other models [50–52] considered back stress to account for internal stress that arises due to bowing-out of dislocation between precipitates. However, these models do not consider the geometry and wall volume fraction that characterize the dislocation substructure. Lemoine et al. [53] proposed a model that considered cell interior surrounded by a wall to account for back stress. However, this model is thermoelastic and compute very high back stress above 10^{-4} plastic strain [54].

Sauzay [49] proposed a model to estimate the back stress induced by dislocation substructure using Eshelby inclusion problem solution. Castelluccio and McDowell [8] proposed a mesoscale substructure-based hardening mechanism that predicts deformation response of low- medium stacking fault energy FCC single crystals at meso and macroscopic scales. They incorporated a physics-based framework to account for back stress associated with mesoscale dislocation substructure. The model [8] reproduced the stress response of different single crystals oriented along different crystallographic directions without changing model parameters.

Mesoscale substructure-based hardening mechanism has several advantages over dislocation density-based hardening. For instance, volume wall fraction of dislocation walls plays a similar role in kinematic hardening in mesoscale substructure as geometry necessary dislocations (GNDs) in dislocation density-based models. However, volume wall fraction can be validated with more accuracy than GNDs using transmission electron microscopy TEM data.

This work aims to study the effect of shallow scribes on MSCs in single grains. Since the dislocation density-based models were calibrated for the average response of grains (polycrystals), the accurate response of single grain may not be guaranteed. Instead, Castelluccio and McDowell [8] model seem more promising as it accounts for the effect of orientation on the deformation of single crystals. Additionally, this work hypothesised that aluminium evolves similar mesoscale dislocation substructures as other FCC metals but under different loading conditions. This also supports Castelluccio and McDowell [8] model due to the same deformation mechanism at the mesoscale. Moreover, TEM images suggest that parameters related to physical processes at mesoscale should not be much different for aluminium compared to other FCC metals. These parameters have been studied independently using experiments and bottom-up approaches for different FCC single crystals. Therefore, uncertainty related to these parameters can be quantified independently.

However, atomistic scale parameters such as glide activation energy have normally been calibrated for specific models using different approaches [8,55,56]. Thus, a comparison of glide activation energy for different FCC metals is difficult. Besides, glide activation energy parameters cannot be inferred from TEM substructures. Recent progress [57–59] with molecular dynamics simulation has successfully quantified the activation energy barrier. However, their high deformation rates and smaller-scale assumptions limit the applicability of results to coarser multiscale models. Other efforts [55,60] employed macroscopic experimental data to estimate activation energy parameters. However, these phenomenological approaches do not anticipate strengthening from point defects, dislocation, and grain boundaries, which operate at different length scales. Hence, this work aims to quantify and compare the activation energy for FCC metals independent of macroscopic response.

1.3 Microstructure-sensitive fatigue cracks

The term microstructure in this thesis is referred to as microstructural attributes with crystallographic orientation, grain size, and grain morphology, etc. Microstructure-sensitive small fatigue cracks (MSCs) are defined as cracks

having dimensions comparable to or smaller than the material‘s microstructure dimensions [61]. Fatigue damage represents crack initiation and crack growth inside a grain. At this length scale, crack initiation and early growth are influenced by the local microstructure and dislocation substructure [62]. Moreover, the kinetics of MSC growth depends on crack length relative to grain size [63]. These characteristics of small cracks reduce the applicability of traditional fracture mechanics (FM) at the microscale level [61,64]. The similitude assumption of FM states that two cracks in different geometric locations with the same stress intensity factor have the same crack driving force and cracks extend at the same rate per fatigue cycle [61].

MSC growth is sensitive to grain anisotropy and controlled by local plastic shear along the slip systems [62]. This local plastic field of small cracks does not resemble a homogenised plastic field far from the crack tip predicted by FM laws and invalidates the similitude assumption. Hence, the driving force for MSCs needs to be characterised by local fields (stress and strains along slip systems).

Sub-grain localization of slip is sensitive to microstructural features such as grain orientation, grain size, and grain boundaries, etc. These microstructural attributes combined with loading conditions define the accumulation of plasticity in individual slip systems, which further result in the formation of mesoscale dislocation substructures e.g. PSBs [10]. These substructures influence MSC growth.

Forsyth [62] noticed that the early growth of MSCs is driven by local shear along the slip bands. Following on, He [62] characterised MSC growth into two stages i.e. stage I and stage II. Stage I represents the initial phase in which plastic deformation preponderantly occurs along the single most active slip plane, which facilitates the crack to grow along a well-defined crystallographic plane as shown in Figure 1-5. On the other hand, stage II corresponds to the activation of multiple slips along different planes, which results in nonplanar crack growth due to multiaxial driving forces.

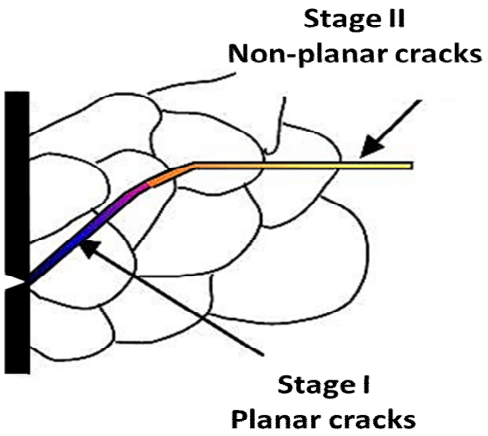

Figure 1-5 Microstructure- sensitive fatigue crack growth: Schematics of transition from planar (stage I) to non-planar (stage II) crack.

The local measures of driving force generally used in continuum models are referred to as fatigue indicator parameters (FIPs). These FIPs are used as a subrogate measure of driving forces that correlated with crack progress. Dunne and their co-workers [65–67] introduced an energy-based FIP to study microstructure-sensitive fatigue crack growth. They proposed that the maximum accumulated energy along the slip systems is an indicator of a crack nucleation site. These efforts [68] also considered predicting crack growth rate from notches using a 2D model, however, the lack of a third dimension may compromise real microstructure-induced fatigue variability. Castelluccio and McDowell [69–71] developed crystal plasticity models to study MSC growth using critical plane-approach based Fatemi-Socie (FS) FIP. They [69] showed an oscillatory crack growth rate inside a grain using FIP as a function of crack length. However, these efforts did not consider the notch effect on microstructural variability of FIPs.

Several other efforts [52,72–74] employed strain accumulation criteria to study MSC growth. Rovinelli et al. [75] performed a probabilistic analysis to assess different energy and slip-based FIPs. The study [75] revealed that all the FIPs show similar behaviour, carry failure information upto an extent, and have an equivalent level of uncertainty. Recently, Wilson et al. [68] argued that energy-based FIP has more physical meaning as compared to FS FIP. In this thesis, cyclic plastic shear strain range (FS FIP) and strain energy along slip systems

that accounts for microstructural sensitivity are used as crack driving force. This work aims to compare FS and energy- based FIPs to study crack propagation in aluminium.

Extensive research [76–80] has been done on studying the effect of a notch on fatigue life. However, these studies considered engineering size (~few mm) notches in which notch root radii was larger compared to the material microstructure. Therefore, a stress field produced by these notches extends many times longer than the microstructure dimensions, which makes these notches insensitive to material microstructure [81]. Contrarily, if the size of the defect is comparable to the grain dimension then crack growth is strongly influenced by local grain anisotropy [32].

The prior literature demonstrates the need for microstructure-sensitive models, however, estimation of fatigue life considering the effect of shallow notches was not studied explicitly. The estimation of fatigue life considering coupled driving forces i.e. geometric and microstructure gradients using crystal plasticity simulations is computationally intensive. This work aims to innovate new computational tools that can predict the effect of geometric gradient on microstructure-sensitive fatigue crack growth.

1.4 Research study rationale

1.4.1 Research aims and objectives

The overall scientific aim of this thesis is to develop a physics-based model that can explain the cyclic response of aluminium single and polycrystals to study microstructure-sensitive fatigue cracks from shallow scribes. The specific objectives are:

I. The dislocation glide activation energy will be estimated for aluminium considering the strain rate effect and methodology will be validated for other FCC metals. Other stochastic scaling level parameters present in the model will be estimated for aluminium independently.

II. The macroscopic cyclic stress-strain response of aluminium will be reproduced by parametrizing the micro and mesoscale attributes. Uncertainty related to model parameters will be quantified independently.

III. The effect of notch geometry and loading conditions will be determined on microstructure-sensitive fatigue crack growth. Models will be compared to experiments in the literature.

1.4.2 Thesis structure

Figure 1-6 presents a graphical summary of the thesis structure. The second chapter (first pillar) overviews the model parameters related to physical processes at atomic scales. Since there is no *ad-hoc* methodology to estimate glide activation energy parameters for different materials, this work proposed the estimation of these parameters for several FCC metals and alloys independent of model response. We consider the interaction of dislocation with point-obstacles as a basic mechanism of strengthening in metals. This work employed a transition state theory (TST) based thermally- activated flow rule, which relates the glide activation barrier with the dependence of yield stress on temperature while coupling information from different scales.

The third chapter (second pillar) considers understanding the cyclic response of aluminium compared to other FCC metals. We recognised that the cyclic response of aluminium is sensitive to number of cycles (*N*) at 298K contrary to other FCC metals. Some efforts [2] have shown the effect of N on dislocation-substructure in stainless steel 316L. However, no other data was found for FCC metals at 298K in this regard. This consideration lacks the attention of researchers. This work aims to predict the explicit effect of *N* along with other loading conditions on the cyclic response of aluminium.

The fourth chapter studies the role of multiple gradients (driving forces) in fatigue crack formation. Since a micron-sized notch has a comparable dimension with grain size, therefore, the local microstructure plays a role in fatigue crack propagation. Hence, fatigue prognosis from a micron-sized notch requires estimating the driving force considering microstructure as well as the geometric

gradient. Firstly, this work aims to study the effect of microstructure and notch geometry on FIPs explicitly. In this thesis, the effect of microstructure on the gradient of FIP as crack extends through a grain is termed as the microstructural gradient. Whereas the effect of notch geometry on the gradient of FIP ahead of notch tip is referred to as geometric gradient. The estimation of coupled geometric and microstructure gradient using crystal plasticity simulation is computationally intensive. This work proposed an engineering approach to couple microstructure and geometric gradients independently to reconstruct an equivalent driving force quantified by crystal plasticity simulation.

The fifth chapter considers estimating microstructure-sensitive transgranular fatigue life using an independently coupled microstructure and geometric gradients proposed in chapter 4. The results are compared with experiments. The approach provides a tool to account for multiple gradients independently that play a role in fatigue crack formation.

The sixth chapter correlates the findings from earlier chapters and discusses the overall impact of the work. Finally, the seventh chapter concludes this work and presents recommendations for future work.

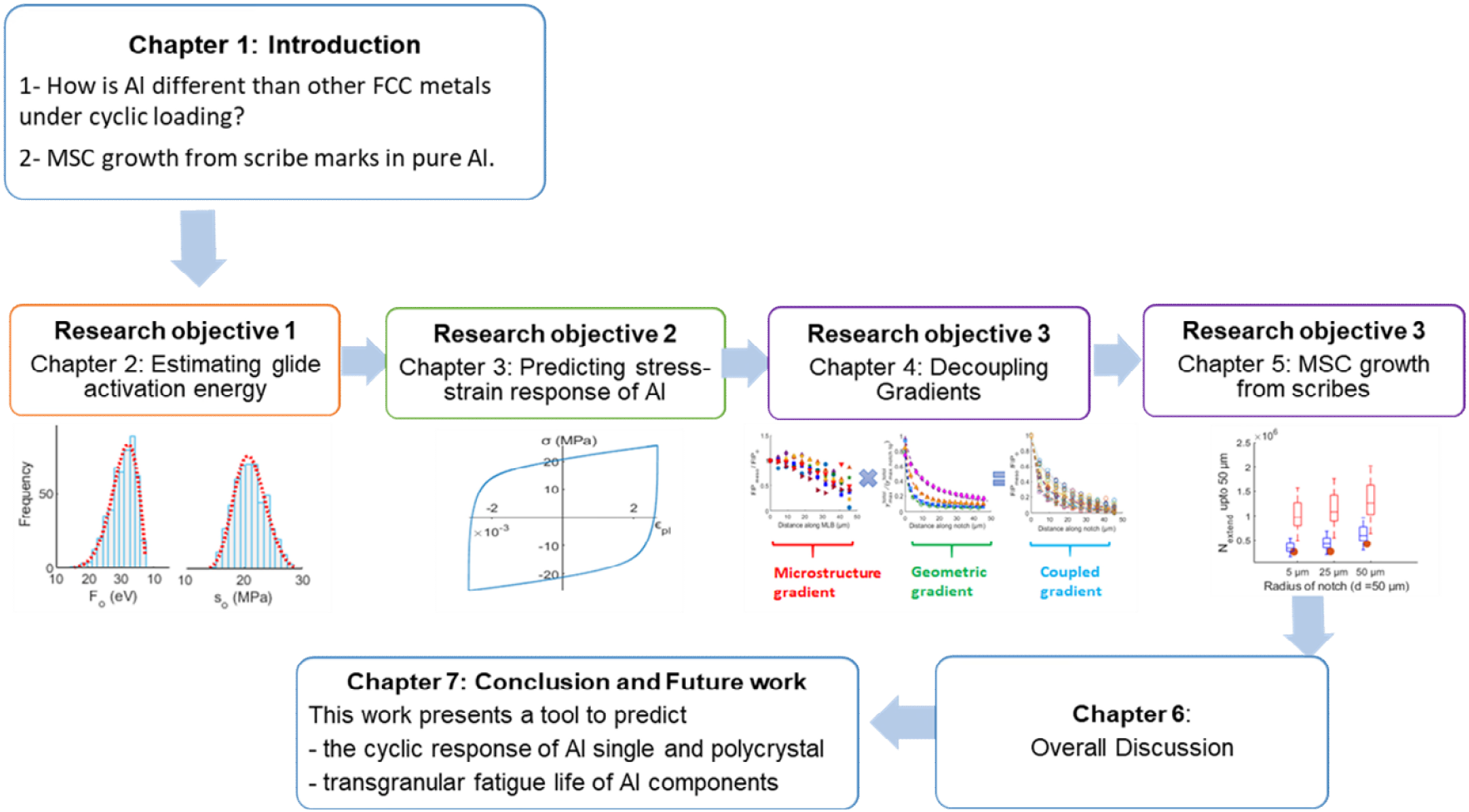

Figure 1-6 Overview of thesis structure.

References

1. FAA. Flight standards information bulletin for airworthiness-FSAW 03-10B: Fuselage skin ‘Scribe Mark’ damage on Boeing 737 aircraft.20/11/2003

2. Vorren O. and Ryum N. Cyclic deformation of Al-single crystals at low constant plastic strain amplitudes. Acta Metallurgica. April 1987; 35(4): 855–866. http://dx.doi.org/10.1016/0001-6160(87)90162-3

3. Vorren O. and Ryum N. Cyclic deformation of Al single crystals: Effect of the crystallographic orientation. Acta Metallurgica. June 1988; 36(6): 1443–1453. http://dx.doi.org/10.1016/0001-6160(88)90212-X

4. Giese A. and Estrin Y. Mechanical behaviour and microstructure of fatigued aluminium single crystals. Scripta Metallurgica et Materiala. 1993; 28(7): 803–807. http://dx.doi.org/10.1016/0956-716X(93)90356-W

5. Li P., Li S,X., Wang Z,G. and Zhang Z.F. Fundamental factors on formation mechanism of dislocation arrangements in cyclically deformed FCC single crystals. Progress in Materials Science. March 2011; 56(3): 328–377. http://dx.doi.org/10.1016/j.pmatsci.2010.12.001

6. Mughrabi H. Dislocation wall and cell structures and long-range internal stresses in deformed metal crystals. Acta Metallurgica. 1983; 31(9): 1367–1379. http://dx.doi.org/10.1016/0001-6160(83)90007-X

7. Mughrabi H. The cyclic hardening and saturation behaviour of copper single crystals. Materials Science and Engineering. 1978; 33(2): 207–223. http://dx.doi.org/10.1016/0025-5416(78)90174-X

8. Castelluccio G.M. and McDowell D.L. Mesoscale cyclic crystal plasticity with dislocation substructures. International Journal of Plasticity. Elsevier Ltd; 2017; 98: 1–26. http://dx.doi.org/10.1016/j.ijplas.2017.06.002

9. Basinski S.J., Basinski Z.S. and Howie A. Early stages of fatigue in copper single crystals. Philosophical Magazine. 1969; 19(161): 899–924. http://dx.doi.org/10.1080/14786436908225856

10. Suresh S. Cyclic deformation in ductile single crystals. Fatigue of Materials. 2012. pp. 39–85. http://dx.doi.org/10.1017/cbo9780511806575.004

11. Tabata T., Fujita H., Hiraoka M.A. and Onishi K. Dislocation behaviour and the formation of persistent slip bands in fatigued copper single crystals observed by high-voltage electron microscopy. Philosophical Magazine A: Physics of Condensed Matter, Structure, Defects and Mechanical Properties. 1983; 47(6): 841–857. http://dx.doi.org/10.1080/01418618308243124

12. Kuhlmann-Wilsdorf D. and Laird C. Dislocation behavior in fatigue. Materials Science and Engineering. February 1977; 27(2): 137–156. http://dx.doi.org/10.1016/0025-5416(77)90166-5

13. Wang Z., Gong B. and Wang Z. Cyclic deformation behavior and dislocation structures of [001] copper single crystals - II. characteristics of dislocation structures. Acta Materialia. April 1997; 45(4): 1379–1391. http://dx.doi.org/10.1016/S1359-6454(96)00289-3

14. Buque C. Dislocation structures and cyclic behaviour of [011] and [1̄11]-oriented nickel single crystals. International Journal of Fatigue. 2001; 23(8): 671–678. http://dx.doi.org/10.1016/S0142-1123(01)00032-9

15. Li X.W., Zhou Y., Guo W.W. and Zhang G.P. Characterization of dislocation structures in [i11] copper single crystals using electron channelling contrast technique in SEM. Crystal Research and Technology. March 2009; 44(3): 315–321. http://dx.doi.org/10.1002/crat.200800346

16. Lukáš P., Kunz L. and Svoboda M. Stress-strain response and fatigue life of copper single crystals cyclically loaded with a positive mean stress. Materials Science and Engineering A. 1999; 272(1): 31–37. http://dx.doi.org/10.1016/S0921-5093(99)00462-1

17. Lisiecki L.L. and Weertman J.R. Orientation effects on the elevated temperature fatigue of copper single crystals. Acta Metallurgica Et Materialia. 1990; 38(3): 509–519. http://dx.doi.org/10.1016/0956-

7151(90)90157-C

18. Holste C., Bretschneider J. and Tippelt B. Effect of deformation temperature on cyclic plasticity. Materials Science and Engineering A. 1997; 234–236: 743–746. http://dx.doi.org/10.1016/s0921-5093(97)00385-7

19. Dhers J. and Driver J. The cyclic response and microstructures of aluminium single crystal. In: Lukáš P, Polak J, editors. Basic mechanisms in fatigue of metals. Materials science monographs, vol. 46. Amsterdam: Elsevier; 1988. p. 33

20. Charsley P., Bangert U. and Appleby L.J. The effect of temperature and amplitude on dislocation structures in cyclically deformed pure aluminium. Materials Science and Engineering A. 1989; 113(C): 231–236. http://dx.doi.org/10.1016/0921-5093(89)90311-0

21. Nakanishi Y., Tanaka H., Fujii T.,Onaka S. and Kato M. Low-temperature fatigue behaviour and development of dislocation structure in aluminium single crystals with single-slip orientation. Philosophical Magazine. 2013; 93(21): 2759–2768. http://dx.doi.org/10.1080/14786435.2013.786193

22. Zhai T., Martin J.W., Briggs G.A.D. and Road P. Fatigue damage at room temperature aluminium single crystals -II. tem. Acta Metallurgica. 1996; 44(5): 1729–1739.

23. Videm M. and Ryum N. Cyclic deformation of [001] aluminium single crystals. Materials Science and Engineering A. November 1996; 219(1–2): 1–10. http://dx.doi.org/10.1016/S0921-5093(96)10261-6

24. El-Madhoun Y., Mohamed A. and Bassim M.N. Cyclic stress-strain response and dislocation structures in polycrystalline aluminum. Materials Science and Engineering A. 2003; 359(1–2): 220–227. http://dx.doi.org/10.1016/S0921-5093(03)00347-2

25. Hollmann M. Strain localization in nickel single crystals cyclically deformed at 77 K. Philosophical Magazine Letters. 2000; 80(9): 613–619.

http://dx.doi.org/10.1080/09500830050134327

26. Bretschneider J., Holste C. and Tippelt B. Cyclic plasticity of nickel single crystals at elevated temperatures. Acta Materialia. September 1997; 45(9): 3775–3783. http://dx.doi.org/10.1016/S1359-6454(97)00030-X

27. Basinski Z.S., Korbel A.S. and Basinski S.J. The temperature dependence of the saturation stress and dislocation substructure in fatigued copper single crystals. Acta Metallurgica. February 1980; 28(2): 191–207. http://dx.doi.org/10.1016/0001-6160(80)90068-1

28. Li P., Zhang Z.F., Li S.X. and Wang Z.G. Cyclic deformation and fatigue damage behaviors of [$\bar{1}414$] oriented Ag single crystal. Philosophical Magazine. 2009; 89(32): 2903–2920. http://dx.doi.org/10.1080/14786430903130847

29. Das G., Kosai M. and Miller M. Development of a method for damage tolerance analysis for scribe marks adjacent to fuselage longitudinal and circumferential splices. International Committee on Aeronautical Fatigue (ICAF) meeting. Napoli, Italy; 2007. pp. 14–18.

30. Paint and sealant removal process. Airworthiness Notice No. B071, 3/11/2004

31. FAA airworthiness directives no. FAA-2005-20918, 31/3/2006

32. Cini A. Scribe marks at fuselage joints:Initiation and propagation of fatigue cracks from mechanical defects in aluminium alloys. PhD thesis. 2012 Cranfield University.UK.

33. Cini A. and Irving P.E. Transformation of defects into fatigue cracks; the role of kt and defect scale on fatigue life of non-pristine components. Procedia Engineering. 2010; 2(1): 667–677. http://dx.doi.org/10.1016/j.proeng.2010.03.072

34. Tokaji k. and Ogawa T. The growth behaviour of microstructurally small fatigue cracks in metals. Mechanical Engineering Publications. London:

Mechanical Engineering Publications; 1992. pp. 85–99.

35. Anand L. and Kothari M. A computational procedure for rate-independent crystal plasticity. Journal of the Mechanics and Physics of Solids. Elsevier Ltd; 1 April 1996; 44(4): 525–558. http://dx.doi.org/10.1016/0022-5096(96)00001-4

36. Gambin W. Refined analysis of elastic-plastic crystals. International Journal of Solids and Structures. Pergamon; 1 January 1992; 29(16): 2013–2021. http://dx.doi.org/10.1016/0020-7683(92)90191-U

37. Asaro R.J. and Needleman A. Overview no. 42 texture development and strain hardening in rate dependent polycrystals. Acta Metallurgica. 1985; 33(6): 923–953. http://dx.doi.org/10.1016/0001-6160(85)90188-9

38. Peirce D., Asaro R.J. and Needleman A. An analysis of nonuniform and localized deformation in ductile single crystals. Acta Metallurgica. 1982; 30(6): 1087–1119. http://dx.doi.org/10.1016/0001-6160(82)90005-0

39. Rice J.R. Inelastic constitutive relations for solids: An internal-variable theory and its application to metal plasticity. Journal of the Mechanics and Physics of Solids. 1971; 19(6): 433–455. http://dx.doi.org/10.1016/0022-5096(71)90010-X

40. Gibbs G.B. Thermodynamic analysis of dislocation glide controlled by dispersed local obstacles. Materials Science and Engineering. 1969; 4(6): 313–328. http://dx.doi.org/10.1016/0025-5416(69)90026-3

41. Liu Y. and Dunne F.P.E. The mechanistic link between macrozones and dwell fatigue in titanium alloys. International Journal of Fatigue. 2021; 142: 105971. http://dx.doi.org/10.1016/j.ijfatigue.2020.105971

42. Paramatmuni C. and Dunne F.P.E. Effect of twin crystallographic orientation on deformation and growth in mg alloy AZ31. International Journal of Plasticity.2020; 135: 102775. http://dx.doi.org/10.1016/j.ijplas.2020.102775

43. Paramatmuni C., Zheng Z.,Rainforth W.M. and Dunne F.P.E. Twin nucleation and variant selection in Mg alloys: An integrated crystal plasticity modelling and experimental approach. International Journal of Plasticity. 2020; 135: 102778. http://dx.doi.org/10.1016/j.ijplas.2020.102778

44. Ma A. and Roters F. A constitutive model for FCC single crystals based on dislocation densities and its application to uniaxial compression of aluminium single crystals. Acta Materialia. July 2004; 52(12): 3603–3612. http://dx.doi.org/10.1016/j.actamat.2004.04.012

45. Ma A., Roters F. and Raabe D. A dislocation density based constitutive model for crystal plasticity fem including geometrically necessary dislocations. 2006; 54: 2169–2179. http://dx.doi.org/10.1016/j.actamat.2006.01.005

46. Ma A., Roters F. and Raabe D. A dislocation density based constitutive model for crystal plasticity FEM. Materials Science Forum. 2005; 495–497: 1007–1012. http://dx.doi.org/10.4028/www.scientific.net/msf.495-497.1007

47. Lu X., Dunne FPE. and Xu Y. A crystal plasticity investigation of slip system interaction, GND density and stored energy in non-proportional fatigue in nickel-based superalloy. International Journal of Fatigue. 2020; 139(April): 105782. http://dx.doi.org/10.1016/j.ijfatigue.2020.105782

48. Chen L., James Edwards T.E., Di Gioacchino F., Clegg W.J., Dunne F.P.E. and Pham M.S. Crystal plasticity analysis of deformation anisotropy of lamellar TiAl alloy: 3D microstructure-based modelling and in-situ microcompression. International Journal of Plasticity. 2019; 119: 344–360. http://dx.doi.org/10.1016/j.ijplas.2019.04.012

49. Sauzay M. Analytical modelling of intragranular backstresses due to deformation induced dislocation microstructures. International Journal of Plasticity. May 2008; 24(5): 727–745. http://dx.doi.org/10.1016/j.ijplas.2007.07.004

50. Lin B., Zhao LG., Tong J. and Christ H.J. Crystal plasticity modeling of cyclic deformation for a polycrystalline nickel-based superalloy at high temperature. Materials Science and Engineering A. 2010; 527(15): 3581–3587. http://dx.doi.org/10.1016/j.msea.2010.02.045

51. Lin B., Zhao LG. and Tong J. A crystal plasticity study of cyclic constitutive behaviour, crack-tip deformation and crack-growth path for a polycrystalline nickel-based superalloy. Engineering Fracture Mechanics. July 2011; 78(10): 2174–2192. http://dx.doi.org/10.1016/j.engfracmech.2011.04.006

52. Farukh F., Zhao LG., Jiang R., Reed P., Proprentner D. and Shollock B.A. Realistic microstructure-based modelling of cyclic deformation and crack growth using crystal plasticity. Computational Materials Science. 2016; 111: 395–405. http://dx.doi.org/10.1016/j.commatsci.2015.09.054

53. Lemoine X., Berveiller M. and Muller D. Texture of microstructures in BCC metals for various loading paths. Materials Science Forum. 1994; 157–6(pt 2): 1821–1826. http://dx.doi.org/10.4028/www.scientific.net/msf.157-162.1821

54. Berveiller M. and Zaoui A. An extension of the self-consistent scheme to plastically-flowing polycrystals. Journal of the Mechanics and Physics of Solids. 1978; 26(5–6): 325–344. http://dx.doi.org/10.1016/0022-5096(78)90003-0

55. Balasubramanian S. and Anand L. Elasto-viscoplastic constitutive equations for polycrystalline FCC materials at low homologous temperatures. Journal of the Mechanics and Physics of Solids. 2002; 50(1): 101–126. http://dx.doi.org/10.1016/S0022-5096(01)00022-9

56. Wilson D., Wan W. and Dunne F.P.E. Microstructurally-sensitive fatigue crack growth in HCP, BCC and FCC polycrystals. Journal of the Mechanics and Physics of Solids. 2019; 126: 204–225. http://dx.doi.org/10.1016/j.jmps.2019.02.012

57. Sobie C., Capolungo L., McDowell D.L. and Martinez E. Thermal activation

of dislocations in large scale obstacle bypass. Journal of the Mechanics and Physics of Solids. 2017; 105: 150–160. http://dx.doi.org/10.1016/j.jmps.2017.05.003

58. Esteban-Manzanares G., Martínez E.,Segurado J., Capolungo L. and LLorca J. An atomistic investigation of the interaction of dislocations with guinier-preston zones in Al-Cu alloys. Acta Materialia. 2019; 162: 189–201. http://dx.doi.org/10.1016/j.actamat.2018.09.052

59. Narayanan S., McDowell D.L. and Zhu T. Crystal plasticity model for BCC iron atomistically informed by kinetics of correlated kinkpair nucleation on screw dislocation. Journal of the Mechanics and Physics of Solids. Elsevier; 2014; 65(1): 54–68. http://dx.doi.org/10.1016/j.jmps.2014.01.004

60. Kocks U.F. Realistic constitutive relations for metal plasticity. Materials Science and Engineering A. 2001; 317(1–2): 181–187. http://dx.doi.org/10.1016/S0921-5093(01)01174-1

61. Suresh S. Small fatigue cracks. Fatigue of materials. 2nd edn. Cambridge University Press; 1998. http://dx.doi.org/10.1017/cbo97805118065755

62. P. J. E. Forsyth. A two stage process of fatigue crack growth royal aircratt establishment. Proceedings of the Crack Propagation Symposium. 1961. pp. 76–94.

63. Miller K.J. The three thresholds for fatigue crack propagation. ASTM Special Technical Publication. ASTM; 1997. pp. 267–286. http://dx.doi.org/10.1520/stp16238s

64. Ritchie R.O. and Suresh S. The fracture mechanics similitude concept: questions concerning its application to the behavior of short fatigue cracks. Materials Science and Engineering. 1983; 57(2): L27–L30. http://dx.doi.org/10.1016/0025-5416(83)90223-9

65. Wan V.V.C., Jiang J., MacLachlan D.W. and Dunne F.P.E. Microstructure-sensitive fatigue crack nucleation in a polycrystalline ni superalloy. International Journal of Fatigue. 2016; 90: 181–190.

http://dx.doi.org/10.1016/j.ijfatigue.2016.04.013

66. Wilson D. and Dunne F.P.E. A mechanistic modelling methodology for microstructure-sensitive fatigue crack growth. Journal of the Mechanics and Physics of Solids. 2019; 124: 827–848. http://dx.doi.org/10.1016/j.jmps.2018.11.023

67. Wan V.V.C., Maclachlan D.W. and Dunne F.P.E. A stored energy criterion for fatigue crack nucleation in polycrystals. International Journal of Fatigue. 2014; 68: 90–102. http://dx.doi.org/10.1016/j.ijfatigue.2014.06.001

68. Wilson D., Zheng Z. and Dunne FPE. A microstructure-sensitive driving force for crack growth. Journal of the Mechanics and Physics of Solids. 2018; 121: 147–174. http://dx.doi.org/10.1016/j.jmps.2018.07.005

69. Castelluccio G.M. and McDowell D.L. A mesoscale approach for growth of 3D microstructurally small fatigue cracks in polycrystals. International Journal of Damage Mechanics. 2014; 23(6): 791–818. http://dx.doi.org/10.1177/1056789513513916

70. Castelluccio G.M. and McDowell D.L. Microstructure-sensitive small fatigue crack growth assessment: effect of strain ratio, multiaxial strain state, and geometric discontinuities. International Journal of Fatigue. 2015; 82: 521–529. http://dx.doi.org/10.1016/j.ijfatigue.2015.09.007

71. Castelluccio G.M. and McDowell D.L. Microstructure and mesh sensitivities of mesoscale surrogate driving force measures for transgranular fatigue cracks in polycrystals. Materials Science and Engineering A. July 2015; 639: 626–639. http://dx.doi.org/10.1016/j.msea.2015.05.048

72. Hochhalter J.D., Littlewood D.J., Christ R.J.,Veilleux M.G., Bozek J.E., Ingraffea A.R.,et al. A geometric approach to modeling microstructurally small fatigue crack formation: II. physically based modeling of microstructure-dependent slip localization and actuation of the crack nucleation mechanism in AA 7075-t651. Modelling and Simulation in Materials Science and Engineering. 2010; 18(4): 045004.

http://dx.doi.org/10.1088/0965-0393/18/4/045004

73. Zhang P., Zhang L., Baxevanakis K.P., Zhao LG. and Bullough C. Modelling short crack propagation in a single crystal nickel-based superalloy using crystal plasticity and XFEM. International Journal of Fatigue. 2020; 136: 105594. http://dx.doi.org/10.1016/j.ijfatigue.2020.105594

74. Zhang L., Zhao L., Jiang R. and Bullough C. Crystal plasticity finite-element modelling of cyclic deformation and crack initiation in a nickel-based single-crystal superalloy under low-cycle fatigue. Fatigue & Fracture of Engineering Materials & Structures. Blackwell Publishing Ltd; 13 August 2020; 43(8): 1769–1783. http://dx.doi.org/10.1111/ffe.13228

75. Rovinelli A., Guilhem Y., Proudhon H., Lebensohn R.A., Ludwig W. and Sangid M.D. Assessing reliability of fatigue indicator parameters for small crack growth via a probabilistic framework. Modelling and Simulation in Materials Science and Engineering. IOP Publishing; 2017; 25(4). http://dx.doi.org/10.1088/1361-651X/aa6c45

76. Smith R.A. and Miller K.J. Prediction of fatigue regimes in notched components. International Journal of Mechanical Sciences. 1978; 20(4): 201–206. http://dx.doi.org/10.1016/0020-7403(78)90082-6

77. Smith R.A. and Miller K.J. Fatigue cracks at notches. International Journal of Mechanical Sciences. Pergamon; 1 January 1977; 19(1): 11–22. http://dx.doi.org/10.1016/0020-7403(77)90011-X

78. Chapetti M.D. and Guerrero A.O. Estimation of notch sensitivity and size effect on fatigue resistance. Procedia Engineering. Elsevier B.V.; 2013; 66: 323–333. http://dx.doi.org/10.1016/j.proeng.2013.12.087

79. Gates N. and Fatemi A. Notched fatigue behavior and stress analysis under multiaxial states of stress. International Journal of Fatigue. October 2014; 67: 2–14. http://dx.doi.org/10.1016/j.ijfatigue.2014.01.014

80. McEvily A.J., Endo M., Yamashita K., Ishihara S. and Matsunaga H.

Fatigue notch sensitivity and the notch size effect. International Journal of Fatigue. 2008; 30(12): 2087–2093. http://dx.doi.org/10.1016/j.ijfatigue.2008.07.001

81. Neuber, H. Theory of notch stresses: Principle for exact stress calculation ed. Ann Arbor, MI: Edwards, 1946.

2 Estimation of Dislocation Glide Barrier in FCC Metals and Alloys

2.1 Introduction

Strain hardening in single-phase metallic materials is often controlled by the production and flux of point and line defects [1]. Vacancies, interstitials and substitutional atoms, dislocations, lattice mismatch, and grain boundaries, etc., independently contribute to hardening and create an energy barrier that needs to be overcome to enable the plastic flow. Frost and Ashby [2] characterised dislocation strengthening by obstacles as weak, medium, and strong based on the type of interactions. Point obstacles such as isolated solute atoms, interstitials, and vacancies are weak strength obstacles; forest dislocations or dislocation- dislocations are medium strength obstacles while precipitates are strong obstacles. In a general engineering alloy, these obstacles coexist and contribute to the overall resistance.

Recent progress with molecular dynamics calculations [3–5] has successfully quantified the energy barrier for simple systems. However, the small scale and high rate of deformation of atomistic models make it difficult to transfer quantitative data to coarser multiscale models. Furthermore, the combinatorial analysis of atoms distributions in alloys is still unresolved and the results are often valid for a specific strengthening mechanism with a certain atomic order. Other efforts [6,7] have attempted to calculate the activation energy for dislocation glide from macroscopic experimental data. For example, Frost and Ashby [2] characterised plastic flow by considering the yield stress at low temperatures. Following this idea, Balasubramanian and Anand [8] calculated activation energy to study the elasto-viscoplastic behaviour of polycrystalline aluminium. Their approach computes the thermal and athermal hardening simultaneously using yield stress data at different temperatures for polycrystalline aluminium. Thermal stress represents thermally activated barrier due to solute atoms, vacancies or short-range interactions that can be overcome with aid of thermal activation at

atomistic scale. Whereas athermal stress corresponds to temperature independent dislocations interactions such as pile ups or long-range interactions at mesoscopic scale. The aforementioned approaches [8] relied on phenomenological constitutive models that do not discern strengthening from point defects, dislocation, and grain boundaries, which operate at different length scales. A further limitation of previous efforts is the simultaneous estimation of multiple parameters, which sums up the uncertainty from various mechanisms across different scales. Indeed, not all mechanisms become active upon a change in loading conditions (e.g., monotonic, cyclic, etc.), so the results are not fully transferable across scales, models, and loading conditions.

Here, we leverage on the approach introduced by Frost and Ashby [2], but we explicitly decouple the contribution of thermal and athermal stresses to parameterize the thermally-activated energy barrier for dislocation glide overcoming point obstacles. The glide activation barrier is characterised with a Monte Carlo approach by fitting a physics-based model that conveys independent strengthening mechanisms across scales to the tabulated yield stress data at different temperatures. Each mechanism is associated with uncertainty related to different input parameters, which are quantified independently. The results for different FCC metals and alloys provide a confined range for activation energies while informing the effect of model uncertainties.

2.2 Mechanisms of dislocation glide

Over 50 years ago, Eyring [9] recognised that inelastic deformation conforms to the principles of transition state theory (TST) and he hypothesised that stochastic perturbations at the atomic level control the rate at which dislocations glide. Indeed, atomistic simulations [4,5] have corroborated the stochastic nature of the mechanisms that control plastic flow. For instance, Esteban et al. [4] used molecular dynamics to compute the glide activation energy from the strengthening of Guinier-Preston zones. Similarly, Dong et al. [10] simulated the glide of a single dislocation to study the strengthening associated with the collaborative response of multiple obstacle types. However, their modelling

framework considered only athermal strengthening and lack of thermal activation explicitly.

Following the TST approach, Gibbs [11] noted that the probability (Γ) of a dislocation to overcome an obstacle can be computed as,

$$\Gamma = \exp\left(\frac{-\Delta G(\tau)}{k_B T}\right) \quad , \qquad \textbf{(2.1)}$$

in which, k_B is the Boltzmann constant, T is the temperature and ΔG is the Gibbs free activation energy required by a dislocation to bypass the barrier, which depends upon the local shear stress (τ). The nature of the Gibbs free activation energy is still of much debate and there is no consensus on the most adequate formulation to estimate ΔG.

Gibbs [11] discussed in detail probably the two most common approaches used to quantify ΔG. On the one hand, Gibbs free energy has been characterised by a dislocation-obstacle interaction potential, whose first derivate corresponds to the evolution of force (F) as a function of the distance travelled by a dislocation over the barrier (x). Seeger [12], Fleischer [13], and Mott and Nabarro [14] independently proposed interaction potentials considering different force-displacement curves such as exponential, local tetragonal distortion, and sinusoidal, respectively. These interaction potentials can be described by,

$$\Delta G = F_0\left(1 - \left(\frac{\tau}{s_0^t}\right)^p\right)^q, \qquad \textbf{(2.2)}$$

in which F_0 is the activation energy at zero stress, s_0^t is the thermal stress at 0 K, and *p* and *q* *are* profile parameters that range between 0 to 1 and 1 to 2, respectively. On the other hand, the Gibbs free energy has also been quantified by,

$$\Delta G = \Delta F - \tau \Delta V \ , \qquad \textbf{(2.3)}$$

in which ΔV corresponds to the thermodynamic activation volume and ΔF is Helmholtz free energy.

Despite the ample use of both formulations, Langer [15] have recently argued about the lack of physical understanding of the origin of these mathematical formulations and has proposed a thermodynamically consistent approach in which:

$$\Delta G = F_0^* \exp\left(-\frac{\tau}{s_0^*}\right). \quad \textbf{(2.4)}$$

Where, F_0^* is the pinning energy at zero stress and s_0^* is the Taylor stress. Equations (2.2), (2.3), and (2.4) assume that their parameters are temperature-independent. As noted by Kocks et al. [16], the temperature-independence of parameters is a reasonable assumption for glide resistance profiles without a plateau, which is the case for most FCC metals and alloys up to moderate temperatures. Since equation (2.2) requires four parameters rather than two as in the other two approaches, it makes the quantification of the parameters more stringent. Hence, we initially focus on determining independently the parameters for equation (2.2), which formulation has been extensively employed to model strain hardening in FCC single and polycrystals [8,17,18].

Following the Orowan equation, we can relate the shear strain rate along the primary slip system (α) with the Gibbs free energy as,

$$\dot{\gamma}^\alpha = \dot{\gamma}_0^\alpha \exp\left(\frac{-\Delta G(\tau)}{k_B T}\right) \quad \textbf{(2.5)}$$

which combined with equation (2.2) leads to [17],

$$\dot{\gamma}^\alpha = \dot{\gamma}_0^\alpha \exp\left[-\frac{F_0}{k_B T}\left\{1 - \left(\frac{\tau_{eff}^\alpha}{s_0^t \frac{\mu}{\mu_0}}\right)^p\right\}^q\right] \quad \textbf{(2.6)}$$

Where, τ_{eff}^α is the effective shear stress, the parameters μ and μ_0 correspond to the shear modulus at T and 0K. Following on, the effective shear stress in equation (2.6) considers dislocation long-range interactions,

$$\tau_{eff}^\alpha = \langle |\tau^\alpha - B^\alpha| - S^\alpha \rangle \quad \textbf{(2.7)}$$

and depends on the local resolved shear stress, (τ^{α}), the athermal stress (S^{α}), and the long-range intragranular back stress (B^{α}) induced by the localization of dislocation densities.

Since multiple deformation mechanisms become operative during deformation, the quantification of all relevant strengthening mechanisms along the entire stress-strain curve is a grand challenge. Instead, we limit the number of mechanisms by analyzing the deformation up to yield. Indeed, the influence of cross slip or long-range back stresses is less likely to be dominant at yield in well-annealed materials. Instead, yielding is more likely to be dominated by the strength of dislocation pinning by point obstacles, as shown by the strong influence of impurities on yield stress [19]. Even when not all deformation mechanisms are activated, the yield stress still carries a significant amount of variability that should be taken into consideration. Based on this, we reorganised equation (2.6) in terms of the yield stress as follows,

$$\sigma_y^{\alpha} = \left[S^{\alpha} + \left(s_0^t \frac{\mu}{\mu_0} \right) \left[1 - \left\{ -\frac{k_B T}{F_0} \ln \left(\frac{\dot{\gamma}_y^{\alpha}}{\dot{\gamma}_0^{\alpha}} \right) \right\}^{\frac{1}{q}} \right]^{\frac{1}{p}} \right] \times C_f . \qquad \textbf{(2.8)}$$

Here, $\dot{\gamma}_y^{\alpha}$ is the strain rate, which corresponds to yield stress, C_f is a conversion factor that projects the mean shear stress into normal stress [20] and has a value that typically ranges from the Taylor factor (3.06) as an upper bound and to the Sachs factor (2.238) as a lower bound. This range represents an independent and approximate estimate of the conversion factor and accounts for some crystallographic variability.

The athermal stress in equation (2.8) follows [17],

$$S^{\alpha} = \alpha_{LE} \frac{\mu b}{2 d_{struc}} + \mu b \sqrt{A_{ii} \rho^{\alpha}} \quad , \qquad \textbf{(2.9)}$$

which conveys the stress required to bow-out dislocations (controlling dislocation production) and dislocation interaction stress (controlling coplanar hardening in Stage I). Here, α_{LE} corresponds to the line energy scaling factor while A_{ii} is the average interaction coefficient. In annealed metals, the contribution from latent

hardening on the stress at the onset of plastic deformation is negligible [21]. The principal role of dislocation production on secondary slip systems consists of promoting the formation of dislocation substructures and limiting the dislocation free path of the dominant slip. The dislocation substructure length scale d_{struc} in equation (2.9) follows a similitude relation [22] as,

$$d_{struc} = K_{struc} \frac{\mu b}{\tau} \quad , \tag{2.10}$$

Where, K_{struc} is the similitude coefficient. By inserting the value of d_{struc} in equation (2.9), we get

$$S^{\alpha} = \alpha_{LE} \frac{\sigma_y^{\alpha}}{2C_f K_{struc}} + \mu b \sqrt{A_{ii} \rho^{\alpha}} \tag{2.11}$$

Here, ρ^{α} is the dislocation density on the primary slip system α. At yielding, macroscopic annealed materials have sparse dislocations and strengthening relies mostly on self-hardening interactions (we assume crystals over 1μm in size to neglect dislocation starvation hardening [23]). We further incorporate the variability of hardening mechanisms by considering the uncertainty of the initial dislocation density and the role of grain size on limiting dislocation glide. Following on, we divide the total dislocation density into two contributions: initial dislocation density after annealing (${\rho_o}^{\alpha}$) and the increase in dislocation density upon loading up to yield ($\Delta{\rho_y}^{\alpha}$),

$$\rho^{\alpha} = {\rho_o}^{\alpha} + \Delta{\rho_y}^{\alpha} \, , \tag{2.12}$$

Hansen [24] demonstrated that the dislocation density depends on grain size for the flow stress at intermediate strains, which is due to differences in the dislocations mean free paths. Hence, $\Delta{\rho_y}^{\alpha}$ follows,

$$\Delta{\rho_y}^{\alpha} = \frac{K_{multi}\, \gamma^{\alpha}}{bd} \quad , \tag{2.13}$$

where, K_{multi} is related to the production of dislocations and its value ranges between 1 and 4 [24–27], while γ^{α} is the shear strain. The mean free path (*d)* can be estimated roughly as half the grain size, which corresponds to the average distance a dislocation would travel through the grain. Since the mean free path

impacts dislocation density and strengthening, equation (2.13) effectively introduces a dependence on the grain size and accounts for Hall-Petch effects.

Finally, $\dot{\gamma}_0^\alpha$ represents the effective shearing rate for a successful thermal activation event. The rate of increment in inelastic strain depends on the frequency, at which dislocations jump over point obstacles,

$$\dot{\gamma}_0^\alpha = \rho^\alpha b l_v \frac{k_B T}{h} \quad , \qquad \textbf{(2.14)}$$

In which h is Planck's constant, and l_v is the mean spacing between point obstacles. The term $k_B T/h$ comes from Eyring's reaction rate theory [28] collectively corresponds to an attempt frequency between 10^{10} to 10^{12} s^{-1}. The obstacle spacing has a significant role in bypassing the energy barrier during thermal activation because a single event can create a cascade of unpinning events [29].

By inserting the S^α and $\dot{\gamma}_0^\alpha$ from equation (2.11) and (2.14) in equation (2.8) and rearranging in terms of σ_y^α, we obtain a formulation that employs the glide activation energy to predict the yield stress as a function of temperature and strain rate,

$$\sigma_y^\alpha(T) = \left[\mu b\sqrt{A_{ii}\rho^\alpha} + \left(s_0^t \frac{\mu}{\mu_0}\right)\left[1 - \left\{-\frac{k_B T}{F_0}\ln\left(\frac{\dot{\gamma}^\alpha}{\rho^\alpha b l_v \frac{k_B T}{h}}\right)\right\}^{\frac{1}{q}}\right]^{\frac{1}{p}}\right] \times \frac{2C_f K_{struc}}{(2K_{struc} - \alpha_{LE})}. \qquad \textbf{(2.15)}$$

Next, we employ experimental data and non-linear minimum-square regression to estimate, F_0, s_0^t, p and q independent of all other parameters.

2.3 Independent estimation of parameters and their uncertainty

We qualitatively divide the parameters in equation (2.15) into two categories related to their uncertainties: the first is related to fundamental parameters with low uncertainty such as k_B and b. The shear modulus (μ) is also a material parameter with relatively low uncertainty, which we accounted for by considering the Reuss and Voigt [30] models as lower and upper bounds respectively. These were computed using the elastic constants dependent on temperature from

Varshni [31]. Overall, the uncertainty of elastic constants has a minor secondary effect as demonstrated in Appendix A.1 (Figure A-1).

High-uncertainty parameters are associated with the description of the mean value of stochastic processes such as atomic jump and dislocation-dislocation interactions. Dislocation density is one of the stochastic parameters that strongly depends on loading history and processing. Since its experimentally difficult and time consuming to precisely determine dislocation density values, these quantities are not frequently reported from experiments. Hence, we consider the typical range of initial dislocation densities for annealed materials as characterised by experimental dislocation density reports for various metals. These are relatively well understood and can be estimated with confidence. Mavlyutov et al. [32] studied the effect of annealing temperature on dislocation densities in ultrafine-grained aluminium and found values between 4 x 10^{12} m^{-2} and 1.5 x 10^{12} m^{-2} for annealing at room temperature and 423 K, respectively. Similarly, Williamson and Smallman [33] estimated dislocation densities between 10^{11} and 10^{12} m^{-2} for different annealed FCC metals. Here we assume an initial dislocation density ($\rho_o{}^{\alpha}$) along primary slip system between 1x10^{8} – 1x10^{11} m^{-2} and $\Delta\rho$ (contribution from yielding) is calculated using equation (2.13) subject to the grain size of material. Typically, $\Delta\rho^{\alpha}$ ranges between 5 x 10^{12} to 1 x10^{10} m^{-2} for grain sizes between 1 to 250 μm [32]. In this analysis, the lower bound of dislocation density will remain 1x10^{8} m^{-2}, however the upper bound will be modified for every material subject to its grain size.

The interaction coefficient (A_{ii}) in equation (2.9) has been extensively estimated through experiments and dislocation dynamics simulations. The results obtained by multiple authors [34–38] reported a range between 0.1 and 0.3 for various materials and even for hydrogen pre-charged samples [39]. Furthermore, Fivel et al. [35] reported that interaction coefficients do not show significant change with the dislocation density and stress. As a result, we consider an average interaction coefficient between 0.1 and 0.3.

The line tension coefficient (α_{LE}) in equation (2.9) is related to the stress required to bow-out and multiplicate dislocations. Szajewski et al. [40] investigated

dislocation bow-out using molecular dynamics and quantified line tension in the range of 0.5 to 0.85. Tabata et al. [27] studied the effect of flow stress on dislocation behaviour in aluminium [111] single crystal assuming that the bow-out is pinned with forest dislocation in dislocation walls and used the line-energy coefficient as 1. Therefore, we assume that the line tension value should be in a range between 0.5 and 1.5. Furthermore, the similitude coefficient (K_{struc}) in equation (2.10), Sauzay and Kubin [22] showed that FCC metals follow the similitude relation under cyclic and monotonic loading. They demonstrated that the similitude coefficient under monotonic loading varies between 5 and 10, which corresponds to the range employed in this study.

Kocks et al. [16] bounded the profile parameters p and q in equation (2.2) between 0 to 1 and 1 to 2, respectively. Their calculations for ΔG considered different values and concluded that $p = 3/4$ and $q = 4/3$ represent an adequate description. Fleischer [13] derived $p = 1/2$ and $q = 2$ for a dislocation interacting with local obstacles creating a tetragonal distortion while Mott and Nabarro [14] proposed a sinusoidal interaction potential between dislocation and a particle in precipitate-hardened material and derived values of $p = 2/3$ and $q = 3/2$. More recently, Dong [41] used molecular dynamics to derive a polynomial expression for a dislocation-point obstacle interaction mechanism that resulted in $p = 2/3$ and $q = 3/2$. Hence, we initially assume $p = 2/3$ and $q = 3/2$, but we will later consider other values in the range proposed by Kocks [16].

Table 2-1 Summary of different scaling level parameters.

Parameters		Values
Initial dislocation density ($\boldsymbol{\rho_o}$) [32,33]		1x10^{8} - 1x10^{11} m^{-2}
Average interaction coefficient ($\boldsymbol{A_{ii}}$) [34–38]		0.1 – 0.3
Line energy ($\boldsymbol{\alpha_{LE}}$) [27,40]		0.5 – 1.5
Similitude coefficient ($\boldsymbol{K_{struc}}$) [22]		5 – 10
$\boldsymbol{K_{multi}}$ [24–27]		1 - 4
Profile parameters [10,13,14,16,41]	p	0 - 1
	q	1 - 2
Mean separation distance between obstacles ($\boldsymbol{l_v}$) [29]		1x10^{-9} - 50x10^{-9} m

Finally, Sobie et al. [29] studied the role of obstacle spacing on glide activation energy and proposed a spacing in the order of tens of nm. Following on, we assume the equivalent range for our analysis i.e. between 1 nm and 50 nm. Table 2-1 summarizes the ranges of the parameters in equation (2.15) that were considered in the Monte Carlo analysis for evaluating F_0 and s_0^t.

2.4 Quantification of glide activation from yield stress data

To quantify glide activation parameters F_0 and s_0^t and their uncertainty, we implement a Monte Carlo approach that fits yield stress data to equation (2.15) as shown in Figure 2-1. There are two types of inputs considered in the analysis: Tabulated input and probabilistic input. The experimental yield stress data at different temperatures is the tabulated input as shown in Figure 2-2 and Figure 2-3. The details of experimental data for different materials are also listed in Table 2-2. The probabilistic inputs correspond to parameters from different deformation mechanisms in equation (2.15) that are known within range as shown in Table 2-1. For each Monte Carlo calculation, a randomly chosen probabilistic inputs along with tabulated data is fitted with equation (2.15) using the least square fitting method to yield F_0 and s_0^t. The lower and upper limits for F_0 and s_0^t were defined between 0 – 5eV and 1 – 500MPa respectively. However, for ensuring the quality of results, we confirm that the results are not sensitive to these limits. Furthermore, the fitting quality is scrutinised and only those results with R-square above 0.8 are considered in the analysis.

A total of 1000 iterations per metal was sufficient to converge the results. Each histogram was further analysed with an algorithm [60] to identify the distribution that best fits the data using the Matlab maximum likelihood estimation function. This function contains distributions such as normal, exponential, gamma, logarithmic, uniform, generalised extreme value (GEV), extreme value (EV), beta, and Weibull. The maximum log-likelihood (MLL) criteria calculate the sum of the log of probability distribution function values and return the mean and variance of the distribution. The analysis of multiple histograms shows that the GEV was optimal to represent the distributions and is used in the rest of the analysis.

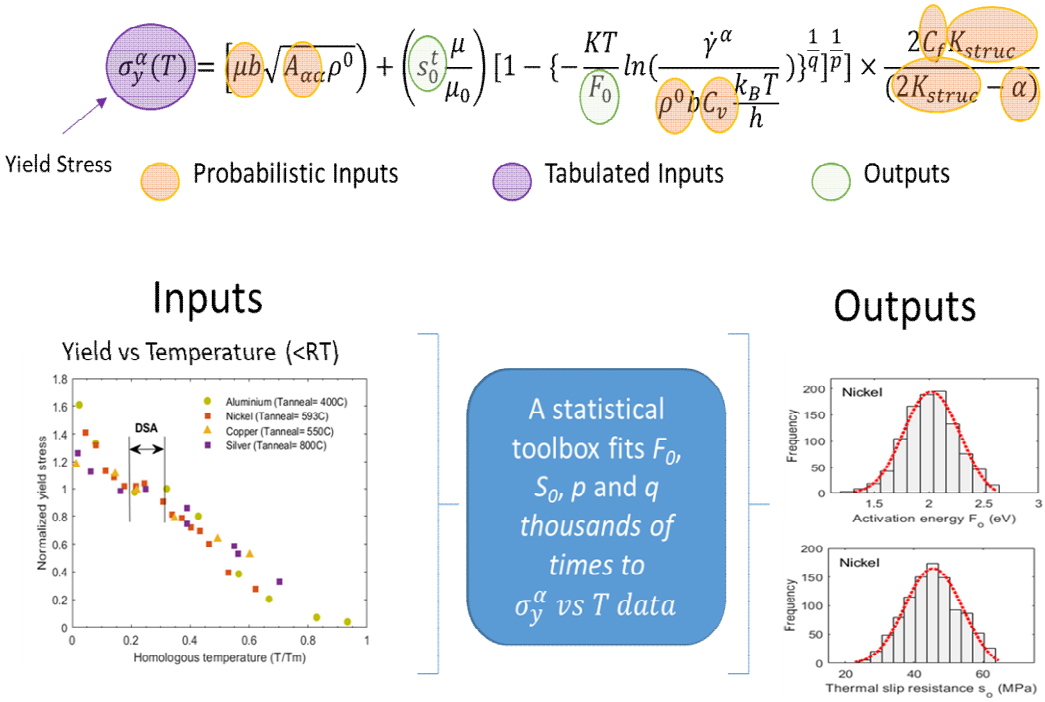

Figure 2-1 Schematic of Monte Carlo approach to estimate F_0 and s_0^t

Pure metals and some alloys usually present a plateau in the yield stress at about 0.2 homologous temperature. Several authors [42–45] associated the plateau with dynamic strain aging (DSA), in which impurities and solute atoms interfere with the mobility of dislocations [46]. Because equation (2.15) does not have any provision to account for the diffusion of point obstacles, we assume that they are static and limit our analysis yielding at low temperatures.

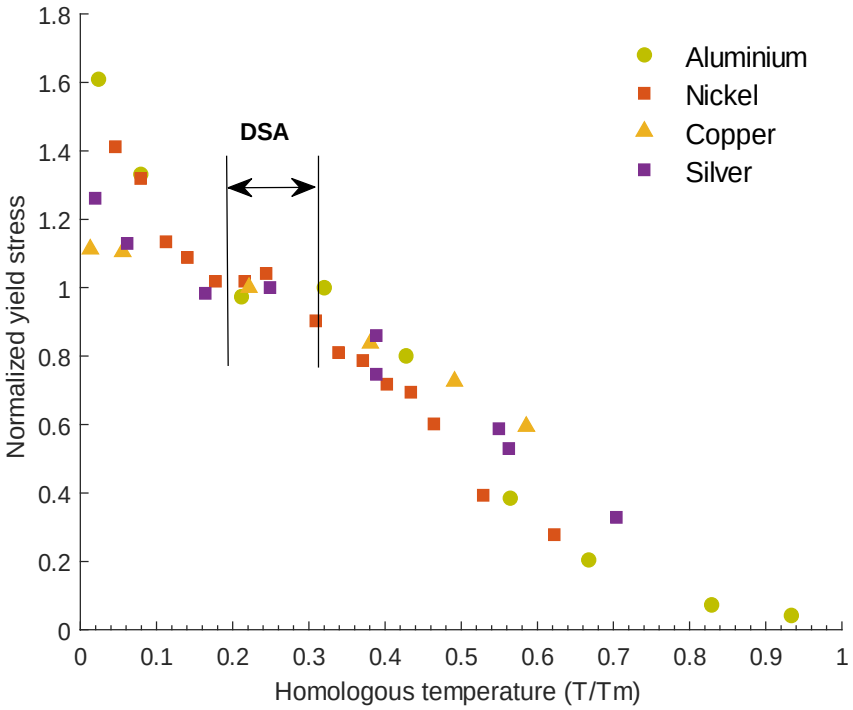

Figure 2-2 Normalised yield stress vs temperature for polycrystalline metals from various sources [42,43,47,48]**. The normalization factor corresponds to the yield stress at room temperature. For aluminium, copper, and silver, yield data corresponds to 0.5% strain but is 0.2% for nickel. We consider each of the strain values as reported in experimental data in our analysis with equation (2.15).**

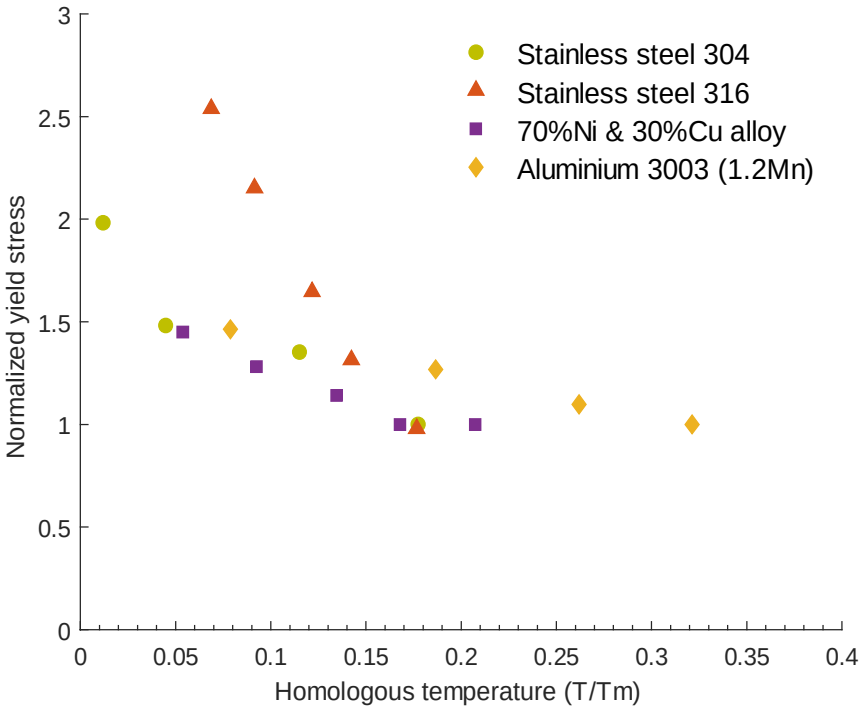

Figure 2-3 Normalised yield stress vs temperature for polycrystalline alloys from various sources [49–52]**. The normalization factor corresponds to the yield stress at room temperature. The yield stress was reported at 0.2% strain for all alloys.**

Table 2-2 Summary of materials and their properties used in Monte Carlo analysis.

Materials	Annealing temp. [K]	Mean grain dia. (d) [μm]	Purity %	Strain rate s^{-1}	Melting point [K]	Stress(σ_y) @ 293K ± 2 [MPa]	SFE* [mJm^{-2}]
Aluminium [43]	673	46	99.975	6×10^{-4}	933.5	26	166 [53]
Copper [47]	1023	45	99.999	6×10^{-4}	1358.2	51	46 [54]
Silver [48]	1073	40	99.97	6×10^{-4}	1234.9	48	17 [55]
Nickel [42]	866	45	99.85	5.1×10^{-4}	1728.2	83	120 [56]
Stainless steel 304 [49]	1344	90	N/A	3.3×10^{-4}	1672-1694K	222	18 [57]
Stainless steel 316 [50]	1423	65	N/A	1×10^{-4}	1663-1713K	255	78 [57]
Cupro - Nickel [51]	866	35	N/A	5.1×10^{-4}	1444.2	149	92 [58]
AA 3003 (1.2Mn) [52]	603	100	N/A	8.3×10^{-4}	928.16	41	140 [59]

* Stacking fault energy (SFE)

Figure 2-4 and Figure 2-5 present the distribution of the glide activation energy and thermal stress respectively, as obtained from the Monte Carlo analysis The red lines in Figure 2-4 and Figure 2-5 depict the fitting of the GEV distribution while the most probable value and 95% confidence interval are summarised in Table 2-3.

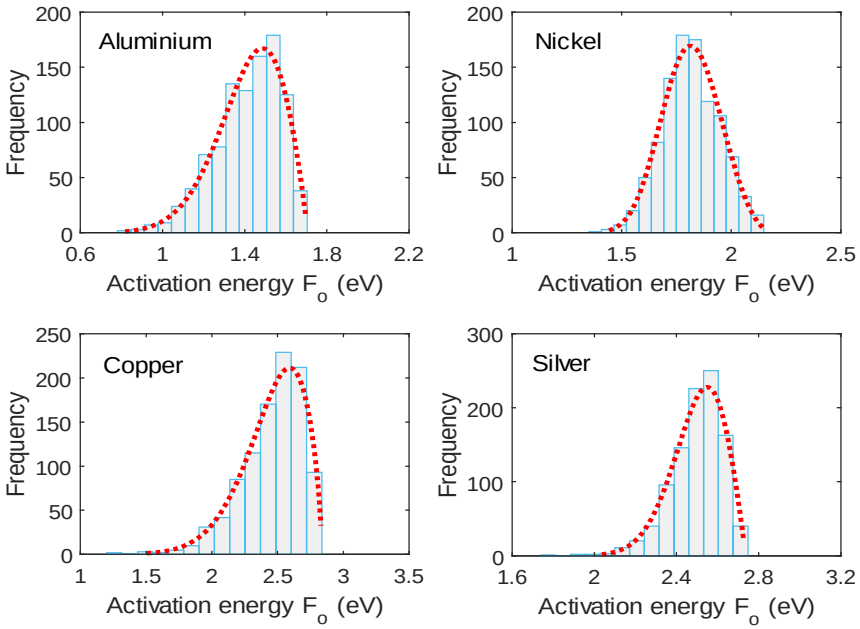

Figure 2-4 Glide activation energy of aluminium, nickel, copper, and silver. The red line is the best fit according to GEV distribution.

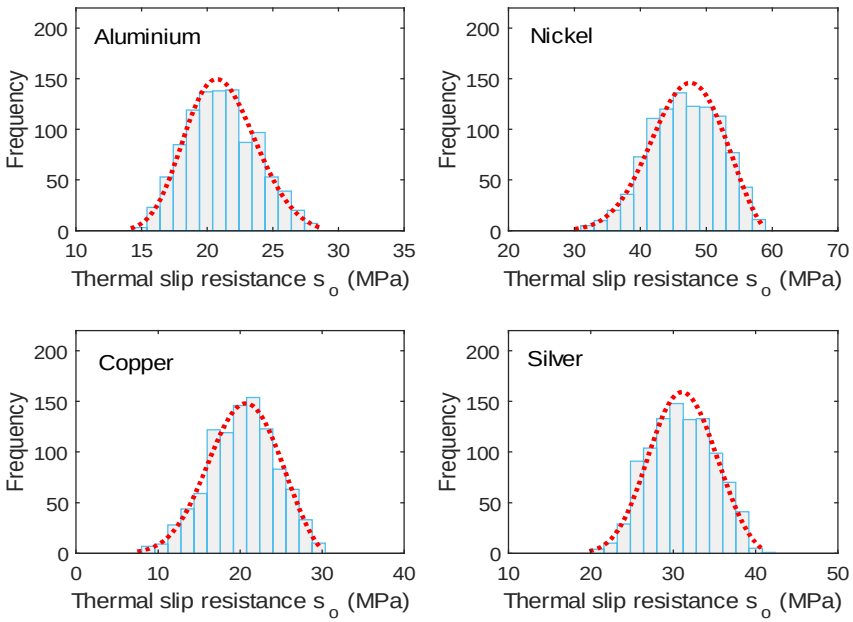

Figure 2-5 Thermal slip resistance of aluminium, nickel, copper, and silver. The red line is the best fit according to GEV distribution.

Figure 2-6 and Figure 2-7 illustrate the glide activation energy and thermal slip resistance computed for multiple alloys respectively. For each material, the activation energy for alloys with the same input parameters as used for pure metals seems to present less variability than thermal slip resistance, especially for alloys with higher yield stress.

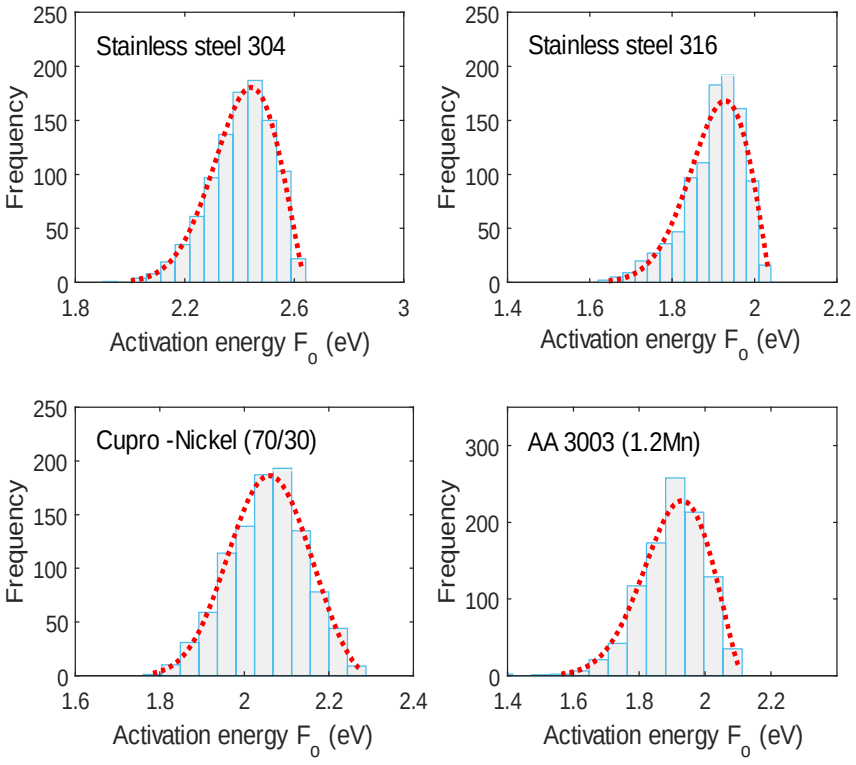

Figure 2-6 Glide activation energy of SS 304, SS316, Cupro-Nickel and AA 3003(1.2Mn). The red line is the best fit according to GEV distribution.

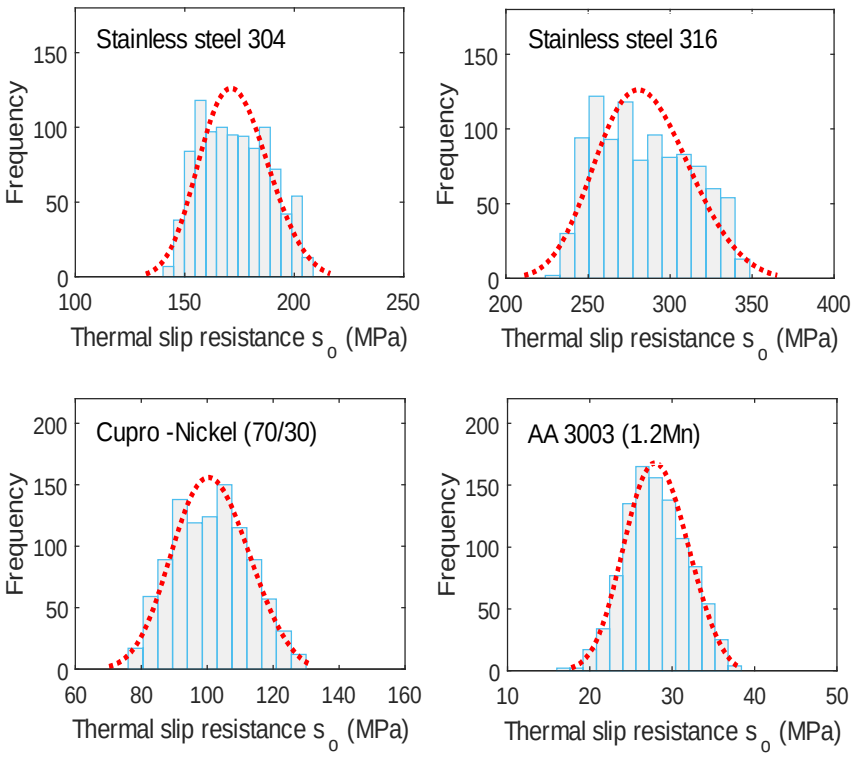

Figure 2-7 Thermal slip resistance of SS 304, SS 316, Cupro-Nickel and AA 3003 (1.2Mn). The red line is the best fit according to GEV distribution.

Overall, activation energy resulted in narrow ranges between 1 and 3 eV, which indicate, as expected, weak point obstacles according to Frost and Ashby [2]. On the contrary, the thermal stress, s_o, presented much wider ranges between 15-350 MPa. To further explore these magnitudes, Figure 2-8 presents the correlation with the stacking fault energy (SFE). Although there seems to be no correlation for the thermal stress, the activation energy presents an inverse proportionality with the SFE that can be parameterised as:

$$F_o = F_{oi} - a * SFE \qquad \textbf{(2.16)}$$

Where F_{oi} = 2.5 ($\pm$0.18), a = 0.0066($\pm$0.00177), are the coefficients of a linear fitting curve. The relation between the SFE and the activation energy has been suggested by Kocks for FCC metals [18].

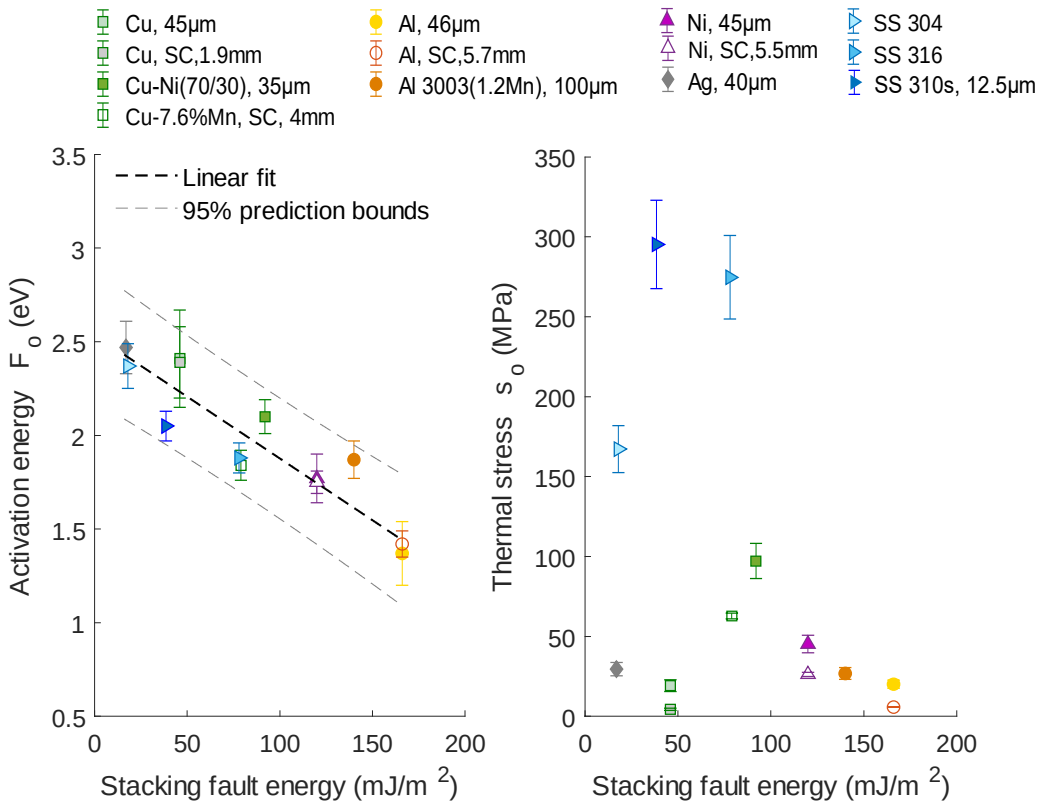

Figure 2-8 Correlation between glide activation and stacking fault energy of different FCC metals and alloys. The experimental data for SS 310s alloy is given in Figure A-2.

Table 2-3. Most likely values and 95% confidence interval of activation energy and thermal slip resistance computed for pure metals and alloys computed from GEV distributions.

Material	Activation energy 'eV'	Thermal slip resistance 'MPa'
Aluminium	1.37 ± 0.17	20.1 ± 2.53
Nickel	1.77 ± 0.13	45.18 ± 5.48
Copper	2.41 ± 0.26	19.2 ± 3.71
Silver	2.47 ± 0.14	29.5 ± 4.2
Stainless steel 304	2.37 ± 0.12	167.2 ± 14.7
Stainless steel 316	1.88 ± 0.08	274.7 ± 26.1
Cupro-Nickel	2.10 ± 0.09	97.18 ± 11.0
AA 3003 (1.2Mn)	1.87 ± 0.10	26.79 ± 3.65
Stainless steel 310s	2.05 ± 0.08	295.27 ± 27.67
Cu- 7.6%Mn	1.84 ± 0.07	62.78 ± 1.8
Aluminium single crystal	1.42 ± 0.08	5.81 ± 0.15
Nickel single crystal	1.75 ± 0.06	26.22 ± 1.28
Copper single crystal	2.39 ± 0.19	4.39 ± 0.62

2.4.1 Effect of solute concentration on F_0 and s_0^t

Continuing with the analysis of thermal stress, we recall the work from Wille et al. [61], who studied the effect of solute concentration on activation energy parameters in Cu-Mn single crystal oriented for single slip. Their analysis used an empirical relation for the activation volume to quantify the sensitivity of activation energy and thermal stress to solute concentration. To validate our approach, we consider the shear stress data at different temperatures from Wille et al. [61] (as shown in Appendix A.2 (Figure A-2)) to compute the activation energy parameters. Figure 2-9 presents the glide activation and thermal stress with a 95% confidence interval determined using GEV distribution. Our results agree with the trends from Wille et al. [61] and demonstrate that an increase in

solute concentration increases primarily the thermal stress rather than the activation energy. We highlight that our analysis does not require the empirical relation proposed by Wille et al. [61], but fully relies on physics-based mechanisms parameterised independently.

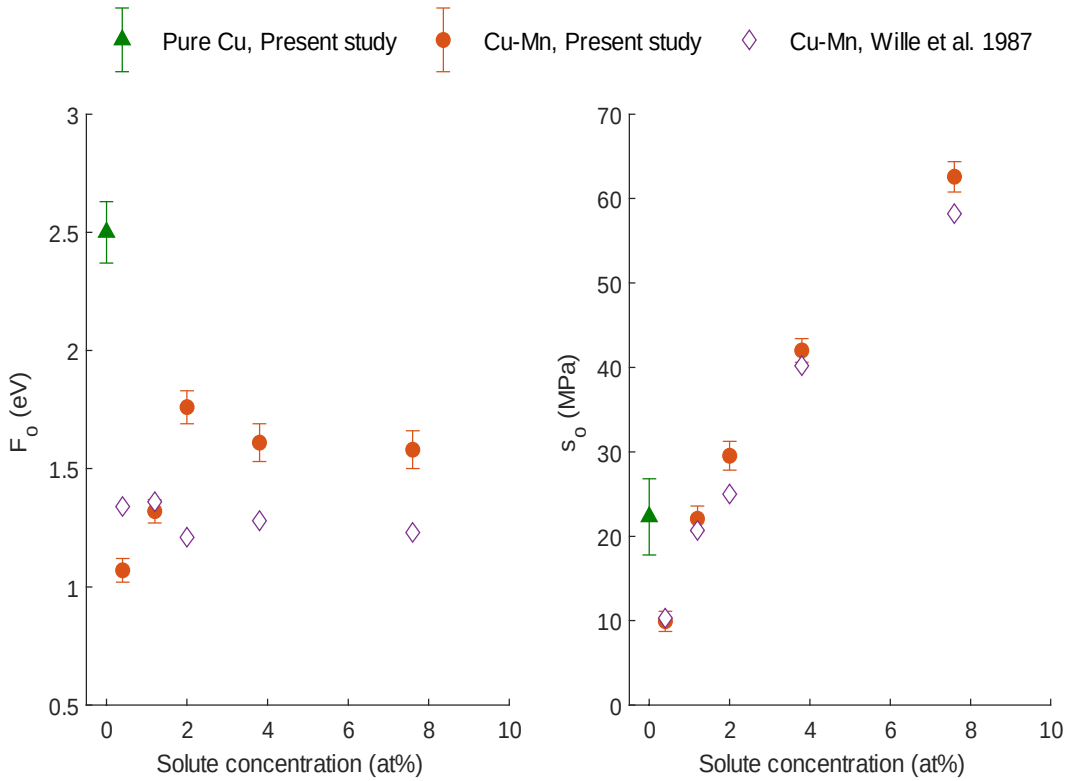

Figure 2-9 Activation energy and thermal stress of Cu-Mn alloy with different solute concentrations. Error bars correspond to a 95% confidence interval.

2.4.2 Effect of hydrogen concentration on F_0 and s_0^t

Figure 2-10 and Figure 2-11 show the effect of hydrogen on activation energy parameters in SS 310s and pure Ni respectively. Both results show that F_0 and s_0^t increase with the increase in hydrogen concentration. The role of hydrogen in mechanical response of metals is stochastic as it appears to soften or harden the FCC metals. Some studies [62] explored the increase of drag stresses in α-Fe while studying hydrogen interaction with vacancy complexes using atomistic simulations. Tehranchi et al. [63] studied the effect of hydrogen interaction with different solutes in the Ni matrix independently. They [63] reported that hydrogen

interaction with vacancies in the Ni matrix causes a softening effect, whereas interaction with carbon and sulphur solute atoms renders a hardening effect. The study [63] reveals that role of hydrogen is also sensitive to the impurities and solute atoms present in metals. The experimental data [64,65] used in Figure 2-10 and Figure 2-11 analysis also has traces of carbon and sulphur solute items along with a hydrogen environment. Hence, the finding [63] indirectly supports the increase of F_0 and s_0^t with an increase of hydrogen concentration.

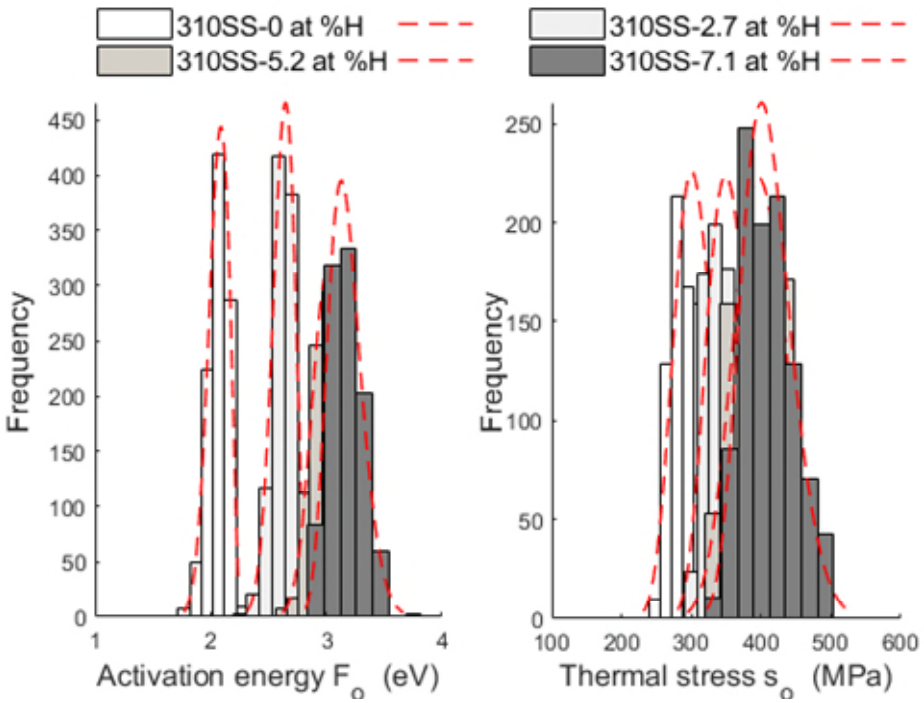

Figure 2-10 Glide activation energy of stainless steel 310s with different concentrations of hydrogen. The red line corresponds to the best fit according to GEV distribution.

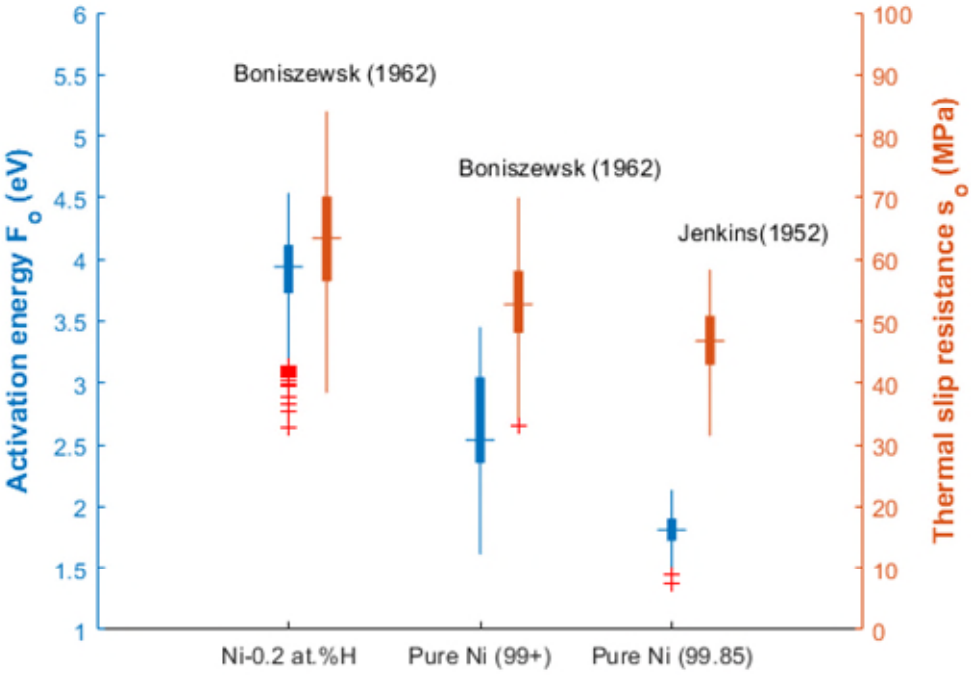

Figure 2-11 Effect of H_2 concentration on glide activation energy and thermal stress of pure Ni.

2.4.3 Single crystal analysis

Further validation proceeds from an analysis of a single crystal oriented for single slip, which does not promote cross slip at low plastic strain amplitude. Hence, to ascertain that the estimated activation energies relate indeed to the gliding process rather than cross-slip, we consider aluminium, nickel, and copper single crystals [66–68]. Figure 2-12 compares the activation energy for these single crystals (SC) and polycrystals (PC); the overlapping of activation energies between single- and poly-crystals supports our methodology. These results also highlight the variability conveyed by polycrystals.

A second consideration is that the thermal stresses in polycrystalline analysis seem consistently higher than that in single crystals. One source for such effect is their difference in the level of impurities as shown before (these materials are effectively not pure when considering the thermal stress).

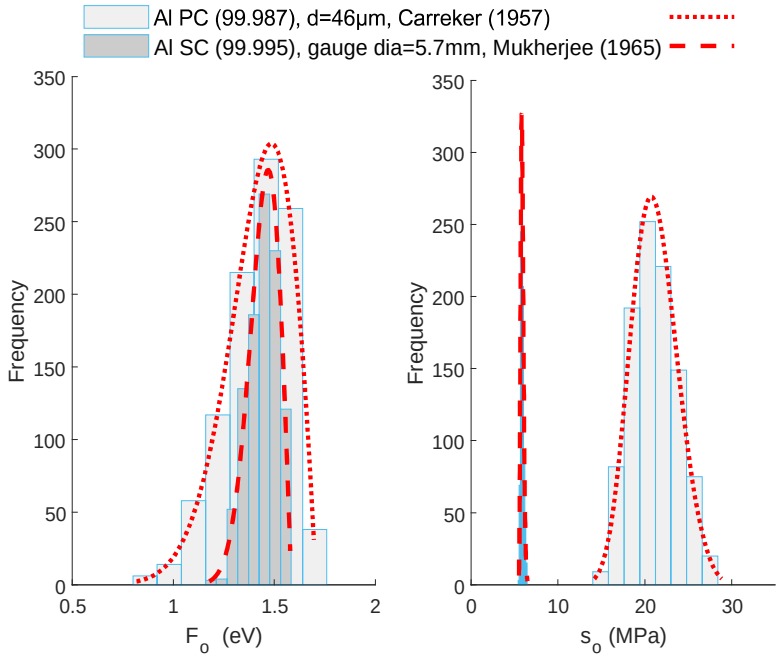
Al PC (99.987), d=46μm, Carreker (1957)
Al SC (99.995), gauge dia=5.7mm, Mukherjee (1965)
Frequency
F0 (eV)
s0 (MPa)

a)

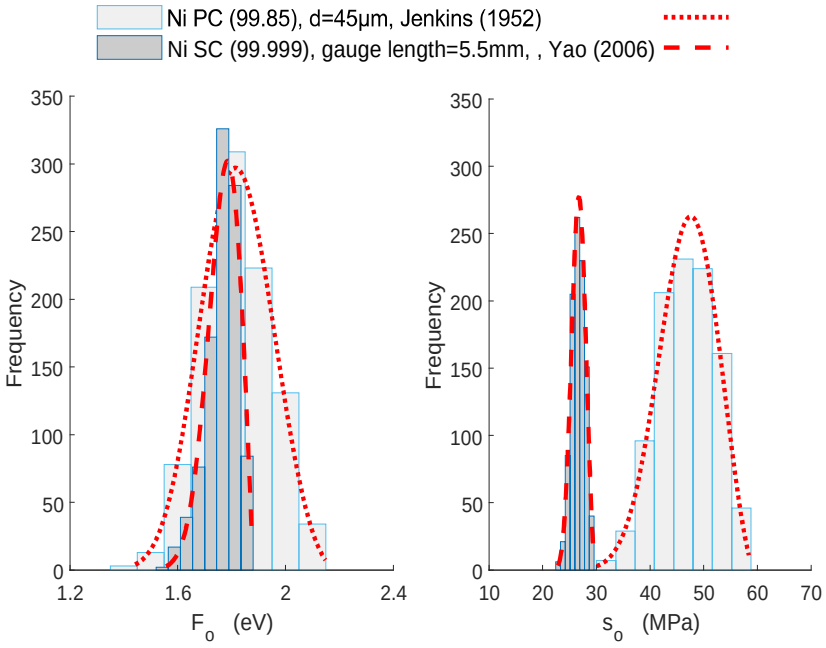
Ni PC (99.85), d=45μm, Jenkins (1952)
Ni SC (99.999), gauge length=5.5mm, , Yao (2006)
Frequency
F0 (eV)
s0 (MPa)

b)

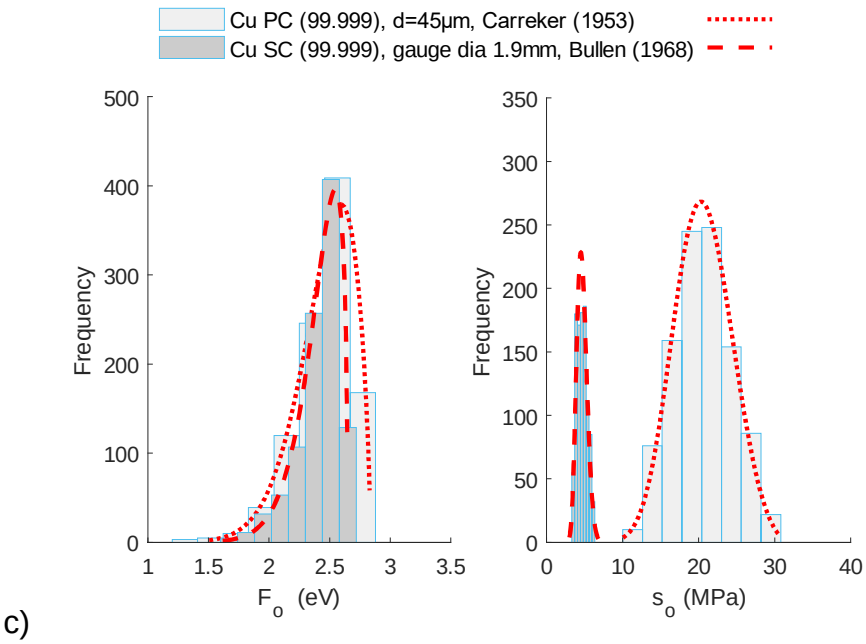

c)

Figure 2-12 Activation energy and thermal stress of a) aluminium, b) nickel, and c) copper single (SC) and polycrystals (PC). Experimental data of polycrystals [43,47,48] **are shown in Figure 2-2 and data for single crystals** [66–68] **are given in Appendix A.2 (Figure A-2). The dimensions correspond to the grain size for polycrystals and crystal size for single crystals.**

2.4.4 Effect of grain size on yield stress

Another aspect that requires consideration is the effect of grain size on yield stress [69], which may affect the estimation of the glide parameters. Figure 2-13 presents the effect of different grain sizes on activation energy parameters. The overlapping of results in Figure 2-13 shows that glide activation energy and thermal stress are not significantly influenced by the grain size. This further validates the incorporation of the grain size effect in equation (2.15).

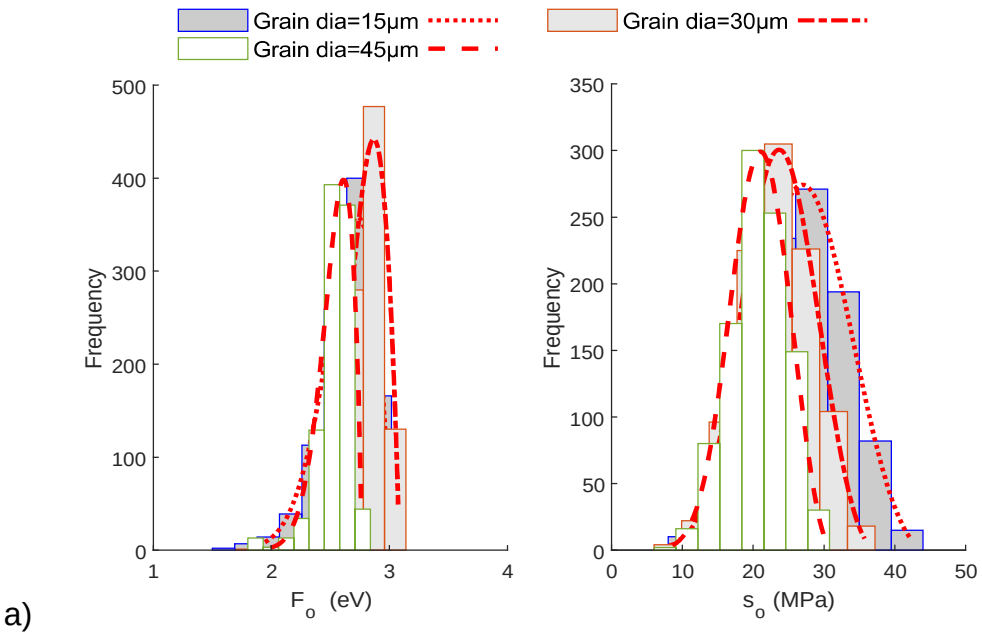

a)

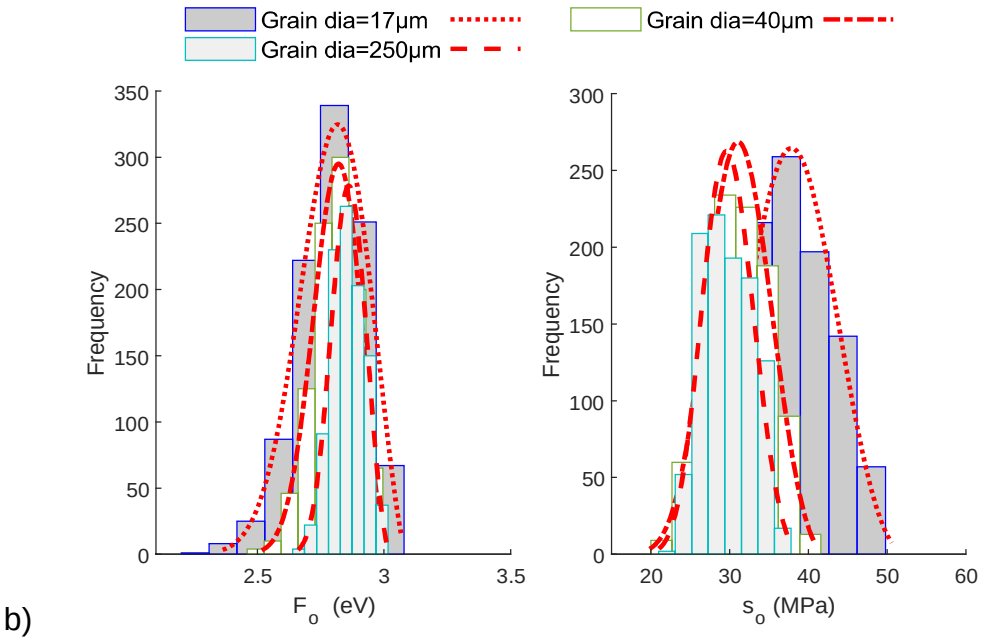

b)

Figure 2-13 Effect of grain size on glide activation energy and thermal stress in a) copper b) silver. The upper bound of the dislocation density range is different for each case subject to the grain size.

2.4.5 Differences among activation energy formulations

Finally, this work explores the role of the activation energy formulation on the activation parameters. First, we consider the effect of choosing different *p* and *q* values in equation (2.2) on the activation energy parameters. Here, we emphasize accessing the quantitative effect on activation energy parameters rather than establishing the phenomenological significance of these parameters. Figure 2-14 shows that changing the values of *p* and *q* between 2/3 to 1 and 1 to 3/2, respectively, have a marginal effect on the activation energy parameters. Hence, we support Kocks [18] recommendation that *p* and *q* should be picked to represent the dominant mechanism and should remain constant for the rest of the analysis.

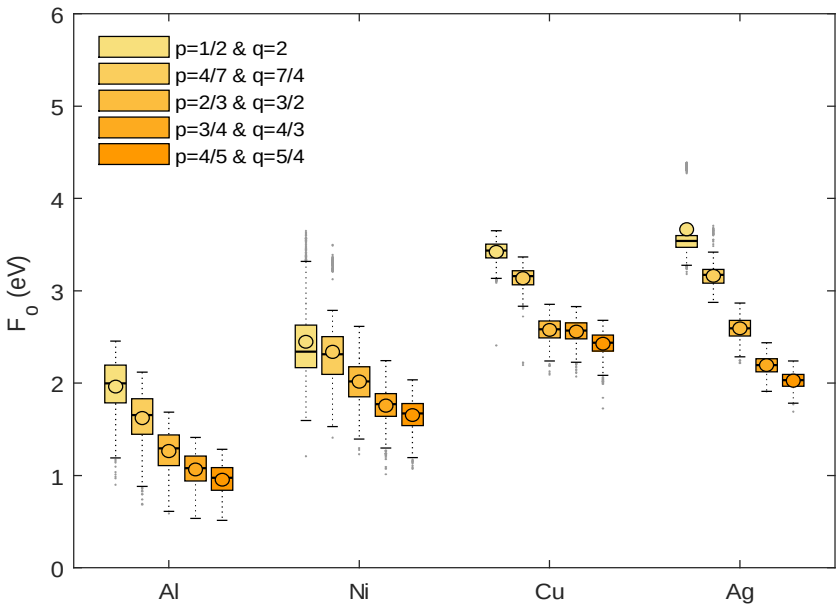

a)

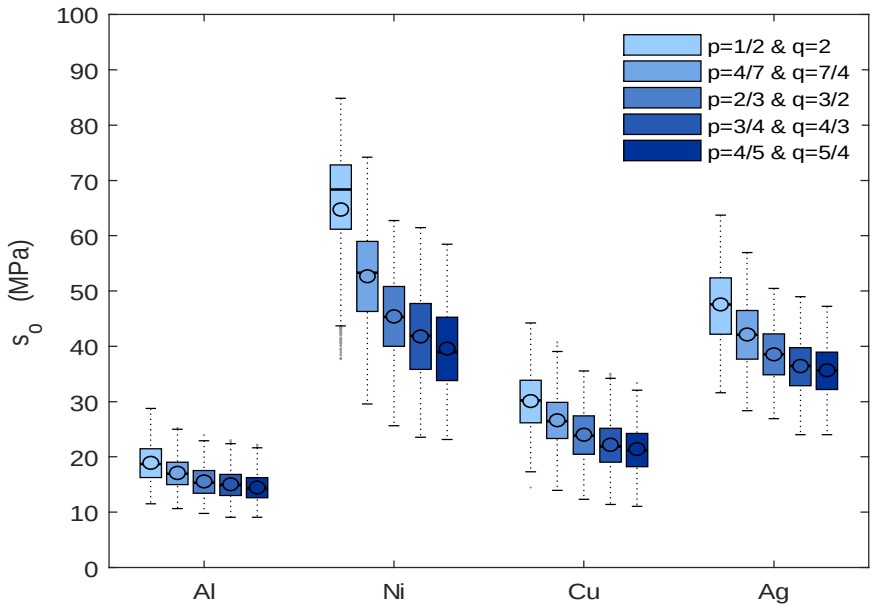

b)

Figure 2-14 Effect of different p and q values on a) glide activation energy and b) thermal slip resistance of different FCC metals.

Next, we repeat the Monte Carlo analysis considering τ_{eff}^{α} and $\dot{\gamma}_0^{\alpha}$ from equations (2.7) and (2.14), respectively, but with the energy barrier proposed on equations (2.3) and (2.4). By combining each of these equations with equation (2.5) and following algebra detailed in section (2.2), we obtain,

$$\sigma_y^{\alpha}(T) = \left[\mu b\sqrt{A_{ii}\rho^{\alpha}} + \left[\frac{\Delta F}{l_v bd} + \left\{\frac{k_B T}{l_v bd} ln\left(\frac{\dot{\gamma}^{\alpha}}{\rho^{\alpha} b l_v \frac{k_B T}{h}}\right)\right\}\right]\right] \times \frac{2C_f K_{struc}}{(2K_{struc} - \alpha_{LE})} \qquad (2.17)$$

$$\sigma_y^{\alpha}(T) = \left[\mu b\sqrt{A_{ii}\rho^{\alpha}} - \left[s_0^* \times ln\left\{-\frac{k_B T}{F_0^*}\ln\left(\frac{\dot{\gamma}^{\alpha}}{\rho^{\alpha} b l_v \frac{k_B T}{h}}\right)\right\}\right]\right] \times \frac{2C_f K_{struc}}{(2K_{struc} - \alpha_{LE})} \qquad (2.18)$$

In equation (2.17), the activation volume is estimated by $(l_v bd)$, in which l_v is separation between point obstacles and d is an unknown average length of thermal activation or height of the barrier. Following the same procedure in section (2.4), we consider equations (2.17) and (2.18) to compute F_0^*, s_0^{t*} and ΔF, d, respectively. The same criteria are employed for ensuring the fitting quality i.e. only fitting with a R-square value greater than 0.8 is considered. The materials that did not satisfy this criterion are not presented.

Figure 2-15 a) demonstrates that the glide activation energy and thermal stress in Langer formulation (equations (2.4)) follow similar trends as those found for Kocks formulation (Figure 2-8). Indeed, the activation energy correlates inversely with the SFE while the thermal stresses computed with equation (2.18) are roughly a third of the stresses computed with equation (2.15).

Similarly, Figure 2-15 b) presents the Helmholtz activation energy and height of the barrier for different materials computed using equation (2.17). Here, the Helmholtz activation is almost independent of the SFE materials whereas, the height of the barrier demonstrates a positive correlation with the SFE.

a)

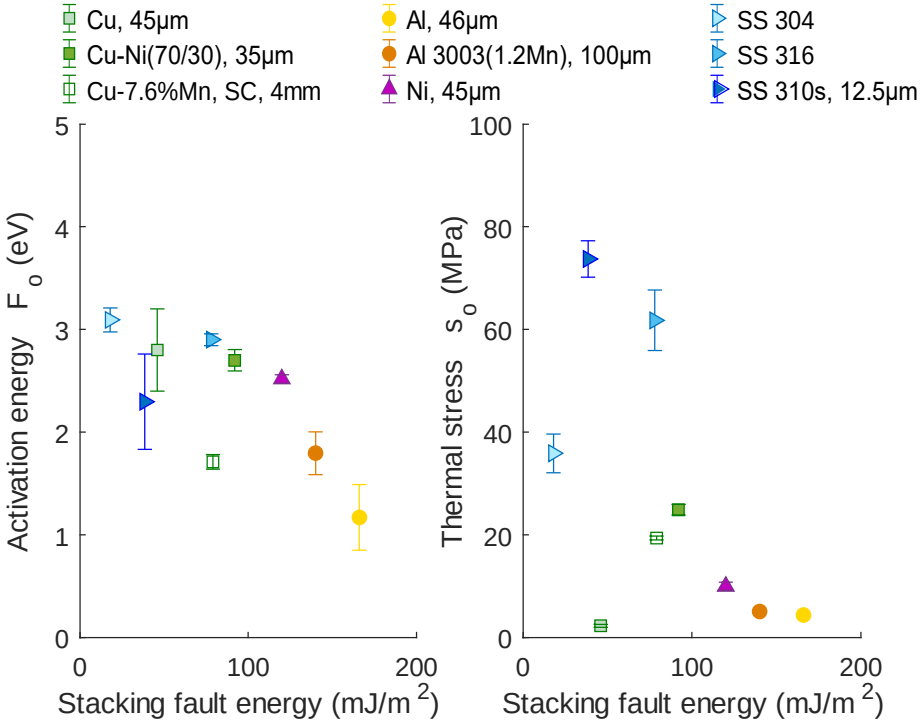

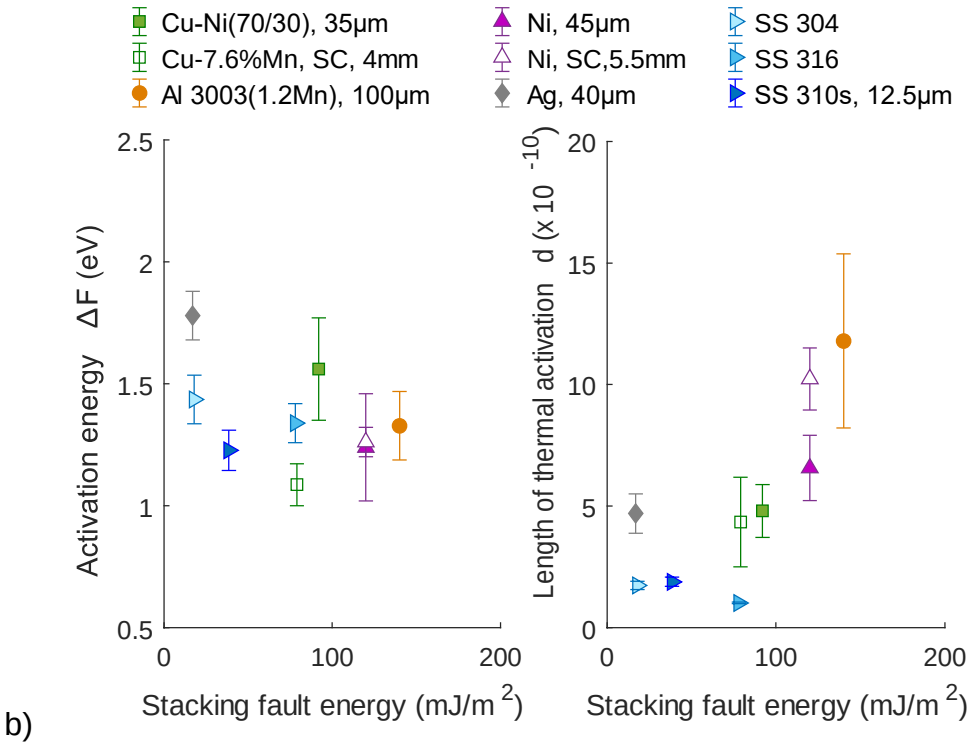

b)

Figure 2-15 Estimation of glide activation energy using a) equation (2.18) and b) equation (2.17).

2.5 Discussion

This study characterised the activation energy for dislocations to glide in FCC metals and alloys by combining physics-based arguments and parameter uncertainty quantification. These results can now be used along with mesoscale parametrisation to study mechanical response of aluminium. We considered three formulations for the Gibbs free energy as a function of the effective stress, which was computed using parameters that were estimated independently. The analysis used the least-square fitting of experimental data to determine only two parameters at a time rather than many coefficients [8,61]. As a result, we mitigated the spurious cancellation of error among parameters and we were able to estimate the uncertainty of the activation energy parameterization. Besides, we found a correlation between the SFE and glide activation energy or the activation volume, which could be further explored with atomistic models.

The comparison among Gibbs free energy formulations showed that Kocks approach (equations (2.2)) yielded the best results when fitting a nonlinear dependence of the yield stress on temperature, even when parameters *p* and *q* were fixed. Equations (2.3) and (2.4), which represent linear and exponential dependencies, respectively, demonstrated some limitations in fitting the yield stress dependence on temperature. Hence, our analysis supports the quantification of Gibbs free energy using Kocks formulation (equations (2.2)) with profile parameters *p* and *q* fixed in the ranges between 2/3 to 1 and 1 to 3/2, respectively. In the usual case of estimating parameters for multiscale models in FCC metals without sufficient data to quantify all parameters independently, we recommend the estimation of F_0 from equation (2.15). Since this magnitude has a low variability, the potential error is small and it is further mitigated by estimating only one parameter (s_0^t) from the available experimental data. This methodology provides a consistent estimation of glide activation parameters and mitigates spurious errors.

Finally, our approach relied on experimental data readily available in the literature to predict the glide activation energy in monolithic FCC metals with weak point obstacles. Future efforts should further explore the extension of the analysis to metals with medium and high strength obstacles. These approaches should add additional strengthening mechanisms to the athermal stress as well as reconsider the dependences of the parameters involved.

2.6 Conclusions

A physics-based predictive framework is presented to estimate the glide activation energy in monolithic metals while considering parameter uncertainties independently. We consider the role of weak point obstacles, dislocation strengthening, and grain size to predict the dependence of yield stress on temperature.

We employed a Monte Carlo procedure to fit the formulation to experimental data and quantify glide activation energy uncertainty. Our calculations found a

correlation of some parameters with the SFE and quantified the effect of impurities on solid solution strengthening.

Our analysis suggests that the formulation proposed by Kocks to parameterize Gibbs free energy can yield superior results, even if parameters *p* and *q* are fixed. Hence, we presented a recommendation for estimating glide activation energy for multiscale models in which limited experimental data is available.

References

1. Krausz A.S., Eyring H. The reaction kinetics of plastic deformation, in: Deformation Kinetics. John Wiley & Sons, Ltd; 1975.

2. Frost H.J. and Ashby M.F. Deformation mechanisms maps. Pergamon Press; 1982.

3. Sobie C., Capolungo L., McDowell D.L. and Martinez E. Thermal activation of dislocations in large scale obstacle bypass. Journal of the Mechanics and Physics of Solids. Elsevier Ltd; 2017; 105: 150–160. http://dx.doi.org/10.1016/j.jmps.2017.05.003

4. Esteban-Manzanares G., Martínez E., Segurado J., Capolungo L. and LLorca J. An atomistic investigation of the interaction of dislocations with Guinier-Preston zones in Al-Cu alloys. Acta Materialia. Elsevier Ltd; 2019; 162: 189–201. http://dx.doi.org/10.1016/j.actamat.2018.09.052

5. Narayanan S., McDowell D.L. and Zhu T. Crystal plasticity model for BCC iron atomistically informed by kinetics of correlated kinkpair nucleation on screw dislocation. Journal of the Mechanics and Physics of Solids. Elsevier; 2014; 65(1): 54–68. http://dx.doi.org/10.1016/j.jmps.2014.01.004

6. Wille T.H. and Schwink C. Precision measurements of critical resolved shear stress in CuMn alloys. Acta Metallurgica. 1986; 34(6): 1059–1069. http://dx.doi.org/10.1016/0001-6160(86)90216-6

7. Kothari M. and Anand L. Elasto-viscoplastic constitutive equations for polycrystalline metals: Application to tantalum. Journal of the Mechanics and Physics of Solids. January 1998; 46(1): 51–67. http://dx.doi.org/10.1016/S0022-5096(97)00037-9

8. Balasubramanian S. and Anand L. Elasto-viscoplastic constitutive equations for polycrystalline FCC materials at low homologous temperatures. Journal of the Mechanics and Physics of Solids. 2002; 50(1): 101–126. http://dx.doi.org/10.1016/S0022-5096(01)00022-9

9. Krausz A.S. and Eyring H. Chemical kinetics of plastic deformation. Journal of Applied Physics. 1971; 42(6): 2382–2385. http://dx.doi.org/10.1063/1.1660552

10. Dong Y., Nogaret T. and Curtin W.A. Scaling of dislocation strengthening by multiple obstacle types. Metallurgical and Materials Transactions A: Physical Metallurgy and Materials Science. 2010; 41(8): 1954–1960. http://dx.doi.org/10.1007/s11661-010-0229-z

11. Gibbs G.B. Thermodynamic analysis of dislocation glide controlled by dispersed local obstacles. Materials Science and Engineering. 1969; 4(6): 313–328. http://dx.doi.org/10.1016/0025-5416(69)90026-3

12. Seeger A.K. On the theory of radiation damage and radiation hardening. Proceedings of 2nd United Nations International Conference on the Peaceful Uses of Atomic Energy. 1959. p. 250.

13. Fleischer R.L. Solution hardening by tetragonal distortions: Application to irradiation hardening in FCC crystals. Acta Metallurgica. 1962; 10(9): 835–842. http://dx.doi.org/10.1016/0001-6160(62)90098-6

14. Mott N.F. and Nabarro F.R.N. Dislocation theory and transient creep. Report on strength of solids. Bristol Physical Society Conference. 1948. pp. 1–19.

15. Langer J.S. Statistical thermodynamics of crystal plasticity. Journal of Statistical Physics. Springer US; 2019; 175(3–4): 531–541. http://dx.doi.org/10.1007/s10955-019-02221-7

16. Kocks U.F., Argon A.S. and Ashby M.F. Thermodynamics and kinetics of slip. Progress in Materials Science. Pergamon Press; 1975.

17. Castelluccio G.M. and McDowell D.L. Mesoscale cyclic crystal plasticity with dislocation substructures. International Journal of Plasticity. Elsevier Ltd; 2017; 98: 1–26. http://dx.doi.org/10.1016/j.ijplas.2017.06.002

18. Kocks U.F. Realistic constitutive relations for metal plasticity. Materials Science and Engineering A. October 2001; 317(1–2): 181–187. http://dx.doi.org/10.1016/S0921-5093(01)01174-1

19. Guo Y.Z., Sun X.Y., Wei Q. and Li Y.L. Compressive responses of ultrafine-grained titanium within a broad range of strain rates and temperatures. Mechanics of Materials. 2017; 115: 22–33. http://dx.doi.org/10.1016/j.mechmat.2017.07.015

20. Sachs G. Zur ableitung einer fließbedingung. Mitteilungen der deutschen Materialprüfungsanstalten. Springer, Berlin, Heidelberg; 1929. pp. 94–97. http://dx.doi.org/10.1007/978-3-642-92045-5_12

21. Franciosi P. The concepts of latent hardening and strain hardening in metallic single crystals. Acta Metallurgica. September 1985; 33(9): 1601–1612. http://dx.doi.org/10.1016/0001-6160(85)90154-3

22. Sauzay M. and Kubin L.P. Scaling laws for dislocation microstructures in monotonic and cyclic deformation of fcc metals. Progress in Materials Science. Elsevier Ltd; 2011; 56(6): 725–784. http://dx.doi.org/10.1016/j.pmatsci.2011.01.006

23. Nix W.D., Greer J.R., Feng G. and Lilleodden E.T. Deformation at the nanometer and micrometer length scales: Effects of strain gradients and dislocation starvation. Thin Solid Films. 2007; 515(6): 3152–3157. http://dx.doi.org/10.1016/j.tsf.2006.01.030

24. Hansen N. The effect of grain size and strain on the tensile flow stress of quenched aluminum. Acta Metallurgica. 1987; 35(1): 227–235. http://dx.doi.org/10.1016/0001-6160(87)90230-6

25. Ashby M.F. The deformation of plastically non-homogeneous materials. Philosophical Magazine. 1970; 21(170): 399–424. http://dx.doi.org/10.1080/14786437008238426

26. Essmann U. and Mughrabi H. Annihilation of dislocations during tensile and cyclic deformation and limits of dislocation densities. Philosophical

Magazine A: Physics of Condensed Matter, Structure, Defects and Mechanical Properties. 1979; 40(6): 731–756. http://dx.doi.org/10.1080/01418617908234871

27. Tabata T., Fujita H., Hiraoka M.A. and Miyake S. The relationship between flow stress and dislocation behaviour in [111] aluminium single crystals. Philosophical Magazine A: Physics of Condensed Matter, Structure, Defects and Mechanical Properties. 1982; 46(5): 801–816. http://dx.doi.org/10.1080/01418618208236932

28. Eyring H. The activated complex in chemical reactions. The Journal of Chemical Physics. 1935; 3(2): 63–71. http://dx.doi.org/10.1063/1.1749604

29. Sobie C., Capolungo L., McDowell D.L. and Martinez E. Scale transition using dislocation dynamics and the nudged elastic band method. Journal of the Mechanics and Physics of Solids. Elsevier Ltd; 2017; 105: 161–178. http://dx.doi.org/10.1016/j.jmps.2017.05.004

30. Ledbetter H.M. and Naimon E.R. Relationship between single-crystal and polycrystal elastic constants. Journal of Applied Physics. 1974; 45(1): 66–69. http://dx.doi.org/10.1063/1.1663019

31. Varshni Y.P. Temperature dependence of the elastic constants. Physical Review B. 1970; 2(10): 3952–3958. http://dx.doi.org/10.1103/PhysRevB.2.3952

32. Mavlyutov A.M., Latynina T.A., Murashkin M.Y., Valiev R.Z. and Orlova T.S. Effect of annealing on the microstructure and mechanical properties of ultrafine-grained commercially pure Al. Physics of the Solid State. 2017; 59(10): 1970–1977. http://dx.doi.org/10.1134/S1063783417100274

33. Williamson G.K. and Smallman R.E. III. Dislocation densities in some annealed and cold-worked metals from measurements on the x-ray Debye-Scherrer spectrum. Philosophical Magazine. Taylor & Francis; January 1956; 1(1): 34–46. http://dx.doi.org/10.1080/14786435608238074

34. Kubin L., Devincre B. and Hoc T. Modeling dislocation storage rates and mean free paths in face-centered cubic crystals. Acta Materialia. 2008; 56(20): 6040–6049. http://dx.doi.org/10.1016/j.actamat.2008.08.012

35. Fivel M., Tabourot L., Rauch E. and Canova G. Identification through mesoscopic simulations of macroscopic parameters of physically based constitutive equations for the plastic behaviour of FCC single crystals. Journal De Physique. IV : JP. 1998; 8(8): 151–158. http://dx.doi.org/10.1051/jp4:1998819

36. Devincre B., Hoc T. and Kubin L. Dislocation mean free paths and strain hardening of crystals. Science. 2008; 320(5884): 1745–1748. http://dx.doi.org/10.1126/science.1156101

37. Schwartz J., Fandeur O. and Rey C. Numerical approach of cyclic behaviour of 316LN stainless steel based on a polycrystal modelling including strain gradients. International Journal of Fatigue. Elsevier Ltd; October 2013; 55: 202–212. http://dx.doi.org/10.1016/j.ijfatigue.2013.07.003

38. Madec R., Devincre B., Kubin L., Hoc T. and Rodney D. The role of collinear interaction in dislocation-induced hardening. Science. 2003; 301(5641): 1879–1882. http://dx.doi.org/10.1126/science.1085477

39. Hachet G., Oudriss A., Barnoush A. ,Milet R., Wan D., Metsue A. and Feaugas X. The influence of hydrogen on cyclic plasticity of <001> oriented nickel single crystal. part I: dislocation organisations and internal stresses. International Journal of Plasticity. Elsevier Ltd; 2020; 126. http://dx.doi.org/10.1016/j.ijplas.2019.09.017

40. Szajewski B.A., Pavia F. and Curtin W.A. Robust atomistic calculation of dislocation line tension. Modelling and Simulation in Materials Science and Engineering. IOP Publishing; 2015; 23(8). http://dx.doi.org/10.1088/0965-0393/23/8/085008

41. Dong Y. Coupled dislocation/dislocation and solute strengthening mechanisms in metal alloys. Ph.D. Thesis, Brown University. 2013.

42. Jenkins W.D. and Digges T.G. Effect of temperature on the tensile properties of high-purity nickel. Journal of Research of the National Bureau of Standards. 1952; 48(4): 313. http://dx.doi.org/10.6028/jres.048.039

43. R.P. Carreker Jr., W.R. Hibbard Jr., Tensile deformation of aluminum as a function of temperature, strain rate, and grain size, J. Met. 9 (1957) 1157–1163. https://doi.org/org/10.1007/BF03398279

44. Voyiadjis G.Z.,Song Y. and Rusinek A. Constitutive model for metals with dynamic strain aging. Mechanics of Materials. Elsevier; 2019; 129(December 2018): 352–360. http://dx.doi.org/10.1016/j.mechmat.2018.12.012

45. Abd El-Azim M.E. Effect of dynamic strain ageing on the deformation behavior of incoloy alloy MA956. Mechanics of Materials. 1997; 25(4): 255–261. http://dx.doi.org/10.1016/S0167-6636(97)00005-7

46. Nabarro F.R. Mechanical effects of carbon in iron. Physical Society Bristol Conference Proc. Phys. Soc., London; 1948. pp. 38–45.

47. Carreker R.P. and Hibbard W.R. Tensile deformation of high-purity copper as a function of temperature, strain rate, and grain size. Acta Metallurgica. 1953; 1(6): 112–115. http://dx.doi.org/10.1016/0001-6160(53)90022-4

48. R.P. Carreker Jr, Tensile deformation of silver as a function of temperature, strain Rate, and grain size, J. Met. Trans. AIME. 169 (1957) 112–115. https://doi.org/org/10.1007/BF03398466

49. Guntner C.J. and Reed R.P. Mechanical properties of four austenitic stainless steels at temperatures between 300° and 20°k. Advances in Cryogenic Engineering. Springer, Boston, MA; 1961. pp. 565–576. http://dx.doi.org/10.1007/978-1-4757-0534-8_60

50. Nickel Development Institute, Materials for cryogenic service: Engineering properties of austenitic stainless steels, 1974. Available at: https://www.nickelinstitute.org/media/1723/materialsforcryogenicservice_engineeringpropertiesofausteniticstainlesssteel_4368_.pdf

51. National Bureau of Standards, Mechanical properties of metals at low temperature.Report: United States Department of Commerce. 1952. Available at: https://ia800809.us.archive.org/9/items/circularofbureau520unse/circularofbureau520unse.pdf

52. ASM Handbook Committee, Properties of wrought aluminum and aluminum alloys. in: ASM Handbook: Properties and Selection: Nonferrous Alloys and Special-Purpose Materials, ASM International, Ohio, 1990. 62-122. https://doi.org/org/10.1361/asmhba000.

53. Murr L.E. Twin boundary energetics in pure aluminium. Acta Metallurgica. 1973; 21(6): 791–797. http://dx.doi.org/10.1016/0001-6160(73)90043-6

54. Devlin J.F. Stacking fault energies of Be, Mg, Al, Cu, Ag, and Au. Journal of Physics F: Metal Physics. 1974; 4(11): 1865–1882. http://dx.doi.org/10.1088/0305-4608/4/11/011

55. Li R., Lu S., Kim D., Schönecker S., Zhao J., Kwon S.K. and Vitos L. Stacking fault energy of face-centered cubic metals: Thermodynamic and ab initio approaches. Journal of Physics Condensed Matter. 2016; 28(39). http://dx.doi.org/10.1088/0953-8984/28/39/395001

56. Carter C.B. and Holmes S.M. The stacking-fault energy of nickel. Philosophical Magazine. 1977; 35(5): 1161–1171. http://dx.doi.org/10.1080/14786437708232942

57. Schramm R.E. and Reed R.P. Stacking fault energies of seven commercial austenitic stainless steels. Metallurgical Transactions A. July 1975; 6(7): 1345–1351. http://dx.doi.org/10.1007/BF02641927

58. Wang Z.Y., Han D. and Li X.W. Competitive effect of stacking fault energy and short-range clustering on the plastic deformation behavior of Cu-Ni alloys. Materials Science and Engineering A. 2017; 679(679): 484–492. http://dx.doi.org/10.1016/j.msea.2016.10.064

59. Muzyk M., Pakieła Z. and Kurzydłowski K.J. Generalized stacking fault energies of aluminum alloys-density functional theory calculations. Metals. 2018; 8(10): 12–14. http://dx.doi.org/10.3390/met8100823

60. Francisco de C., Best-fitting distribution to data vector using fitmethis, MATLAB Central File Exchange (2018). Retrieved Sep 19, 2018. Available at: https://uk.mathworks.com/matlabcentral/fileexchange/40167-fitmethis.

61. Wille T.H., .Gieseke W. and Schwink C.H. Quantitative analysis of solution hardening in selected copper alloys. Acta Metallurgica. 1987; 35(11): 2679–2693. http://dx.doi.org/10.1016/0001-6160(87)90267-7

62. Li S., Li Y., Lo Y.C., Neeraj T., Srinivasan R., Ding X.,et al. The interaction of dislocations and hydrogen-vacancy complexes and its importance for deformation-induced proto nano-voids formation in α-fe. International Journal of Plasticity. 2015; 74: 175–191. http://dx.doi.org/10.1016/j.ijplas.2015.05.017

63. Tehranchi A., Yin B. and Curtin W.A. Softening and hardening of yield stress by hydrogen–solute interactions. Philosophical Magazine. February 2017; 97(6): 400–418. http://dx.doi.org/10.1080/14786435.2016.1263402

64. Abraham D.P. and Altstetter C.J. The effect of hydrogen on the yield and flow stress of an austenitic stainless steel. Metallurgical and Materials Transactions A. 1995; 26(11): 2849–2858. http://dx.doi.org/10.1007/BF02669643

65. Boniszewski T. and Smith G.C. The influence of hydrogen on the plastic deformation ductility, and fracture of nickel in tension. Acta Metallurgica. March 1963; 11(3): 165–178. http://dx.doi.org/10.1016/0001-6160(63)90209-8

66. Mukherjee A.K., Mote J.D. and Dorn J.E. Strain hardening of single aluminum crystals during polyslip. Transactions of AIME. Berkeley, California; 1965. Available at: https://escholarship.org/uc/item/2523939t

67. Yao Z., Schäublin R., Spätig P. and Victoria M. The tensile properties of irradiated Ni single crystals and their temperature dependence. Philosophical Magazine. 2005; 85: 745–755. http://dx.doi.org/10.1080/14786430412331319947

68. Bullen F. P. and Cousland McK. S. The temperature dependence of the flow stress of copper single crystals. Physica Status Solidi (B). 1968; 27(2): 501–512. http://dx.doi.org/10.1002/pssb.19680270205

69. Hall E.O. The deformation and ageing of mild steel: II characteristics of the lüders deformation. Proceedings of the Physical Society. Section B. 1951. pp. 742–747. http://dx.doi.org/10.1088/0370-1301/64/9/302

3 Unravelling the Effect of Number of Cycles on Mesoscale Dislocation Substructures Under Cyclic Deformation

3.1 Introduction

Researchers [1–3] have shown that aluminium single crystal oriented for single slip does not form a plateau region in the cyclic stress-strain curve at 298K. Dhers and Drivers [4] revealed that stress response in [$\bar{1}23$] aluminium single crystal is sensitive to the number of cycles (*N*), however, they did not study the effect of *N* on dislocation substructures. Instead, the study [4] reported cell structure at a higher number of cycles. Some efforts [2,3] recognised that aluminium has a relatively higher T/T_m corresponding to 298K and tried to compare the stress level with Ni and Cu based on this difference. However, the simple arithmetic comparison did not explain the response of aluminium. Following these findings, it was conceived that the cyclic response of aluminium differs substantially compared to other FCC metals.

Following extensive literature data related to cyclic deformation of Ni, Cu, and Ag single crystals under different loading conditions, Li et al. [5] summarised the fundamental mechanisms related to the formation of mesoscale dislocation substructures and its corresponding relation with the macroscopic stress-strain response. They [5] showed that Ni, Cu, and Ag evolve similar dislocation substructure under fully reversed cyclic loading. However, they [5] missed recognizing that aluminium also evolves similar substructures likewise other FCC metals, but at different temperatures [6].

The TEM analysis [7] of cyclically deformed Cu single crystal at higher temperature showed that *N* has a significant effect on changing PSBs into cell structure. Since mesoscale substructures have a characteristic relation with stress response, therefore Lisiecki and Weertman's [7] finding indirectly supports the Dhers and Drivers [4] results related to aluminium at 298K. However,

estimation of the explicit effect of *N* on the evolution of mesoscale substructure is an open question and needs to be addressed. This work aims to reveal the cyclic response of aluminium single and polycrystal while considering mesoscale substructure as invariant among FCC metals.

The rate-dependent crystal plasticity models mainly depends on two aspects i) ΔG (energy barrier) dependence on effective stress, and ii) hardening mechanisms. The activation energy parameters considering different ΔG formulations have been discussed in the previous chapter in section 2.4.5. The results showed that Kock's formulation provides better results with nonlinear dependence of yield stress on temperature. Regarding the hardening mechanisms, the mesoscale substructure-based hardening has several advantages over dislocation density-based hardening as outlined in Section 1.2.

This work hypothesised that aluminium evolves similar mesoscale substructures as other FCC metals, however at different homologous temperatures. Therefore, we considered the same physics-based constitutive model that was used to study the cyclic response of nickel [8] previously. However, this work modifies the framework [8] to account for the explicit effect of *N,* temperature, and strain amplitude on the mesoscale substructure. The framework is implemented in Abaqus UMAT to study the response of aluminium single and polycrystal.

3.2 Physics-based crystal plasticity model

Crystal plasticity models rely on the multiplicative decomposition of the elastic and plastic components of the deformation gradient as [9],

$$\boldsymbol{F} = \boldsymbol{F^e F^p}, \tag{3.1}$$

The velocity gradient depends on slip system shear rate ($\dot{\gamma^{\alpha}}$) following,

$$\boldsymbol{L^p} = \sum_{\alpha=1}^{m} \dot{\gamma^{\alpha}} \, (\boldsymbol{s^{\alpha}} \otimes \boldsymbol{n^{\alpha}}), \tag{3.2}$$

Here, m is the total number of slip systems e.g. 12 for FCC crystal, $\boldsymbol{s^{\alpha}}$ and $\boldsymbol{n^{\alpha}}$ are the slip and normal directions of α^{th}slip system respectively. Kocks [10] proposed a thermally activated flow rule to quantify a shear rate along α^{th} slip system as,

$$\dot{\gamma}^{\alpha} = \dot{\gamma}_0^{\alpha} \exp\left[-\frac{F_0}{k_B T}\langle 1 - [\frac{\langle|\tau^{\alpha}-B^{\alpha}|-S^{\alpha}\rangle}{s_0^t \frac{\mu}{\mu_0}}]^p\rangle^q\right] sgn(\tau^{\alpha}-B^{\alpha}), \qquad \textbf{(3.3)}$$

where, $\dot{\gamma}_0^{\alpha}$ is the effective shearing rate, k_B is the Boltzmann constant, T is the temperature, F_0 is the glide activation energy, s_0^t is the thermal stress at 0 K, and p and q are the profile parameters. Also, μ and μ_0 are the shear modulus at temperatures *T* and 0K. Additionally, the Macaulay brackets follow $\langle G\rangle = 0$ if $G \leq 0$ or $\langle G\rangle = G$ if $G > 0$

The flow rule in equation (3.3) has been extensively used in crystal plasticity models with different hardening mechanisms [11–16]. In this work, equation (3.3) relates the rate of reaction (increment in plastic strain) with the height of the energy barrier (effective stress) and has an Arrhenius thermal dependence. For continuing flow, dislocation must overcome obstacles with aid of thermal activation. Moreover, effective shear stress (τ_{eff}^{α}) i.e. $|\tau^{\alpha}-B^{\alpha}|-S^{\alpha}$ that drive dislocation glide depends on the local resolved shear stress (τ^{α}), athermal stress (S^{α}) and intragranular back stress (B^{α}) due to dislocation long-range interactions at mesoscale.

The athermal stress in equation (3.3) has two components, i) the stress required to bow-out dislocations (controlling dislocation production) and ii) dislocation self-interaction stress controlling coplanar hardening proposed by Franciosi et al. [17].

$$S^{\alpha} = \alpha_{LE}\ \frac{\mu b}{2d_{struc}} + \mu b\sqrt{A_{ii}\rho^{\alpha}} \quad , \qquad \textbf{(3.4)}$$

In equation (3.4), α_{LE} is the dislocation line energy coefficient, A_{ii} is the self-interaction coefficient, ρ^{α} is the density of mobile dislocations.

Following Sauzay's approach of Eshelby inclusion problem [18], the intragranular back stress in equation (3.3) follows,

$$\dot{B}^{\alpha} = \frac{f_w}{1-f_w} \frac{2\mu(1-2S_{1212})}{1+4S_{1212}\mu f_{Hill}^{S}} \dot{\gamma}^{\alpha} \quad , \tag{3.5}$$

Where, f_w is the wall volume fraction, f_{Hill}^{S} is the instantaneous macroscopic plastic deformation tangent. The Eshelby tensor components for a prolate spheroid coordinate system follows [19],

$$S_{1212} = \frac{\pi\eta^2 + (\eta^2 - 1.75 - 2v_p\eta^2 + 2v_p)C_{12}}{8\pi(1-v_p)(\eta^2-1)} \quad , \tag{3.6}$$

$$C_{12} = \frac{2\pi\eta(\eta\sqrt{(\eta^2-1)} - \cosh^{-1}\eta)}{\sqrt[3]{(\eta^2-1)}} \quad , \tag{3.7}$$

And,

$$v_p = \frac{\nu + \frac{2}{3}\mu(1+\nu)f_{Hill}^{S}}{1+\frac{4}{3}\mu(1+\nu)f_{Hill}^{S}} \quad , \tag{3.8}$$

Here, v_p is the tangent elasto-plastic Poisson's ratio, and ν is the elastic Poisson's ratio. The parameter η is the ratio of ${l_{struc}}/{d_{struc}}$ that is the characteristic spacing of dislocation substructure. l_{struc} is the length that corresponds to the distance between two walls along the dominant slip plane and d_{struc} is the adjacent wall spacing.

Finally, Kocks [10] proposed that the effective shearing rate in equation (3.3) depends on the frequency (v_G) at which dislocations jump over point obstacles and density of mobile dislocations as,

$$\dot{\gamma}_0^{\alpha} = \rho^{\alpha} b l_{struc} v_G \quad , \tag{3.9}$$

The density of mobile dislocations in equation (3.4) and (3.9) follows,

$$\dot{\rho}_m^{s\alpha} = \frac{k_{multi}}{bl_{struc}}|\dot{\gamma}^{\alpha}| - \frac{2y_s^{edge}}{b}\rho_m^{s\alpha}|\dot{\gamma}^{\alpha}| - \frac{2\pi}{\mu b d_{struc}}\left|\dot{\tau_{eff}}\right|^{unload} + v_G\frac{d_{struc}}{d_0}\left(\phi_{cs}\sum_{\xi=1\,(\xi\neq\alpha)}^{N}\rho_m^{s\xi}e^{\left(-V_{CS}^{\alpha}\frac{\frac{\mu b}{4\pi y_s^{screw}}-|\tau^{\alpha}-B^{\alpha}|}{k_B T}\right)} - (1-\phi)\sum_{\xi=1\,(\xi\neq\alpha)}^{N}\rho_m^{s\alpha}e^{\left(-V_{CS}^{\xi}\frac{\frac{\mu b}{4\pi y_s^{screw}}-\left|\tau^{\xi}-B^{\xi}\right|}{k_B T}\right)}\right), \quad \textbf{(3.10)}$$

which is the net result of dislocation multiplication, annihilation, and cross slip [20–22]. In equation (3.10), $\rho_m^{s\alpha}$ and $\rho_m^{s\xi}$ is the density of mobile screw dislocation in primary and cross slip plane respectively, V_{CS}^{α} and V_{CS}^{ξ} is the cross slip activation volume in primary and cross slip plane respectively, y_s^{edge} and y_s^{screw} are the annihilation distances for edge and screw dislocations respectively, d_0 is the initial structural distance and k_{multi} determines the number of dislocations produced. Since two screw dislocation bows out of parallel walls [21], therefore Its value is 1 for the cells and 2 for parallel walls such as labyrinth or PSBs. The parameter ϕ_{cs} is the cross-slip efficiency that compensates for the inefficiency because some dislocations annihilate while cross slipping.

3.3 Effect of *N* on the mesoscale substructure

The effect of *N* on mesoscale substructure has not been studied explicitly with models. However, some researchers [7] showed that further cycling can change PSB into cells in Cu single crystal at 523K ($\frac{T}{T_m} = 0.38$). Figure 3-1 shows that dislocation substructure changes from veins-type dislocation walls into elongated cells with the explicit effect of number of cycles.

a) 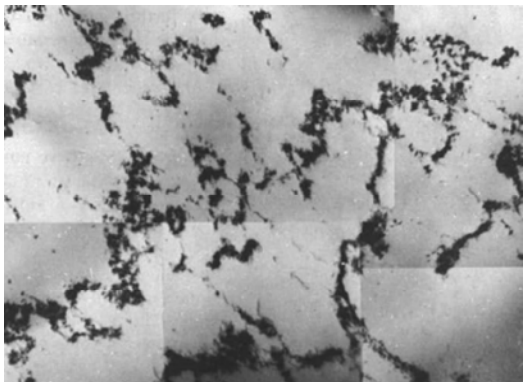 b) 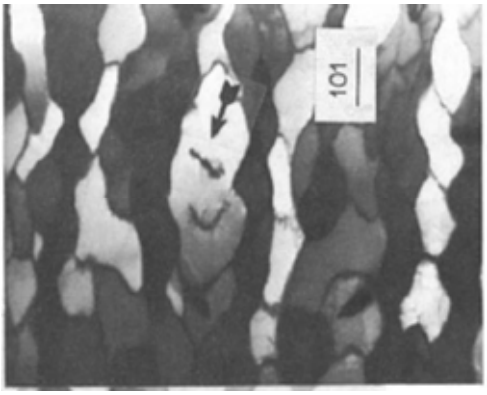

Figure 3-1 Dislocation substructure along ($1\bar{2}1$) plane of Cu single crystal oriented near [221] cycled at a) 523K, $\frac{\Delta\gamma_{pl}}{2} = 1 \times 10^{-3}$ and $\Delta\gamma_{cum}^{pl} = 4$ b) 523K, $\frac{\Delta\gamma_{pl}}{2} = 8.84 \times 10^{-4}$ and $\Delta\gamma_{cum}^{pl} = 73$.

The TEM data as shown in Figure 3-1 (a) and (b) correspond to slightly different strain amplitudes and different number of cycles. However, this is the best available data that shows the change of PSB into cells with increasing *N*. Figure 3-1(a) shows loose dislocation walls with short tentative PSBs, which transformed into well developed cells with the increasing number of cycles. Since cell structure evolves with the cross slip, Figure 3-1 supports the notion that plastic shear strain in cross slip plane should be a function of *N* at higher homologous temperature. It is well understood that cross slip activates due to activation of multiple slip systems at higher strain amplitude and higher temperature. However, this work reveals that cross slip can also increase with increasing *N* at higher homologous temperature.

To justify that plastic shear strain in cross slip plane increases as cell structure forms, this work analyses the TEM data in Cu single crystal at different temperatures. Lisiecki and Weertman [7] showed that Cu single crystal evolves PSB at 523 K, however no PSBs were found at 678K. Figure 3-2(a) shows how PSBs along primary [101] and secondary [110] slip direction intersects to form cell walls at 523 K, $\frac{\Delta\gamma_{pl}}{2} = 3.5 \times 10^{-4}$, and $\Delta\gamma_p^{cum} = 31$. In Figure 3-2(a), the walls along [211] are less dense due to limited cross slip at 523 K. Figure 3-2(b) shows the cell structure along same plane at 678K, $\frac{\Delta\gamma_{pl}}{2} = 3.5 \times 10^{-4}$, and $\Delta\gamma_p^{cum} = 31$,

which shows denser walls due to profuse cross slip and increase in cyclic plastic shear strain in cross plane.

a)

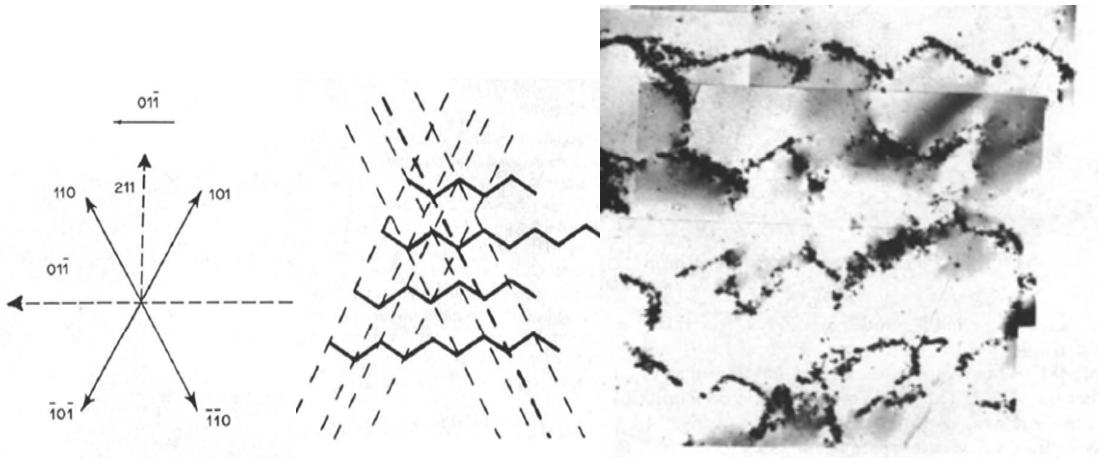

b)

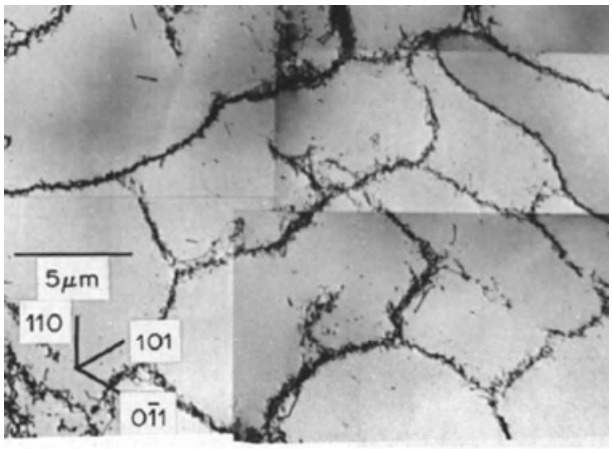

Figure 3-2 Dislocation substructure along ($1\bar{1}\bar{1}$) common cross slip plane of Cu single crystal oriented near [211] cycled at a) 523K, $\frac{\Delta\gamma_{pl}}{2} = 3.5 \times 10^{-4}$ and $\Delta\gamma_{cum}^{pl} = 31$ b) 678K, $\frac{\Delta\gamma_{pl}}{2} = 3.5 \times 10^{-4}$ and $\Delta\gamma_{cum}^{pl} = 31$.

The findings [7] shown in Figure 3-1 demonstrate the effect of *N* on transformation of PSBs into cells in Cu single crystal at $\frac{T}{T_m} = 0.38$. Since the aluminium has $\frac{T}{T_m} = 0.32$ at room temperature, which corresponds to higher temperatures for Ni (600K) and Cu (~523K), therefore Figure 3-1 likely explains why most studies reported cells in aluminium. This work hypothesises that the cyclic response of aluminium at 298K is sensitive to *N* [4] and it evolves slip bands that transform into cells with increasing *N*. Following on, this work proposed that *N* has a

noticeable effect on the mesoscale substructure at higher $\frac{T}{T_m}$ and needs to be accounted to predict the cyclic response of FCC metal.

The cell structure forms when abundant cross slip is activated, and plastic strain started accumulating in the cross slip plane as shown in Figure 3-2. This reflects that the amount of cumulative plastic strain in cross-plane can be used as an indicator to quantify the effect of *N* on transformation of PSB into cells. Following on, we proposed a relationship between plastic shear strain range in cross slip plane ($\Delta\gamma^{Cross}$) and *N* as,

$$\Delta\gamma^{Cross} = \frac{\gamma_{cum}^{Cross}}{N} \quad \textbf{(3.11)}$$

Here, γ_{cum}^{Cross} is the cumulative plastic shear strain in the cross slip plane. As mentioned earlier, there is no TEM data available to quantify this parameter. Therefore, we calibrate this while comparing the model stress-strain response with experiments for aluminium single crystal oriented for a single slip at 298K. Following on, we kept γ_{cum}^{Cross} constant for evaluating different temperatures and multiple slip orientations.

3.4 Mesoscale crystal plasticity framework

Literature [5] showed that FCC metals develop four saturated substructures: veins, PSBs, cell, and labyrinth during cyclic deformation. The formation of these substructures is controlled by dislocation interactions and loading conditions. Here, we summaries the existing literature findings related to cyclic deformation of aluminium:

- Aluminium single crystals oriented for single slip develop vein structure at 77K [23] that transform into PSBs at higher strains [24] similar to Ni and Cu [5]. At room temperature mostly cells are observed however, TEM data recorded in experiments mostly corresponding to higher *N* [3,4]. Following the literature related to aluminium [4] and Cu at ~0.32 and 0.38 homologous temperature respectively, this work proposed that aluminium evolve slip bands at lower *N* that transformed later into cells

with increasing *N.* Since cell structure is associated with cross slip, we propose equation (3.11) explicitly accounting for the effect of *N* on PSB transformation into cells.

- Aluminium single crystal oriented along [001] direction [25] shows labyrinth structure due to the activation of Hirth locks. If both Hirth locks pairs form on the most active slip system ($\Delta\gamma^{Hirth}$), then labyrinth substructure will form [5].
- Crystals oriented along [011] form wall structure [26].

Following the above finding, this work considered the same saturated substructure i.e. veins, PSBs, cells, and labyrinth to study the cyclic response of aluminium. The crystal plasticity framework [8] is modified to further include the effect of temperature and number of cycles using equation (3.11) as shown in Figure 3-3. We considered predicting the saturated mesoscale substructures based on plastic shear strain ($\Delta\gamma^{\alpha}$) among different slip systems α,

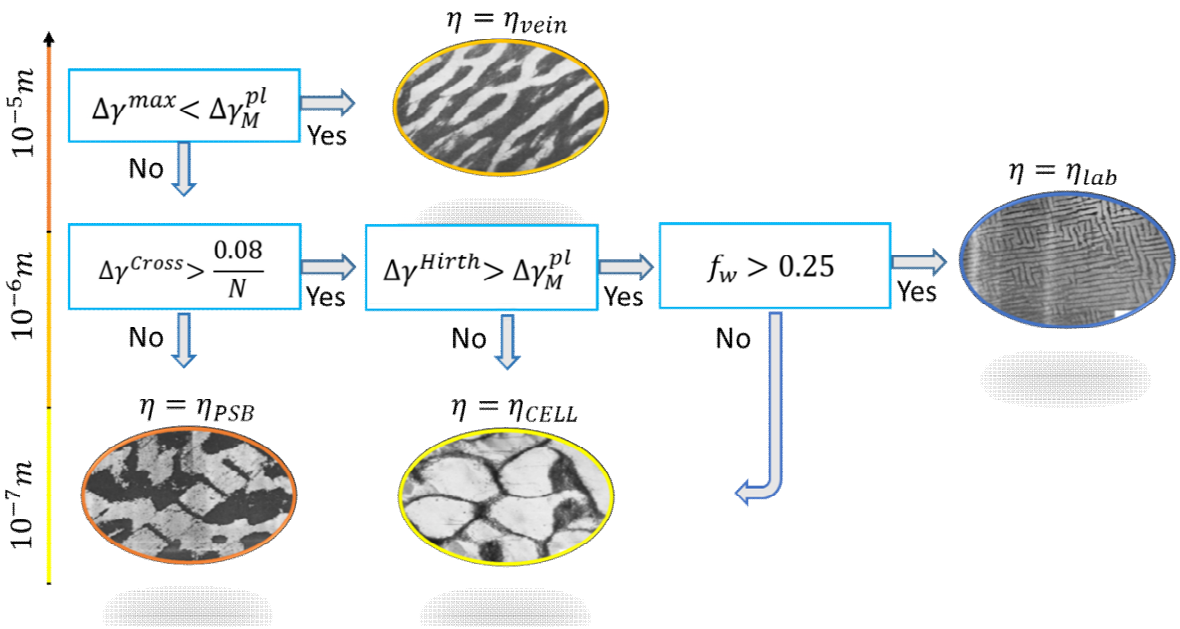

Figure 3-3 Proposed framework for assigning saturated dislocation substructure at each FE integration point depending on $\Delta\gamma_{pl}$ among slip systems that are a function of different loading conditions applied at a time.

The flowchart in Figure 3-3 predicts the saturated substructure for a given state of plastic strain range among slip systems over a loading cycle. At low strain amplitude, when cyclic plastic shear in primary slip system ($\Delta\gamma^{max}$) is less than $\Delta\gamma_M^{pl}$, vein structure will form. If $\Delta\gamma^{max}$ exceeds $\Delta\gamma_M^{pl}$ but there is no cross slip, then PSB will form. This is the case of a single slip oriented crystal at low strain amplitude $<10^{-3}$ and low T/T_m. if multiple slip activates either due to crystallographic orientation, high strain amplitude, or high T/T_m, then a complex labyrinth or cell structure will form. After computing the structure, the parameters related to mesoscale substructures i.e. (η, d_{struc}, f_w) will be updated to compute the back stress, bow-out stress, and dislocation density.

The parameter $\Delta\gamma^{max}$ in Figure 3-3 represents maximum plastic shear strain range in the most active slip system. $\Delta\gamma^{cross}$ and $\Delta\gamma^{Hirth}$ represent the range of plastic shear strain in cross slip and Hirth plane respectively. The parameter $\Delta\gamma_M^{pl}$ represents the range of plastic strain accommodated in vein structure and serves as a transition point between veins and PSBs as shown in Figure 3-4. For Cu and Ni single crystals [27], its value is found to be ~ 5×10^{-5}.

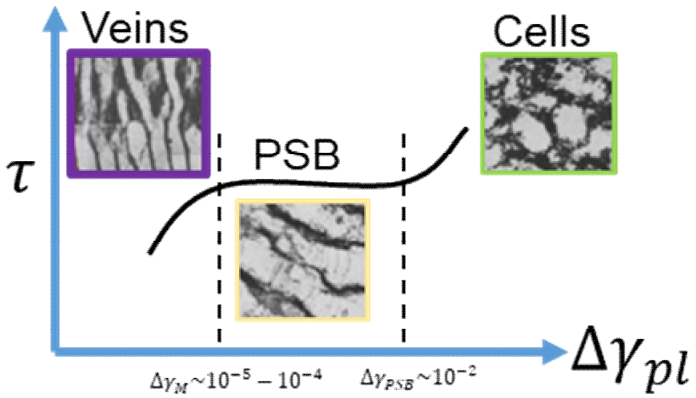

Figure 3-4 Cyclic stress-strain response of Cu single crystal and correspond dislocation substructure at different plastic shear strain amplitude [28]**.**

Hahner et al. [29] mentioned that the stability of dipoles in dislocation walls is a function of the amount of plastic strain (dislocation density). Since aluminium evolve cross slip much earlier that can annihilate the mobile dislocations. Thus,

justifies higher γ_M^{pl} as compared to other FCC metals. Moreover, literature [24,28] also showed that parameter ($\Delta\gamma_M^{pl}$) is a function of temperature and has a higher value corresponding to lower temperature. Here, this work considered $\Delta\gamma_M^{pl} = 1 \times 10^{-4}$ at 298 K and $\Delta\gamma_M^{pl} = 1 \times 10^{-3}$ at 77K for aluminium [4,24].

The next sections explain the quantification of model parameters using literature data related to FCC metals and implementation of crystal plasticity framework (Figure 3-3) in Abaqus to study the cyclic response of aluminium single and polycrystal.

3.5 Model implementation for aluminium

The present work validates and extends the applicability of the physics-based model [8] from Ni to high SFE aluminium using a modified crystal plasticity framework (Figure 3-3). The framework is implemented using Abaqus UMAT and UXTERNALDB subroutines [30]. A simple mesh is created in Abaqus containing 500 brick elements (C3D8R) as shown in Figure 3-5. Four crystal orientations i.e. [149], [011], [001], and [111] are considered along the loading direction for single crystal meshes (Figure 3-5). For polycrystals, each element represents a single grain, and a different random orientation is assigned to each element for representing a collective response as shown in Figure 3-6. The displacement and periodic boundary conditions are specified along the x-axis and the remaining four faces of the model are left as a traction free surface in all simulations.

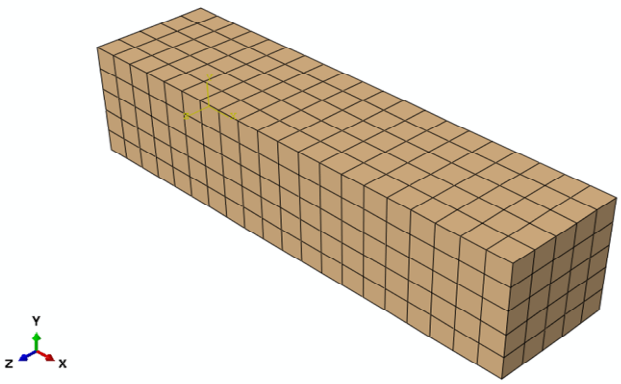

Figure 3-5 Single crystal specimen with the Voxellated finite element mesh containing 500 elements.

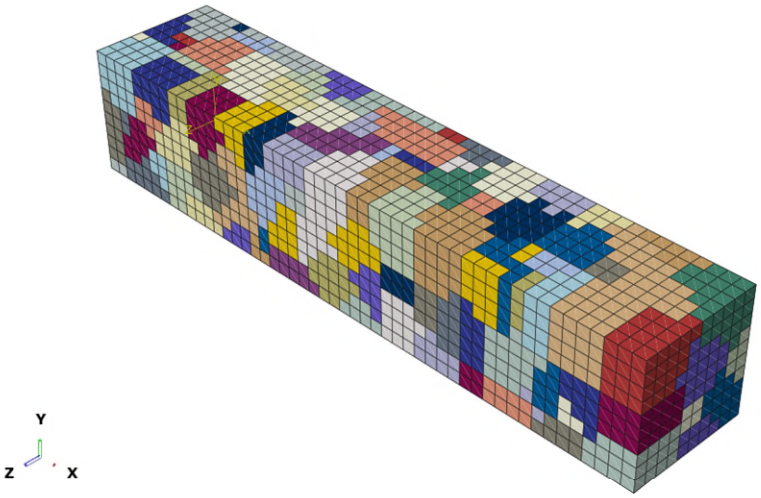

Figure 3-6 Finite element mesh of a polycrystal specimen. Colors represent the different grains. Model contains 237 grains, 5000 elements.

In the high cycle fatigue regime, the evolution of saturated dislocation substructure requires thousand and millions of physical cycles. It is computationally infeasible to run thousands of cycles for crystal plasticity calculations. This work employed the same decoupling time scale strategy as proposed by Castelluccio and McDowell [8] to implement the new crystal plasticity framework. The saturated substructures are updated once per computational cycle depending on the plastic shear strain range among active slip planes as shown in Figure 3-3.

3.5.1 Independent quantification of model parameters

The estimation of model input parameters is an important prerequisite to study the physics-based material response. The physical approximation of input parameters determines the physical nature of a model. This work aims to estimate the input parameters and their underlying uncertainties independently using experimental data related to FCC metals. The constitutive model mentioned in section 3.2 consists of two types of parameters: Fundamental parameters with low uncertainty and model parameters related to different

deformation mechanisms. The summary of fundamental parameters is shown in Table 3-1.

Table 3-1 Fundamental parameters for aluminium.

Elastic constants [31] (GPa)	$C_{11} = 114.216 - 10.11141/(exp(258.4/T) - 1)$ $C_{12} = 61.9493 - 2.05109/(exp(293.6/T) - 1)$ $C_{44} = 31.6054 - 2.56479/(exp(168/T) - 1)$
Boltzmann constant (k_B) ($JK^{-1}\,mol^{-1}$)	8.314
Attempt frequency (s^{-1})	$5x10^{11}$ [32]
Burgers vector (10^{-10} m)	2.86 [10]

The model parameters are related to deformation mechanisms occurring at multiple scales under cyclic loading and having relatively high uncertainty compared to fundamental parameters. These constants include glide activation energy parameters, dislocation interaction parameters, and parameters related to saturated dislocation substructures. The model parameters can be quantified by indirect measurement from experiments and dislocation dynamics simulations.

The parameters related to glide activation energy are estimated in Chapter 2 as shown in Figure (2-11). Following on, this work considered $F_0 = 0.8\,eV$ and s_o = 12 MPa. The unique values of F_0 and s_o are computed by rerunning the analysis (Section 2.4) using the fixed values of other parameters used in this work. Similarly, the quantification of self-interaction coefficient (A_{ii}) and line tension coefficient (α) in equation (3.4) has already been described in the previous chapter (Section 2.3). Following on, this work considered A_{ii} = 0.1 and α=1.

In equation (3.10), the parameter related to annihilation distances for edge and screw dislocations can be quantified using experiment and TEM data. Tippelt et

al. [33] found that the dislocation dipoles are stable only if their heights (h) lie between critical annihilation distance for edge dislocation (y_e) and critical height of dipoles. They [33] proposed minimum dipole height as annihilation distance for edge dislocation i.e. y_e= 2.6 nm for Ni at 293 K. Kassner and wall [34] calculated the minimum dipole height in Al is 3 nm at 77 K. Since, the annihilation distance is not sensitive to temperature [33,35]. Therefore, we considered the same annihilation distance ~ 3-3.5 nm for Al. The annihilation distance for screw dislocation was considered to be 50 nm as suggested by Feaugas [36] and Essmann and Mughrabi [21].

The cross-slip activation volume in equation (3.10) is also a dislocation interaction parameter, whose quantification is sensitive to the length scales. Since cross slip is a microscopic phenomenon. Therefore, we relied on the studies [37] that estimated the activation volume at a microscopic scale. We considered the activation volume ~1000b^3 for aluminium in the present work.

The cross-slip efficiency parameter ($\emptyset cs$) is introduced in equation (3.10) to compensate for the inefficiency of the annihilation of dislocation in the cross slip plane. The value of this coefficient is around 0.5.

This work hypothesised that mesoscale substructures control strain hardening and back stress by constraining the motion of dislocation (mean free path). Hence, the characteristic spacing η in equation (3.8) represents the mean value for corresponding substructures as shown in Table 3-2.

Table 3-2 The constant η provide the approximate distance dislocation (*l*) can glide along a dominant slip system relative to the distance between channel walls (d_{struc}).

Dislocation substructure	Veins	PSBs	Labyrinth	Cells
$\eta = {}^{l}/_{d_{struc}}$	~50	~20	~2	~1

The similitude coefficient (k_{struc}) is another parameter related to the substructures, which relates the dependence of shear stress on channel width (d_{struc}). Sauzay and Kubin [38] have shown that Cu and Ni follow the similitude relation under cyclic and monotonic loading conditions. However, some efforts have independently [24,39] showed the similitude relation in aluminium and suggested k_{struc} equals to be 2.5. Therefore, we assume the same k_{struc} for present work.

Wall thickness is another characteristic distance related to mesoscale substructures, which determines the wall volume fraction (f_w) and quantifies the structural spacing. Although the quantification of wall size is hard because of assumptions and idealization in geometric configurations and lack of TEM data for various loading conditions. Here, this work considered calculating the wall volume fraction using a phenomenological approach resembles Estrin et al. [40],

$$f_w = f_{inf} + \left(f_0 - f_{inf}\right) exp\left(\frac{-\Delta\gamma^{max}/2}{g_p}\right) \quad \textbf{(3.12)}$$

Where f_0 and f_{inf} are the initial and saturation values of wall volume fraction and g_p describes the rate of decrease of f_w with strain rate and equals to 1.5. The parameters in equation (3.12) can be estimated by measuring f_w from TEM data. Several efforts [36,40–42] computed f_w using different geometric models depending on wall characteristic spacing measurements. Here, this work considered Feaugas [36] approach to estimate the f_{inf} as the ratio of wall thickness (W) divided by the wall spacing (d_{struc}).

Studies related to cyclic deformation of Ni, Cu, and stainless steel [29,43–45] showed that the wall thickness when a crystal is fully covered with PSBs is not a function of temperature. However, the spacing between adjacent walls (d_{struc}) increases with temperature [38]. The TEM analysis [23,46] of aluminium single crystals under cyclic deformation also showed that wall thickness does not vary with temperature as shown in Figure 3-7. However, the wall spacing was found to be roughly 2 μm at 298K [25] and ~0.5 μm at 77K [24]. Using TEM data [23,46] as shown in Appendix B.1, we measured the wall thickness equals to be ~0.15μm

corresponding to 77K and 298K. Following on, f_{inf} can be estimated as the ratio of W/ d_{struc}, which is equal to ~0.1 at 298K and 0.29 at 77K. The peak value of wall fraction (f_0) corresponds to the volume fraction occupied by the veins, which is approximated to be 45% [47,48].

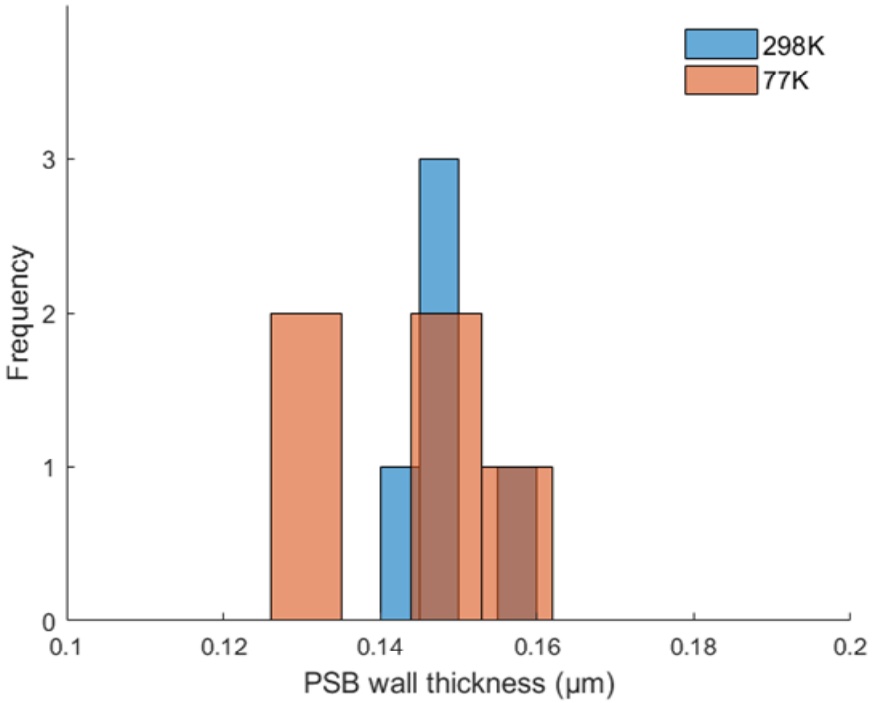

Figure 3-7 PSB wall thickness at 298K and 77K computed from TEM data [23,46]**.**

This work computed the cell wall thickness and cell size using the TEM data [49–52] at 77K and 298K for pure aluminium as shown in Appendix B.2. The cell size varies as a function of applied strain. For instance, cells are larger and coarser at lower strains due to potential lack of saturation and equiaxed at higher strains. Here, we computed the multiple cell sizes from each TEM data rather than estimating an average cell size to quantify the uncertainty. In Figure 3-8, the data with a large errorbar represent coarser cells correspond to low temperature or lower applied strains and vice versa. Figure 3-8(b) shows that the ratio of W/ d_{struc} for cells is constant on average, which follows that f_{inf} for cells is not a function of temperature. Here, this work considered f_{inf}= 0.2 for cells.

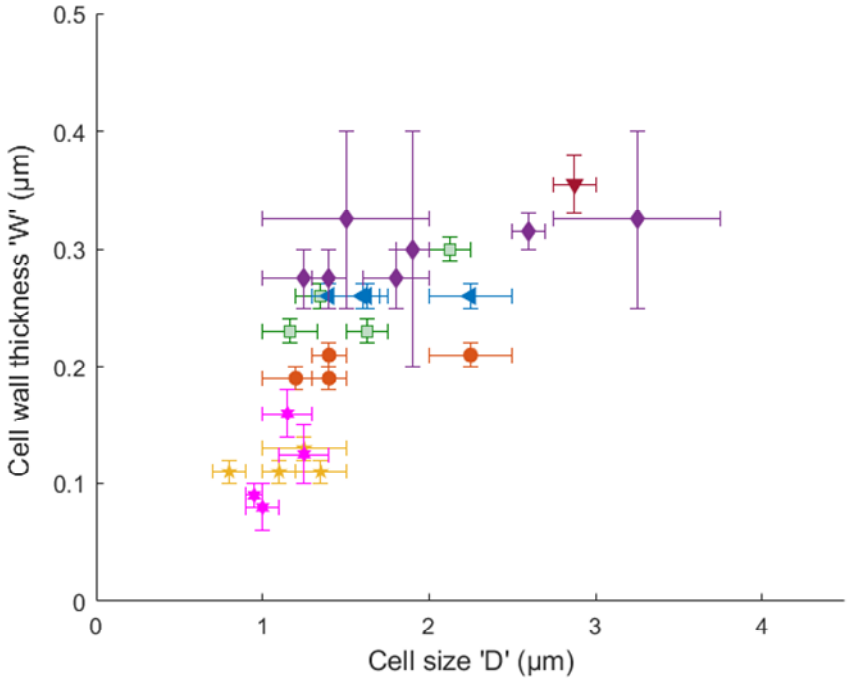

a)

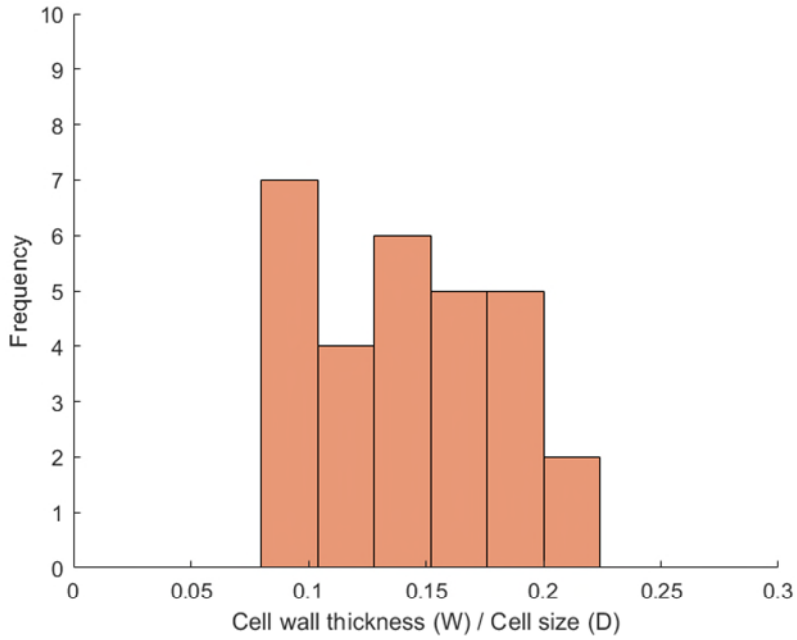

b)

Figure 3-8 a) Correlation between cell wall size and wall thickness at different temperatures b) Histogram showing the ratio of cell thickness and cell size.

Finally, Table 3-3 and Table 3-4 shows a summary of the physical constants and temperature dependent parameters used in the model respectively. The summary of initial values for internal state variables are:

The density of mobile (screw) dislocations (ρ_{m0}^{s})= 10^9 m^{-2}

The initial structure distance (d_{struc}^{o})= 10 μm

The normalised glide $\eta = \eta_{veins}$, the f_w is initiated at low values for convergence (f_w^0) = 0.1

The cross-slip activation volume (V_{CS}^0) = $1000b^3$

Table 3-3 Summary of physical constants used in the constitutive model.

Parameter	Value	Parameter	Value
F_o	0.8 eV	G_{PSB}	2×10^{-2}
s_o^t	12 MPa	K_{multi}^{walls}	2
p	0.667	K_{multi}^{cell}	1
q	1.5	y_s	$50\ nm$
f_{inf}^{cells}	0.2	y_e	$3.5\ nm$
f_o	0.45	K_{struc}	2.5
g_p	1.5×10^{-3}	A_{ii}	0.1
α_{LE}	1		

Table 3-4 Summary of temperature dependent parameters used in the model.

Parameters (*T*)	298K	77K
*μ (*GPa*)*	25.9	28.9
f_{inf}^{PSB}	0.1	0.29
G_M	1×10^{-4}	1×10^{-3}

3.5.2 Comparison of model results with experiments

Figure 3-9 compares the experiment and model results for the cyclic stress-strain response of [149] aluminium single crystals at 298K and $\dot{\epsilon}$ =1 x10^{-3} s^{-1} and $R_\epsilon = -1$. Each point in Figure 3-9 corresponds to a new simulation at different total applied strain and stabilised computational cycle. It is important to distinguish the terms physical and computational cycles used in experiments and modelling respectively. The latter represents the number of cycles to achieve a stabilised stress-strain response of the model whereas, the former corresponds to number of cycles physically applied in the experiments. In this work, each simulation result (each point in Figure 3-9) corresponds to 25 computational steps, which was enough to achieve the convergence of stress response. Besides, this work predicted the effect of number of physical cycles using crystal plasticity framework (Figure 3-3) without running it.

In Figure 3-9, the stress response is studied for a fixed physical number of cycles i.e. *N*=50 and $\gamma_{cum} = 50$ at 298K following experiment [4]. The γ_{cum} is calculated using $4N\gamma_{pl}$ [47], where γ_{pl} is the plastic strain amplitude. Figure 3-9 shows the change of peak stress level with increasing number of physical cycles above 0.1% plastic strain and agrees with the experiment [4]. Moreover, this variation of stress with *N* follows the framework shown in Figure 3-3. This implies that at *N*=50 model predicted slip bands corresponds to lower stress level (black diamond). However, at higher N ($\gamma_{cum} = 50$) and above 0.1% plastic strain, blue diamond represents cells that showed a higher stress level with explicit effect of *N*.

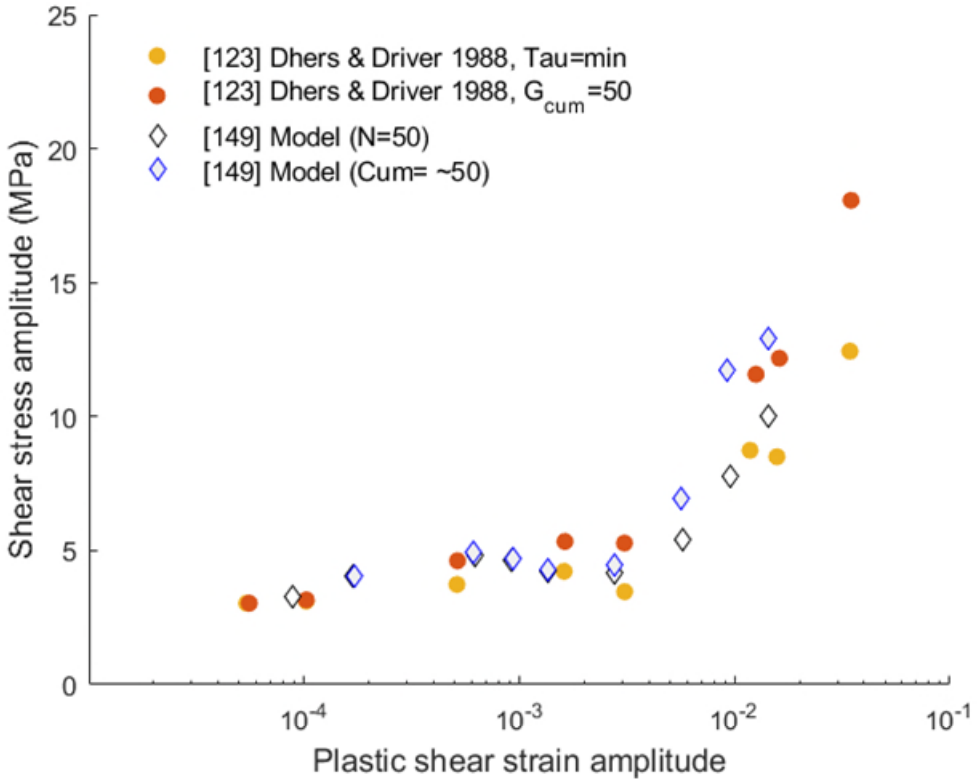

Figure 3-9 Cyclic stress-strain response of [149] aluminium single crystal under fully reversed strain-controlled loading ($R_\epsilon = -1$) at 298K. The stress response as a function of *N* is compared with experiments [4]**.**

Figure 3-10 presents the cyclic stress-strain response of [149] aluminium single crystal at 77K, $\dot{\epsilon}$ =1x10^{-3} s^{-1} and $R_\epsilon = -1$. Each point in Figure 3-10 corresponds to a simulation at different total applied strain, stabilized computational cycle and 5000 physical cycle. The choice of 5000 physical cycles is associated with the saturated stress state in experiment [24]. The stress-strain curve shows a clear plateau region correspond to PSBs similar to Ni and Cu. Besides, the results are in agreement with experiments for aluminium [24].

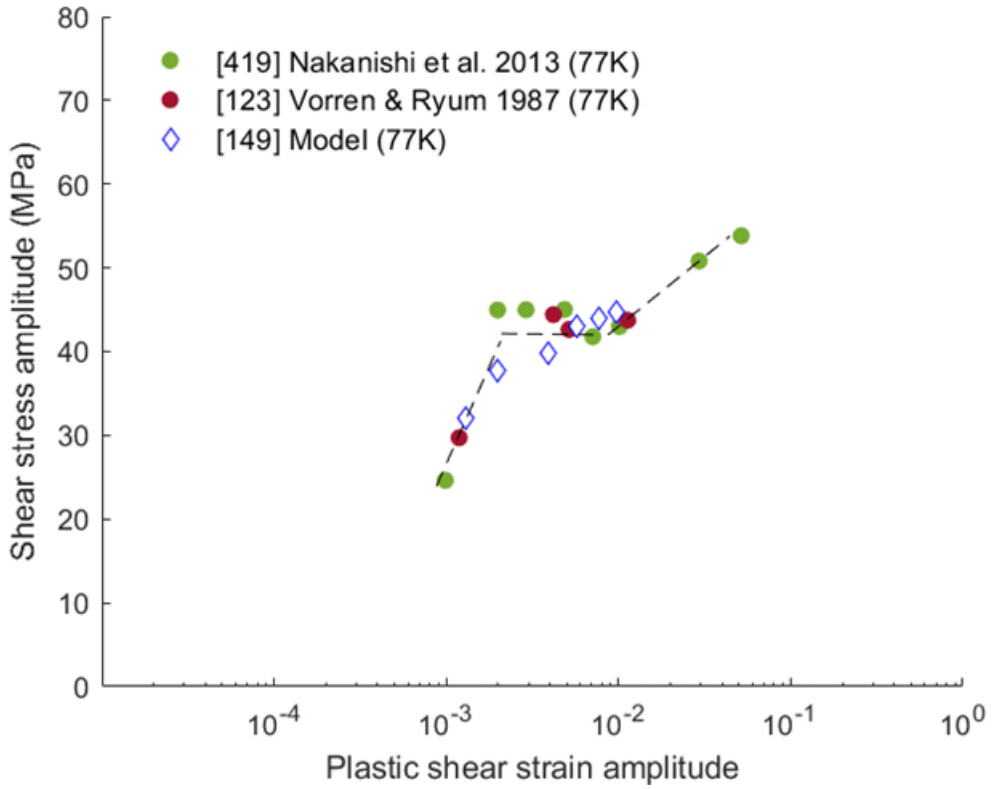

Figure 3-10 Cyclic stress-strain response of [149] aluminium single crystal under fully reversed strain-controlled loading ($R_\epsilon = -1$) at 77K.

Figure 3-11 presents the complete stress-strain curve for [149] aluminium single crystal corresponds to the stabilised cycle at 298K and 77K. The model results show a good agreement with experiments [2]. However, the shape of cyclic stress-strain obtained from the model is more rectangular compared to experiments as shown in Figure 3-11. Since the finite element geometry (Figure 3-5) is different from the real specimens used in experiments in terms of shape and microstructural history, thereby a difference in the stress-strain curve could be expected. Overall, the peak stresses and area under the stress-strain curve (strain energy) agrees well with experiments, which are more relevant for fatigue prognosis than the shape of the entire curve because these are the indicators of fatigue response of material [53].

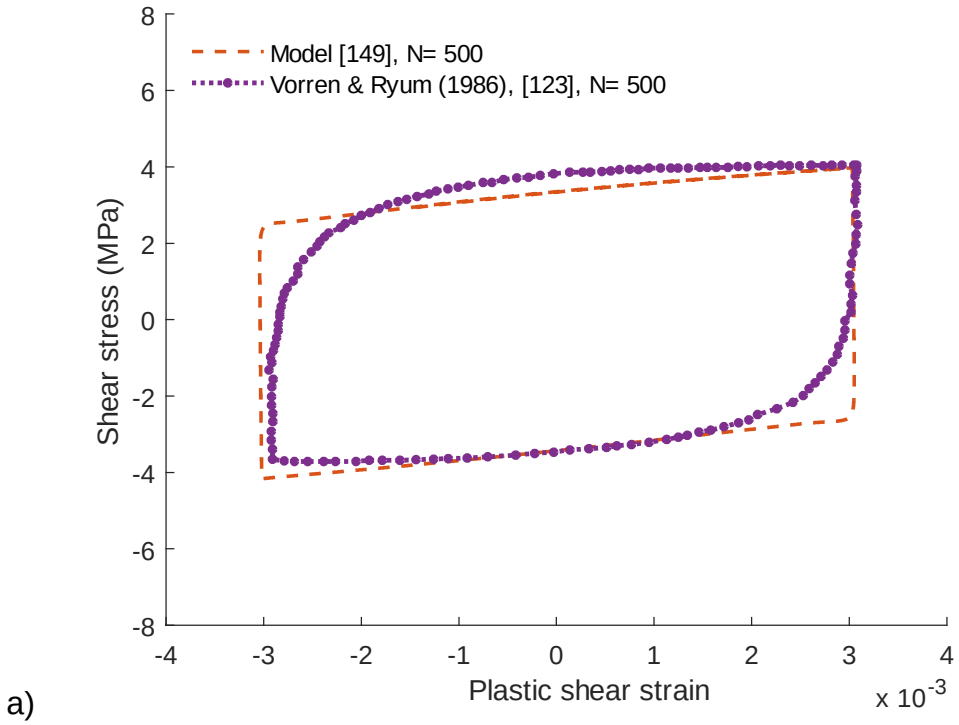

a)

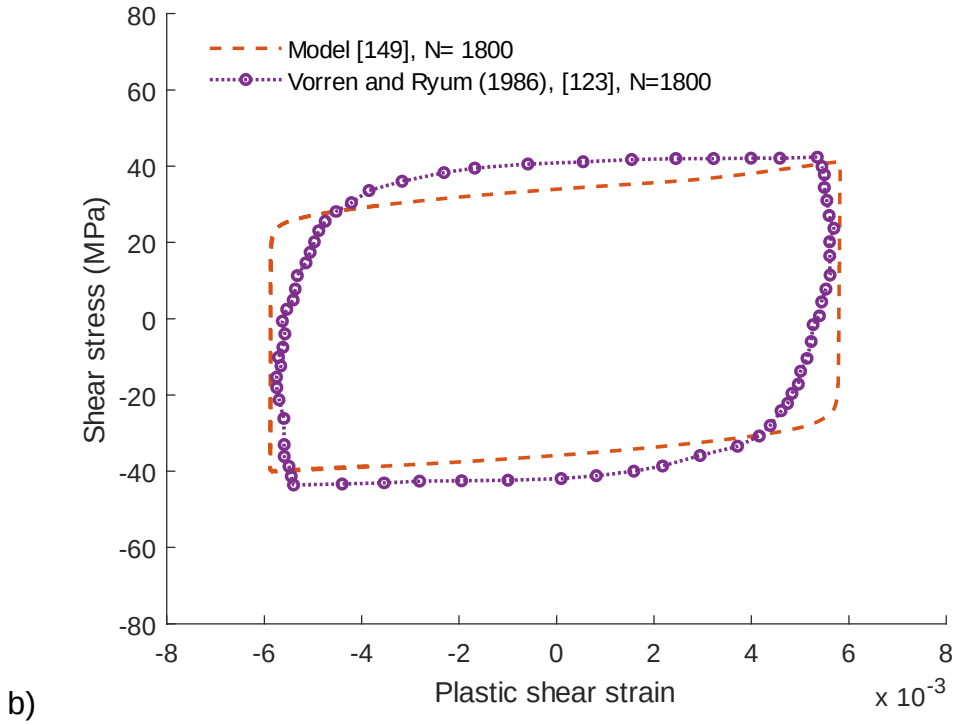

b)

Figure 3-11 Comparison of complete stress-strain curve of [149] aluminium single crystal with the experiment at a) $\frac{\Delta\gamma_{pl}}{2} = \sim 3 \times 10^{-3}$ and 298K [2] b) $\frac{\Delta\gamma_{pl}}{2} = \sim 6 \times 10^{-3}$ and 77K [2].

Figure 3-12 compares hardening curves in model and experiments for aluminium single crystal oriented for single slip. Each point corresponds to a different simulation at the different number of physical cycles and at room temperature. The mesoscale substructures shown in Figure 3-12 are the representative substructures obtained in simulations. Since the mesoscale substructure is computed over each element, the percentage of cell structure mentioned in Figure 3-12 corresponds to the elements that have cells. The model results are in good agreement with the experiments. Figure 3-12 demonstrates that N has a significant effect on mesoscale substructure particularly in aluminium due to its high homologous temperature at 298K.

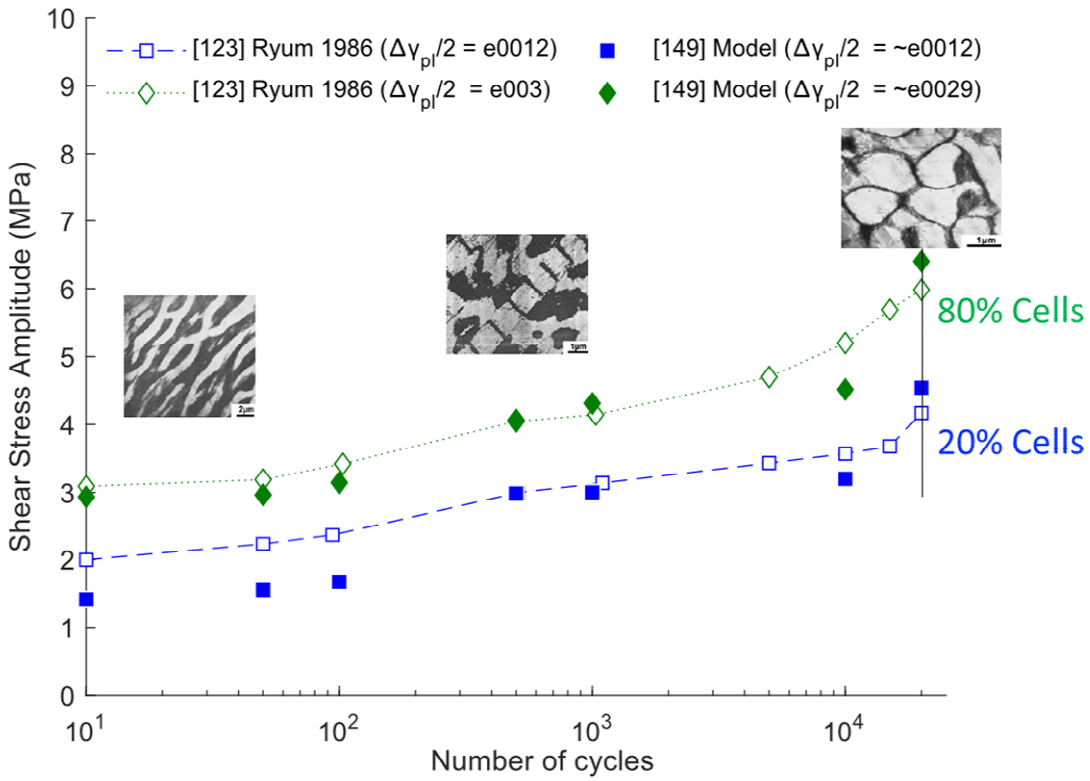

Figure 3-12 Cyclic hardening of aluminium single crystal oriented for single slip.

Figure 3-13 presents the cyclic stress-strain response of aluminium single crystal oriented along [011] [001], and [111] at 298K, $\dot{\epsilon}$ =1 x10^{-3} s^{-1} and $R_\epsilon = -1$. Each point in Figure 3-13 corresponds to a simulation at different total applied strain,

stabilized computational cycle, and 5000 physical cycles. The choice of 5000 physical cycles is associated with the saturated stress state in the experiment [25,26]. The stress level and overall trends for [001] and [011] crystal agree with experiments [25,26]. Figure 3-13 also shows the stress-strain response of [111] single crystal. The trend of stress evolution corresponding [111] single crystal agrees with Cu single crystals [54]. However, there is currently no experimental data available to compare [111] model results. This work considered predicting the cyclic stress-strain response of aluminium single crystal along single and multiple slip orientation before predicting the polycrystal response. In other words, we calibrate the individual response of grains to mitigate the uncertainties underlying polycrystal.

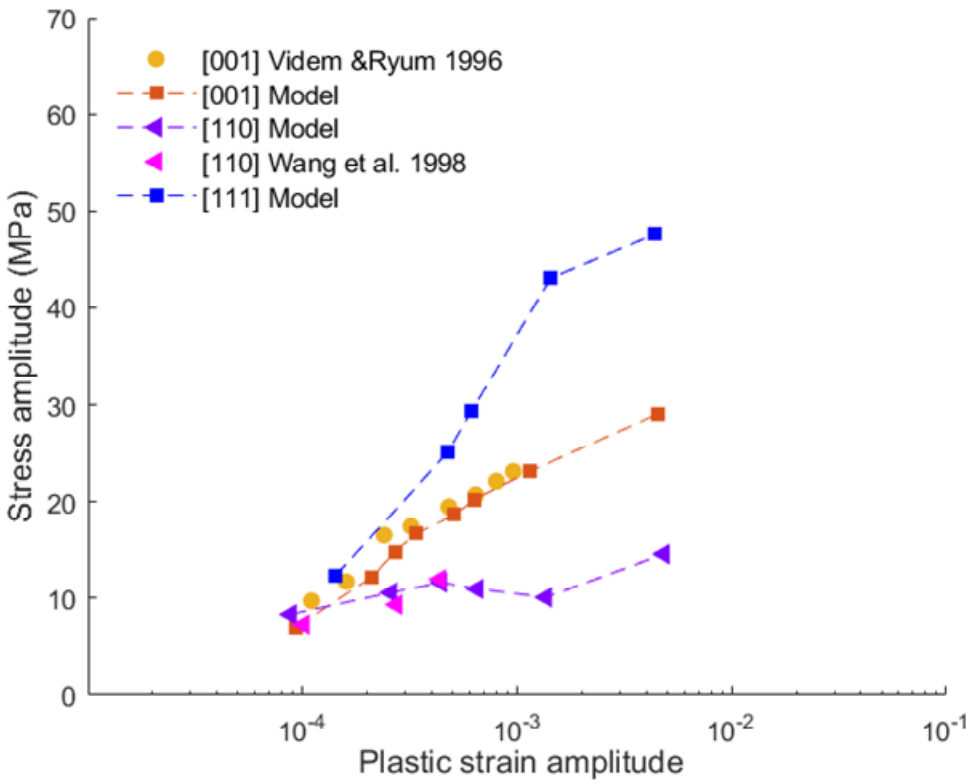

Figure 3-13 Cyclic stress-strain response of aluminium single crystal oriented along [001], [011], and [111] direction under fully reversed strain-controlled loading ($R_\epsilon = -1$) at 298K. The [001] and [011] results were compared with available experimental data [25,26]**.**

Figure 3-14 presents the comparison of stress-strain response of pure aluminium polycrystal between model and experiments [55–57]. Each point in Figure 3-14 corresponds to a simulation at different total applied strain, stabilized computational cycle and 5000 physical cycle. The mechanism of cyclic deformation in single crystals are generally applicable to the grains of polycrystals [47]. However, grain boundaries significantly affect the cyclic deformation response [47]. Because the model was calibrated with large single crystals, the results in Figure 3-14 are representative of large grains when the grain size effect saturates. Thus, the results agree well with large grain experimental data [55–57]. At this stage, the model does not have an explicit grain size effect, but future efforts will introduce the explicit size effect in the model to study the cyclic response of polycrystals with different grain sizes.

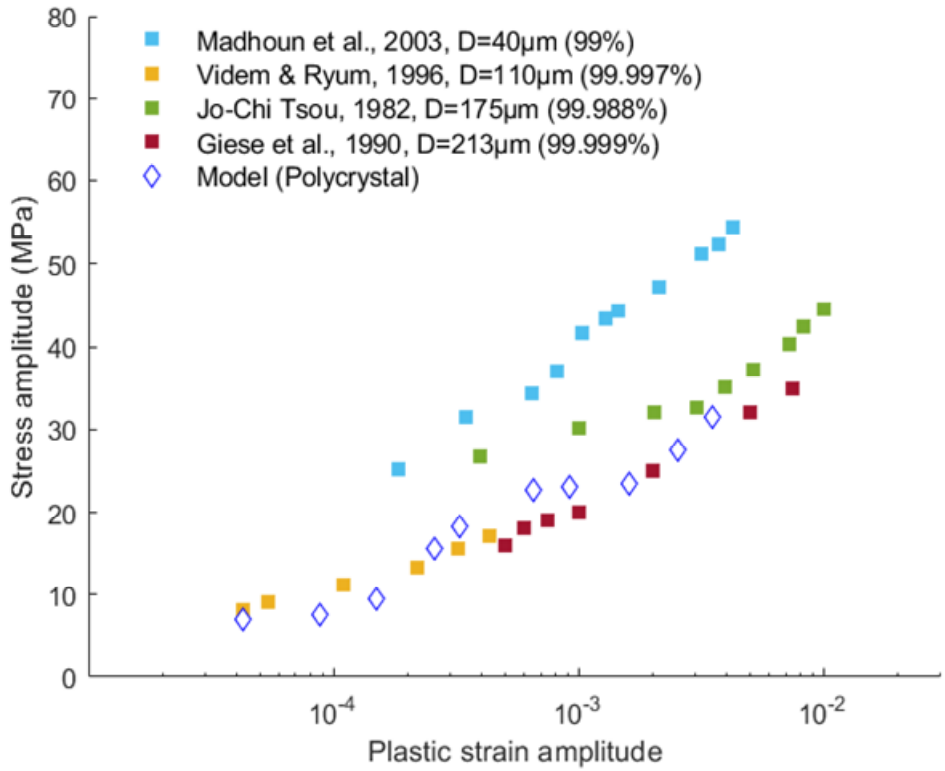

Figure 3-14 Comparison between model and experiment [49,55–57]**.: Cyclic stress-strain response of different polycrystals. Filled square markers represent experiments and empty diamonds correspond to Model results.**

Figure 3-15 presents the complete cyclic stress-strain response of aluminium polycrystal correspond to the stabilised cycle at 298K and $\frac{\Delta\epsilon_{pl}}{2} = \sim 1 \times 10^{-3}$. The model results show a good agreement with experiments [57].

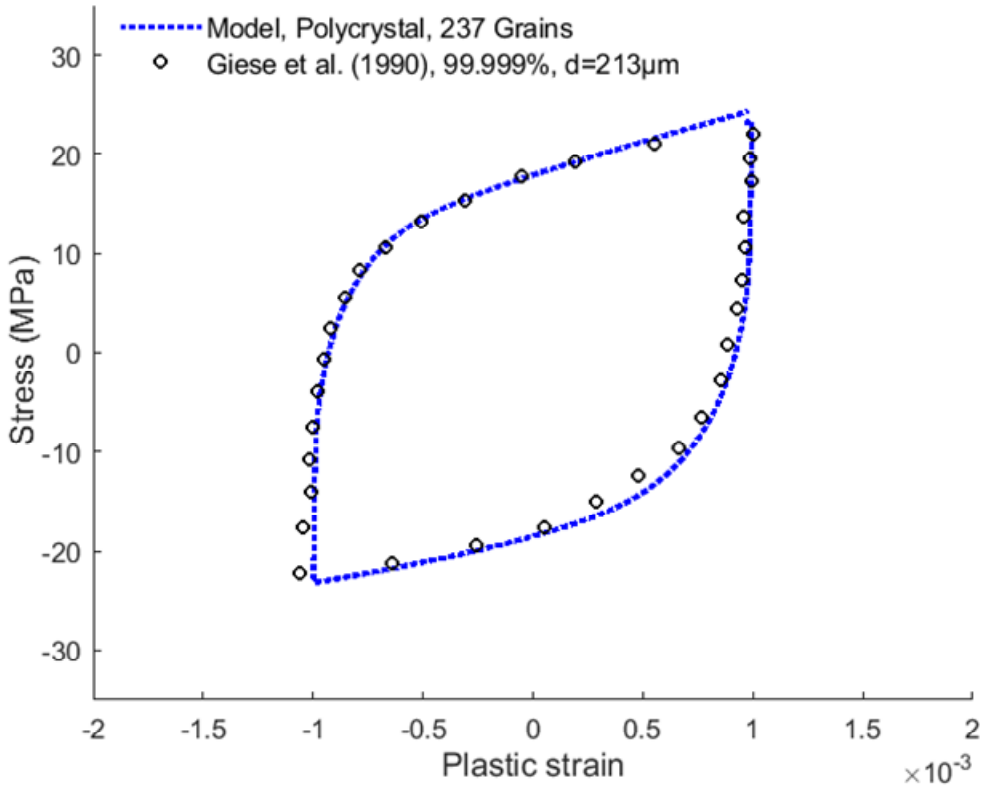

Figure 3-15 Comparison of complete cyclic stress-strain response of aluminium polycrystal between model and experiment [57]**.**

Sauzay and Kubin [38] showed that Cu and Ni follow similitude relation under cyclic and monotonic loading conditions as,

$$K_{strtuc} = \frac{\tau/\mu}{b/d_{struc}} \qquad \textbf{(3.13)}$$

Following on, we plotted the similitude relation for aluminium using the shear stress and wall spacing (d_{struc}) computed from model results. Figure 3-16 shows the agreement of similitude relation between model and experiments [24,25,58]

for aluminium. This is a mesoscale validation of the model and hypotheses that FCC metals have the same operating mechanisms under cyclic loading.

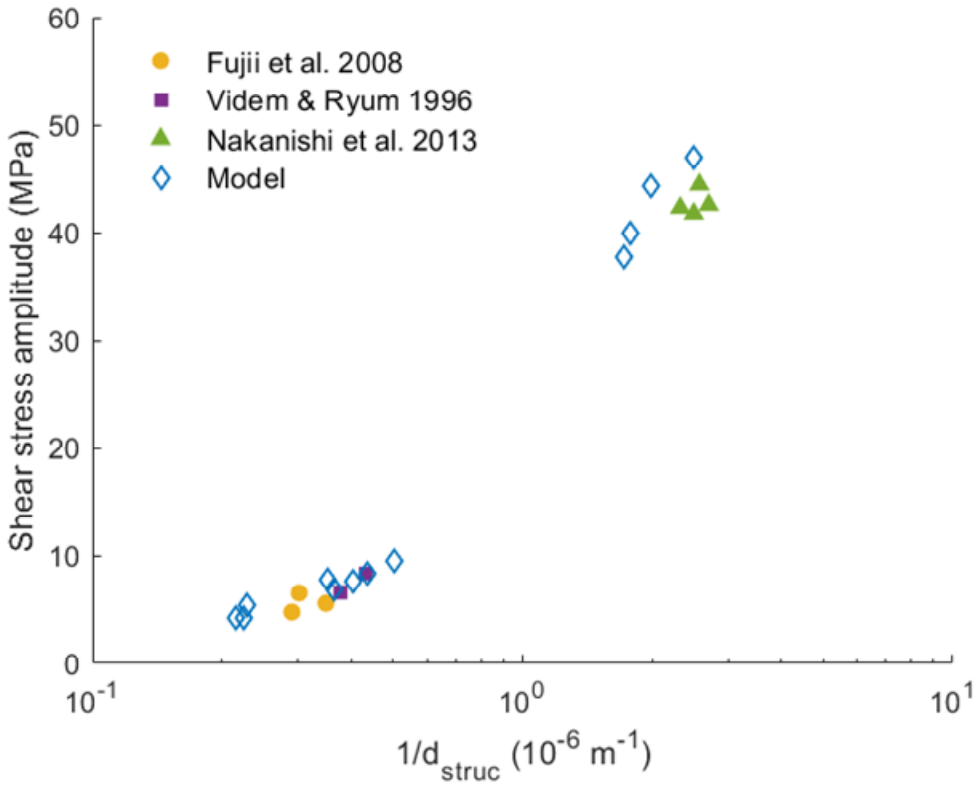

Figure 3-16 Validation of similitude relation for aluminium using shear stresses and wall spacing (d_{struc}) data from model and experiments [24,25,58] **at different temperatures.**

3.6 Discussion

This work was motivated by the challenge that aluminium under cyclic deformation also evolves the similar mesoscale substructures as other FCC metals, however at different loading conditions. This work demonstrates that *N* has a significant effect on the mesoscale substructure at higher homologous temperatures for all FCC metals. Following on, we proposed a framework that predicts the mesoscale substructure with the explicit effect of *N*. Since the

mesoscale substructure has a characteristic relation with the stress response [5], this work considered validating the effect of *N* with existing experimental data [4].

The work considered comparing the deformation response of aluminium with other FCC metals at different scales. We quantified the model input parameters while considering the physics related to the deformation processes. Since the deformation processes among FCC are the same, we only changed those parameters that are intrinsic to material properties such as $F_o, s_o^t,$ and μ. All the remaining parameters related to the mesoscale substructure and dislocation interactions were the same as proposed for Ni [8].

The physical nature of the model manifests that the similar mesoscale substructures can be used as an invariant to predict the cyclic response of FCC metals. The current model is capable of predicting the cyclic response of low-high stacking fault energy FCC metals. Moreover, the current model can also be used to predict the response of other metals and alloys, which show similar mesoscale substructures. Future efforts will explore the cyclic response of aluminium alloy using the current model.

Another important aspect of this work is the prediction of macroscopic stress-strain response as a function of the number of cycles, which has a unique importance in fatigue prognosis. The peak stresses correspond to shear strain and strain energy (area under the stress-strain curve) are the fatigue indicator parameters that inform about the hotspot for nucleation and propagation of microstructurally small fatigue cracks [16]. Hence, the current crystal plasticity framework can be used as a tool to predict the nucleation and propagation life of microstructurally small cracks.

This work considered comparing the cyclic response of aluminium with other FCC metals at the same $\frac{T}{T_m}$. Figure 3-17 compares the cyclic stress-strain response of different FCC single crystals at the same homologous temperatures ($\frac{T}{T_m} = 0.17$).

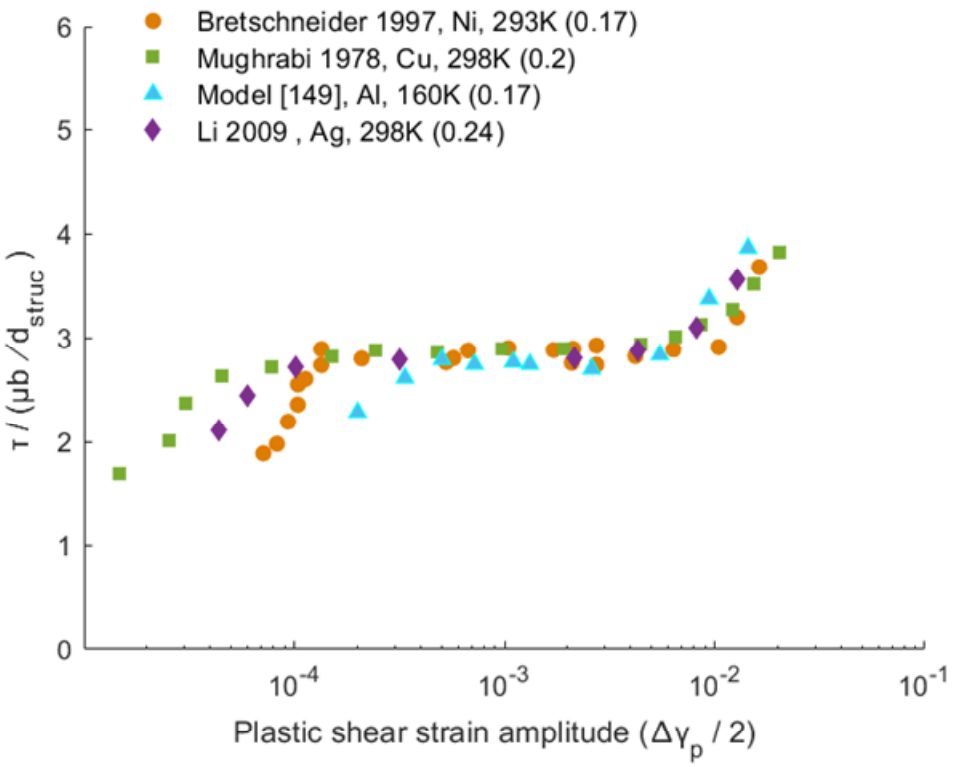

Figure 3-17 Cyclic stress-strain response of Ni, Cu, Ag, and aluminium single crystals at the same homologous temperature, the y-axis is normalised with the bow-out stress [59]**.**

The current findings reinforce the physical nature of crystal plasticity framework, which is capable of predicting the cyclic response of low –high SFE FCC metals under different orientation, temperature, and *N*. However, this is only valid for fully reverse straining (R_ϵ= -1) and at strain rate below 0.1 s^{-1}. Future efforts are required to understand the effect of different stress ratios and higher strain rates on cyclic deformation.

Several aspects require future consideration to improve the model. The grain size dependence needs to be considered explicitly in the model to predict the cyclic response of different grain sizes. Another aspect that needs to be introduced is the initial hardening stage i.e. increase in stress with few initial cycles. Experiments [27,60,61] showed that the increase in stress during the onset of cyclic deformation is a function of plastic strain amplitude and number of cycles.

Future efforts will consider implementing the initial hardening stage to study the cyclic hardening.

The current framework can predict the cyclic response only up to 0.5 $\frac{T}{T_m}$. Since some other deformation processes such as dislocation climb become activated above 0.5 $\frac{T}{T_m}$, which needs to be considered in the framework. Further effort will focus on understanding the deformation mechanism above 0.5 $\frac{T}{T_m}$, which is of interest in creep analysis.

3.7 Conclusions

This work bridges the gap between cyclic deformation of Cu, Ni, and aluminium using mesoscale substructure as an invariant. This research highlights that the number of cycles has a significant effect on mesoscale substructures and macroscopic stress-strain response at higher homologous temperatures. Following on, we modified the crystal plasticity framework that can predict the mesoscale substructure and stress-strain response as a function of *N*, strain amplitude, and temperature.

References

1. Vorren O. and Ryum N. Cyclic deformation of A single crystals: Effect of the crystallographic orientation. Acta Metallurgica. 1988; 36(6): 1443–1453. http://dx.doi.org/10.1016/0001-6160(88)90212-X

2. Vorren O. and Ryum N. Cyclic deformation of Al-single crystals at low constant plastic strain amplitudes. Acta Metallurgica. 1987; 35(4): 855–866. http://dx.doi.org/10.1016/0001-6160(87)90162-3

3. Giese A. and Estrin Y. Mechanical behaviour and microstructure of fatigued aluminium single crystals. Scripta Metallurgica et Materiala. 1993; 28(7): 803–807. http://dx.doi.org/10.1016/0956-716X(93)90356-W

4. Dhers J. and Driver J. The cyclic response and microstructures of aluminium single crystal. In: Lukáš P, Polak J, editors. Basic mechanisms in fatigue of metals. Materials science monographs, vol. 46. Amsterdam: Elsevier; 1988. p. 33.

5. Li P., Li S.X., Wang Z.G. and Zhang Z.F. Fundamental factors on formation mechanism of dislocation arrangements in cyclically deformed FCC single crystals. Progress in Materials Science. March 2011; 56(3): 328–377. http://dx.doi.org/10.1016/j.pmatsci.2010.12.001

6. Charsley P., Bangert U. and Appleby L.J. The effect of temperature and amplitude on dislocation structures in cyclically deformed pure aluminium. Materials Science and Engineering A. 1989; 113(C): 231–236. http://dx.doi.org/10.1016/0921-5093(89)90311-0

7. Lisiecki L.L. and Weertman J.R. Orientation effects on the elevated temperature fatigue of copper single crystals. Acta Metallurgica Et Materialia. 1990; 38(3): 509–519. http://dx.doi.org/10.1016/0956-7151(90)90157-C

8. Castelluccio G.M. and McDowell D.L. Mesoscale cyclic crystal plasticity with dislocation substructures. International Journal of Plasticity. 2017; 98: 1–26. http://dx.doi.org/10.1016/j.ijplas.2017.06.002

9. Khan A.S. and Huang S. Continuum theory of plasticity. John Wiley & Sons, Ltd; New York. 1995.

10. Kocks U.F., Argon A,S. and Ashby M.F. Thermodynamics and kinetics of slip. Progress in Materials Science. Pergamon Press; 1975.

11. Busso E.P. Cyclic deformation of monocrystalline nickel aluminide and high temperature coatings. PhD Thesis. Massachusetts Institute of Technology. Cambridge, MA, USA; 1990.

12. Lin B., Zhao LG., Tong J. and Christ H.J. Crystal plasticity modeling of cyclic deformation for a polycrystalline nickel-based superalloy at high temperature. Materials Science and Engineering A. Elsevier; 2010; 527(15): 3581–3587. http://dx.doi.org/10.1016/j.msea.2010.02.045

13. Lin B., Zhao L.G. and Tong J. A crystal plasticity study of cyclic constitutive behaviour, crack-tip deformation and crack-growth path for a polycrystalline nickel-based superalloy. Engineering Fracture Mechanics. July 2011; 78(10): 2174–2192. http://dx.doi.org/10.1016/j.engfracmech.2011.04.006

14. Farukh F., Zhao L.G., Jiang R., Reed P., Proprentner D. and Shollock B.A. Realistic microstructure-based modelling of cyclic deformation and crack growth using crystal plasticity. Computational Materials Science. Elsevier B.V.; 2016; 111: 395–405. http://dx.doi.org/10.1016/j.commatsci.2015.09.054

15. Castelluccio G.M. A study on the influence of microstructure on small fatigue cracks. PhD Thesis. Georgia Institute of Technology Atlanta, GA, USA; 2012; 277.

16. Castelluccio G.M. and McDowell D.L. A mesoscale approach for growth of 3D microstructurally small fatigue cracks in polycrystals. International Journal of Damage Mechanics. 2014; 23(6): 791–818.

http://dx.doi.org/10.1177/1056789513513916

17. Franciosi P., Berveiller M. and Zaoui A. Latent hardening in copper and aluminium single crystals. Acta Metallurgica. 1980; 28(3): 273–283. http://dx.doi.10.1016/0001-6160(80)90162-5

18. Sauzay M. Analytical modelling of intragranular backstresses due to deformation induced dislocation microstructures. International Journal of Plasticity. May 2008; 24(5): 727–745. http://dx.doi.10.1016/j.ijplas.2007.07.004

19. Mura R. and Ting T.C.T. Micromechanics of defects in solids (2nd rev. ed.). Journal of Applied Mechanics. Dordrecht: Martinus Nijhoff Publishers; 1989; 56(2): 487–488. http://dx.doi.org/10.1115/1.3176116

20. Arsenlis A. and Parks D.M. Modeling the evolution of crystallographic dislocation density in crystal plasticity. Journal of the Mechanics and Physics of Solids. September 2002; 50(9): 1979–2009. http://dx.doi.10.1016/S0022-5096(01)00134-X

21. Essmann U. and Mughrabi H. Annihilation of dislocations during tensile and cyclic deformation and limits of dislocation densities. Philosophical Magazine A: Physics of Condensed Matter, Structure, Defects and Mechanical Properties. 1979; 40(6): 731–756. http://dx.doi.org/10.1080/01418617908234871

22. Patra A. and McDowell D.L. Crystal plasticity-based constitutive modelling of irradiated bcc structures. Philosophical Magazine. 2012; 92(7): 861–887. http://dx.doi.10.1080/14786435.2011.634855

23. Kassner M.E., Wall M.A. and Delos-Reyes M.A. Microstructure and mechanisms of cyclic deformation of aluminum single crystals at 77 K. Metallurgical and Materials Transactions A: Physical Metallurgy and Materials Science. March 1997; 28 A(3): 595–609. http://dx.doi.org/10.1007/s11661-997-0045-2

24. Nakanishi Y., Tanaka H., Fujii T., Onaka S. and Kato M. Low-temperature fatigue behaviour and development of dislocation structure in aluminium single crystals with single-slip orientation. Philosophical Magazine. 2013; 93(21): 2759–2768. http://dx.doi.org/10.1080/14786435.2013.786193

25. Videm M. and Ryum N. Cyclic deformation of [001] aluminium single crystals. Materials Science and Engineering A. November 1996; 219(1–2): 1–10. http://dx.doi.org/10.1016/S0921-5093(96)10261-6

26. Wang J., Zhu Z.G., Fang Q.F. and Liu G.D. Influence of the crystallographic orientation on the behavior of fatigue in Al single crystals. Materials Research Bulletin. Elsevier Science Ltd; 1 February 1999; 34(3): 407–413. http://dx.doi.org/10.1016/S0025-5408(99)00024-0

27. Mughrabi H. The cyclic hardening and saturation behaviour of copper single crystals. Materials Science and Engineering. 1978; 33(2): 207–223. http://dx.doi.org/10.1016/0025-5416(78)90174-X

28. Mughrabi H., Ackermann F. and Herz K. Persistent slipbands in fatigued face-centered and body-centered cubic metals. ASTM Special Technical Publication. ASTM; 1979; 4(675): 69–105.

29. Hähner P., Tippelt B. and Holste C. On the dislocation dynamics of persistent slip bands in cyclically deformed f.c.c. metals. Acta Materialia. 1998; 46(14): 5073–5084. http://dx.doi.org/10.1016/S1359-6454(98)00161-X

30. ABAQUS. FEM software v2017. Providence, RI, USA: Simulia Inc.; 2017.

31. Varshni Y.P. Temperature dependence of the elastic constants. Physical Review B. 1970; 2(10): 3952–3958. http://dx.doi.org/10.1103/PhysRevB.2.3952

32. Langer JS., Bouchbinder E. and Lookman T. Thermodynamic theory of dislocation-mediated plasticity. Acta Materialia. June 2010; 58(10): 3718–3732. http://dx.doi.org/10.1016/j.actamat.2010.03.009

33. Tippelt B., Bretschneider J. and Hähner P. The dislocation microstructure of cyclically deformed nickel single crystals at different temperatures. Physica Status Solidi (A) Applied Research. September 1997; 163(1): 11–26. http://dx.doi.org/10.1002/1521-396X(199709)163:1<11::AID-PSSA11>3.0.CO;2-X

34. Kassner M.E. and Wall M.A. Microstructure and mechanisms of cyclic deformation in aluminum single crystals at 77 K: part II. edge dislocation dipole heights. Metallurgical and Materials Transactions A: Physical Metallurgy and Materials Science. 1999; 30(3): 777–779. http://dx.doi.org/10.1007/s11661-999-0069-x

35. Basinski Z.S., Korbel A.S. and Basinski S.J. The temperature dependence of the saturation stress and dislocation substructure in fatigued copper single crystals. Acta Metallurgica. February 1980; 28(2): 191–207. http://dx.doi.org/10.1016/0001-6160(80)90068-1

36. Feaugas X. On the origin of the tensile flow stress in the stainless steel AISI 316L at 300 K: Back stress and effective stress. Acta Materialia. 1999; 47(1): 3617–3632. http://dx.doi.org/10.1016/S1359-6454(99)00222-0

37. Armstrong R.W. and Rodriguez P. Flow stress/strain rate/grain size coupling for FCC nanopolycrystals. Philosophical Magazine. 2006; 86(36): 5787–5796. http://dx.doi.org/10.1080/14786430600764872

38. Sauzay M. and Kubin L.P. Scaling laws for dislocation microstructures in monotonic and cyclic deformation of FCC metals. Progress in Materials Science. 2011; 56(6): 725–784. http://dx.doi.org/10.1016/j.pmatsci.2011.01.006

39. Tabata T., Yamanaka S. and Fujita H. In situ deformation of the [111] aluminum single crystals observed by high voltage electron microscopy. Acta Metallurgica. 1978; 26(3): 405–411. http://dx.doi.org/10.1016/0001-6160(78)90167-0

40. Estrin Y., Tóth LS., Molinari A. and Bréchet Y. A dislocation-based model for all hardening stages in large strain deformation. Acta Materialia. 1998; 46(15): 5509–5522. http://dx.doi.org/10.1016/S1359-6454(98)00196-7

41. Nahm H., Moteff J. and Diercks D.R. Substructural development during low cycle fatigue of AISI 304 stainless steel at 649°C. Acta Metallurgica. 1977; 25(2): 107–116. http://dx.doi.org/10.1016/0001-6160(77)90114-6

42. Tóth L.S., Molinari A. and Estrin Y. Strain hardening at large strains as predicted by dislocation based polycrystal plasticity model. Journal of Engineering Materials and Technology, Transactions of the ASME. 2002; 124(1): 71–77. http://dx.doi.org/10.1115/1.1421350

43. Pham M.S., Iadicola M., Creuziger A., Hu L. and Rollett A,D. Thermally-activated constitutive model including dislocation interactions, aging and recovery for strain path dependence of solid solution strengthened alloys: application to AA5754-O. International Journal of Plasticity. 2015; 75: 226–243. http://dx.doi.org/10.1016/j.ijplas.2014.09.010

44. Holzwarth U. and Essmann U. Temperature-induced rearrangement of the dislocation pattern of persistent slip bands in copper single crystals. Applied Physics A Solids and Surfaces. March 1994; 58(3): 197–210. http://dx.doi.org/10.1007/BF00324376

45. Differt K. and Essmann U. Dynamical model of the wall structure in persistent slip bands of fatigued metals I. dynamical model of edge dislocation walls. Materials Science and Engineering A. 1993; 164(1–2): 295–299. http://dx.doi.org/10.1016/0921-5093(93)90681-4

46. Zhai T., Martin JW., Briggs G.A.D. and Road P. Fatigue damage at room temperature aluminium single crystals -II. tem. Acta Metallurgica. 1996; 44(5): 1729–1739.

47. Suresh S. Fatigue of materials. 2nd edn. Fatigue of Materials. Cambridge University Press; 1998. http://dx.doi.org/10.1017/cbo9780511806575

48. Hecker M., Thiele E. and Holste C. X-ray diffraction analysis of internal stresses in the dislocation structure of cyclically deformed nickel single crystals. Materials Science and Engineering A. 1997; 234–236: 806–809. http://dx.doi.org/10.1016/s0921-5093(97)00370-5

49. El-Madhoun Y., Mohamed A. and Bassim M.N. Cyclic stress-strain response and dislocation structures in polycrystalline aluminum. Materials Science and Engineering A. October 2003; 359(1–2): 220–227. http://dx.doi.org/10.1016/S0921-5093(03)00347-2

50. Feltner C.E. Dislocation arrangements in aluminum deformed by repeated tensile stresses. Acta Metallurgica. 1963; 11(7): 817–828. http://dx.doi.org/10.1016/0001-6160(63)90021-X

51. Feltner C.E. Dislocation debris in aluminium fatigued at 78°K. Philosophical Magazine. 1963; 8(96): 2121–2124. http://dx.doi.org/10.1080/14786436308209107

52. Kayali E.S. and Plumtree A. Stress-substructure relationships in cyclically and monotonically deformed wavy slip mode metals. Metallurgical Transactions A. 1982; 13(6): 1033–1041. http://dx.doi.org/10.1007/BF02643400

53. Socie D.F. and Marquis G.B. Multiaxial fatigue. ASTM Special Technical Publication. SAE International; 1985.

54. Lepistö T.K. and Kettunen P.O. Comparison of the cyclic stress-strain behaviour of single-and 〈111〉 multiple-slip-oriented copper single crystals. Materials Science and Engineering. October 1986; 83(1): 1–15. http://dx.doi.org/10.1016/0025-5416(86)90169-2

55. Videm M. and Ryum N. Cyclic deformation and fracture of pure aluminium polycrystals. Materials Science and Engineering A. November 1996; 219(1–2): 11–20. http://dx.doi.org/10.1016/S0921-5093(96)10262-8

56. Tsou J.C. and Quesnel D.J. Internal stress measurments during the saturation fatigue of polycrystalline aluminum. Materials Science and

Engineering. December 1982; 56(3): 289–299. http://dx.doi.org/10.1016/0025-5416(82)90105-7

57. Giese A., Styczynski A. and Estrin Y. Cyclic hardening behaviour of polycrystalline aluminium under tension-compression. Materials Science and Engineering A. 1990; 124(2): 13–15. http://dx.doi.org/10.1016/0921-5093(90)90160-5

58. Fujii T., Uju S., Tanaka H., Murayama T., Watanabe C., Onaka S.,et al. Plasticity, failure and fatigue in structural materials from macro to nano. In: Hsia KJ, M.Göken, Pollock T, Portella PD, Moody NR (eds.) In Proc. of the Hael Mughrabi Honorary Symposium. Warrendale, Pa.: The Minerals, Metals & Material Society; 2008. p. 123.

59. Brown L.M. Dislocation bowing and passing in persistent slip bands. Philosophical Magazine. 2006; 86(25–26): 4055–4068. http://dx.doi.org/10.1080/14786430500501689

60. Bretschneider J., Holste C. and Tippelt B. Cyclic plasticity of nickel single crystals at elevated temperatures. Acta Materialia. September 1997; 45(9): 3775–3783. http://dx.doi.org/10.1016/S1359-6454(97)00030-X

61. Alhamany A., Chicois J. ,Fougères R. and Hamel A. Effet bauschinger lors de la plasticité cyclique de l’aluminium pur monocristallin. Journal de Physique III. 1992; 2(8): 1491–1508. http://dx.doi.org/10.1051/jp3:1992195

4 Decoupling Geometric and Microstructural Gradients in Fatigue Crack Formation

4.1 Introduction

Scribe marks are maintenance-induced defects often introduced in fuselage joints during the sealant removal process before repainting. These shallow marks as shown in Figure 4-1 are micron-size surface scratches that behave as a notch under service loads [1–3]. Research studies [1,4] have shown that these notches can nucleate multiple cracks and significantly reduce the fatigue life of aircraft components. The potential detrimental role of small surface defects on early failure highlights the importance of accurate prognosis of their fatigue lives. Cini and Irving [1] characterised the size effect of notches on fatigue crack nucleation in aluminium and found that the early fatigue crack growth is affected by notch geometry. Since the size of scribe marks and microstructure attributes (e.g., grains) are often of comparable dimensions, the microstructure plays a role in fatigue crack initiation.

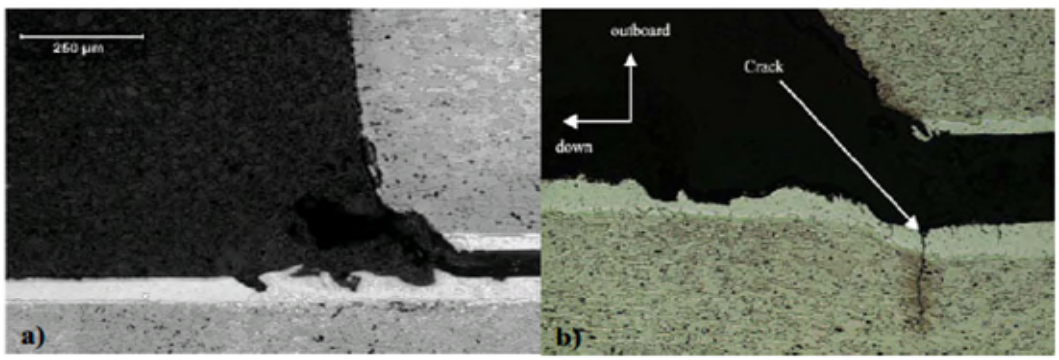

Figure 4-1 Scribe marks at fuselage joints [5] a) a scribe in cladding b) extension of a crack from scribe.

Fatigue crack nucleation in metallic materials is usually controlled by microplasticity shear strain and is sensitive to local elastic and plastic anisotropy [6]. These characteristics of microstructure sensitive (MS) small cracks reduces the validity of far-field fracture mechanics laws at the microscale [7,8]. Since small

cracks from shallow notches spent 90 -95% of their fatigue life inside a grain [9], it becomes essential to consider the role of the local crystal plasticity response on small crack formation and propagation. The below section reviews the existing literature related to recent advances in modelling MS fatigue crack growth.

4.1.1 Models of MS fatigue crack growth

Fatigue prognosis includes several aspects such as rate of crack growth, crack path, and the number of cycles to failure. From the design perspective, predicting the life (number of cycles to failure) is of greater engineering interest than predicting the crack path or rate of crack growth.

Several studies [10,11] investigated the MS crack path and crack growth rate using accumulated plastic strain and stored energy criteria. However, they showed that the crack path predicted normal to maximum principal direction is less microstructural sensitive. Zhang et al. [12] evaluated the short crack propagation using maximum cumulative shear strain along slip systems. The model captured the tortuous crack path observed experimentally. However, their model was not able to predict cracks with sharp deflections due to computational cost and XFEM limitations. Besides, these studies [10–12] considered 2-dimensional models to simulate small cracks. However, the lack of a third dimension may affect the microstructure-induced fatigue variability.

Some efforts [13] proposed a framework to explicitly model discrete slip bands to study the deflection of short cracks. They [13] considered upscaling the numerical cycles to compare the number of cycles to failure with experiments due to high computational demand. However, simple upscaling or direct comparison of number of cycles between experiment and simulation with the initial and final crack lengths might not be appropriate due to the complexity and non-linearity of the problem.

Some models [14] estimated the nucleation life considering only one parameter i.e., critical stored energy. However, model results agree with experimental data for R =0.1, however, underpredicted the results for R=-1. This infers that one

parameter (critical stored energy) might not be sufficient to capture the variability of fatigue damage under different loading conditions.

Recently, Xu et al. [15] derived an analytical solution for stored energy density in terms of stress intensity factor while assuming the elastic shear solution equivalent to plastic shear at the crack tip. The analytical stored energy densities were compared with crystal plasticity solution for a fixed crack length of 500 μm and found to be good in agreement. However, the analytical solution assumed for plastic shear is arguable for microstructurally small cracks with cracks length of few ten microns.

Castelluccio and McDowell [16] developed crystal plasticity models to study the effects of microstructure on fatigue indicator parameters (FIPs), which are subrogates of the fatigue driving force. Their results demonstrated that FIPs tend to decrease as cracks extend inside a grain, which agrees with the oscillatory fatigue crack growth rate found in experiments [17]. Furthermore, they proposed an empirical relation between FIP and crack length while considering the explicit effect of microstructure. Thereby, the study proposed a unique solution to relate the microstructure-sensitive crack growth rate with FIP and crack length to compute the number of cycles to failure. However, these studies did not account for the role of notch geometry on the gradient of FIP at notch tip to predict fatigue life. Besides, their [16] approach considered only the planar cracks along slip bands.

Some studies [18–21] have studied the initiation of MS fatigue cracks from notches with crystal plasticity models that explicitly introduce geometrical gradients. However, these studies are computationally expensive and require a large set of simulations to predict the microstructural and geometric variability.

So far the existing models have demonstrated many features of MS fatigue crack growth with several criteria. However, none have shown the effect of shallow notches on microstructure-sensitive fatigue crack growth and fatigue life. Some experiments [22] depicted that aluminium alloy has a similar decaying pattern of crack growth rate inside a grain. Therefore, Castelluccio and McDowell [16]

approach seems most promising for further study. However, the model needs to be modified to account for multislip FIP due to profuse cross slip in aluminium.

This work aims to quantify independently the effect of notch geometry and microstructure on gradients of FIPs as crack extends through a grain to innovate on engineering approaches that can predict fatigue cracking from shallow notches in aluminium. By coupling microstructural variability from crystal plasticity simulations without geometric gradient [16] and the decay of the maximum plastic shear away from a notch in elastoplastic simulation [23], we predict the early stages of fatigue cracks in notches.

4.2 Crystal plasticity modelling of fatigue driving force gradient

4.2.1 Fatigue crack driving force

Pioneer work from Morrow [24], and Brown and Miller [25] served as a basis for energy and critical plane approach based models respectively to predict the fatigue life of engineering materials. Energy-based approaches [24,26,27] employed hysteresis energy per cycle or strain energy density as a crack driving force to predict the fatigue crack growth. With five decades of progress in multiaxial fatigue assessment, several studies [28–30] demonstrated that these energy and critical plane approach based parameters can be used as fatigue indicators for initiation and propagation.

Dunne and his co-workers [28,29] proposed crystallographic energy-based FIP (FIP_E^{α}), whose fundamentals are similar to earlier energy based approaches to predict the MS fatigue crack growth as,

$$FIP_E^{\alpha} = \int_0^{N_c} \tau^{\alpha} d\gamma_{pl}^{\alpha} \qquad \textbf{(4.1)}$$

Where, τ^{α} is the resolved shear stress, $d\gamma_{pl}^{\alpha}$ is the plastic shear strain increment in α slip system and N_c is the number of computational steps. The FIP_E^{α} in equation (4.1) demonstrates plastic strain energy stored over each time increment for computational cycles (N_c) .

Critical plane approaches used the plastic strain range to predict fatigue failure using experimental data. These approaches [25,31], which considered only the strain terms (normal and shear) were unable to account for the effect of mean stress or strain path dependent hardening [32]. Following on, Fatemi and Socie [33] upbuilt the Kandil et al. [34] model by replacing the normal strain with maximum normal stress on a maximum shear plane to account for the effect of mean stress and non-proportional hardening. They [33] proposed a parameter as shown in equation (4.2) that can be related to total fatigue life.

$$\gamma_{max}\left[1 + k\frac{\sigma_n^{max}}{\sigma_y}\right] = constant \qquad \textbf{(4.2)}$$

Where, γ_{max} is the maximum shear strain, which is the measure of plastic slip activity over a loading cycle, σ_n^{max} is the maximum normal stress on γ_{max} plane normalised by yield stress and k is a material constant normally ranges between 0.5 and 1 [33].

Castelluccio and McDowell [30,35] correlated the Fatemi-Socie parameter with crack tip displacement for several multiaxial loading conditions. They proposed that Fatemi-Socie parameter can be used as a fatigue indicator to study the MS fatigue crack initiation and growth. Castelluccio and McDowell wrote Fatemi-Socie parameter in terms of fatigue indicator parameter (FIP) as,

$$FIP_{FS} = \Delta\gamma_{max}^{P}\left[1 + k\frac{\sigma_n^{max}}{\sigma_y}\right] \qquad \textbf{(4.3)}$$

Where, $\Delta\gamma_{max}^{P}$ is the maximum plastic shear strain range, which is the measure of plastic slip activity over a loading cycle. For microstructurally small fatigue cracks (MSCs), the driving force in the early stages of nucleation and crack growth is influenced by the local microstructure [17]. The sub-grain localization of slip along active slip systems plays a role in defining the fatigue driving force. Thereby, those crystallographic planes can be considered critical planes. Castelluccio and McDowell [30] emphasised that FIP_{FS}^{α} along individual slip systems are more appropriate for early crack growth and can be reformulated as,

$$FIP_{FS}^{\alpha} = \frac{1}{2}\Delta\gamma^{\alpha}|_{cyc}\left[1 + k\frac{\sigma_n^{\alpha}}{\sigma_y}\right] \quad \textbf{(4.4)}$$

Where, $\Delta\gamma^{\alpha}$ is the cyclic plastic shear strain range in slip plane α, σ_n^{α} is the peak stress normal to the slip plane α and σ_y is the cyclic yield strength.

Several investigations [36,37] have shown that both energy (FIP_E^{α}) and shear range (FIP_{FS}^{α}) based FIPs have microstructural sensitivity and describes local fields. Therefore, these FIPs can be used as subrogate measure of fatigue driving force. In addition, Rovinelli et al. [38] performed a probabilistic analysis to assess the uncertainty associated with slip/energy-based FIPs. They considered a crack driving force matrix containing several FIPs based on accumulated slip and energy similar to equations (4.1) and (4.4). They mentioned that all the FIPs demonstrate similar behaviour, having an equivalent level of uncertainties, and carry failure information upto a certain extent.

This work considered both crystallographic energy and shear range based FIPs to make a comparison of fatigue driving forces. The calculation of FIP_E^{α} using equation (4.1) is not computationally intensive, however it requires large storage space to save the data each cycle. Therefore, this work adopted a slightly different approach to compute accumulated strain energy, which is equivalent to equation (4.1). Since the accumulation of plastic strain energy over each time increment is computationally challenging for a large number of cycles, alternatively, this work considered computing the range of FIP_E^{α} over a stabilised cycle multiplied by the number of cycles (*N*) to compute FIP_E^{α} as,

$$FIP_E^{\alpha} = \Delta(\tau^{\alpha} d\gamma_{pl}^{\alpha})\big|_{cyc} \times N \quad \textbf{(4.5)}$$

Equation (4.5) renders equivalent accumulated plastic strain energy for the same *N* but requires less data storage and save computational time. Finally, this work considered equation (4.4) and equation (4.5) as small fatigue crack driving force to study the effect of microstructure and geometric gradient in the following section.

4.2.2 Effect of microstructural gradient

The term microstructural gradient refers to the explicit effect of microstructure on FIP variation as a crack propagates inside a grain. In the previous chapter, we demonstrated that aluminium has similar deformation mechanisms as other FCC metals under different loading conditions. To further validate this notion independently, this work employed the Castelluccio and McDowell [16] approach to study the explicit effect of microstructure on transgranular FIP in pure aluminium. Furthermore, they proposed [16] that a planar FIP decays quadratically as a crack approaches the grain boundary. This approach has been implemented for low- medium stacking fault energy FCC metals i.e. Ni-based superalloys and bridge steel [39], which normally show planar crack growth behaviour. Here, we implemented the same approach in pure aluminium, which is a high SFE metal and facilitates the nonplanar crack growth. Therefore, we proposed a new strategy to account for the multislip FIP effect on the net crack driving force as explained later in Section 4.2.2.3. Figure 4-2 outlines the process of transgranular crack propagation. Several simulations are run with different microstructural attributes while following the same process shown in Figure 4-2 to study the explicit effect of microstructure on FIP variation as a function of crack length.

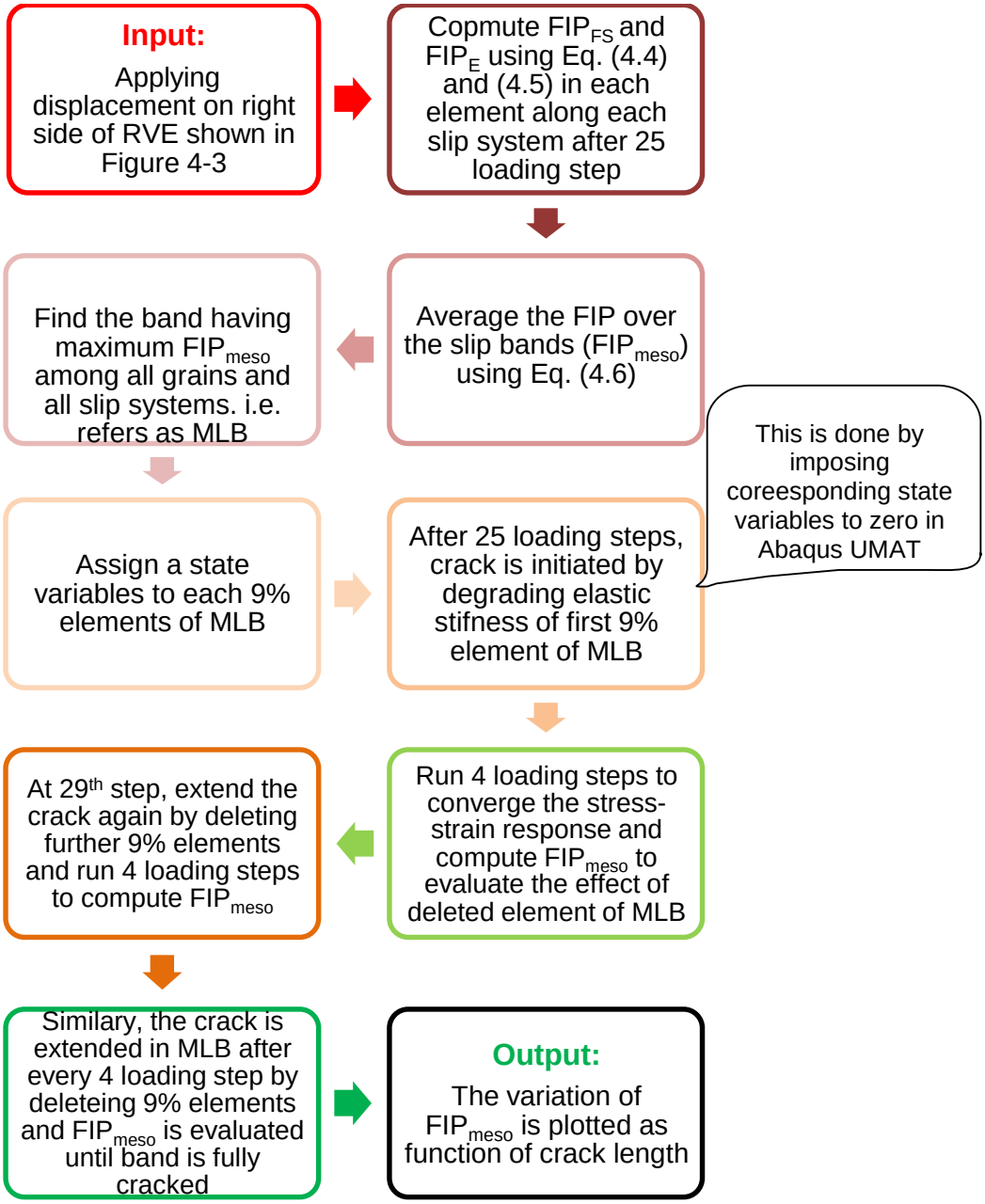

Figure 4-2 Graphical summary of the process that computes FIP_{meso} and extend a crack inside a grain

A simple cubic geometry is created with 3375 (C3D8R) brick elements, roughly 54 grains (average grain diameter= 50 μm) using Abaqus v2017 [40], Dream3D [41], and in house Matlab code as shown in Figure 4-3. The physics-based crystal plasticity framework explained in the previous Chapter 3 is employed in Abaqus UMAT with a cubic FE model (Figure 4-3).

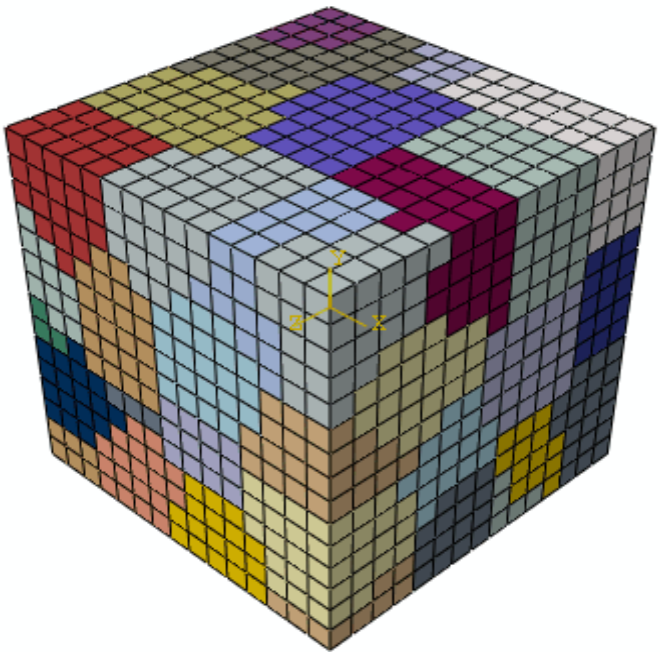

Figure 4-3 Finite element mesh for a simple cubic model. The size of RVE is 150 μm x 150 μm x 150 μm. The number of elements is 3375 and the number of grains is 54.

The simulations apply twenty-five computational cycles, which are enough to achieve convergence of the stress-strain response and FIPs as shown in Figure 4-4. Following on, the crystallographic FIP is estimated for all slip systems for all elements following equations (4.4) and (4.5).

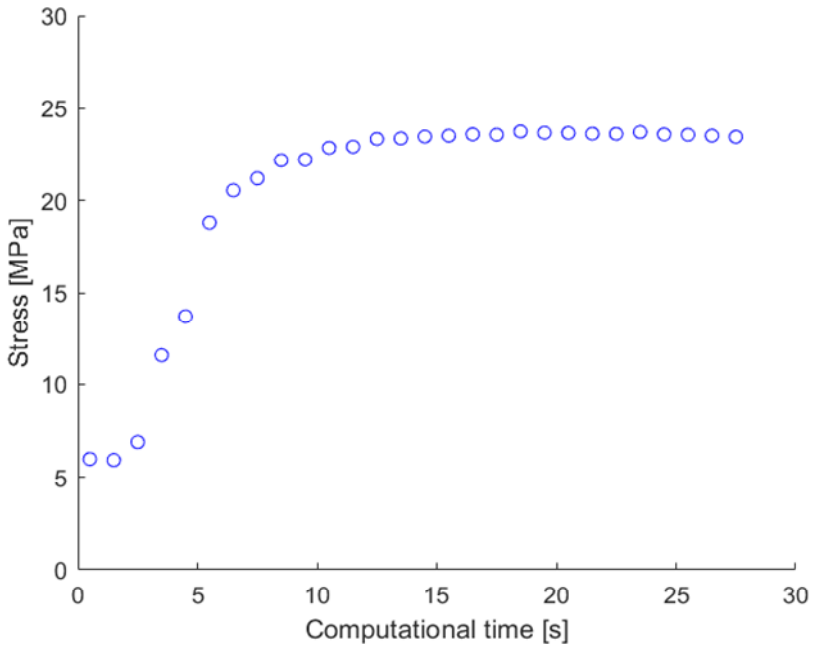

Figure 4-4 Evolution of cyclic peak stress with computational time for pure aluminium under $\Delta\epsilon/2$ =0.05%, 0.1% s^{-1}, and $R_\epsilon = -1$.

4.2.2.1 Effect of local and non-local averaging domains on FIP

One of the significant aspects of fatigue damage prognosis is the domain over which FIPs are evaluated. In this thesis, elements are referred to as local domain, whereas volume averaging domain is referred to as non-local domain. In order to quantify the mesh insensitive FIPs and consider the finite volume of fatigue process zone, this work adopted a nonlocal (volume-averaged) estimation of FIPs. A volume-averaged FIP can better represent the fatigue damage zone and mitigate mesh uncertainties [42].

Some studies [43] have considered evaluating the fatigue damage by averaging the FIP over entire grains. Consequently, they underestimated the driving force and reported lower FIP values. Some other studies [28] have considered a non-local averaging scheme based on a Gaussian weighting function applied to a volume integral around a given point. This procedure facilitates mesh independent FIP however, averaging outside the gradient path is less effective. Castelluccio and McDowell [42] rationalised the effect of the domain on FIPs by

comparing the averaged FIP over grains, slip bands, and elements. Their study [42] showed that band averaging provides a good estimate of FIP corresponding to damage process zone and mitigates mesh uncertainties. Here, this work compared FIP_{FS}^{α} and FIP_{E}^{α} over different domains such as grains, slip bands and elements.

The slip bands at mesoscale evolve as a result of slip activity along most active slip planes. Forsyth [6,44] noticed that small cracks grow along the slip bands during the early stages. Following on, He [6] characterised the onset of fatigue damage into two stages i.e. stage I and stage II. Stage I represents the initial phase in which plastic deformation preponderantly occurs along the single most active slip plane, which facilitates the crack to grow along a well-defined crystallographic plane. On the other hand, stage II corresponds to the activation of multiple slips along different planes, which results in nonplanar crack growth due to multislip driving force.

Following the characteristic growth of small cracks along the slip bands, Castelluccio and McDowell [42] proposed the artificial slip bands along crystallographic planes that represent the local damage zone and mitigate mesh uncertainties. This work initially adopted the same approach to create slip bands along crystallographic planes. The detailed procedure of creating the slip bands in a grain follows,

Since FCCs materials have four slip planes, thereby each element was assigned four different bands inside a grain. The elements are assigned to each band as,

- Firstly, the centroid of the grain is determined as shown by the plus sign in Figure 4-5.
- The grain is rotated along slip normal direction using the rotation matrix and sets of planes (black lines in Figure 4-5) perpendicular to slip plane normal directions are created. The distance between these planes is one band width, which is set to be the size of element in one dimension due to homogeneity. Bands with less than one element spacing tend to be discontinuous and may have disconnected elements.

- Now, the elements are assigned to the respective bands according to their centroids position in between two planes, which are then named as shown in Figure 4-5 at right side.
- In the schematic shown below, 5 planes were created inside a grain perpendicular to slip normal direction. The number assigned to a band formed by planes is called layer number and is shown with unique color below. For example, layer five is shown by a green band. Finally, GLP abbreviation is used in code to identify a particular band with its plane and grain, where G is the grain number, L is the layer number and P is the plane number.

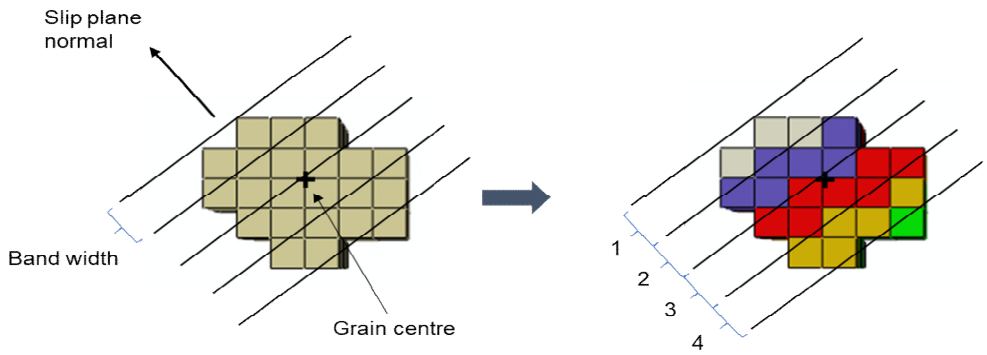

Figure 4-5 Schematic illustration of assigning elements to a slip band inside the grain.

Figure 4-6 demonstrates the slip bands inside a grain. Four sets of slip bands corresponding to FCC slip planes are shown. In Figure 4-6, the details of grain orientations are given in Appendix C.1. For averaging the FIPs over elements, bands and grains, firstly we define a threshold to eliminate the values that are too small and less likely to contribute to fatigue crack formation. Since the grain has a larger averaging volume compared to bands and elements, this work estimated the threshold as FIP_{thres} =max ((FIP_{grain})/1000).

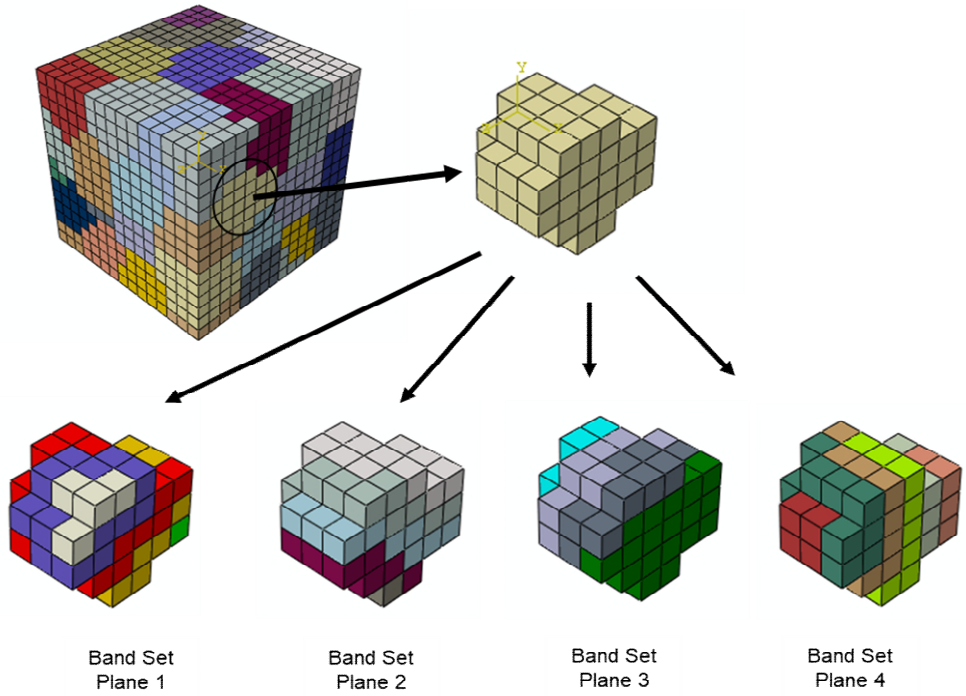

Figure 4-6 Set of bands with the plane perpendicular to FCC slip normal direcion.

Figure 4-7 compares the frequency distribution for FIP_{FS}^{α} and FIP_{E}^{α} averaged over elements, bands, and grains after twenty-five computational cycles. The data corresponding to FIP_{domain}^{FS} and FIP_{domain}^{E} consider each element and each octahedral slip system from eight different realisations.

Each element in each grain has 12 FIP values corresponding to 12 slip systems. For element- averaged FIP ($FIP_{element}$) consider only those values in slip systems that are higher than FIP_{thres} as shown in Figure 4-7(a). Slip Bands consists of set of elements as shown in Figure 4-6. For averaging along slip bands (FIP_{band}), FIPs are averaged along respective slip systems of elements of bands. Consequently, FIP_{band} has 12 values that averaged along slip systems. Figure 4-7 (b), only those values are considered that are higher than FIP_{thres}.

For estimating grain- averaged FIP (FIP_{grain}), FIPs are averaged along respective slip systems for all elements inside a grain. In Figure 4-7, only those FIP_{grain} are considered that are higher than FIP_{thres}.

a)

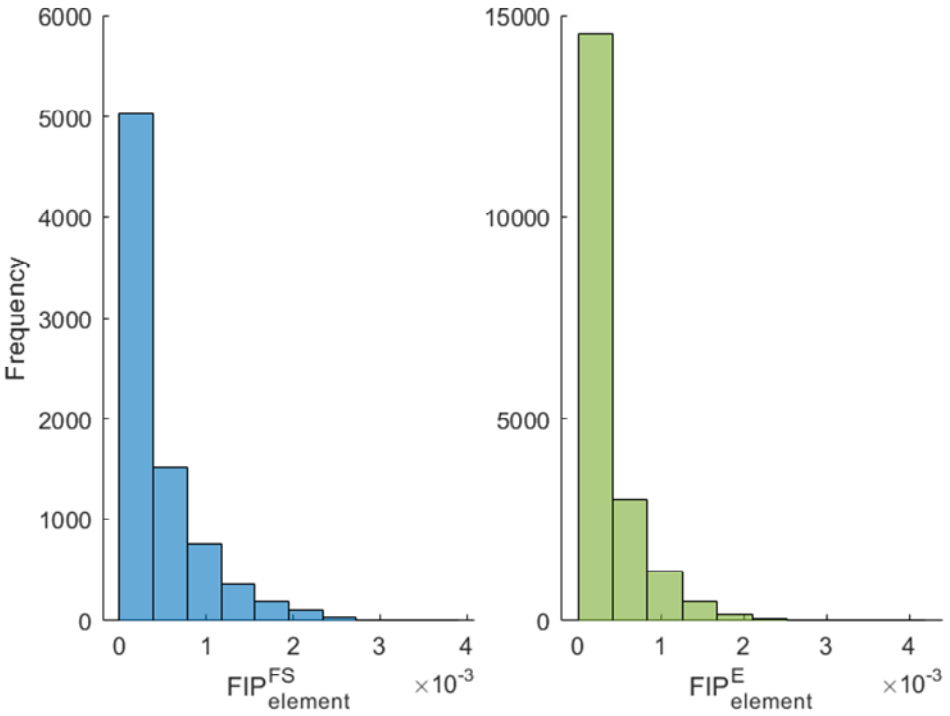
Frequency
6000
5000
4000
3000
2000
1000
0
0
1
2
3
4
FIP FS element
×10-3
15000
10000
5000
0
0
1
2
3
4
FIP E element
×10-3

b)

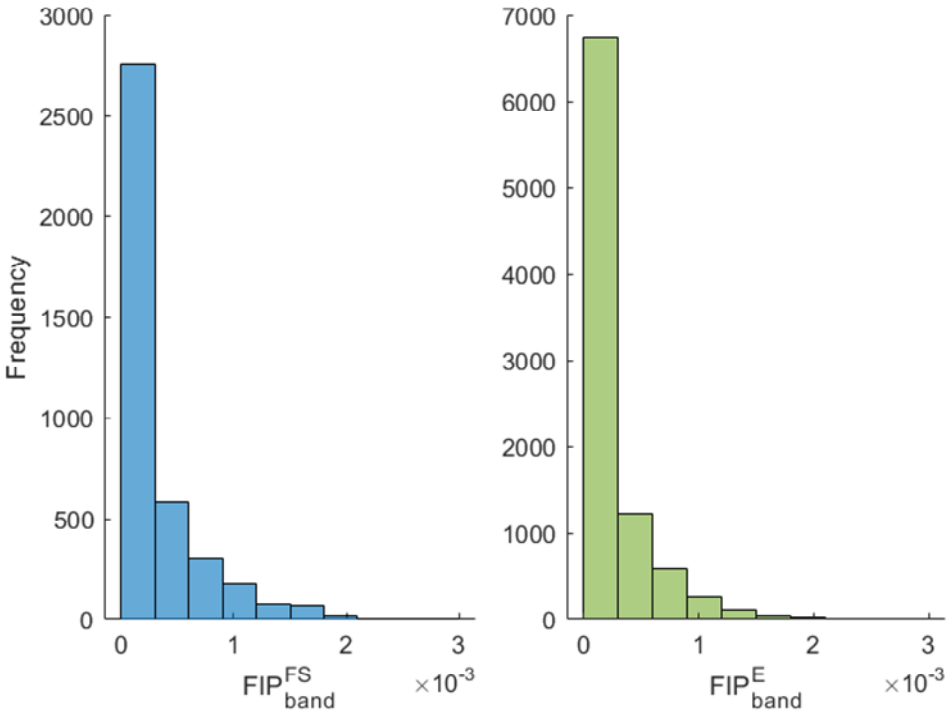
Frequency
3000
2500
2000
1500
1000
500
0
0
1
2
3
FIP FS band
×10-3
7000
6000
5000
4000
3000
2000
1000
0
0
1
2
3
FIP E band
×10-3

c)

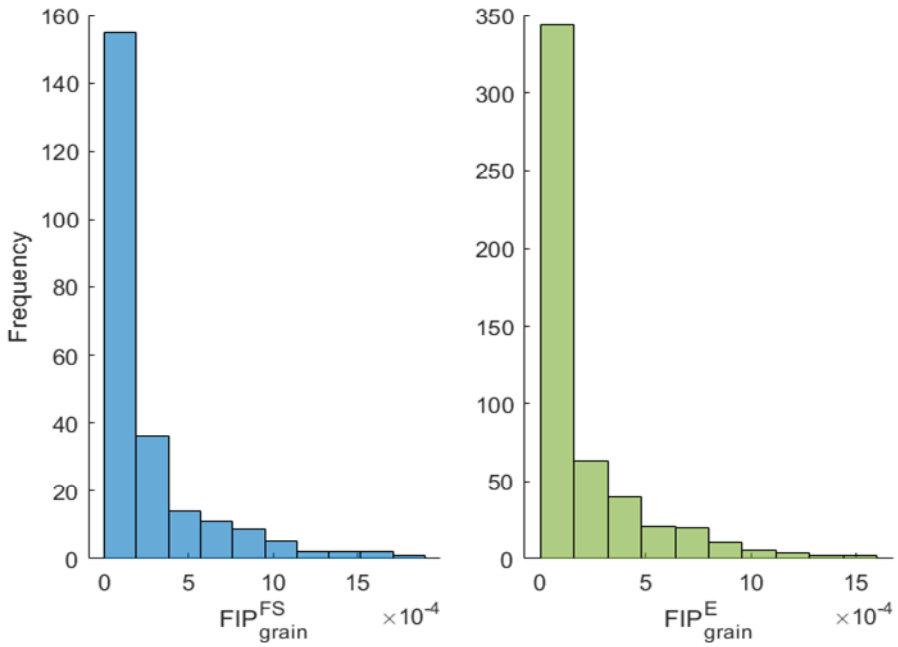

Figure 4-7 Comparison of FIP_{FS}^{α} and FIP_{E}^{α} over different domains a) elements b) bands c) grains.

In Figure 4-7, higher values of FIPs (tail of distribution) lead the fatigue crack formation, therefore neglecting the FIPs below the threshold does not affect the fatigue life estimation in the next chapter.

The distribution of averaged FIP over elements, band, and grains as though look similar, however, the extreme values decrease as the volume of the domain increases. Figure 4-7 elucidates that band-averaged FIP demonstrates a good quantitative balance between element-averaged and grain-averaged FIP and better represents a fatigue damage zone. Moreover, the trend of distributions agrees with Castelluccio and McDowell's findings [42].

Both FIP_{FS}^{α} and FIP_{E}^{α} show similar distributions regardless of different domains. However, the frequency of FIP_{E}^{α} seems to be twice of FIP_{FS}^{α} within the same range of data. This difference might be due to mesh sensitivity or due to elements at grain boundary. Since the amount of shear stress and shear strain in slip systems is sensitive to the microstructural features e.g. grain orientation and grain size, Thereby, we plotted $FIP_{element}^{\alpha}$ along all slip systems separately to elucidate the direct relation between FIP_{FS}^{α} and FIP_{E}^{α}. Figure 4-8 relates FIP_{FS}^{α} and FIP_{E}^{α}

along each slip system in a grain having maximum FIP_{grain}. The extreme values of FIP_{FS} and FIP_E shows a linear relationship (subplot 3 and 6 in Figure 4-8), which leads to the crack formation. The encircled data in the remaining subplots show the slip systems that have a higher value of FIP_E as compared FIP_{FS} and this probably increase the frequency of FIP_E in Figure 4-7. These values might result from mesh sensitivity, however, are less likely to contribute to fatigue crack formation.

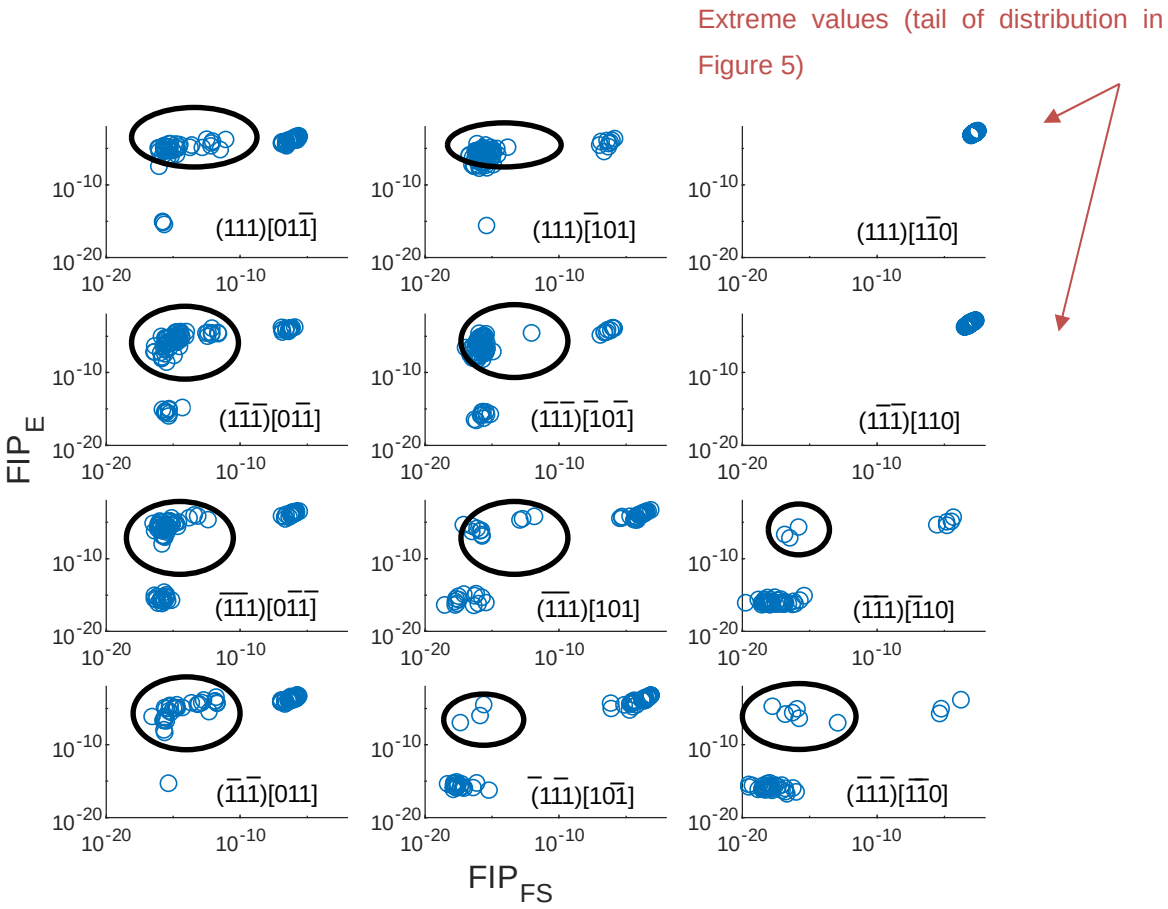

Figure 4-8 Comparison of FIP_{FS} and FIP_E along each slip system. Each point in the subplot correspond to an element of a grain that has the highest FIP_{grain}. Each subplot corresponds to a distinct FCC slip system.

Figure 4-8 also manifests the uncertainty associated with local $FIP_{element}$ and demonstrates the need for non-local FIP. Figure 4-9 presents the band averaged FIP along each slip system from the same grain data as shown in Figure 4-8. The schematic of slip bands and their sizes insides the grain is shown adjacent to

Figure 4-9. Both FIP_{FS} and FIP_E are averaged along respective slip systems of each element of slip band. Each subplot represents a slip system and each circle in a subplot corresponds to a band-averaged FIP. The color of the circle corresponds to the position and size of the slip band in the schematic. Figure 4-9 shows a better agreement between FIP_{FS} and FIP_E. It can be seen that bands near the grain boundary consist of only few elements and still show a marginal difference between FIP_{FS} and FIP_E.

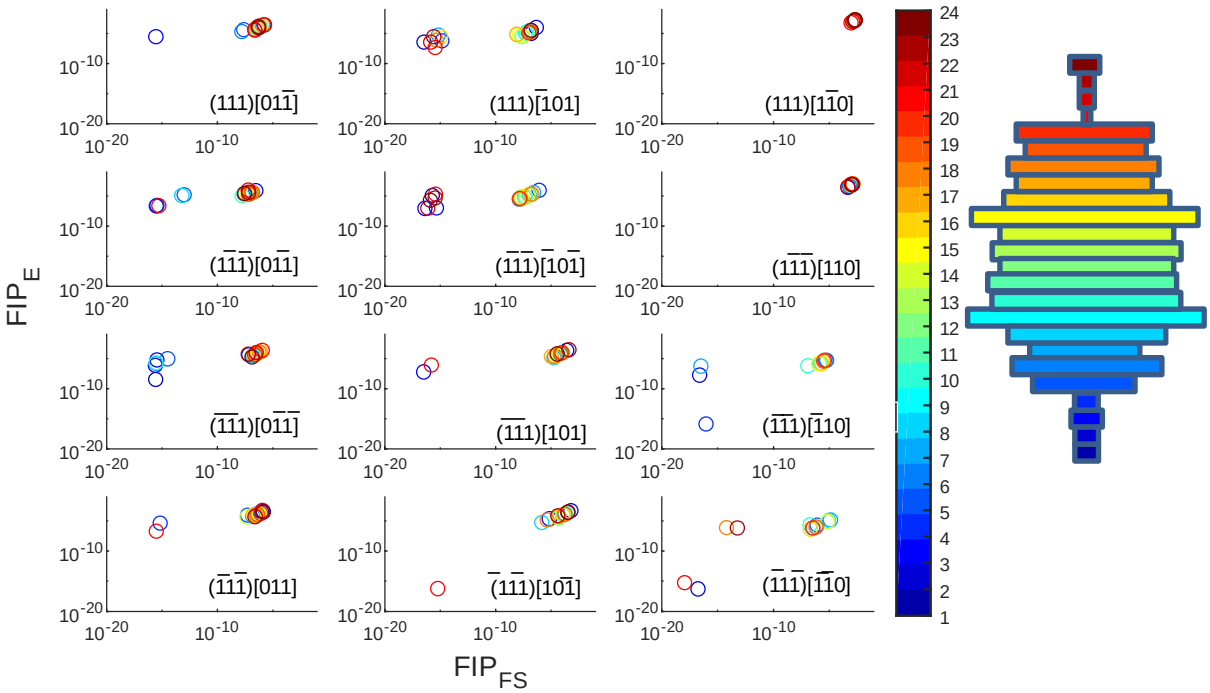

Figure 4-9 Comparison of band averaged FIP_{FS} and FIP_E along each slip system. Each point in the subplot corresponds to an averaged FIP along slip band in a grain, which has the highest FIP_{band} among all grain. The colormap represents the band number inside a grain. The schematic of the location and relative size of slip bands inside the grain in association with colormap is also shown adjacent to FIgure. Each subplot corresponds to a distinct FCC slip system.

Figure 4-9 also demonstrates that slip bands correspond to the (111) slip plane (subplot 3) has extreme values of FIP_{band} and value of FIP_{band} across slip bands in this plane is not very different from each other. To further show this explicitly, we replotted the FIP_{band} in all slip bands along the same plane that corresponds to extreme values. Figure 4-10 shows the FIP_{band} correspond to all slip bands

along the same plane from four random realisations. Each subplot belongs to a different simulation with different microstructural attributes. The slip plane that has a maximum value of FIP_{band} is considered and FIP_{band} of all the slip bands across that plane is used to plot Figure 4-10.

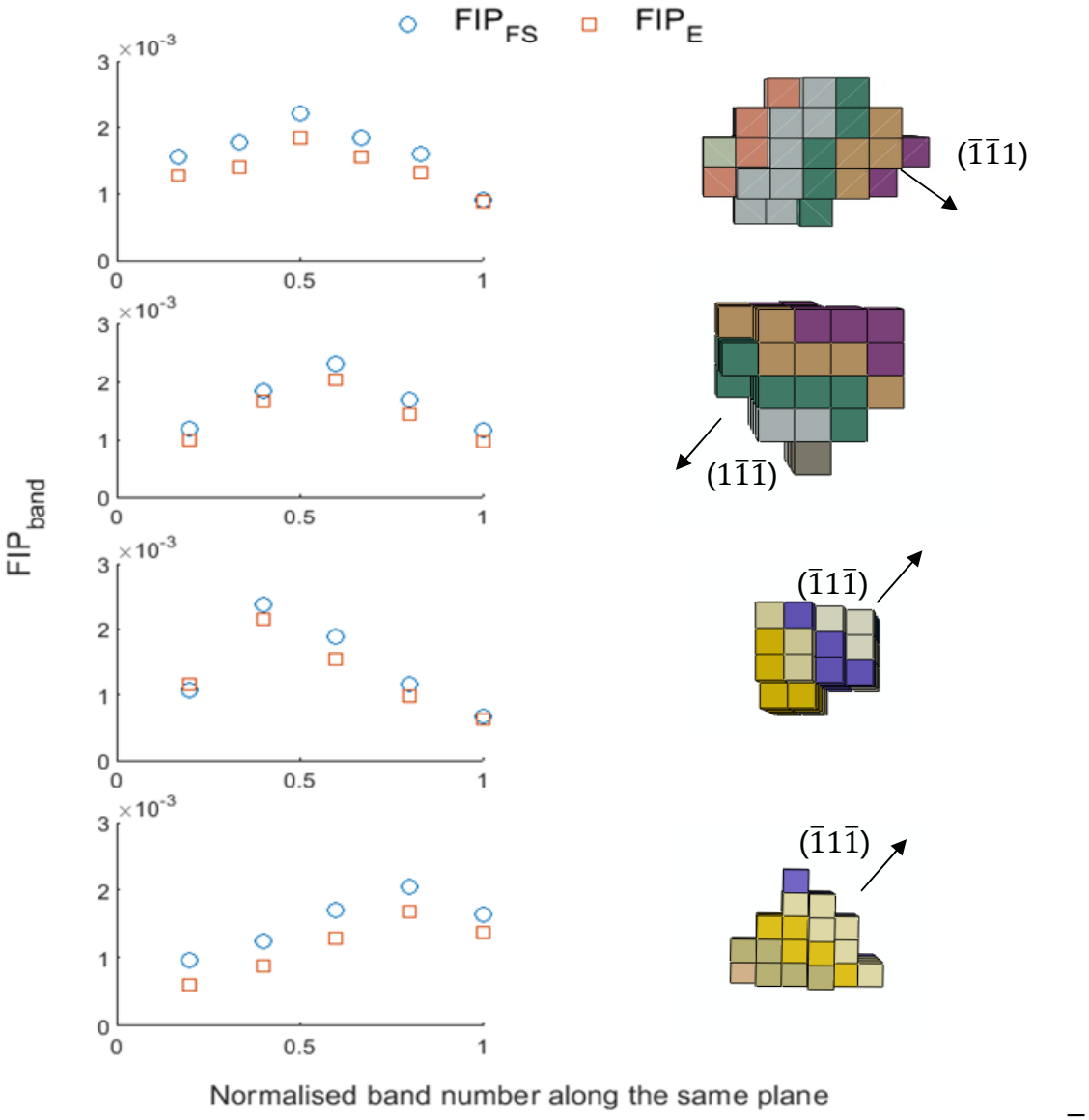

Figure 4-10 Comparison of band averaged-FIP between all bands along the same slip plane normal direction. The x-axis is normalised with the maximum number of bands along the same plane. Each subplot corresponds to a different simulation with a different microstructure. Each point in the subplot represents an average FIP correspond to a band along the same plane as shown in Figure (right). The arrows on Figure(right) shows slip normal directions.

Both FIP_{band}^{FS} and FIP_{band}^{E} shows similar trends and agrees with Figure 4-9. Moreover, Figure 4-10 manifests that all the bands correspond to extreme values and the same plane normal has comparatively equivalent potential to contribute to fatigue crack formation. This implies that for a grain having extreme values of FIPs, any part of the entire grain has an equal probability to initiate a crack. Note that this work account only for different microstructural attributes without any defects such as precipitate and inclusions, which can play a role locally to initiate a crack. The intrinsic variability of FIP_{band} inside a grain is seemed to be not sensitive to the material as similar behaviour was observed in Ni-based superalloys [42].

4.2.2.2 Transgranular crack extension along one plane

Following on, this work considered slip bands as volume averaged domains of FIPs and propagation path of cracks. After twenty-five computational steps, the average of FIP_{FS}^{α} and FIP_{E}^{α} in each band from each grain is referred to as the mesoscale driving force FIP_{meso},

$$FIP_{meso} = \frac{d_{gr}}{d_{gr}^{ref}} \frac{\sum_{1}^{n} FIP_{FS}^{\alpha}}{n}\,, \qquad \textbf{(4.6)}$$

in which n corresponds to the number of elements in each band. Moreover, the FIP_{meso} is normalised with the grain size length scale $\frac{d_{gr}}{d_{gr}^{ref}}$, in which d_{gr}^{ref} is the reference grain size and d_{gr} represents the size of the slip band diameter and follows,

$$d_{gr} = l_{el}\sqrt{n_{el}}. \qquad \textbf{(4.7)}$$

Where, l_{el} is the length of the element and n_{el} is the number of elements of the band under consideration. Note that equation (4.7) is only valid for a regular mesh. The FIP_{meso} normalization with length scale as shown in equation (4.6) supports the size dependence of an irreversible slip proposed by Risbet and Feaugas [45]. The band having maximum normalised FIP_{meso} across all grains is

referred to as minimum life band (MLB) and is considered to initiate a fatigue crack first.

Degrading the elastic stiffness tensor is one of the computationally efficient methods to study crack propagation. The crack extends by decreasing the elastic stiffness of elements of the slip bands in a grain. Once stiffness is degraded, those elements are removed from the calculation and only a few steps are required to update the FIPs. The degradation of stiffness only play role in stress tensor calculation that makes use of the elastic component. This calculation is performed after solving the elastic and plastic strains. Thereby, change in elastic stiffness does not affect the convergence of plastic components.

To evaluate the FIP_{meso} after partial cracking of a band within a grain, a crack is extended inside the MLB by deleting 9% elements of the bands at a time. Elements are deleted every 2 cycles by imposing corresponding state variable values to zero in the Abaqus UMAT subroutine. As the crack extends, the FIP_{FS} is averaged i.e. FIP_{meso} in remaining elements of MLB after every two cycles. The schematic demonstration of crack extension inside the MLB is shown in Figure 4-11 and a process map of crack extension is shown in Figure 4-2. Figure 4-11 demonstrates the variation of FIP_{meso} as crack extend in MLB.

In Figure 4-11, the MLB is shown at the top of the plot and the increasing blue color in MLB shows the cracked elements. The averaged FIP in the remaining elements is shown by the blue dots in the plot. The first point in Figure 4-11 corresponds to maximum FIP_{meso} and zero crack length. Few blue elements in the 2nd image from left on top of Figure 4-11 represents 9% element deletion and the corresponding 2nd blue dot in the Figure represents the averaged FIP in the remaining elements of MLB. The blue color in the third image on the top represents 18% elements and vice versa. The decaying trend of FIP_{meso} with crack propagation agrees with experiments [22].

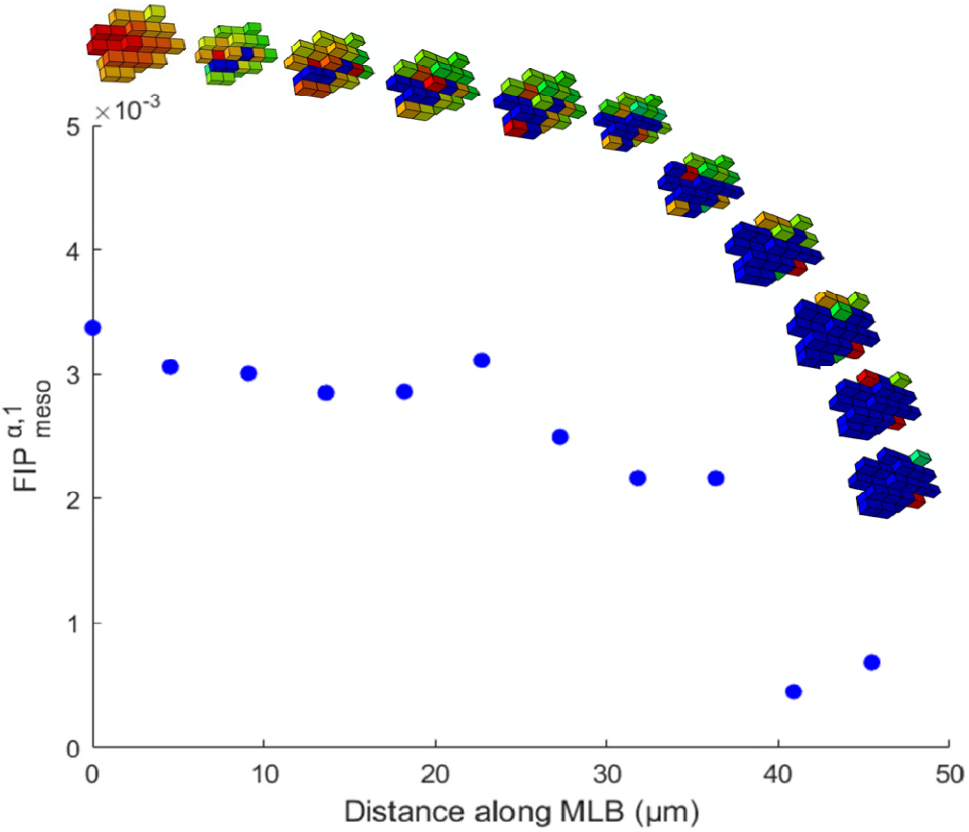

Figure 4-11 FIP_{meso} variation as crack extends inside a MLB.

Following Figure 4-11, this work considered several microstructure realisations to study the explicit effect of microstructure on FIP_{meso} variation as a function of crack length. Figure 4-12 presents the FIP_{meso} as a function of crack length from several microstructure realisations. The FIP_{meso} correspond to FIP_{FS} and FIP_{E} show exactly the same trend for each realisations, which supports Rovinelli et al. [38] findings.

Figure 4-12 shows a decaying trend of FIP_{meso}, which is not consistent among all realisations. For example, the pink and dark red points show a sharp decreasing trend compared to other data. It is likely that FIP_{meso} in another plane might be increasing while it's decreasing in the MLB. To further explore this notion, we compared the FIP_{meso} between 1st and 2nd MLB as a function of crack length. The 2nd MLB corresponds to the band having 2nd highest among FIP_{band} at 25 computational cycles. Note that 1st and 2nd MLB belongs to the same grain.

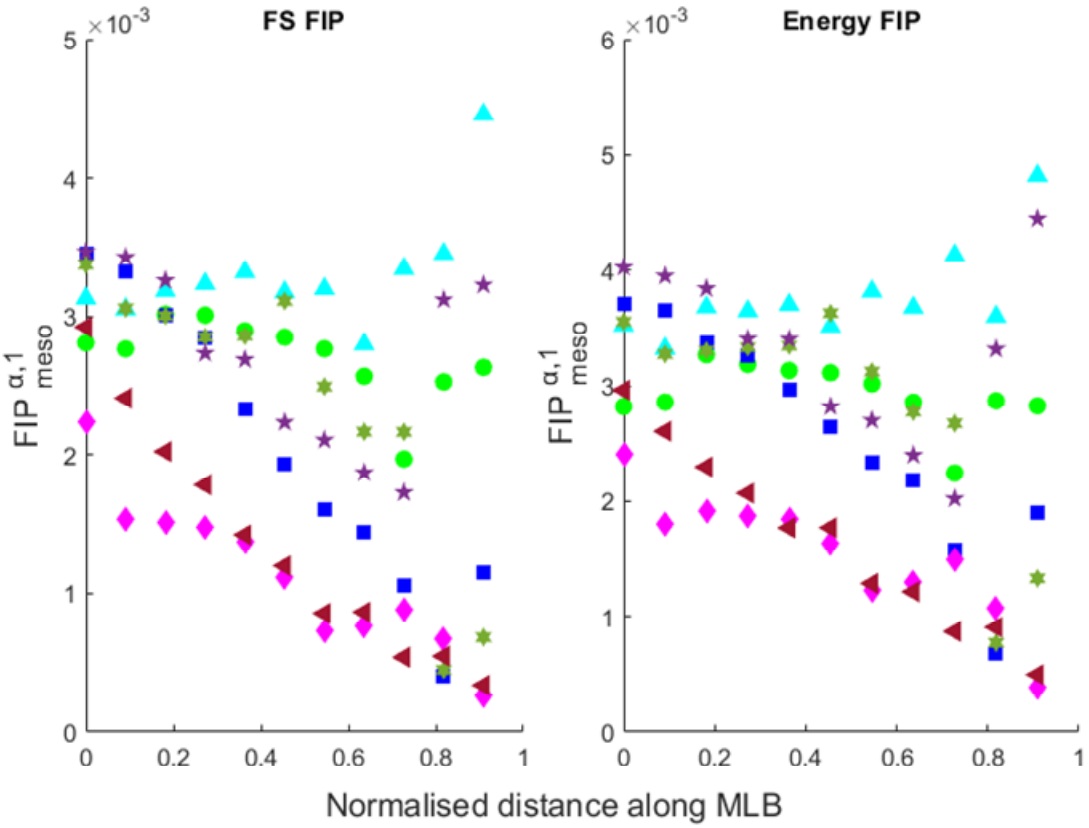

Figure 4-12 FIP_{meso} variation as the crack extends along a MLB with the explicit effect of microstructure. Each curve corresponds to a different simulation with a different microstructure realisation. The distance on the x-axis is normalized by maximum distance along MLB.

Figure 4-13 compared the FIP_{meso} variation along 1st and 2nd MLB as the crack extend for four random realisations. This clearly shows that the driving force in the 2nd MLB (different plane) can exceed the driving force in the 1st MLB, which is not being accounted for in Figure 4-12. This justifies the wide dispersion of FIP_{meso} in different realisations.

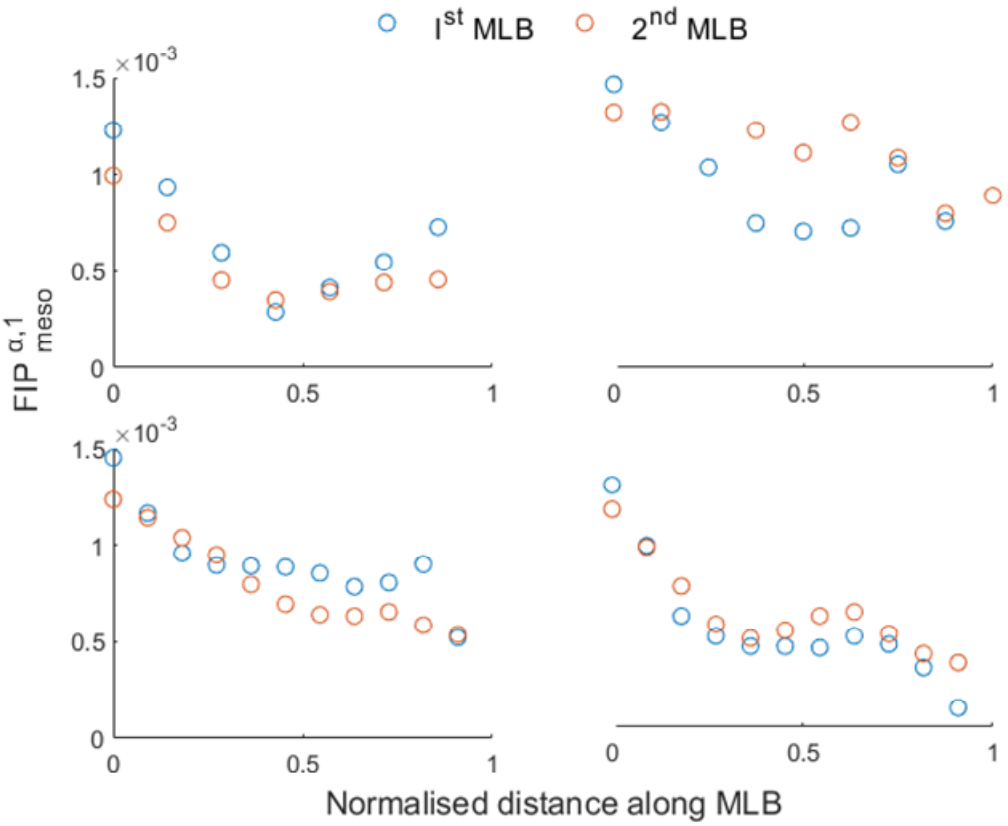

Figure 4-13 Variation of FIP_{meso} along 1st and 2nd MLB as crack extends in 1st MLB for four random realisations. The distance on the x-axis is normalized by maximum distance along MLB.

Figure 4-13 highlights the need for multislip FIP in aluminium since it activates multiple slip systems easily. This notion is further supported by the findings [46] that show perpendicular fracture between the slip bands in an aluminium single crystal.

4.2.2.3 Multislip crystallographic FIP

Several efforts [43,47] have proposed strategies to account for non-planar crack growth in aluminium alloys. Hennessey [47] considered non-planar crack growth in Al 7075 while extending the crack from one grain into the adjacent grain. He created two sets of slip bands A and B in an uncracked grain corresponding to

two slip normal directions ahead of the crack tip as shown in Figure 4-14. Following on, an intermediate plane was created by finding the intersection of crack with each band set A and band set B. The element of uncracked grain was assigned to the intermediate band by mapping the centroid of elements inside the band. Finally, the cracked is extended into the intermediate band by deleting the proportion of elements after regular intervals of computational cycles. The FIP_{meso} on the intermediate plan was evaluated by summing the normalised FIP on the bands intersected with crack front (e.g. 3B and 5A as shown in Figure 4-14). The FIP was normalised by a reference length scale of band over mean grain diameter i.e. $\frac{d_{gr}}{d_{gr}^{ref}}$.

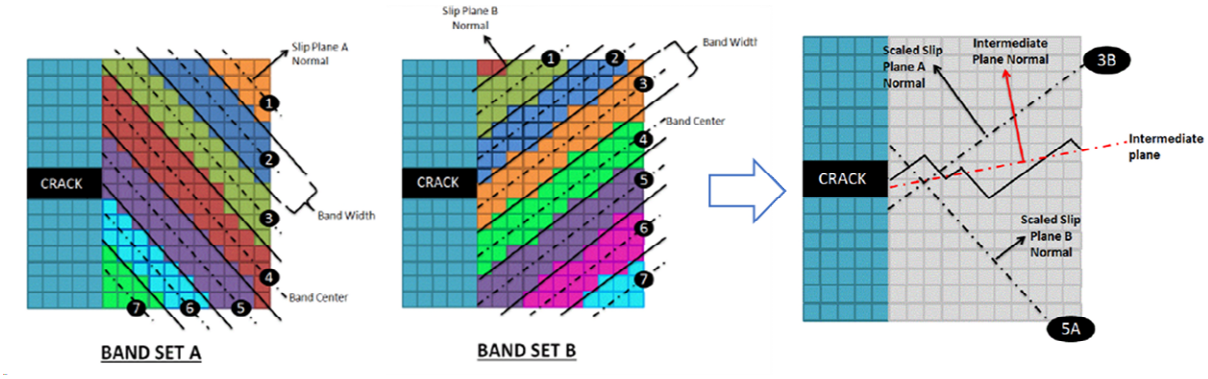

Figure 4-14 Pictorial illustration of intermediate slip bands to account for non-planar slip (Copied from Hennessey [47]**).**

The proposed approach [47] demonstrated stage II crack growth by averaging the FIP along the potential candidate bands. However, the study did not mention the choice of slip plane normal as only two planes normal out of four were considered to evaluate intersection with the crack front. The evaluation of non-planar crack only at the grain boundary is another assumption that limits the applicability of the approach. Overall, the approach is computationally burdensome and requires a complex effort of creating slip bands ahead of the crack tip, evaluating the intersection with crack front, and then extending non-planar crack while evaluating damage on intersected bands.

Some other efforts [43] have implemented the same approach [47] without slip bands to study fatigue damage in 7075-T651. They considered averaging the FIP over the grains and summing two highest FIP values among four slip planes to evaluate non-crystallographic FIP. However, the study missed grain variability by averaging over a larger volume.

Here, this work proposes a strategy to account for the multislip transgranular driving force using slip bands along the crystallographic direction. After twenty-five computation steps, we computed FIP_{meso} following equation (4.6) and found the grain having a maximum value of FIP_{meso} among all grains. Following on, we sorted all the bands in that grain in descending order of FIP_{meso} and selected the first three consecutive bands along different planes. Those bands were referred to as the 1st, 2nd, and 3rd MLB respectively. It is worth mentioning that in most realisations, the first three bands were normally having different slip planes.and found to be connected in all simulations.

Following on, the crack is extended in each band the same way as explained in the previous section i.e. by degrading the elastic stiffness of the band element incrementally after every two cycles until the band is fully cracked. The resultant driving force $FIP_{meso,,net}$ is estimated by the vector sum of FIP_{meso} along 1st, 2nd and 3rd MLB after every two loading cycles as,

$$\boldsymbol{FIP_{meso,\,net}} = \frac{\mathbf{1}}{\boldsymbol{d_{gr}^{ref}}}\left[\boldsymbol{d_{gr,i}}\overline{\boldsymbol{FIP_{meso}(i)}} + \boldsymbol{d_{gr,j}}\overline{\boldsymbol{FIP_{meso}(j)}} + \boldsymbol{d_{gr,k}}\overline{\boldsymbol{FIP_{meso}(k)}}\right]. \tag{4.8}$$

Where, $FIP(i)$, $FIP(j)$, and $FIP(k)$ are the average FIPs in the 1st, 2nd, and 3rd MLB along different planes. Since FIP averaging along a band introduce a directional character to driving force (FIP), thereby equation (4.8) shows the vector sum of averaged FIP along different planes. Figure 4-15 infer the effect of FIP_{meso} along different planes on crack extension. During the first 20% of propagation, crack is dominated by driving force along 1st MLB then it changes its path along the different plane and dominated by 2nd MLB until it reaches the grain boundary.

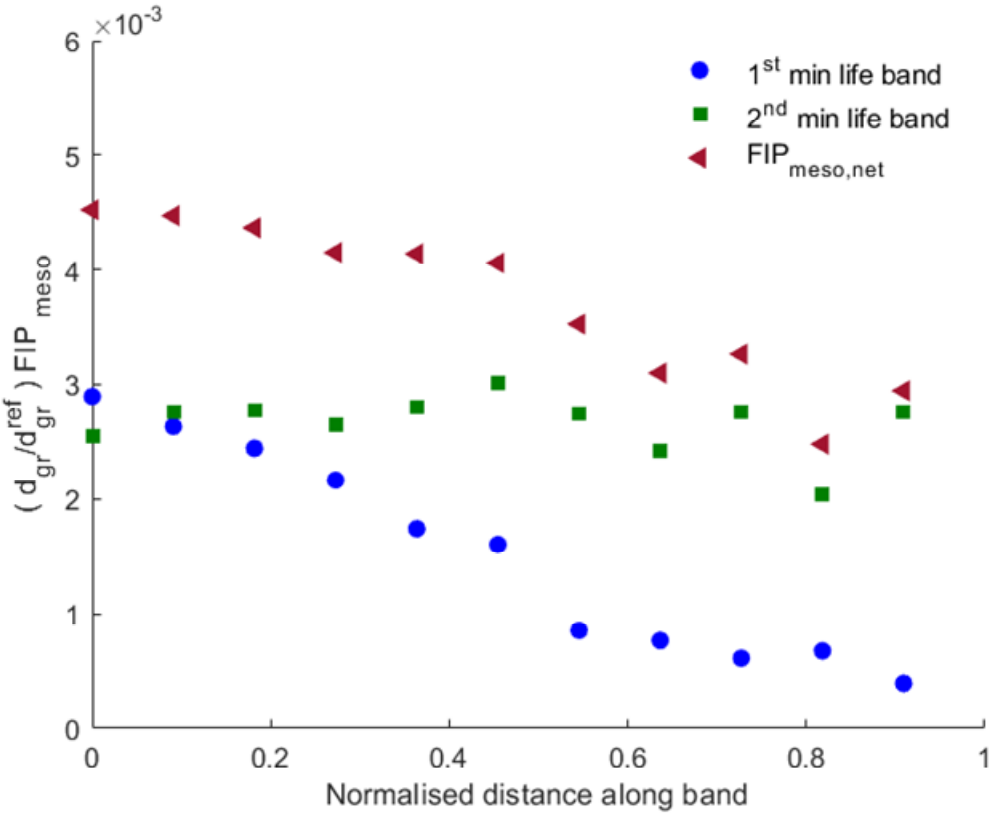

Figure 4-15 Effect of multislip FIP on crack extension following equation (4.8). The distance on x-axis is normalized by maximum distance along the band.

Figure 4-16 shows the multislip $FIP_{meso,\,net}$ computed using equation (4.8) for 8 realisations. Contrary to Figure 4-12, $FIP_{meso,\,net}$ shows a consistent decaying trend for all realisations. Interestingly, both FIP_{FS} and FIP_E follow the same trend regardless of cracking along uniaxial plane (Figure 4-12) or multislip plane (Figure 4-16).

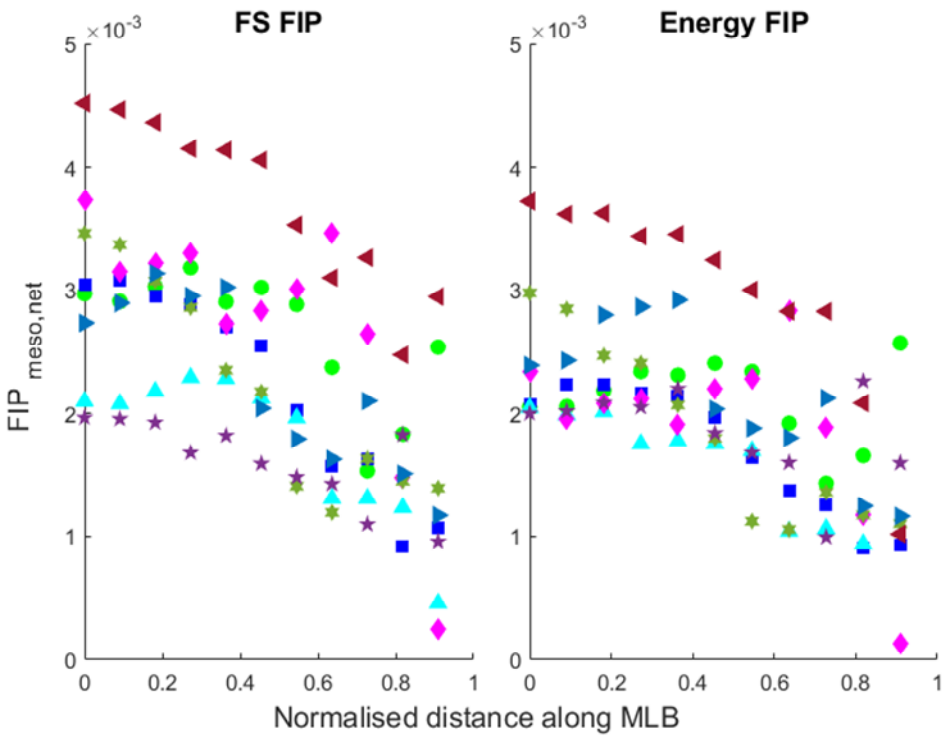

Figure 4-16 Multislip $FIP_{meso,net}$ as a function of crack extension with the explicit effect of microstructure. The distance on x-axis is normalized by maximum distance along MLB.

Figure 4-17 shows normalised $FIP^{FS}_{meso,net}$ as a function of crack length for 8 realisations. The $FIP^{FS}_{meso,net}$ is normalised by the $FIP^{FS}_{meso,net}$ at 0% crack length and distance along the x-axis is normalised by the maximum distance along the MLB. The decaying trend of $FIP_{meso,\,net}|^{Multislip}$ in aluminium agrees with the decaying trend of $FIP_{meso}|^{Uniaxial}$ in Ni based super alloys [16]. Castelluccio and McDowell [16] parametrised the fatigue driving force (normalised $FIP_{meso}|^{Uniaxial}$) as a function of crack length in Ni based superalloy as,

$$FIP_{meso}/FIP_{o} = 1 - P_g\left(a_i/d_{gr}\right)^m \qquad \textbf{(4.9)}$$

Where p and m are the scaling constants. Yuan et al. [39] implemented the approach [16] in bridge steel to evaluate various alternatives of FIP evolution inside a grain using equation (4.9). Here, this work found that a similar relation is

still valid for $FIP_{meso,net}\big|^{Multislip}$ as shown in Figure 4-17. The $^{a_i}/_{d_{gr}}$ term in equation (4.9) represents the proportion of the crack length inside MLB. Following on, equation (4.9) is referred as microstructural gradient, which is found to be less sensitive to material.

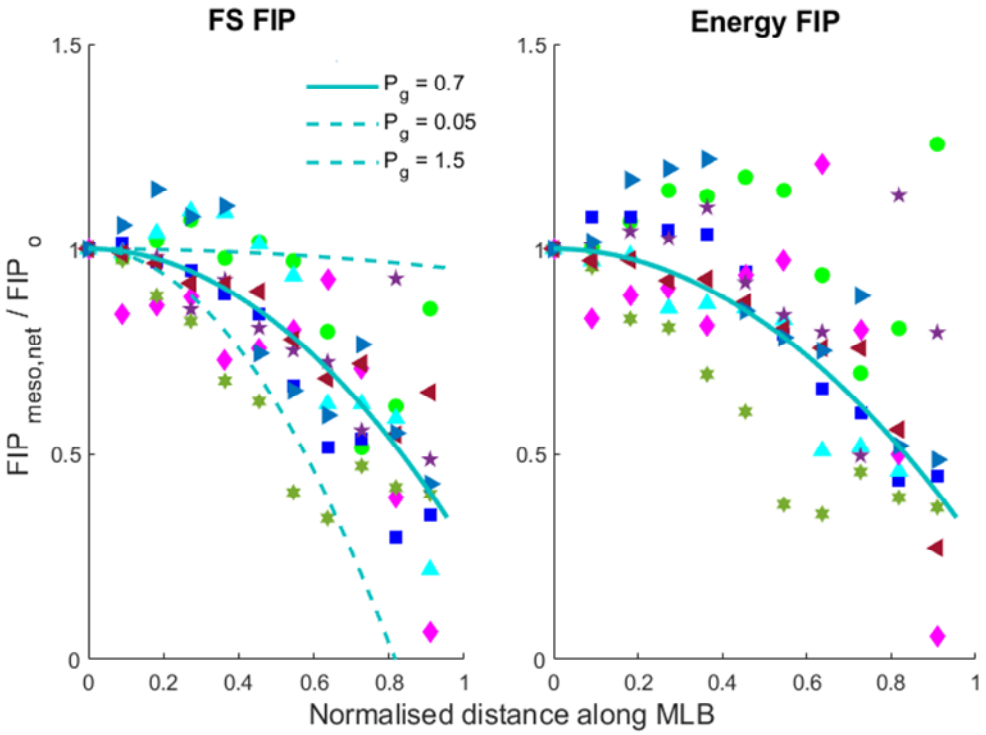

Figure 4-17 Normalised $FIP_{meso,net}$ with the transgranular crack extension. The scaling relation follows equation (4.9). The distance on x-axis is normalized by maximum distance along MLB.

4.3 Coupled effect of microstructure and geometric gradient on FIPs

4.3.1 Explicit coupling using crystal plasticity simulation

Following on, we employed the same approach as mentioned in the previous section to evaluate the coupled microstructure and geometric gradient. A cubic geometry with a notch of radius 5 μm and depth 25 μm is created in Abaqus v2017 [40] as shown in Figure 4-18. The microstructure (~16 grains and average

grain diameter of 50 μm along the x-y direction and 120 μm along the z-direction) is created alongside the notch using an in-house Matlab code. The model geometry is used to implement the crystal plasticity formulation in Abaqus UMAT [40].

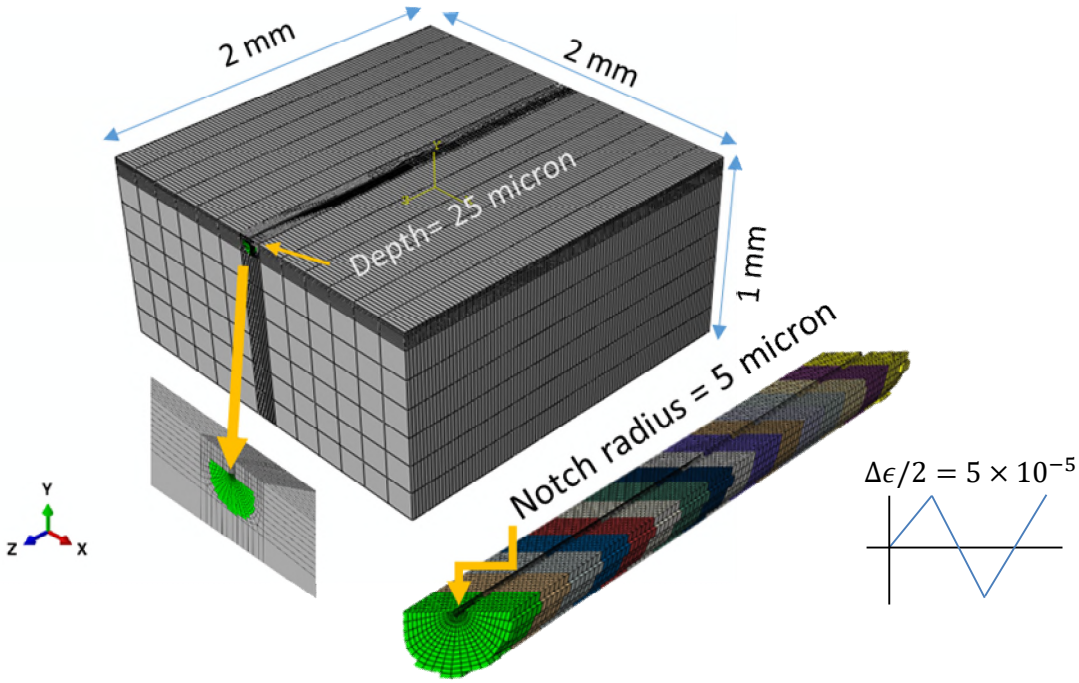

Figure 4-18 Finite element mesh to study the effect of microstructure and notch on fatigue crack driving force.

Figure 4-19 shows the combined effect of microstructure and geometric gradient on normalised $FIP_{meso,net}$ as a function of crack length. The decaying trend of normalised $FIP_{meso,net}$ agrees with Figure 4-17, but it is steeper due to the notch. This reveals that the gradient in Figure 4-17 can be calibrated to the gradient in Figure 4-19 with the addition of an independent geometric gradient.

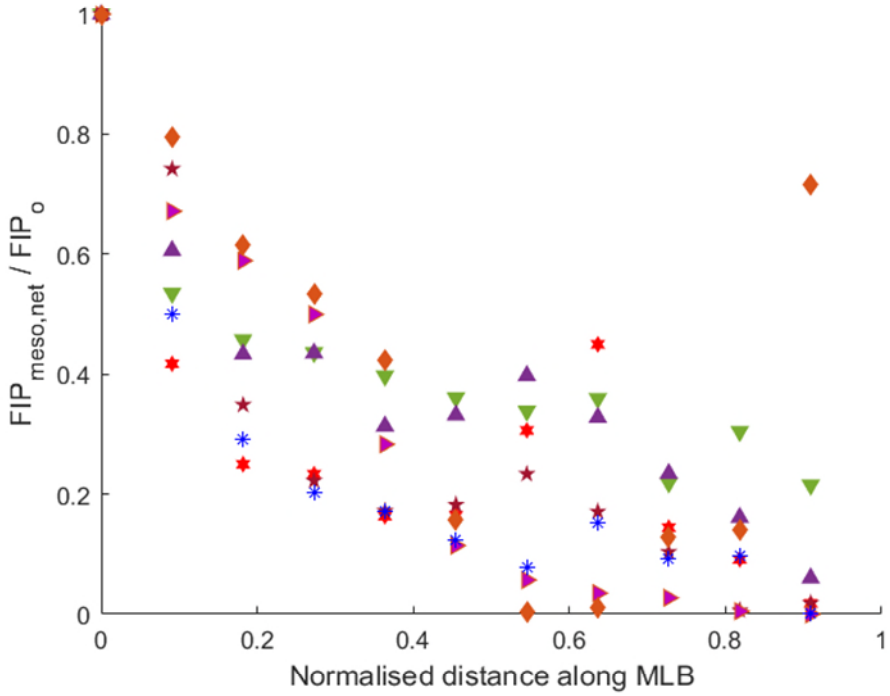

Figure 4-19 Effect of microstructure and geometric gradient on normalised $FIP_{meso,net}$ with crack extension in MLB at nominal strain amplitude of 5×10^{-5}. The ordinate is normalised by on FIP_o, which is a $FIP_{meso,net}$ at 0% crack length. The distance on x-axis is normalized by maximum distance along MLB. Each color and marker correspond to a realisation with a different microstructure. Each point represents the crack extension by deleting 10% element every two-cycle after nucleation evaluation i.e. 25 loading steps.

4.4 Independent quantification of geometric gradient

The evaluation of the cracking within grains shown in the prior section is time consuming and computationally intensive, so this work seeks a simple method that modulates microstructural variability with a homogenised solution for the geometric gradient. Rovinelli et al. [38] showed that the FIP_{FS} and plastic shear strain range are equivalent parameters in predicting the fatigue damage. This work proposed an engineering solution to evaluate the homogenised geometric gradient by estimating the maximum plastic shear strain (γ_{max}^{pl}) along the radial distance ahead of notch root using following equations,

$$\gamma_{max}^{pl} = \gamma_{max}^{total} - \gamma_{max}^{el}, \quad \textbf{(4.10)}$$

where,

$$\gamma_{max}^{total} = \frac{\epsilon_1 - \epsilon_2}{2}, \text{ and} \quad \textbf{(4.11)}$$

$$\gamma_{max}^{el} = \frac{\sigma_1 - \sigma_2}{2\mu} \quad \textbf{(4.12)}$$

where, ϵ_1, ϵ_2 and σ_1, σ_2 are maximum and minimum principal strains and stresses respectively computed from elastoplastic simulations. The parameter μ in equation (4.12) represents the shear modulus. A notched specimen with approximately 150,000 elements was created as shown in Figure 4-20 The periodic boundary conditions are applied at the left side of the specimen in Figure 4-20, whereas nominal cyclic strain of 2.8×10^{-3} was applied to the right-hand side along the x-axis. The input plastic stress-strain properties for elastoplastic simulation were obtained from crystal plasticity model results.

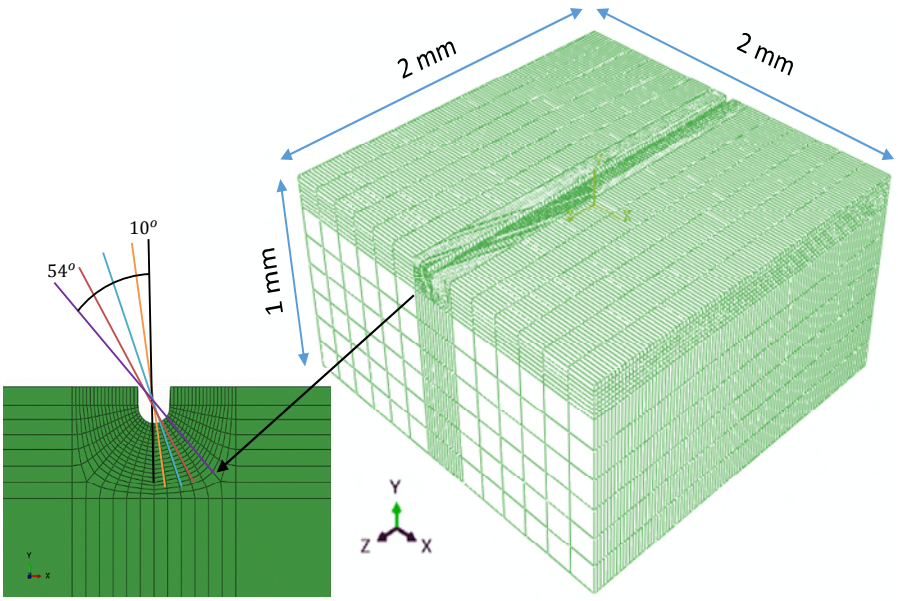

Figure 4-20 Finite element mesh for notched specimens used for evaluating the homogenised geometry gradient in elastoplastic simulations.

a)

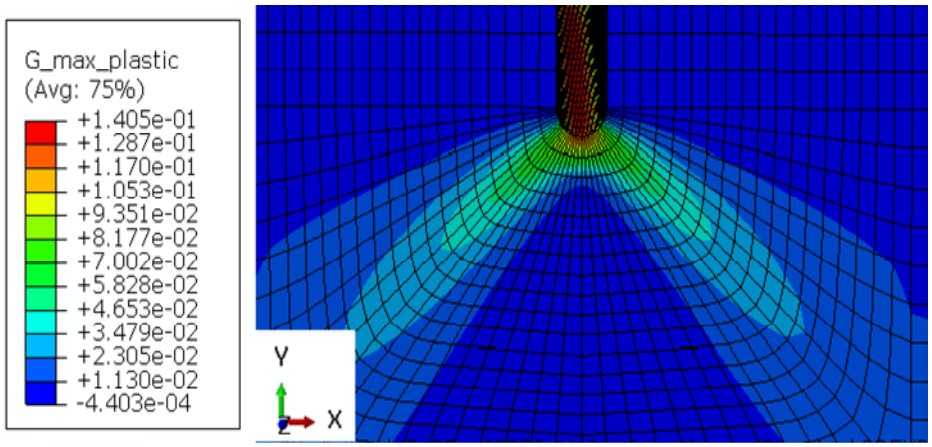

b)

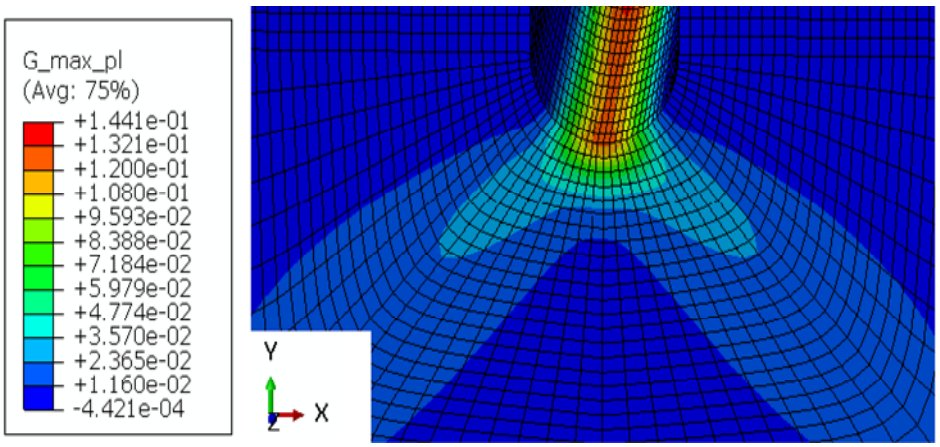

c)

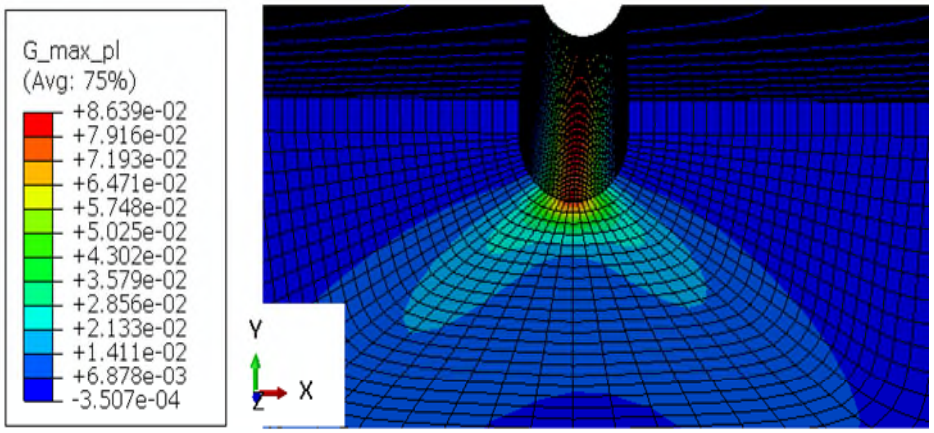

Figure 4-21 Effect of notch radius on γ_{max}^{pl}along the notch root for notches of radius a) 5 μm b) 25 μm c) 50 μm at the nominal strain of 2.8×10^{-3}.

Figure 4-21 presents the γ_{max}^{pl} gradient for different notch radii typical of scribe marks. The evolution of a strain field in form of a continuous loop at the notch root shows refined mesh quality. Since the extension of the crack (Figure 4-17) has a directional character due to grain anisotropy, we computed the angles that crack along MLB (in each realisation of Figure 4-17) form with the y-axis. Firstly, we extracted the Euler angles and normal plane direction of the band that failed from all realisations. We used the rotation matrix from these Euler angles to rotate the plane and finally computed the angle using the rotated vector and vertical axis as shown in Figure 4-22.

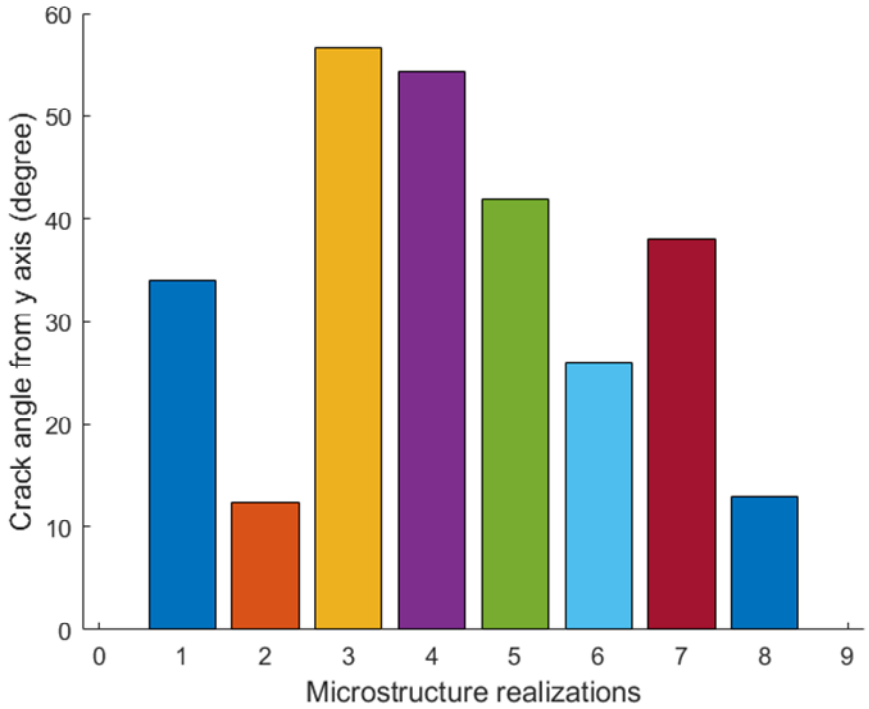

Figure 4-22 Angles between crack along the MLB and y-axis for different realisations.

Following on, these angles were used to quantify the γ_{max}^{pl} away from the notch tip. Figure 4-23 shows the normalised γ_{max}^{pl} as a function of normalised radial distance from the notch at different angles and notch radius. The ordinate of Figure 4-23 is normalised by the maximum γ_{max} at the notch tip, whereas the

abscissa is normalised by the average grain size used for microstructural gradient i.e. 50 µm. Following on, we parametrised the relation between normalised γ_{max}^{pl} and normalised radial distance with inverse of Taylor series of order 2 as,

$$\gamma_{max}^{pl} \Big/ \gamma_{\max,\ notch\ tip}^{pl} = {}^{1}\Big/ (1 + k_1 x + k_2 x^2) \qquad \textbf{(4.13)}$$

Where, k_1 and k_2 are the fitting parameters for each notch radius as shown in Figure 4-23. Equation (4.13) is referred to as the geometric gradient.

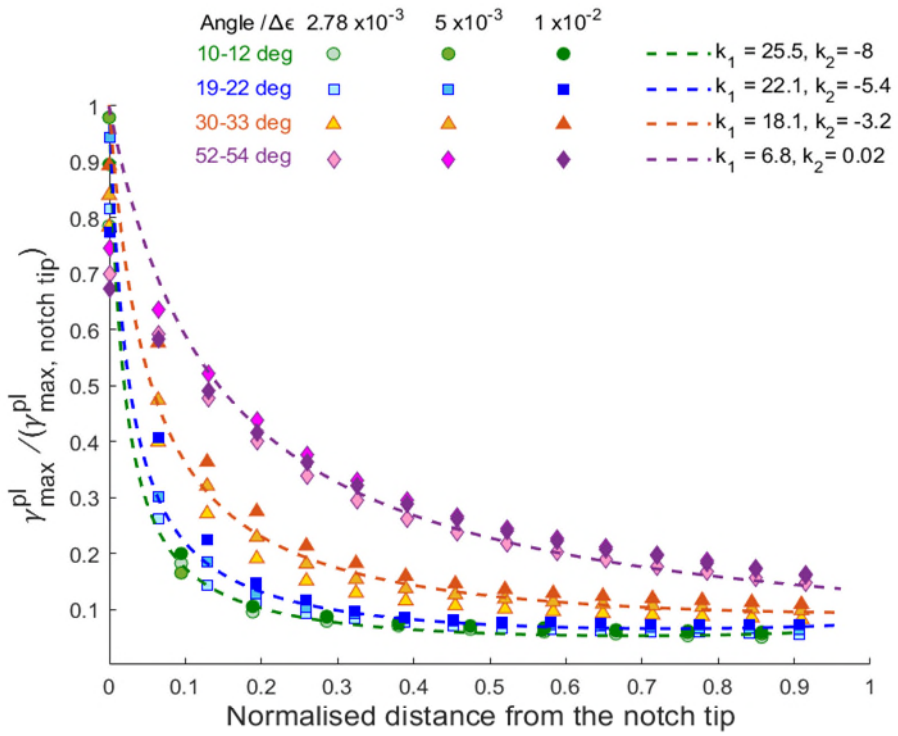

a)

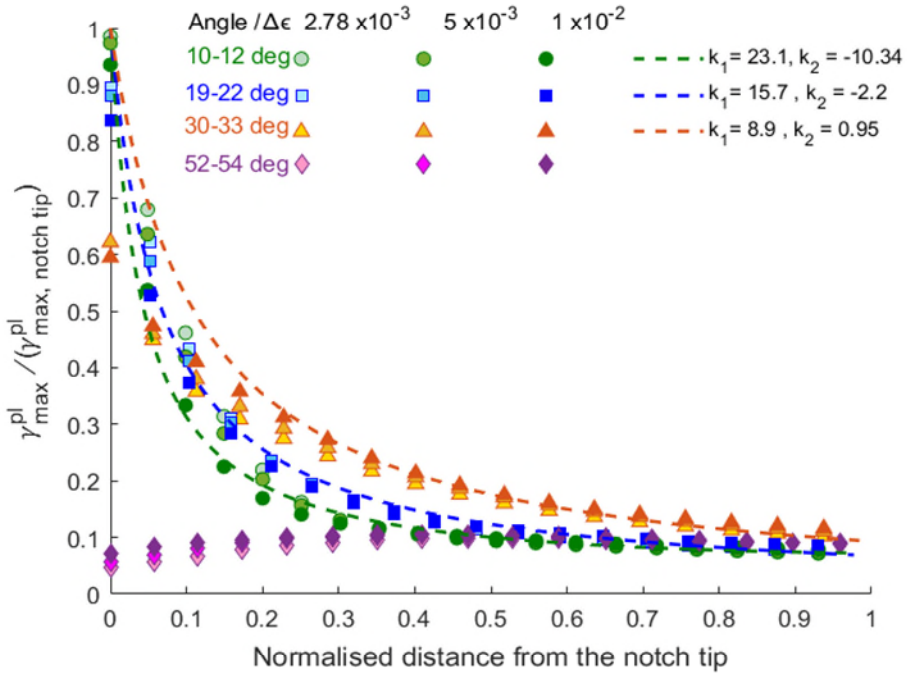

b)

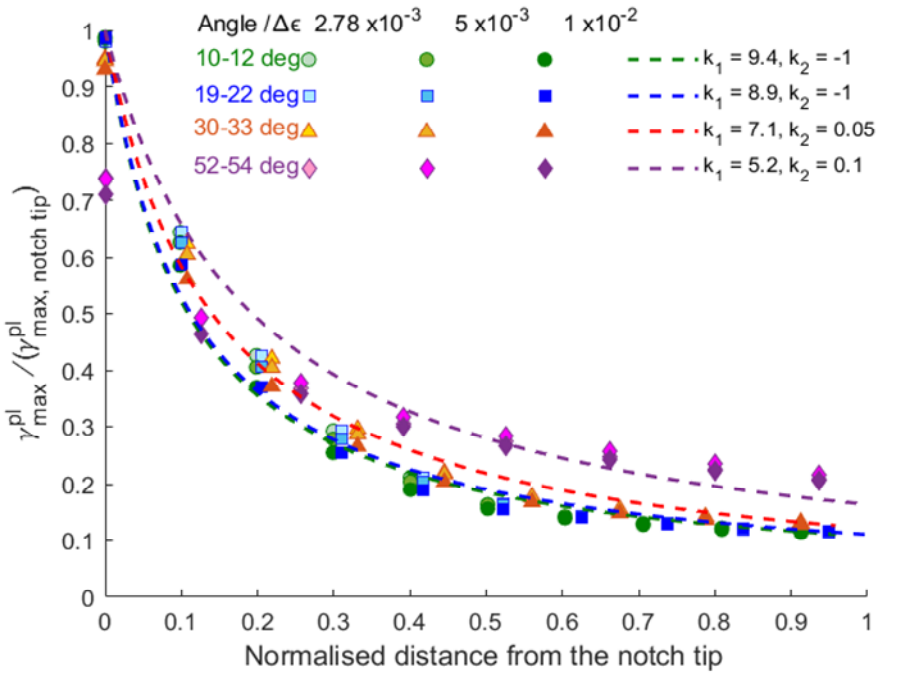

c)

Figure 4-23 The gradient of normalised γ_{max}^{pl} away from the notch tip for radius a) 5 µm b) 25 µm and c) 50 µm at different nominal strains. The γ_{max}^{pl} was normalised with the maximum γ_{max}^{pl} at the notch tip. The distance is normalised by the average grain size used for microstructural gradient i.e. 50 µm.

Figure 4-24 compares the γ_{max}^{pl} and γ_{max}^{total} gradient at different angles and different strain amplitudes, which shows that both gradients are the same. However, the large difference between γ_{max}^{pl} and γ_{max}^{total} could be expected if there is not enough plasticity corresponding to lower nominal strains. We recommend computing the γ_{max}^{total} corresponding higher nominal strains as it requires less computation and provides an engineering solution.

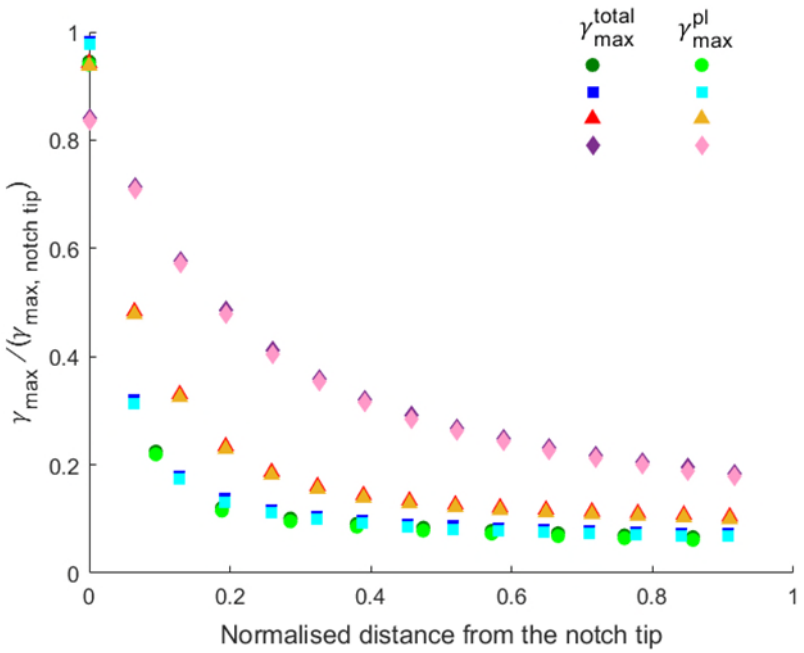

a)

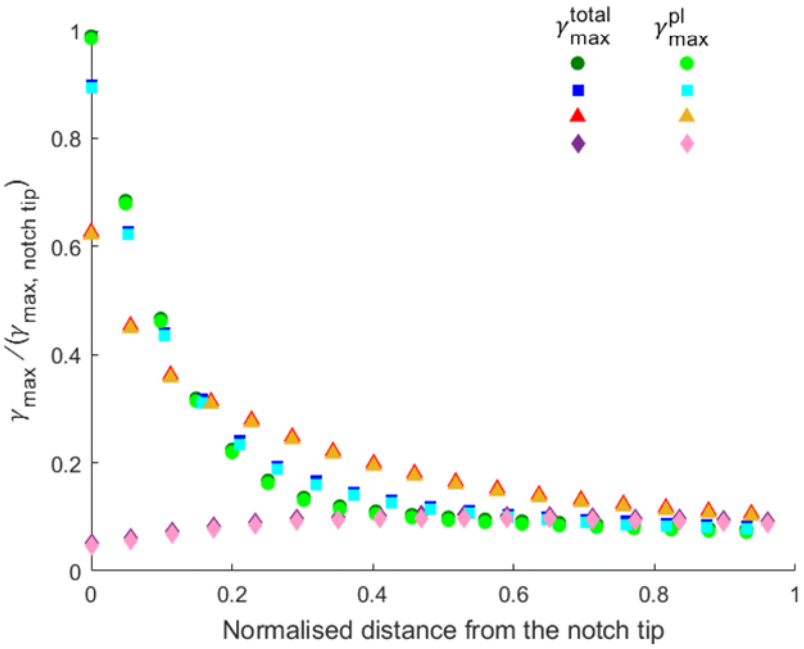

b)

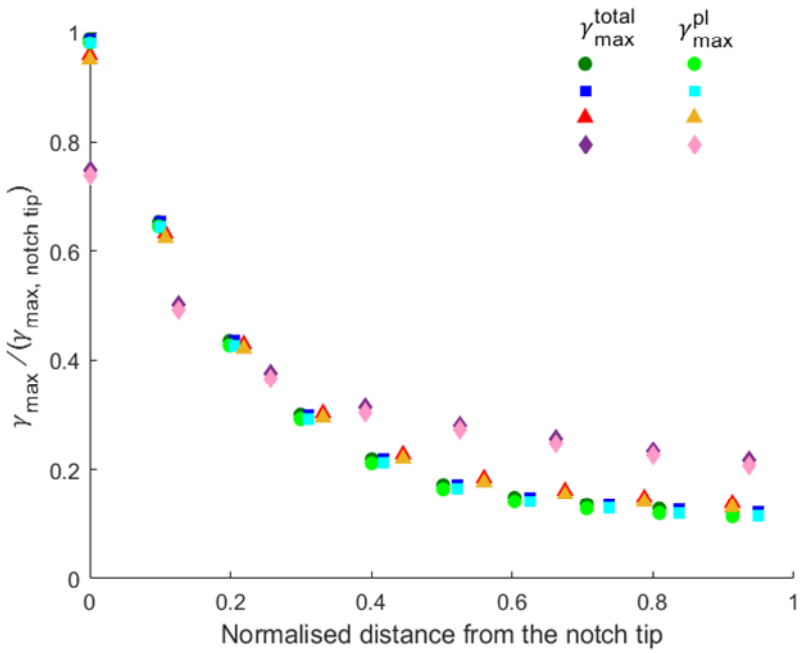

c)

Figure 4-24 Comparison between γ_{max}^{total} and γ_{max}^{pl} gradient for notches with different root radii. The distance is normalised by the average grain size used for microstructural gradient i.e. 50 μm.

4.5 Integration of independent gradients

This work explored that the empirical relation related to microstructural gradient [16] is also valid for aluminium irrespective of planar (uniaxial) and multislip FIP. Hence, this reflects a notion to use the same microstructural gradient [16] with an independently estimated geometric gradient to reconstruct the FIP that represents the coupled effect.

Here, we propose a reconstruction of microstructural variability of the notch without the computational cost of the entire simulation by multiplying equation (4.13) with the microstructure-sensitive results without notches (equation (4.9)). However, we consider equation (4.13) with k_1 and k_2 correspond to range of angles i.e. 10 degree, 23 degree and 54 degree. Figure 4-25 depicts the microstructural gradient estimated in section 4.2.2 without notches (left) multiplied by the homogenised geometric gradient (center, Figure 4-23(a)) to obtain the equivalent results for notches in Figure 4-25 (right).

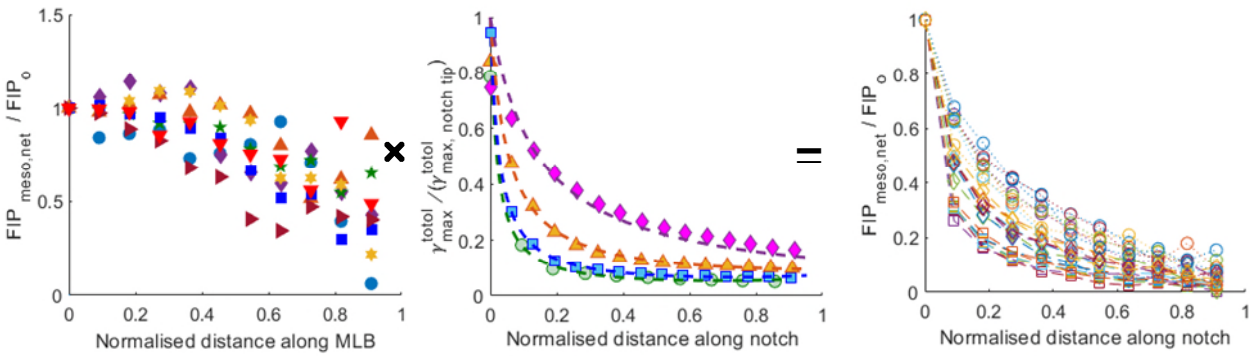

$$1 - P_g\left({}^{a_i}/_{d_{gr}}\right)^m \times \frac{1}{1+k_1\left({}^{a_i}/_{d_{gr}}\right)+k_2\left({}^{a_i}/_{d_{gr}}\right)^2} = \frac{1-P_g\left({}^{a_i}/_{d_{gr}}\right)^m}{1+k_1\left({}^{a_i}/_{d_{gr}}\right)+k_2\left({}^{a_i}/_{d_{gr}}\right)^2}$$

Microstructural gradient **Geometric gradient** **Coupled gradient**

Figure 4-25 Integration of microstructural (a) and geometric gradient (b) to reconstruct combined gradient (c). In Figure (c), the circle, square, and diamond markers correspond to the geometric gradient at 10^o, 30^o,and 54^o respectively. Each color in Figure (left) represents different simulation result with different microstructure and morphological properties whereas, each color in Figure

(center) corresponds to decay of γ_{max}^{pl} along different angles. The normalization distance on x-axis corresponds to average grain size used for microstructural gradient i.e. 50 µm.

Since FIP_{FS} is the range of cycle plastic shear strain multiplied by normalised stress factor, thereby multiplying that maximum plastic shear strain in dimensionally justified. Furthermore, Figure 4-26 compares the microstructure-sensitive simulations with and without explicit notches. The results demonstrate that geometric and microstructural gradients can be decoupled and estimated independently to produce comparable FIP results. Besides, Figure 4-26 shows that the variability induces by the different angular positions of the geometric gradient (right) is comparable with that from crystal plasticity simulations (left).

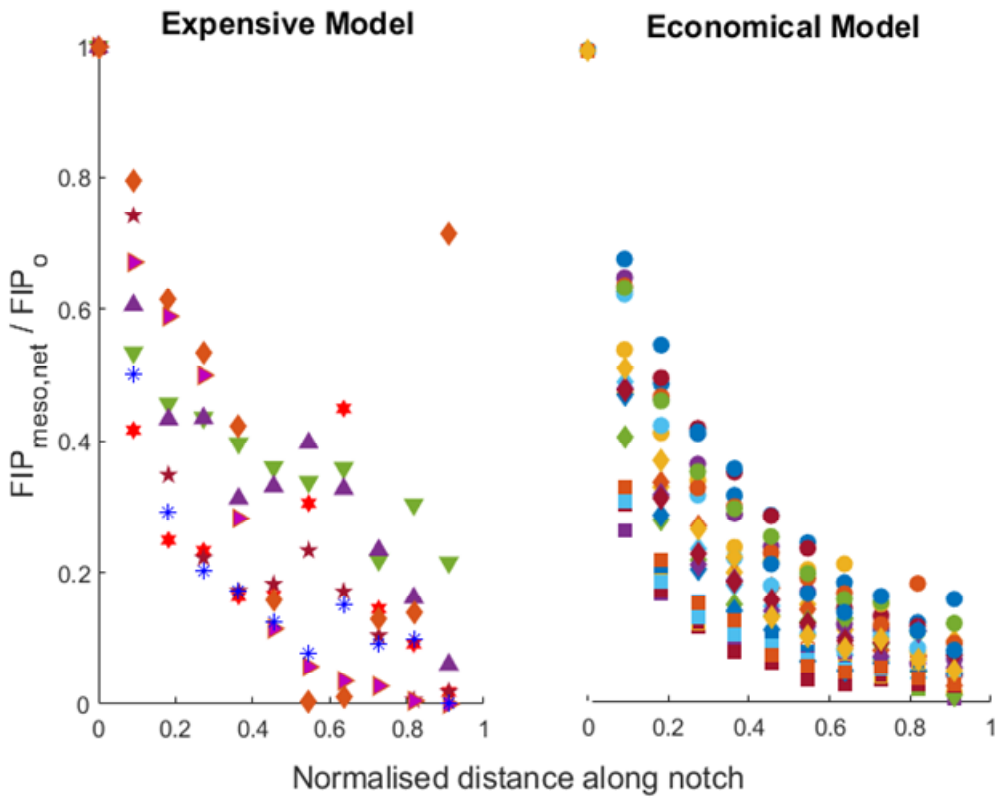

Figure 4-26 Comparison between simultaneous estimation and independent coupling of gradients. $FIP_{meso,net}$ is normalised by FIP_o, which is a FIP_{meso} at 0% crack extension. The normalization distance on x-axis corresponds to average

grain size used for microstructural gradient i.e. 50 µm. Each color in Figure (left) represents different simulation result with different microstructure and morphological properties. Each circle, square, and diamond markers in Figure (right) represents independently coupled FIP with both microstructure and geometric gradient.

4.6 Discussion

This work is motivated by the challenge of evaluating the multiple driving force gradients that play a substantial role in fatigue crack formation from shallow notches. However, simultaneous evaluation of multiple gradients using crystal plasticity simulations is computationally challenging. Here, we introduced a notion to evaluate and couple geometric and microstructural gradients independently to predict fatigue crack formation.

Firstly, we evaluated the microstructural gradient with and without notch while implementing an existing approach [16] using crystal plasticity simulations. Some studies [28] have emphasised that the choice of FIP_E has more physical meaning as compared to FIP_{FS}. Contrarily, other efforts [38] have found that energy and shear range based FIPs are equivalent predictors of fatigue process and have similar levels of uncertainty. Following on, this work considered both FIP_{FS} and FIP_E as a subrogate measure of driving force to elucidate the choice of FIP. Moreover, we also compared both FIPs as volume averaged FIPs over different domains i.e. element, bands and grains. Figure 4-7 shows that both FIPs have similar distributions over different domains. However, FIP_E has higher frequency compared to FIP_{FS} over the same range. The one-to-one (element based) comparison of FIP_{FS} and FIP_E (Figure 4-8) shows that they have a linear relationship correspond to their extreme values. However, some elements have higher FIP_E as compared to FIP_{FS}. This difference belongs to the elements at the grain boundary as shown in Figure 4-9 or is due to mesh sensitivity. Since the extreme values (tail of distribution) of FIP lead crack growth, therefore, the difference among small values of both FIPs can be ignored.

This work further showed that the volume averaged FIP mitigates the mesh uncertainty and present a good agreement between FIP_{FS} and FIP_{E}. However, averaging FIPs over larger domains such as grain volume missed the variability associated with sub grain fields and thereby may underestimate the fatigue driving force. Therefore, slip band with their reference length scale comparable to the fatigue damage process zone presents a balanced estimate of averaged FIP between element and grain averaged FIP, which agrees with Castelluccio and McDowell's [42] finding. They also argued that FIP averaging over bands represents a better estimate than refining the mesh and also facilitates in reducing the computational load.

Since aluminium has lower plastic shear activation energy (Chapter 2) that facilitates slip activity over multiple planes, therefore the fatigue prognosis of aluminium requires multislip driving force. This work extended the applicability of the existing approach [16] from uniaxial FIP_{meso} estimation to multislip FIP_{meso} as a function of crack length. Following on, we evaluated the microstructural gradient considering several realisations using proposed $FIP_{meso,\,net}\big|^{Multislip}$, which shows a decaying trend as the crack extend inside a grain. The microstructural gradient in aluminium is found to be the similar as estimated in Ni based superalloy [16], although, the gradient in Ni-based superalloy was computed using a planar driving force ($FIP_{meso}|^{uniaxial}$). This finding reveals that microstructural gradient among FCC metals is less sensitive to material. Moreover, this finding also supports the centralised hypothesis of this thesis that FCC metals has same deformation mechanisms under different loading condition.

Following on, we computed the combined effect of geometric and microstructure gradients on FIPs using crystal plasticity simulations, which were found to be steeper than the explicit microstructural gradient. Following the findings from crystal plasticity simulation of microstructural gradient with and without notch, this work introduced a notion to decouple geometric and microstructural gradients. Since the microstructure gradient is material insensitive, it can be coupled with

an independent geometric gradient to reconstruct the FIP that represents the effect of both gradients.

This work proposed a homogenised engineering solution for the independent quantification of geometric gradient. A simple elastoplastic model is considered to capture the notch gradient by estimating the γ_{max}^{total} at the notch root along the different radial path. Since the gradient estimated using crystal plasticity simulation has large variability, we proposed to estimate the γ_{max}^{total} along the angle that cracks follow in crystal plasticity simulations. This strategy imparts variability to independently coupled gradients and agrees with crystal plasticity results (Figure 4-26).

The proposed approach enables quantification of notch gradient with a large mesh size, which mitigates the mesh sensitivity issues inherently associated with notch problems. Besides, we proposed this approach with a broader scope of accounting for the role of complex gradients on MS fatigue crack formation. Future efforts will consider coupling the complex gradients with microstructure gradient using the current approach to predict fatigue life.

4.7 Conclusions

This work analysed Fatemi-Socie and Energy based FIPs over different volume averaging domains and compared its variation as a function of crack length inside a grain. Both FIPs showed a linear relationship correspond to their extreme values. Moreover, both FIPs present the same variation as the crack propagates inside the grain. We found that the choice of domain is more important as compared to the choice of FIP.

This work proposes a strategy to estimate multislip FIP to study the transgranular crack propagation. The effect of the microstructure is analysed on multislip FIP variation while extending the crack inside a grain. The microstructure gradient in FCC metals is found to be the same however, fundamental mechanisms need to be considered. For instance, multislip FIP is essential for aluminium as a high

SFE metal, whereas uniaxial FIP works for low- medium SFE metal at room temperature.

Following the outcome of crystal plasticity simulations with or without a notch, this work decoupled microstructure and geometric gradients in fatigue crack formation. We proposed an economical solution (less computationally intensive) for coupling independent gradients.

References

1. Cini A. and Irving P.E. Development of fatigue cracks from mechanically machined scratches on 2024-T351 aluminium alloy—Part I: Experimentation and fractographic analysis. Fatigue and Fracture of Engineering Materials and Structures. 2017; 40(5): 776–789. http://dx.doi.10.1111/ffe.12544

2. Khan M.K. Scribe marks at fuselage joints- determination of residual stress and effects of fatigue loading using nanoindentation and synchrotron X-ray diffraction. The Open University.UK; 2010.

3. Nader N.A. The effect of scratches on fatigue life and fatigue crack growth of Al 2024-T3 clad. PhD thesis. Wichita State University; 1993.

4. FAA airworthiness directives no. FAA-2005-20918, 31/3/2006

5. Das G., Kosai M. and Miller M. Development of a method for damage tolerance analysis for scribe marks adjacent to fuselage longitudinal and circumferential splices. International Committee on Aeronautical Fatigue (ICAF) meeting. Napoli, Italy; pp. 14–18.

6. P. J. E. Forsyth. A two stage process of fatigue crack growth royal aircratt establishment. Proceedings of the Crack Propagation Symposium. 1961. pp. 76–94.

7. Ritchie R.O. and Suresh S. The fracture mechanics similitude concept: questions concerning its application to the behavior of short fatigue cracks. Materials Science and Engineering. 1983; 57(2): 27–30. http://dx.doi.10.1016/0025-5416(83)90223-9

8. McDowell D.L. Basic issues in the mechanics of high cycle metal fatigue. International Journal of Fracture. 1989; 80(2): 103–145. http://dx.doi.10.1007/BF00012666

9. Cini A. Scribe marks at fuselage joints:Initiation and propagation of fatigue cracks from mechanical defects in aluminium alloys. PhD thesis. 2012 Cranfield University.UK.

10. Farukh F., Zhao L.G., Jiang R., Reed P., Proprentner D. and Shollock B.A. Realistic microstructure-based modelling of cyclic deformation and crack growth using crystal plasticity. Computational Materials Science. 2016; 111: 395–405. http://dx.doi.org/10.1016/j.commatsci.2015.09.054

11. Wilson D. and Dunne F.P.E. A mechanistic modelling methodology for microstructure-sensitive fatigue crack growth. Journal of the Mechanics and Physics of Solids. 2019; 124: 827–848. http://dx.doi.org/10.1016/j.jmps.2018.11.023

12. Zhang P., Zhang L., Baxevanakis K.P., Zhao L.G. and Bullough C. Modelling short crack propagation in a single crystal nickel-based superalloy using crystal plasticity and XFEM. International Journal of Fatigue. 2020; 136: 105594. http://dx.doi.10.1016/j.ijfatigue.2020.105594

13. Zhang P., Zhang L., Baxevanakis K.P., Lu S., Zhao L.G. and Bullough C. Discrete crystal plasticity modelling of slip-controlled cyclic deformation and short crack growth under low cycle fatigue. International Journal of Fatigue. 2021; 145: 106095. http://dx.doi.10.1016/j.ijfatigue.2020.106095

14. Pan Y Bin., Dunne F.P.E. and MacLachlan D.W. A mechanistic and stochastic approach to fatigue crack nucleation in coarse grain RR1000 using local stored energy. Fatigue and Fracture of Engineering Materials and Structures. 2021; 44(2): 505–520. http://dx.doi.10.1111/ffe.13376

15. Xu Y., Wan W. and Dunne F.P.E. Microstructural fracture mechanics: stored energy density at fatigue cracks. Journal of the Mechanics and Physics of Solids. 2021; 146: 104209. http://dx.doi.10.1016/j.jmps.2020.104209

16. Castelluccio G.M. and McDowell D.L. A mesoscale approach for growth of

3D microstructurally small fatigue cracks in polycrystals. International Journal of Damage Mechanics. 2014; 23(6): 791–818. http://dx.doi.10.1177/1056789513513916

17. Tokaji K. and Ogawa T. The growth behaviour of microstructurally small fatigue cracks in metals. In: Miller KJ, Rios and ER de los (eds.) Mechanical Engineering Publications. London: Mechanical Engineering Publications; 1992. pp. 85–99.

18. Yuan GJ., Wang R.Z., Gong C.Y., Zhang X.C. and Tu S.T. Investigations of micro-notch effect on small fatigue crack initiation behaviour in nickel-based alloy GH4169: Experiments and simulations. International Journal of Fatigue. 2020; 136: 105578. http://dx.doi.org/10.1016/j.ijfatigue.2020.105578

19. Musinski W.D. and McDowell D.L. Microstructure-sensitive probabilistic modeling of HCF crack initiation and early crack growth in Ni-base superalloy IN100 notched components. International Journal of Fatigue. Elsevier Ltd; 2012; 37: 41–53. http://dx.doi.10.1016/j.ijfatigue.2011.09.014

20. Kakandar E., Barrios A., Michler J., Maeder X., Pierron O.N. and Castelluccio G.M. A computational and experimental comparison on the nucleation of fatigue cracks in statistical volume elements. International Journal of Fatigue. 2020; 137: 105633. http://dx.doi.org/10.1016/j.ijfatigue.2020.105633

21. Wan V.V.C., Jiang J., MacLachlan D.W. and Dunne F.P.E. Microstructure-sensitive fatigue crack nucleation in a polycrystalline Ni superalloy. International Journal of Fatigue. Elsevier Ltd; 2016; 90: 181–190. http://dx.doi.org/10.1016/j.ijfatigue.2016.04.013

22. Tanaka K. and Akiniwa Y. Propagation and non-propagation of small fatigue cracks. Proceedings of The 7th International Conference On Fracture (ICF7). Houston, Texas,; 1989. pp. 869–887. http://dx.doi.org/10.1016/b978-0-08-034341-9.50100-5

23. Glinka G. and Newport A. Universal features of elastic notch-tip stress fields. International Journal of Fatigue. 1987; 9(3): 143–150. http://dx.doi.10.1016/0142-1123(87)90069-7

24. Morrow J. Cyclic plastic strain energy and fatigue of metals. Internal Friction, Damping, and Cyclic Plasticity. West Conshohocken, PA: American Society of Testing and Materials; 2009. pp. 45-45–43. http://dx.doi.10.1520/stp43764s

25. Brown M.W. and Miller K.J. A theory for fatigue failure under multiaxial stress-strain conditions. Proceedings of the Institution of Mechanical Engineers. 1973; 187(1): 745–755. http://dx.doi.10.1243/pime_proc_1973_187_161_02

26. Garud Y.S. A new approach to the evaluation of fatigue under multiaxial loadings. Journal of Engineering Materials and Technology, Transactions of the ASME. 1981; 103(2): 118–125. http://dx.doi.10.1115/1.3224982

27. Ellyin F. and Xia Z. A general fatigue theory and its application to out-of-phase cyclic loading. Journal of Engineering Materials and Technology, Transactions of the ASME. 1993; 115(4): 411–416. http://dx.doi.10.1115/1.2904239

28. Wilson D.,Zheng Z. and Dunne FPE. A microstructure-sensitive driving force for crack growth. Journal of the Mechanics and Physics of Solids. Elsevier Ltd; 2018; 121: 147–174. http://dx.doi.10.1016/j.jmps.2018.07.005

29. Wan V.V.C.,Maclachlan D.W. and Dunne F.P.E. A stored energy criterion for fatigue crack nucleation in polycrystals. International Journal of Fatigue. 2014; 68: 90–102. http://dx.doi.10.1016/j.ijfatigue.2014.06.001

30. Castelluccio G.M. A study on the influence of microstructure on small fatigue cracks. PhD Thesis. Georgia Institute of Technology Atlanta, GA, USA; 2012; 277.

31. Brown M.W. and Miller K.J. High temperature low cycle biaxial fatigue of two steels. Fatigue & Fracture of Engineering Materials & Structures. 1979; 1(2): 217–229. http://dx.doi.org/10.1111/j.1460-2695.1979.tb00379.x

32. Socie D.F. and Marquis G.B. Multiaxial fatigue. ASTM Special Technical Publication. SAE International; 1985.

33. Fatemi A. and Socie D.F. A critical plane approach to multiaxial fatigue damage including out-of-phase loading. Fatigue & Fracture of Engineering Materials & Structures. 1988; 11(3): 149–165. http://dx.doi.10.1111/j.1460-2695.1988.tb01169.x

34. Kandil F.A., Brown M.W. and Miller K.J. Biaxial low cycle fatigue failure of 316 stainless steel at elevated temperatures. Metal Society book 280. Metal Society of London; 1981. pp. 203–210.

35. Castelluccio G.M. and McDowell D.L. Assessment of small fatigue crack growth driving forces in single crystals with and without slip bands. International Journal of Fracture. July 2012; 176(1): 49–64. http://dx.doi.10.1007/s10704-012-9726-y

36. McDowell D.L. and Berard J -Y. A δj-based approach to biaxial fatigue. Fatigue & Fracture of Engineering Materials & Structures. 1992; 15(8): 719–741. http://dx.doi.10.1111/j.1460-2695.1992.tb00053.x

37. Lucarini S. and Segurado J. An upscaling approach for micromechanics based fatigue: from RVES to specimens and component life prediction. International Journal of Fracture. Springer Netherlands; 2020; 223(1–2): 93–108. http://dx.doi.10.1007/s10704-019-00406-5

38. Rovinelli A., Guilhem Y., Proudhon H., Lebensohn R.A., Ludwig W. and Sangid M.D. Assessing reliability of fatigue indicator parameters for small crack growth via a probabilistic framework. Modelling and Simulation in Materials Science and Engineering. IOP Publishing; 2017; 25(4). http://dx.doi.10.1088/1361-651X/aa6c45

39. Yuan H., Zhang W., Castelluccio G.M., Kim J. and Liu Y. Microstructure-sensitive estimation of small fatigue crack growth in bridge steel welds. International Journal of Fatigue. Elsevier; 2018; 112(December 2017): 183–197. http://dx.doi.10.1016/j.ijfatigue.2018.03.015

40. ABAQUS. FEM software v2017. Providence, RI, USA: Simulia Inc.; 2017.

41. Groeber MA. and Jackson M.A. DREAM.3D: A digital representation environment for the analysis of microstructure in 3D. Integrating Materials and Manufacturing Innovation. 2014; 3(1): 56–72. http://dx.doi.10.1186/2193-9772-3-5

42. Castelluccio G.M. and McDowell D.L. Microstructure and mesh sensitivities of mesoscale surrogate driving force measures for transgranular fatigue cracks in polycrystals. Materials Science and Engineering A. July 2015; 639: 626–639. http://dx.doi.10.1016/j.msea.2015.05.048

43. Yeratapally S.R., Leser P.E., Hochhalter J,D., Leser W.P. and Ruggles T.J. A digital twin feasibility study (part I): Non-deterministic predictions of fatigue life in aluminum alloy 7075-t651 using a microstructure-based multi-scale model. Engineering Fracture Mechanics. Elsevier Ltd; 2020; 228(Part I): 106888. http://dx.doi.10.1016/j.engfracmech.2020.106888

44. Forsyth P.J.E. Fatigue damage and crack growth in aluminium alloys. Acta Metallurgica. Pergamon; 1 July 1963; 11(7): 703–715. http://dx.doi.10.1016/0001-6160(63)90008-7

45. Risbet M. and Feaugas X. Some comments about fatigue crack initiation in relation to cyclic slip irreversibility. Engineering Fracture Mechanics. 2008. pp. 3511–3519. http://dx.doi.10.1016/j.engfracmech.2007.04.014

46. Grosskreutz J.C. Fatigue crack propagation in aluminum single crystals. Journal of Applied Physics. 1962; 33(5): 1787–1792. http://dx.doi.10.1063/1.1728832

47. Hennessey C.D. Modelling microstructurally small crack growth in Al 7075-T6. Master's thesis. Georgia Institute of Technology; Atlanta, GA, USA. 2015.

5 Coupling Microstructure and Geometric Gradients Independently to Predict Transgranular Fatigue Life

5.1 Introduction

Extensive research [1–4] has been done on predicting the fatigue life of a notched component. However, these studies considered the engineering size (~few mm) notches in which notch root radii was larger compared to the material microstructure. Therefore, a stress field produced by these notches extends many times longer than typical microstructure dimensions, which makes these notches insensitive to material microstructure [5]. Contrarily, if the size of the defect is comparable to the grain dimension then crack growth is strongly influenced by local microstructure [6].

Scribe marks are induced on the aircraft fuselage joints as a result of improper maintenance procedure [7]. Several efforts [8] have shown that these scribe marks on fuselage joints act as micron-sized notches and lead the fatigue crack propagation through the thickness. Some other efforts [9] have noticed that the early crack growth from scribes was strongly influenced by local microstructure irrespective of scribe geometry. Since microstructure-sensitive small crack growth is controlled by the local shear along the crystallographic plane [10], the estimation of fatigue life of a scribed component requires computing the local driving force using crystal plasticity simulations.

Several studies [11,12] have attempted to predict the fatigue life of metals using crystal plasticity simulations without considering the geometric gradient. Some efforts [13] have attempted to study the effect of notch on microstructure-sensitive crack growth at 2.7×10^{-4} strain amplitude. However, their mesh sensitivity analysis showed that a notch of 1000 μm root radii requires 15 μm mesh seed size. The study [13] explicitly mentioned that a smaller mesh size may provide better results. However, it is computationally intensive to run the analysis using crystal plasticity simulations. In the present work, we considered notches with

root radii comparable to shallow scribe marks (5- 25 μm) that require even smaller mesh seed size. In the previous chapter, we proposed a less computationally intensive solution to compute the coupled microstructure and geometric gradients. Here, this work aims to employ the independently coupled gradient to predict the transgranular fatigue life in pure aluminium and compare it with experiments [14].

5.2 Transgranular MSC growth law

The microstructure sensitive (MS) crack growth rate is proportional to the irreversible dislocation emissions after a cycle, which is related to crack tip displacement ΔCTD [15] as,

$$\frac{da}{dN} = \emptyset\langle \Delta CTD - \Delta CTD_{th} \rangle \quad \textbf{(5.1)}$$

Where $\emptyset$ is the proportionality factor represents the mechanical irreversibility and determines the number of irreversible dislocations emitted from the crack tip. Besides, the parameter $\emptyset$ strongly depends on the environment and its value typically ranges between 0.01 -0.2 [16] for transgranular crack growth. The ΔCTD_{th} is a threshold recognises minimum driving force below which no dislocation emission take place i.e. Burgers vector. Here, ΔCTD_{th} is considered as $2.86 \times 10^{-4}\ \mu m$ i.e. size of a Burger vector of aluminium. The crack growth rate in equation (5.1) follows Macaulay's brackets i.e. growth rate is zero if net crack driving force is less than the threshold. The estimation of ΔCTD requires detailed representation of crack tip geometry and a tedious process. Instead, FIP provides an efficient way to estimate the fatigue driving force for MS crack growth [17].

Castelluccio and McDowell [18] found a correlation between FIP_{FS} and $\Delta\mathrm{CTD}$ for crystallographic cracks under shear and mixed-mode loading conditions. They proposed a surrogate for ΔCTD as,

$$FIP = \mathrm{A}\,(\Delta CTD)^b \quad \textbf{(5.2)}$$

where *A* and *b* are the constants resulting from linear regression [19] to minimize the mean square error. The parameter *A* is the scaling constant that relates FIP with ΔCTD and may depend on the grain size. Castelluccio and McDowell [18] proposed the linear relation between FIP and ΔCTD for a Ni base superalloy by modelling explicit cracks in single crystal simulations. Some other efforts [20,21] have implemented equation (5.2) to study microstructure sensitive fatigue crack in Al 7075-T6. Following on, this work also considered the same relation to study the fatigue response of pure aluminium. Risbet and Feaugas [22] proposed size dependence of irreversible slip that strongly resembles $\frac{d_{gr}}{d_{gr}^{ref}}$ as ,

$$\gamma_{irr,local,\,pl} = \frac{h_c}{D} \quad \textbf{(5.3)}$$

Where, h_c is the height of extrusion in the slip band and D is the grain size along the slip band direction. They [22] argued that the critical value of local plastic shear strain must be reached for inducing a crack inside a band. Since FIP represent the range of plastic shear strain, therefore, ΔCTD in equation (5.2) is comparable to height of extrusion in equation (5.3) which shows that A should be an inverse coefficient with the dimension of length, which may be the grain size. This highlights the need for a length scale $\frac{d_{gr}}{d_{gr}^{ref}}$ in equation (5.2). By introducing the length scale in equation (5.2) and putting its value in equation (5.1) results,

$$FIP = \mathrm{A}\frac{d_{gr}^{ref}}{d_{gr}}\,(\Delta CTD)^b \quad \textbf{(5.4)}$$

Since the parameter A has the size effect, Castelluccio and McDowell [18] calibrated A=2 for 20 μm grain size. we write equation (5.4) as,

$$FIP = \frac{40}{d_{gr}}\,\Delta CTD \quad \textbf{(5.5)}$$

By putting the *FIP* in equation (5.1),

$$\frac{da}{dN} = \emptyset \left\langle \frac{d_{gr}}{40} FIP_{meso,net}(j,\alpha) - \Delta CTD_{th} \right\rangle \quad \textbf{(5.6)}$$

Here, $FIP_{meso,net}$ correspond to the coupled microstructure and geometric gradient as shown in the previous chapter to predict the transgranular fatigue crack driving force as,

$$FIP_{meso,net}/FIP_o = \frac{1 - P_g \left(a_i/d_{gr}\right)^m}{1 + k_1 \left(a_i/d_{gr}\right) + k_2 \left(a_i/d_{gr}\right)^2} \quad \textbf{(5.7)}$$

Where, P_g & m and k_1 & k_2 are fitting parameters correspond to microstructure and geometric gradients and are given in Figure 4-14 and Figure 4-19 respectively. By putting equation (5.7) in equation (5.6) to estimate the transgranular crack growth rate,

$$\frac{da}{dN} = \emptyset \left\langle \frac{d_{gr}}{40} FIP_o \left(\frac{1 - P_g \left(a_i/d_{gr}\right)^m}{1 + k_1 \left(a_i/d_{gr}\right) + k_2 \left(a_i/d_{gr}\right)^2} \right) - \Delta CTD_{th} \right\rangle \quad \textbf{(5.8)}$$

By rearranging and simplifying the equation (5.8),

$$\frac{da}{dN} = \emptyset \left\langle \frac{\frac{d_{gr}}{40} FIP_o \left(1 - P_g \left(a_i/d_{gr}\right)^m\right) - \Delta CTD_{th} \left(1 + k_1 \left(a_i/d_{gr}\right) + k_2 \left(a_i/d_{gr}\right)^2\right)}{1 + k_1 \left(a_i/d_{gr}\right) + k_2 \left(a_i/d_{gr}\right)^2} \right\rangle \quad \textbf{(5.9)}$$

At a nominal strain range ($\Delta\epsilon$) roughly $> 10^{-3}$, numerical calculations show that the driving force proportional to ΔCTD is significantly larger than ΔCTD_{th} in equation (5.8). Therefore, the higher-order term in equation (5.9) with ΔCTD_{th} can be ignored due to negligibly small value compared to the crack driving force. However, we considered computing the error associated with this assumption as discussed in later Section 5.4. Thus, equation (5.9) may be rewritten as,

$$N_{extend} = \int_{o}^{a_i} \frac{1}{\emptyset} \left\langle \frac{1 + k_1\left({a_i}/{d_{gr}}\right) + k_2\left({a_i}/{d_{gr}}\right)^2}{\frac{d_{gr}}{40} FIP_o \left(1 - P_g \left({a_i}/{d_{gr}}\right)^m\right) - \Delta CTD_{th}} \right\rangle da_i \quad \textbf{(5.10)}$$

Assuming,

$$c_{1=} \ \frac{d_{gr}}{40} FIP_o - \Delta CTD_{th} \qquad \& \qquad c_2 = P_g \frac{d_{gr}}{40} FIP_o$$

By combining the constant terms in equation (5.10), we get,

$$N_{extend} = \int_{o}^{a_i} \frac{1}{\emptyset} \left\langle \frac{1 + k_1\left({a_i}/{d_{gr}}\right) + k_2\left({a_i}/{d_{gr}}\right)^2}{c_1 - c_2\left({a_i}/{d_{gr}}\right)^m} \right\rangle da_i \quad \textbf{(5.11)}$$

Where, N_{extend} is the number of cycles to extend the crack in ith band and a_i is the crack length in ith band. By simplifying,

$$N_{extend} = \int_{o}^{a_i} \frac{1}{\emptyset} \left\langle \underbrace{\frac{1}{c_1 - c_2\left({a_i}/{d_{gr}}\right)^m}}_{\text{Microstructure gradient [23]}} + \underbrace{\frac{k_1\left({a_i}/{d_{gr}}\right)}{c_1 - c_2\left({a_i}/{d_{gr}}\right)^m} + \frac{k_2\left({a_i}/{d_{gr}}\right)^2}{c_1 - c_2\left({a_i}/{d_{gr}}\right)^m}}_{\text{Geometric gradient}} \right\rangle da_i \quad \textbf{(5.12)}$$

The first term in equation (5.12) inside integration corresponds to the microstructural gradient proposed by Castelluccio and McDowell [23]. While the linear and quadratic terms represent the contribution from the geometric gradient. The analytical integration of equation (5.12) with m=2 results in,

$$N_{extend} = \frac{1}{\emptyset} \left\langle \underbrace{\frac{1}{\sqrt{c_1 c_2}} tanh^{-1}\left(a\sqrt{\frac{c_2}{c_1}}\right)}_{\text{Microstructure gradient [23]}} \underbrace{- k_1 \frac{ln(c_1 - a^2 c_2)}{2c_2} + k_2 \frac{\sqrt{c_1} tanh^{-1}\left(a\sqrt{\frac{c_2}{c_1}}\right) - a\sqrt{c_2}}{\sqrt[3]{c_2}}}_{\text{Geometric gradient}} \right\rangle \quad \textbf{(5.13)}$$

In equation (5.13), the normalised crack length (a) correspond to ${a_i}/{d_{gr}}$. Equation (5.13) estimates the fatigue life to extend the crack inside a grain while unifying the contribution from independent gradients. The formation of equation (5.13) conveys a notion that fatigue life corresponds to several gradients can be added independently without re-estimating the existing gradients.

5.3 Model and experiment

Research studies [14] have shown that scribe marks at fuselage joints behave as micron-sized notches fostering the small crack propagation through the thickness. Since these cracks are comparable to grain size, the prognosis of crack growth from scribes involves both geometric and microstructure gradients. Hence, this work considered equation (5.13) that accounts for both geometric and microstructure gradients independently to predict the number of cycles to extend a crack in pure aluminium and compared with experiments [14].

Cini A. [14] studied the effects of scribe marks on fatigue failure of cladded 2024-T351 aluminium alloy. The aluminium alloy was cladded with highly pure aluminium up to a thickness of 80 μm on each side of the sample. Scratches of different sizes were marked at the gauge section perpendicular to the loading direction. Fatigue tests were performed at room temperature under maximum stress of 200 MPa, R=0.1, and a constant frequency of 10 Hz.

This work is primarily focused on crystal plasticity modelling of aluminium single and polycrystals. Therefore, the present work only considered predicting the fatigue behaviour of cladding material [14] i.e. pure aluminium. Following on, we reckoned only smaller notches that nucleate and extend cracks inside the cladding layer. Cini A. [14] mentioned that cladding appears to be more sensitive under 25 μm deep scribes below 50 μm radius. Therefore, we considered 25 μm deep notches with 5 μm, 25 μm, and 50 μm radius to compare the model with experiments.

Cini A. [14] showed that the substrate was fully elastic under the applied nominal stress of 200 MPa, which is lower than its yield stress i.e. 360 MPa. He assumed

that the gauge section withstands the nominal equivalent stress, which means that clad has also the same nominal equivalent stress. However, under the same applied loading, the stresses in cladding and substrate should be different due to the material mismatch. But the elastic mismatch between substrate and cladding is minimum because they are both inherently aluminium. This work considered the nominal elastic strain as total strain and calculated using Hook's law,

$$\epsilon = \frac{\sigma}{E} \qquad \textbf{(5.14)}$$

In experiments, the cross section is dominated by the substrate. Therefore, when substrate is strained, cladding should undergo the same nominal strain. Following the maximum nominal stress of 200 MPa and Young's modulus of 60.5 -70.5 GPa [14], equation (5.14) estimates the nominal strain ($\Delta\epsilon$) to be ~2.8×10^{-3}. Following on, we considered this nominal strain as a reference to compute the model results and compared with experiments [14].

The estimation of N_{extend} in equation (5.13) requires computing FIP_o after 25 loading steps with both microstructure and geometric gradients using crystal plasticity simulation. The choice of 25 loading steps corresponds to the minimum number of steps required to achieve stress-strain convergence (Figure 4-3). The notches induce large plastic deformation close to the notch tip based on their stress concentration factor (K_t). Thereby, it is computationally challenging to run the crystal plasticity analysis with coupled microstructure and notch geometry at $\Delta\epsilon = \sim 2.8 \times 10^{-3}$, and mesh size of >35K.

Cini and Irving [9] mentioned that crack growth from scribes was primarily affected by material microstructure. Furthermore, they found that scribe geometry only influenced stage-I crack growth. The notch geometry escalates the plastic deformation at the notch root that can trigger the nucleation phase of fatigue damage. This work proposes to estimate the maximum γ_{pl}^{max} at the notch tip for each notch case under consideration using elastoplastic simulations and apply that as a nominal strain ($\Delta\epsilon$) on a simple beam without a notch. Table 5-1 shows the γ_{pl}^{max} at the notch root for each notch case computed at $\Delta\epsilon$ of $\sim 2.8 \times 10^{-3}$ using the model shown in Figure 4-17. Following on, the nominal strain ($\Delta\epsilon$)

corresponds to these γ_{pl}^{max} are applied on a simple beam to estimate the fatigue life to compare with experiments [14].

Table 5-1 γ_{pl}^{max} at the notch root for notches with different radii and same depth i.e. 25 μm.

Notch radius	5 μm	25 μm	50 μm
γ_{pl}^{max}	1.4×10^{-1}	1.44×10^{-1}	8.6×10^{-2}
$\Delta\epsilon$	7.02×10^{-2}	7.2×10^{-2}	4.3×10^{-2}

A simple beam with elongated grains is created using Abaqus v2017 [24] and Dream3D [25] software. Cini and Irving [9] mentioned that an elongated grain structure appears in clad Al2024 specimens and cladding has an equiaxed grains that extend across the entire average cladding thickness of 70-80 μm. This work considered similar grain dimensions as reported by Cini and Irving [9], i.e. 150-200 μm along rolling direction, 80-100 μm along transverse and 20 μm along thickness direction. The geometry of a simple beam and representative microstructure is shown in Figure 5-1. The detail of finite element mesh and microstructural features is given in Table 5-2.

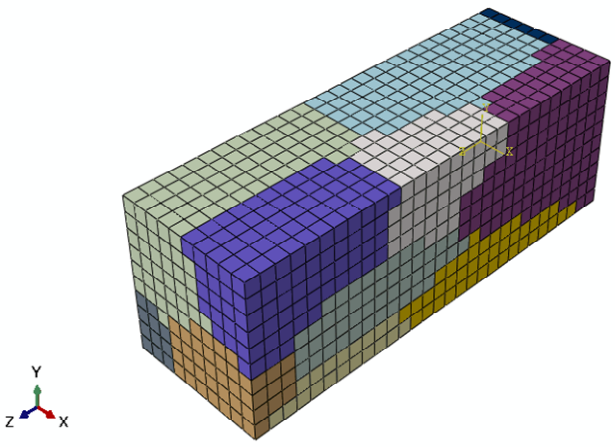

Figure 5-1 Finite element mesh of a simple beam without notch with elongated grains.

Table 5-2 The details of finite element model and representative microstructure.

Number of grains	Number of elements	Size of elements (μm^3)	Size of the specimen (μm)	Average grain size (μm)
~16	3000	$10 \times 10 \times 10$	$100 \times 100 \times 300$	~70- 90

Cini A. [14] measured the fatigue crack nucleation life up to $50\ \mu m$ for notches with different root radii. He mentioned that the nucleation life at the notch root was controlled by the notch geometry. In modelling, we assume that the nucleation phase is instantaneous due to the large plastic gradient (Figure 4.18). Following on, we computed the minimum number of cycles (N_{extend}) to extend a crack up to $50\ \mu m$ inside each band in each grain using equation (5.13).

This work implemented the finite element model (Figure 5-1) with UMAT subroutine in Abaqus v.2017 [24] to compute the FIP_o after 25 loading steps at the nominal strains shown in Table 5-1. However, it was computationally challenging to compute the FIP_o for large strains. Alternatively, we run the simulations (25 computational steps) at different strain amplitudes i.e. between $10^{-3} - \sim 10^{-2}$ and noticed that FIP_o (equation (5.13) can be up-scaled as,

$$FIP_o|_{\Delta\epsilon} = \frac{\Delta\epsilon}{\Delta\epsilon_{ref}} FIP_{o,ref} \qquad \textbf{(5.15)}$$

Where, $FIP_{o,ref}$ is the reference FIP and correspond to FIP at 1×10^{-3} strain amplitude. Figure 5-2 demonstrates that crystal plasticity prediction agree with the upscaling of FIP_o across all grains at higher strain amplitude using lower strain data following equation (5.15). Lucarini and Segurado [26] have also proposed an upscaling considering extensive microstructure simulations to predict fatigue life. The findings [26] support equation (5.15) independently. Following on, this work employed equation (5.15) to compute the FIP_o at different strain amplitudes mentioned in Table 5-1.

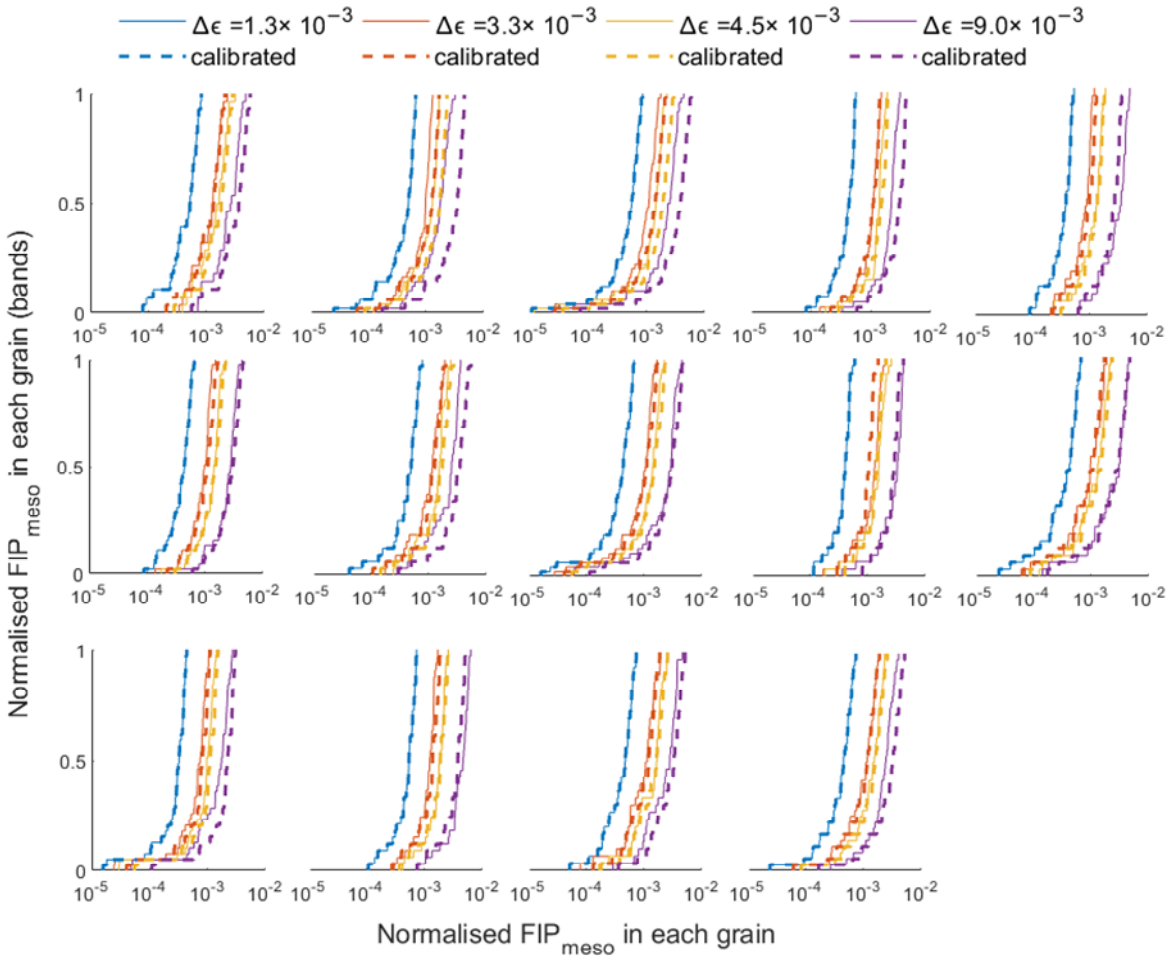

Figure 5-2 Comparison between the calibrated and actual normalised FIP_{meso} across all grains with one microstructure realisation.

Figure 5-3 explains the steps required to estimate N_{extend} using equation (5.13). Figure 5-4 presents the comparison of N_{extend} upto 50 μm between model and experiment [14]. The minimum N_{extend} to extend a crack upto 50 μm from all grains is plotted using boxplot for each notch case. In the previous chapter, this work estimated the geometric gradient at different angles (Figure 4.19), which shows that the $\Delta\gamma_{pl}^{max}$ gradient correspond to $\sim 10^o$ and $\sim 50^o$ represent lower and upper bounds respectively. Thereby, weestimated the N_{extend} upto 50 μm correspond to lower ($\sim 10^o$) and upper bound ($\sim 50^o$) of k_1 and k_2 to capture variability. The N_{extend} corresponds to upper bound geometric gradient predicts the minimum life for different notches, which is in good agreement with experiments.

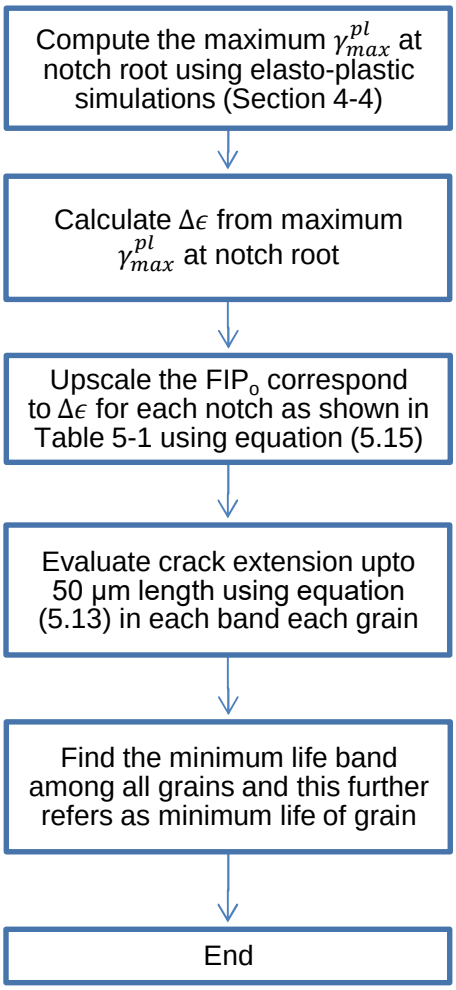

Figure 5-3 Steps to estimate the minimum N_{extend} in each band each grain.

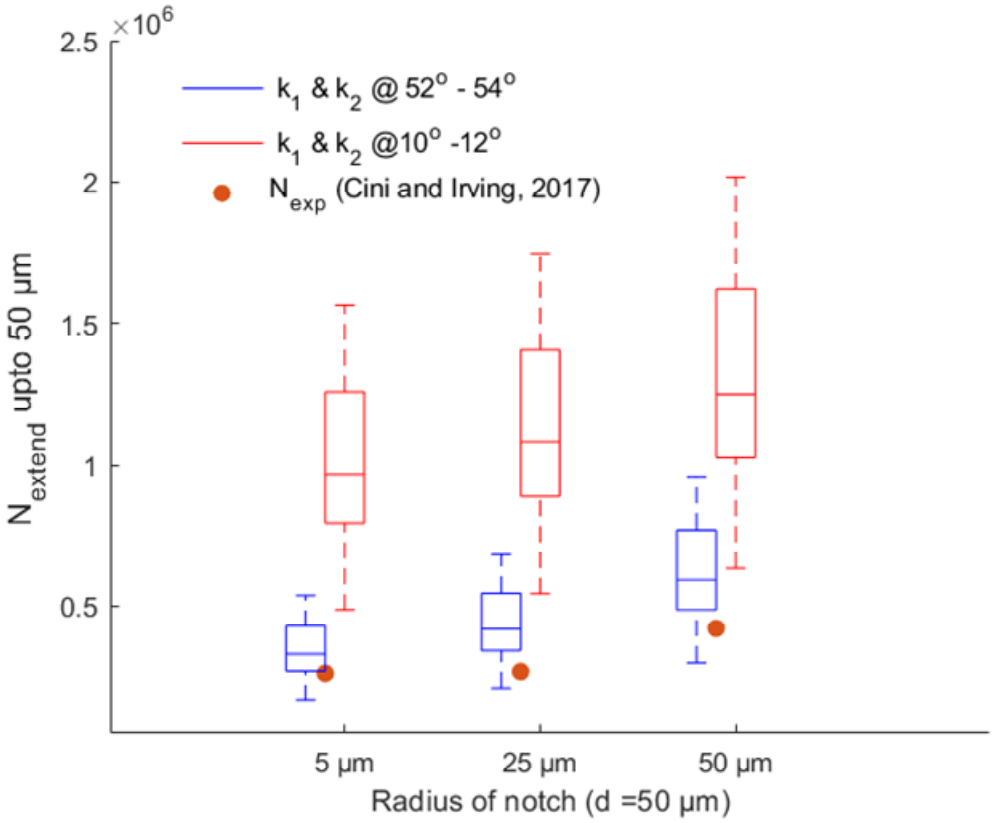

Figure 5-4 Comparison of number of cycles to extend the crack upto 50 μm between model and experiment [14]**.**

Figure 5-5 presents the crack growth rate as a function of crack length for different notches as predicted by equation (5.8). In Figure 5-5, color differentiate the notches with different root radii. The range of boxplot corresponds to the maximum crack growth rate in all grains. Overall, the crack growth rate is decreasing as crack extends inside a grain irrespective of notch size, which agrees with the experiment [27]. However, for the same notch depth, the crack growth rate is slightly higher for the smaller radius notch corresponds to each crack length. The direct comparison of Figure 5-5 results with the experiment is difficult due to the unavailability of data. However, Cini [14] measured the number of cycles to extend the crack upto 50 μm as shown in Figure 5-4. If we estimate the crack growth using this data, its results 1.89×10^{-4} $\mu m/_{cycle}$ for notch radius 5 μm, which agrees with the results in Figure 5-5.

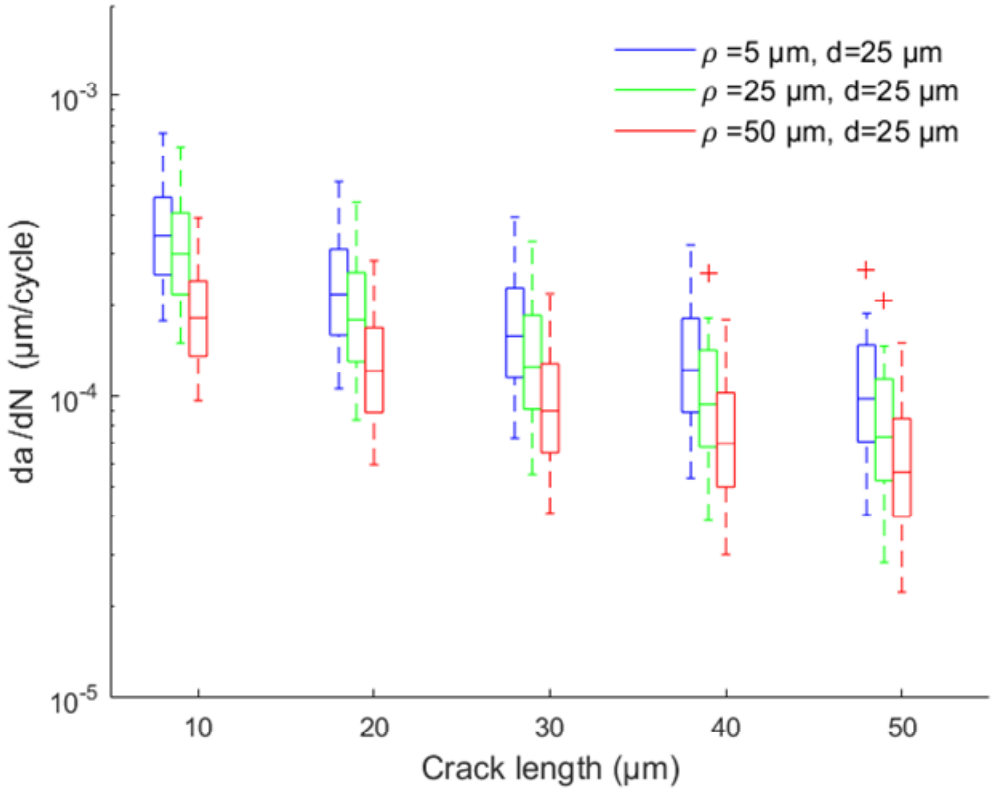

Figure 5-5 Comparison of crack growth rate for different notches upto a crack length of 50 μm.

Cini and Irving [9] found that the notches with depth 25 μm nucleated multiple cracks and the number of cracks varies with the radius of notch. They measured the number of cracks after specimen failure, which corresponds to different number of cycles. In simulations, this work considered estimating the number of cracks as the number of grains cracked corresponding experimental number of cycles to failure for each notch case [9]. Since notches with root radii 5 μm and 25 μm have about the same life [9], we employed one threshold for both 5 and 25 μm radii notches represented by N_1 in Figure 5-6. On the other hand, the threshold for the notch with 50 μm root radii is denoted by N_2.

Figure 5-6 shows the cumulative distribution of cracked grains as a function of number of cycle. The distribution in Figure 5-6 shows the number of grains fully

cracked corresponding number of cycles on x-axis. Only the minimum N_{extend} to extend a 50 μm crack from all grains is considered in Figure 5-6. Table 5-3 compares the experiment and model results for the effect of scribe radii on the nucleation of multiple cracks. The ratio of cracks between 5 μm and 25 μm notches corresponds to N_1 (threshold) results 1.41 following Figure 5-6, which is 1.25 according to experiments [9]. Hence, model results agree with experiments within 11% error. The ratio of cracks between 5 μm and 25 μm notches still agrees experiments [9] corresponding threshold N_2. However, the comparison of 50 μm notch with smaller radii notches is not appropriate because they were calculated at a different number of cycles. Overall, the model predicts the trends observed in the experiment i.e. number of cracks decreases with the increase in notch radii as found by the experiments [9].

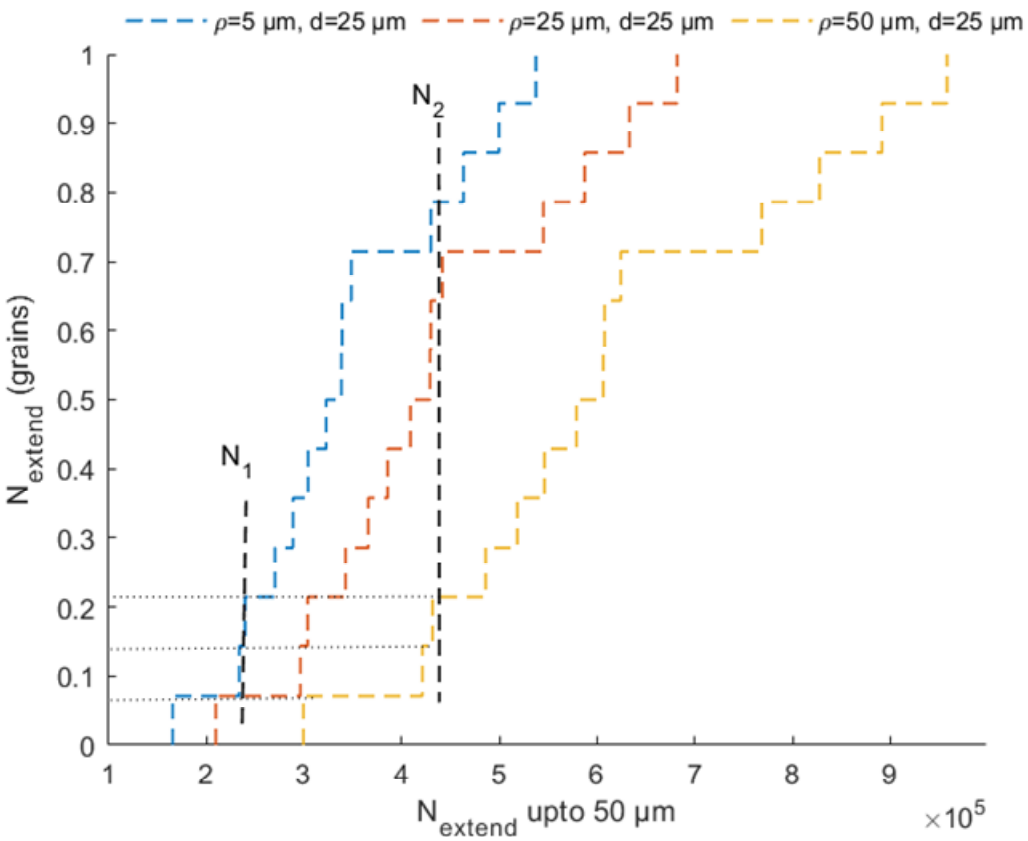

Figure 5-6 Effect of notch radius on the number of cracks. The vertical lines (N_1 and N_2) represent threshold life following the experiment [9].

Table 5-3 Comparison between model and experiment: Effect of scribe root radii on the number of crack nucleation.

Radius (μm)	$N_1 = 2.4 \times 10^5$		$N_2 = 4.4 \times 10^5$	
	Number of cracks (experiment) [9]	Number of grains failed (Model)	Number of cracks (experiment) [9]	Number of grains failed (Model)
5	10	1.92	-	12.8
25	8	1.36	-	10.8
50	-	0	5	3.36

This work also compared the density of cracks along the notch with experiments [9]. We computed the density of cracks by dividing the number of cracks by the length of the notch. Table 5-4 shows that the model overestimated the density of cracks compared to the experiment. The density of cracks reported in the experiment [9] corresponds to the scribe of 80 mm length, which is 267 times larger than the model dimension i.e. 300 μm. This highlights that the model lacks the microstructure statistics (number of grains) along the notch.

For comparing the density of cracks over a length, the model should have equivalent and comparable dimensions with the experiments. For notch with 5 μm root radii, Cini and Irving [9] found 1 crack per 8 mm. Alternatively, a model with 8 mm dimension and random microstructural features can be employed to run 10 simulations to find the equivalent ratio of the density of cracks. Future work will consider recalibrating the model with a larger number of simulations to study the effect of scribe root on the density of crack.

Table 5-4 Comparison between model and experiment: Effect of scribe root radii on the density of cracks.

Radius (μm)	Density of cracks		N_{exp} at which density measured
	Experiment [9]	Model	
5	0.125	6.4	2.4×10^5
25	0.1	4.5	2.4×10^5
50	0.0625	11.2	4.4×10^5

5.4 Discussion

This work is motivated by predicting the transgranular fatigue life in pure aluminium using the independently coupled gradients proposed in the previous chapter. Here, we relate the crack driving force with MS fatigue crack growth rate following Castelluccio and McDowell [23]. However, this work accounts for the explicit effect of microstructure and geometric gradients on MS transgranular fatigue life. The effect of notch root radii on transgranular fatigue life is estimated, which showed a good agreement with experiments [14].

Fatigue prognosis of geometric gradients using crystal plasticity simulations is computationally demanding in low cycle fatigue (LCF) regime. This work proposed an independent estimation of the geometric gradient, which significantly reduces the computational burden in several aspects. One aspect was highlighted in the previous chapter where we coupled geometric and microstructure gradient independently to reconstruct the equivalent FIP_{meso} as shown in equation (5.7). This mitigates the need for running damage with crystal plasticity simulations (cracking element one by one) with both microstructure and geometric gradient. However, equation (5.7) still require computing FIP_o from crystal plasticity simulation with both gradients. The estimation of FIP_o corresponding experimental loading condition ($\Delta\epsilon = 2.8 \times 10^{-3}$) was challenging with available computational resources due to the large mesh size. Alternatively, this work proposed to compute γ_{max}^{pl} at the notch root with nominal strain of

2.8×10^{-3} using homogenised geometric gradient and use that γ_{max}^{pl} to compute FIP_o with smooth specimen without notch. Hence, this approach enables the quantification of equivalent FIP_o that represent both geometric and microstructure gradients.

Following on, this work further explored that estimation of FIP_o even with the smooth specimen is highly computationally demanding above 1% strain amplitude. Alternatively, we proposed an upscaling strategy to quantify FIP_o above $\Delta\epsilon$ =1% using lower $\Delta\epsilon$ data. Finally, this work explored several challenges and proposed a less computationally intensive solution to estimate the fatigue life while accounting for multiple gradients above 1% strain amplitude. However, future efforts require consideration to estimate the uncertainty related to upscaling in equation (5.15). An explicit analysis with large statistics of microstructure attributes is required to further explore the upscaling relation as it is useful in reducing the computational burden.

Another aspect that requires consideration is the uncertainty quantification related to higher-order terms of the geometric gradient with ΔCTD_{th} in equation (5.9), which was ignored to make analytical integration easier. Here, we estimated the uncertainty underlying this assumption by evaluating the crack growth rate with or without a higher-order term corresponding nominal strains mentioned in Table 5-1. Figure 5-7 shows that higher-order terms with ΔCTD_{th} did not contribute much towards the results, therefore ignoring these terms to make analytical integration simpler can be justified.

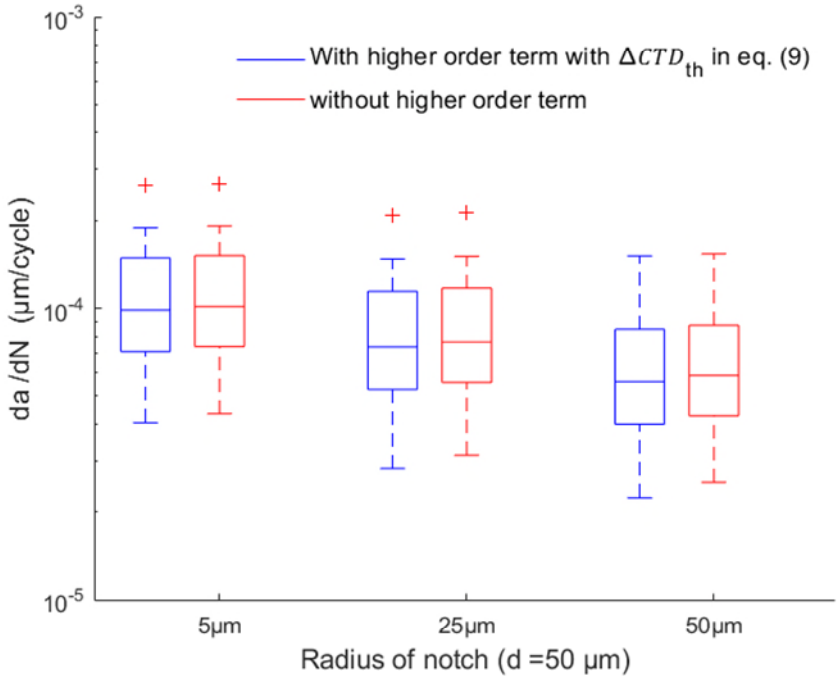

Figure 5-7 Estimation of uncertainty with and without higher-order term in equation (5.9).

Cini and Irving [9] showed that shallow notches nucleate multiple cracks at the surface. For the same notch depth i.e. 25µm, the number of cracks decreases as the notch root radii increases [9]. Here, this work computed the number of cracks nucleated by shallow notches with different root radii and compared with experiments [9]. We estimated the number of grains cracked corresponding to the life of failure given in the experiment for each notch case under consideration [9]. The notch with smaller root radii has a larger plastic gradient at the notch root (Figure 4.19), thereby, it nucleates higher number of cracks as shown in Figure 5-6. The present analysis shows that the nucleation of multiple cracks is a function of the plastic gradient at the notch root.

This work correlated the independently coupled geometric and microstructure gradients with MS crack growth rate to predict the fatigue life from shallow notches in pure aluminium. The results showed a good agreement with experiments and manifest the predictability of the model in assessing fatigue damage. Future efforts will consider estimating the effect of deeper notches on

fatigue crack nucleation in 2024- T351 aluminium alloy using the current approach. Future efforts will also attempt studying the crack extension upto few grains.

5.5 Conclusions

This work proposed a less computationally intensive solution to compute the effect of geometric and microstructure gradient on transgranular fatigue life in LCF regime. The model showed good predictability and agreement with the experiments. However, some areas require consideration to improve model prediction. For instance, future efforts should consider predicting the density of cracks with large microstructural statistics to validate the trend with experiments. Overall, the current approach presented a different less computationally intensive solution to study the effect of multiple gradients independently on fatigue crack formation in the LCF regime. Future efforts will also consider estimating the multiple gradients on fatigue failure using the current approach.

References

1. Smith R.A. and Miller K.J. Fatigue cracks at notches. International Journal of Mechanical Sciences. 1977; 19(1): 11–22. http://dx.doi.org/10.1016/0020-7403(77)90011-X

2. Du Quesnay D.L., Yu M.T., Topper T.H. and Quesnay D. An analysis of notch-size effects at the fatigue limit. Journal of Testing and Evaluation; 1988. 16(4): 375-385. https://doi.org/10.1520/JTE11081J

3. Liao D., Zhu S.P., Correia J.A.F.O., De Jesus A.M.P. and Calçada R. Computational framework for multiaxial fatigue life prediction of compressor discs considering notch effects. Engineering Fracture Mechanics. Elsevier Ltd; 15 October 2018; 202: 423–435. http://dx.doi.org/10.1016/j.engfracmech.2018.08.009

4. Tao Z. and Shang D. A new approach to the fatigue life prediction for notched components under multiaxial cyclic loading. DES*tech* Transactions on Engineering and Technology Research. 2017: 19–23. http://dx.doi.org/10.12783/dtetr/ameme2017/16189

5. Neuber, H. Theory of notch stresses: Principle for exact stress calculation ed. Ann Arbor, MI: Edwards, 1946.

6. Cini A. and Irving PE. Transformation of defects into fatigue cracks; the role of K_t and defect scale on fatigue life of non-pristine components. Procedia Engineering. 2010; 2(1): 667–677. http://dx.doi.org/10.1016/j.proeng.2010.03.072

7. Paint and sealant removal process. Airworthiness Notice No. B071, 3/11/2004

8. FAA airworthiness directives no. FAA-2005-20918, 31/3/2006

9. Cini A. and Irving P.E. Development of fatigue cracks from mechanically machined scratches on 2024-t351 aluminium alloy—part I: experimentation and fractographic analysis. Fatigue and Fracture of

Engineering Materials and Structures. 2017; 40(5): 776–789. http://dx.doi.org/10.1111/ffe.12544

10. P. J. E. Forsyth. A two stage process of fatigue crack growth royal aircratt establishment. Proceedings of the Crack Propagation Symposium. 1961. pp. 76–94.

11. Zhang K-S., Ju J.W., Li Z., Bai Y-L. and Brocks W. Micromechanics based fatigue life prediction of a polycrystalline metal applying crystal plasticity. Mechanics of Materials. 2015; 85: 16–37. http://dx.doi.org/10.1016/j.mechmat.2015.01.020

12. Yuan H., Zhang W., Castelluccio G.M., Kim J. and Liu Y. Microstructure-sensitive estimation of small fatigue crack growth in bridge steel welds. International Journal of Fatigue. Elsevier; 2018; 112(December 2017): 183–197. http://dx.doi.org/10.1016/j.ijfatigue.2018.03.015

13. Owolabi G., Egboiyi B., Shi L. and Whitworth H. Microstructure-dependent fatigue damage process zone and notch sensitivity index. International Journal of Fracture. 2011; 170(2): 159–173. http://dx.doi.org/10.1007/s10704-011-9620-z

14. Cini A. Scribe marks at fuselage joints:Initiation and propagation of fatigue cracks from mechanical defects in aluminium alloys. PhD thesis. 2012 Cranfield University.UK.

15. McDowell D.L., Gall K., Horstemeyer M.F. and Fan J. Microstructure-based fatigue modelling of cast A356-T6 alloy. Engineering Fracture Mechanics. 2003; 70(1): 49–80. http://dx.doi.org/10.1016/S0013-7944(02)00021-8

16. Castelluccio G.M. and McDowell D.L. Mesoscale modelling of microstructurally small fatigue cracks in metallic polycrystals. Materials Science and Engineering A. Elsevier; 2014; 598: 34–55. http://dx.doi.org/10.1016/j.msea.2014.01.015

17. McDowell D.L. Simulation-based strategies for microstructure-sensitive fatigue modelling. Materials Science and Engineering A. 2007; 468–470:

4–14. http://dx.doi.org/10.1016/j.msea.2006.08.129

18. Castelluccio G.M. and McDowell D.L. Assessment of small fatigue crack growth driving forces in single crystals with and without slip bands. International Journal of Fracture. 2012; 176(1): 49–64. http://dx.doi.org/10.1007/s10704-012-9726-y

19. Lansey J. Matlab *logfit* subroutine. www.mathworks.com/matlabcentral/. 2010.

20. Hennessey C.D. Modelling microstructurally small crack growth in Al 7075-T6. Master's thesis. Georgia Institute of Technology; Atlanta, GA, USA. 2015.

21. Yeratapally S.R., Leser P.E., Hochhalter J.D., Leser W.P. and Ruggles T.J. A digital twin feasibility study (part I): non-deterministic predictions of fatigue life in aluminium alloy 7075-T651 using a microstructure-based multi-scale model. Engineering Fracture Mechanics. Elsevier Ltd; 2020; 228(Part I): 106888. http://dx.doi.org/10.1016/j.engfracmech.2020.106888

22. Risbet M. and Feaugas X. Some comments about fatigue crack initiation in relation to cyclic slip irreversibility. Engineering Fracture Mechanics. 2008. pp. 3511–3519. http://dx.doi.org/10.1016/j.engfracmech.2007.04.014

23. Castelluccio G.M. and McDowell D.L. A mesoscale approach for growth of 3D microstructurally small fatigue cracks in polycrystals. International Journal of Damage Mechanics. 2014; 23(6): 791–818. http://dx.doi.org/10.1177/1056789513513916

24. ABAQUS. FEM software v2017. Providence, RI, USA: Simulia Inc.; 2017.

25. Groeber M.A. and Jackson M.A. DREAM.3D: A digital representation environment for the analysis of microstructure in 3D. Integrating Materials and Manufacturing Innovation. 2014; 3(1): 56–72. http://dx.doi.org/10.1186/2193-9772-3-5

26. Lucarini S. and Segurado J. An upscaling approach for micromechanics based fatigue: from RVEs to specimens and component life prediction. International Journal of Fracture. Springer Netherlands; 2020; 223(1–2): 93–108. http://dx.doi.org/10.1007/s10704-019-00406-5

27. Tokaji K. and Ogawa T. The growth behaviour of microstructurally small fatigue cracks in metals. In: Miller KJ, Rios E.R de los (eds.) Mechanical Engineering Publications. London: Mechanical Engineering Publications; 1992. pp. 85–99.

6 Implications of Overall Work

This thesis focuses on the cyclic deformation of aluminium while comparing its response with other FCC metals. We demonstrate a way to study the atomistic scale effect (Chapter 2) and mesoscale effect (Chapter 3) independently. A modified crystal plasticity framework is used to predict the microstructure-sensitive transgranular crack propagation from shallow scribes. Coherently, the understanding from the first chapters is essential for the later ones due to the local microstructure sensitivity of small cracks.

6.1 Cyclic response of aluminium

This work hypothesised that aluminium evolves similar dislocation substructures as other FCC metals at the same homologous temperatures under cyclic loading. Following on, mesoscale substructures can be used as an invariant to predict the cyclic response of aluminium. The findings presented in chapters three and four support this hypothesis.

6.1.1 The role of activation energy

The key finding of Chapter 2 (Figure 2-7) revealed that the activation energy (F_o) in FCC metals and alloys is inversely proportional to its stacking fault energy (SFE). This implies that aluminium as a higher SFE metal has lower activation energy as compared to other FCC metals. This justifies the low stresses in aluminium during the early stages of plastic deformation as compared to other FCC metals.

The activation energy parameters are found to be sensitive to solute concentrations (Section 2-4.1). Both activation energy and thermal stress increase with increasing solute concentration. Since the solute atom hinders the motion of dislocations and increases the height of the energy barrier, it increases the stresses in the material. The dependence of F_o and s_o^t on solute concentrations proposed a simple way to study the cyclic response of alloys using

F_o and s_o^t with simple microstructure instead of explicitly modelling the real microstructure.

6.1.2 Mesoscale dislocation substructures

Recent research [1] showed that the evolution of mesoscale substructures in low-medium stacking energy FCC metals under fully reversed cyclic loading represents physics-based hardening mechanisms. Some studies [2–5] showed that aluminium also evolved similar dislocation substructures as other FCC metals, however at different temperatures. This work highlighted that the number of cycles (*N)* has a significant effect on mesoscale substructure in all FCC metals above roughly 0.3 $\frac{T}{T_m}$. This work modified the crystal plasticity framework [1] by incorporating the effect of N, temperature, strain amplitude and crystal orientation on mesoscale substructure using existing literature data related to cyclic deformation of FCC metals.

The results of chapter 3 show the effect of different loading on the cyclic response of aluminium single crystal, which reinforces the hypothesis that aluminium evolves similar substructures and has similar deformation mechanisms as other FCC metals at similar homologous temperatures. Besides, this work also validated the model at mesoscale i.e. estimating the wall spacing against the shear stress level (similitude relation). The similitude relation has been proposed by Sauzay and Kubin [6] for Ni, Cu, and Ag. Interestingly, few studies [4,5] also proposed this relation for aluminium with experiments. This work used these experiments [4,5] to validate the similitude relation in aluminium (Figure 3- 14). Moreover, the findings [4,5] also support building the current hypothesis.

6.1.2.1 Effect of activation energy on mesoscale substructure

As discussed in the previous section 6.1.1, the solute concentrations increase F_o and s_o^t. The increase in F_o makes dislocation glide difficult and reduces secondary slip. Fujii et al. [7] studied the cyclic response of Al-0.7%Mg single crystal oriented along a single slip direction at 298K. They [7] showed that the cyclic stress-strain response of Al-0.7%Mg evolves a plateau region corresponding to PSBs similar

to Cu, Ni, and Ag single crystal at 298K. The findings of Fujii et al. [7] independently manifest the effect of solute concentration on the cyclic response of metals. Besides, the findings [7] also support the current hypothesis and implications of chapter 2 and chapter 3.

The evolution of saturated dislocation substructures at the mesoscale is associated with specific dislocation mechanisms under cyclic loading. For example, cross slip dominates cell structure and Hirth locks facilitate labyrinth structure, etc. [8,9]. The underlying mechanism that controls hardening in mesoscale substructure is the mean free path of mobile dislocations (screw dislocations) [1]. For instance, during the early stages of cyclic deformation, dislocations can travel up to 5-10 micron in veins and PSBs. However, with increasing plastic strain, the mean free path is significantly reduced in cells that causes hardening [1]. The mean free path of dislocation is a more generalised aspect than saturated substructures and its correlation with other mesoscale characteristic lengths such as wall volume fraction can help in understanding intermediate mesoscale substructure.

Literature [10] showed that deformation mechanisms at the atomistic scale are a function of the material. For instance, Cu has a different yield point with different solute concentrations under similar loading conditions, etc. [10]. However, mechanisms at the mesoscale scale related to dislocation substructures are less material sensitive [11]. This demonstrates the need for estimation of Fo & s_o and supports the hypothesis.

Generally, several reasons support the use of mesoscale dislocation substructures to define the hardening in metals as compared to dislocation-density based models such as,

- The substructures can be estimated with relatively low uncertainty using TEM data as compared to dislocation density. For instance, the volume fraction of dislocation walls (static dislocations) can be quantified using TEM data with relatively low uncertainty (Appendix B.2) as compared to the dislocation density.

- Similar mesoscale substructures are evident in many materials, which provides a path to bridge the difference between different materials by understanding the physics driving local mechanisms to reach a similar conclusion (mesoscale substructure).

6.2 Effect of shallow scribes on MSC growth

This work considered implementing crystal plasticity simulations to study the explicit effect of microstructure on the variation of FIP as a function of crack length in pure aluminium to test the hypothesis. Since aluminium has relatively high stacking fault energy and activates secondary slip earlier (Chapter 3), therefore this work proposed a strategy to estimate a multislip FIP. The decaying trend of multislip FIP as a function of crack length in pure aluminium is found to be similar to other FCC alloys [12,13]. This shows that the empirical relation for microstructure gradient [12] is also valid for aluminium in addition to bridge steel [14], and Ni-based superalloy [12].

This work proposed a less computationally intensive and homogenised solution to quantify notch sensitivity using elastoplastic simulations. By coupling the microstructure gradient from a crystal plasticity simulation with a geometric gradient from elastoplastic simulation, we reconstructed the equivalent FIP as computed by crystal plasticity simulation at a lower computational cost. Hence, this work proposed an engineering solution to estimate the driving force from multiple gradients to study fatigue crack formation.

Since the microstructure gradient is found to be similar in several microstructural realisations, changing geometric gradient would not require rerunning the computationally intensive crystal plasticity analysis. Instead, the geometric gradient can be quantified with elastoplastic simulations independently and coupled with the existing microstructure gradient to study fatigue crack formation.

Finally, we employed the coupled gradients to predict transgranular fatigue life in pure aluminium and compared it with experiments. Overall, this work provides an engineering tool to estimate the effect of multiple gradients on small fatigue crack

growth using less computationally intensive models. The proposed approach enables saving computational time from days to hours.

References

1. Castelluccio G.M. and McDowell D.L. Mesoscale cyclic crystal plasticity with dislocation substructures. International Journal of Plasticity. Elsevier Ltd; 2017; 98: 1–26. http://dx.doi.org/10.1016/j.ijplas.2017.06.002

2. Wang J., Zhu Z.G., Fang Q.F. and Liu G.D. Influence of the crystallographic orientation on the behaviour of fatigue in Al single crystals. Materials Research Bulletin. Elsevier Science Ltd; 1 February 1999; 34(3): 407–413. http://dx.doi.org/10.1016/S0025-5408(99)00024-0

3. Dhers J. and Driver J. The cyclic response and microstructures of aluminium single crystal. In: Lukáš P, Polak J, editors. Basic mechanisms in fatigue of metals. Materials science monographs, vol. 46. Amsterdam: Elsevier; 1988. p. 33

4. Nakanishi Y., Tanaka H., Fujii T., Onaka S. and Kato M. Low-temperature fatigue behaviour and development of dislocation structure in aluminium single crystals with single-slip orientation. Philosophical Magazine. 2013; 93(21): 2759–2768. http://dx.doi.org/10.1080/14786435.2013.786193

5. Videm M. and Ryum N. Cyclic deformation of [001] aluminium single crystals. Materials Science and Engineering A. November 1996; 219(1–2): 1–10. http://dx.doi.org/10.1016/S0921-5093(96)10261-6

6. Sauzay M. and Kubin LP. Scaling laws for dislocation microstructures in monotonic and cyclic deformation of fcc metals. Progress in Materials Science. Elsevier Ltd; 2011; 56(6): 725–784. http://dx.doi.org/10.1016/j.pmatsci.2011.01.006

7. Fujii T., Uju S., Watanabe C., Onaka S. and Kato M. Cyclic deformation of Al-Mg single crystals with a single slip orientation. Materials Science Forum. 2007; 561–565(PART 3): 2213–2216. http://dx.doi.org/10.4028/0-87849-462-6.2213

8. Tabata T., Fujita H., Hiraoka M.A. and Onishi K. Dislocation behaviour and the formation of persistent slip bands in fatigued copper single crystals observed by high-voltage electron microscopy. Philosophical Magazine A: Physics of Condensed Matter, Structure, Defects and Mechanical Properties. 1983; 47(6): 841–857. http://dx.doi.org/10.1080/01418618308243124

9. Kuhlmann-Wilsdorf D. and Laird C. Dislocation behaviour in fatigue. Materials Science and Engineering. February 1977; 27(2): 137–156. http://dx.doi.org/10.1016/0025-5416(77)90166-5

10. Wille T.H., Gieseke W. and Schwink C.H. Quantitative analysis of solution hardening in selected copper alloys. Acta Metallurgica. 1987; 35(11): 2679–2693. http://dx.doi.org/10.1016/0001-6160(87)90267-7

11. Li P., Li S.X., Wang Z.G. and Zhang Z.F. Fundamental factors on formation mechanism of dislocation arrangements in cyclically deformed FCC single crystals. Progress in Materials Science. March 2011; 56(3): 328–377. http://dx.doi.org/10.1016/j.pmatsci.2010.12.001

12. Castelluccio G.M. and McDowell D.L. A mesoscale approach for growth of 3D microstructurally small fatigue cracks in polycrystals. International Journal of Damage Mechanics. 2014; 23(6): 791–818. http://dx.doi.org/10.1177/1056789513513916

13. Tokaji K. and Ogawa T. The growth behaviour of microstructurally small fatigue cracks in metals. In: Miller KJ, Rios E.R de los (eds.) Mechanical Engineering Publications. London: Mechanical Engineering Publications; 1992. pp. 85–99.

14. Yuan H., Zhang W., Castelluccio G.M., Kim J. and Liu Y. Microstructure-sensitive estimation of small fatigue crack growth in bridge steel welds. International Journal of Fatigue. Elsevier; 2018; 112(December 2017): 183–197. http://dx.doi.org/10.1016/j.ijfatigue.2018.03.015

7 Conclusion and Future Work

The major conclusion of this work is that it provides understanding about the,

- Cyclic response of aluminium single and polycrystals under different temperatures, strain amplitude, and number of cycles.
- Effect of geometric gradient on microstructure-sensitive transgranular fatigue crack growth in pure aluminium.

7.1 Contribution to knowledge

7.1.1 Regarding the parametrization of glide

- Activation energy is estimated using three different formulations normally employed in constitutive models. The Kocks approach yielded the best results as compared to Langer and Taylor's approach when fitting a nonlinear dependence of yield stress on temperature.
- For Kocks formulation, this work estimated the glide activation energy ($F_o \& s_o^t$) for several metals and alloys while considering other model parameters and their uncertainties independently. The results related to different metals and alloys showed that both activation energy (F_o) and thermal stress (s_o^t) are sensitive to solute concentrations.
- The effect of profile parameters (*p* and *q*) is quantified on $F_o \; and \; s_o^t$. The results show that values of p and q between 2/3 to 1 and 1 to 3/2, respectively, have a marginal effect on the activation energy parameters.

7.1.2 Regarding aluminium mesoscopic response

- This work highlighted that the number of cycles has a significant effect on the mesoscale substructures and correspondingly macroscopic stress response for all FCC metals at relatively higher homologous temperatures ($\frac{T}{T_m} > 0.3$).

- The comparison of aluminium with low-medium stacking fault energy FCC metals under cyclic loading is not appropriate at 298K. Aluminium has a higher homologous temperature at 298K that makes him sensitive to the number of cycles in addition to other loading conditions. However, aluminium evolves similar substructure as other FCC metals but at different temperatures.

7.1.3 Regarding the microstructure-sensitive fatigue crack formation

- The comparison of energy and Fatemi-Socie fatigue indicator parameter (FIPs) over different domains shows that they have the same potential to predict the small fatigue cracks. However, the choice of domain is important than the choice of FIPs. The averaging along slip bands represents a better estimation of fatigue damage than the local or larger averaging domains.
- The decay of FIP as a function of crack length under the explicit of microstructure in aluminium is found to be similar in Ni-based superalloy. This revealed that the proposed relation for microstructure gradient is still valid for different materials as it has been implemented for bridge steel, Ni-based superalloy, and aluminium.
- The independent coupling of microstructure (crystal plasticity simulation) and geometric gradients (elastoplastic simulations) reconstructed the similar FIPs as estimated by the crystal plasticity simulations (both gradients).
- The effect of shallow scribes on transgranular fatigue life and nucleation of multiple fatigue cracks was estimated using independently coupled microstructure and geometric gradient.

7.2 Potential impact of findings

- This work proposed an empirical relationship between the glide activation energy and stacking fault energy for several FCC metals and alloys. This enables the estimation of glide activation energy for any FCC material within a range independently. Moreover, the glide activation energy is an

important parameter of a crystal plasticity model and often calibrated using different approaches. This work provides an ad-hoc methodology to quantify this parameter relative to other materials. Besides, this work also provides a tool to quantify the effect of solute concentration on cyclic deformation.

- This work demonstrates that mesoscale dislocation substructures can be used as an invariant to study the cyclic deformation of FCC metals. The evolution of dislocation substructures at mesoscale is not a material property rather it belongs to the dislocation interaction mechanisms occurring along different slip planes (slip systems). Hence, this implies that a crystal plasticity framework based on similar mesoscale substructures as proposed in the previous work can be used to study a broad range of materials. Moreover, employing an invariant to study the response of different materials can help to bridge the gap between them and this could further help to unify the constitutive models.
- This work provides an engineering solution to predict the effect of multiple gradients on microstructure-sensitive crack growth rate. This further enables to test and improve the microstructure-sensitive designs to avoid fatigue.

7.3 Future recommendations

Several areas for future research have been explored during this work. These are summarised as follows,

- Glide activation energy parameters are found to be sensitive to impurities. Since impurities have different sizes and different concentrations in engineering materials, therefore they have a different effect on activation energy parameters. Future efforts would consider estimating the explicit effect of impurities on activation energy parameters.
- The presence of hydrogen in FCC metal and alloys has a significant effect on its activation energy and thermal stress. Both activation energy parameters increased with increasing hydrogen concentration. Future

efforts should explore the effect of hydrogen on stress-strain response of FCC metal and alloys using activation energy parameters as a function of concentration.

- The current crystal plasticity model is capable of predicting the stress-strain response of aluminium polycrystal with larger grain sizes when the grain size effect saturates. Future efforts will modify the model to implement the grain size effect.
- The present model innovates a less computationally intensive framework to predict the stress response of FCC metals for a specific number of cycles. However, future effort requires predicting the initial hardening stage i.e. stress response in first few hundred cycles.
- Several aluminium alloys such as Al 3003 and Al-Mg have been found to have similar mesoscale substructures as FCC metals. Future efforts should consider predicting the cyclic response of those alloys using the current framework.
- This work considered only pure aluminum (cladding) to study the microstructure-sensitive crack growth from shallow scribes. However, there is sufficient experimental data available for Al 2024-T351. Future efforts should consider studying the cyclic response of Al 2024-T351 and predicting the effect of deep scribes in Al 2024-T351 using the current approach.
- This work overestimated the nucleation density of cracks due to a significantly large difference in model and experiment specimen size. Future efforts should consider predicting the nucleation density with a large specimen size and more microstructural attributes.
- This work considered fully reversed cycling while estimating the fatigue life of pure aluminium. Future efforts require estimating the effect of mean stress on fatigue life.
- The current work used the existing experimental data to understand material behaviour. This further encourages the use of existing worthy

knowledge to understand the deformation mechanisms and transform them into models. Future efforts should consider existing experiments to understand the mechanisms that control material response.

Appendices

Appendix A

A.1 Effect of shear modulus range on Fo and so

Table A-1 presents the shear modulus and Burgers vector for different metals and alloys used in the current analysis. Figure A-1 showed that glide activation energy and thermal stresses for different FCC metals are less sensitive to the uncertainty underlying shear modulus.

Table A-1 Shear modulus for different FCC metals and alloys.

Materials	Shear Modulus				$\boldsymbol{b}$ [10^{-10} m]
	Reuss model		Voigt model		
	μ (300 K) [GPa]	μ_0 (0 K) [GPa]	μ (300 K) [GPa]	μ_0 (0 K) [GPa]	
Aluminium	25.9 [1]	29.1 [1]	26.2 [2]	29.4 [2]	2.86 [3]
Nickel	78.2 [1]	84.7 [1]	94.2 [2]	101 [2]	2.49 [3]
Copper	41.7 [1]	43.5 [1]	54.6 [2]	59.3 [2]	2.56 [3]
Silver	25.4 [1]	28.4 [1]	33.5 [2]	37.5 [2]	2.89 [3]
Stainless steel 304	77.3 [4]	82.1 [4]	-	-	2.58 [5]
Stainless steel 316	75.1 [4]	81.0 [4]	-	-	2.58 [6]
Cupro-Nickel	57.0 [7]	60.6 [7]	-	-	2.56 [3]
AA 3003 (1.2) Mn	25.9 [8]	29.2 [8]	-	-	2.87 [3]

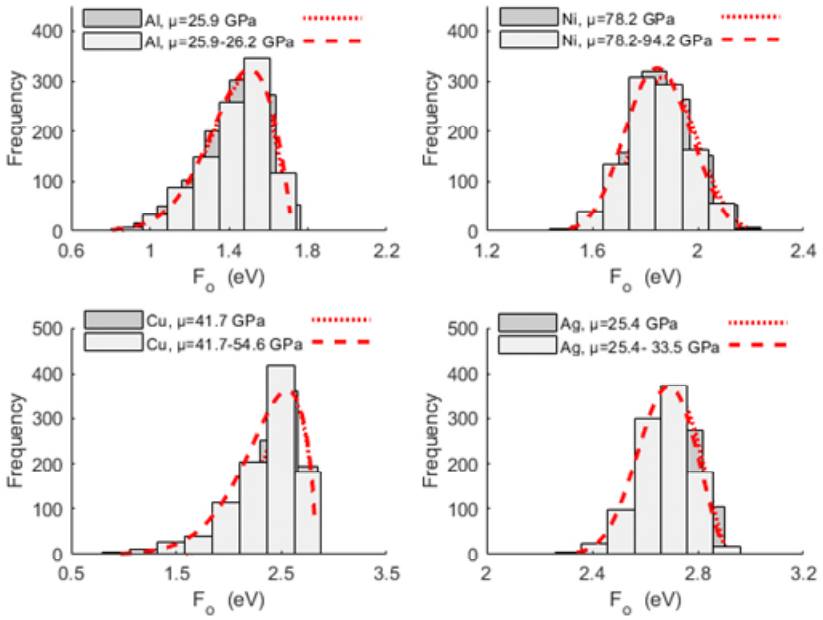

a)

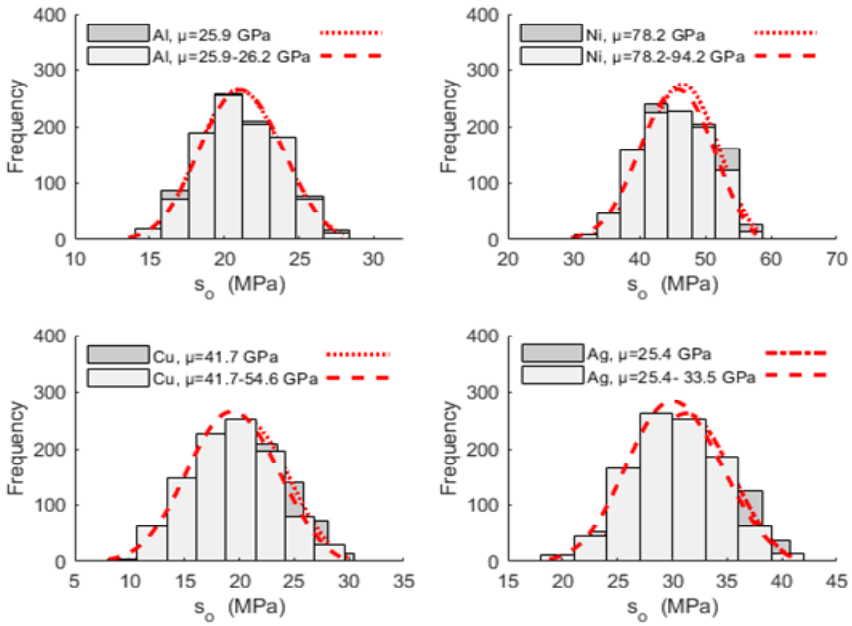

b)

Figure A-1 Effect of shear modulus range on a) activation energy b) thermal stress. For shear modulus range, Reuss model is used as a lower bound and Voigt model as an upper bound.

A.2 Experimental data used in the analysis

Figure A-2 shows the experimental data for aluminium, nickel, and Cu single crystals, Cu-Mn single crystal, and stainless steel 310s respectively. The data is used to calculate activation energy parameters shown in Figure 2-8, Figure 2-9, and Figure 2-12.

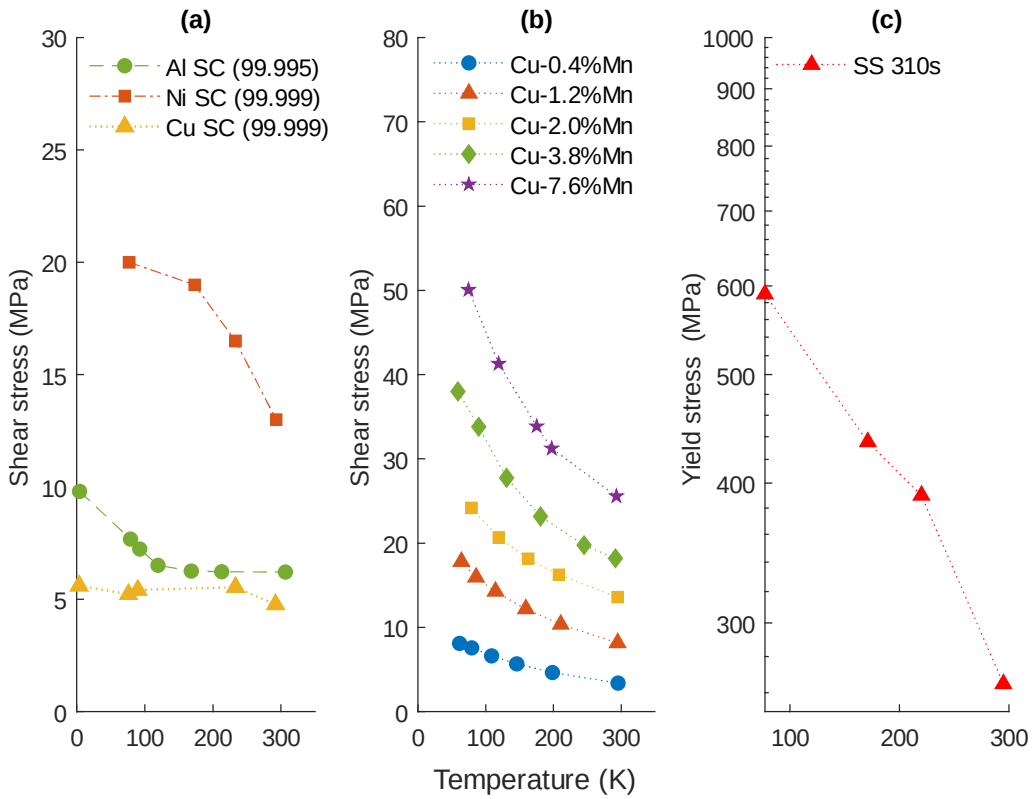

Figure A-2 Shear stress data at different temperatures for a) aluminium, nickel and copper single crystals [9–11] b) Cu-Mn with different solute concentrations [12] c) stainless steel 310s [13].

Appendix B

B.1 TEM data showing persistent slip bands in an aluminium single crystal at room temperature

Figure B-1 shows the PSB substructure in aluminium single crystal oriented for single slip deformed under cyclic loading at 298K and 77K. PSB wall thickness is measured at 77K and 298K using the reference length scale given on respective TEM. The data is plotted using the histogram and shown in Figure 3-7.

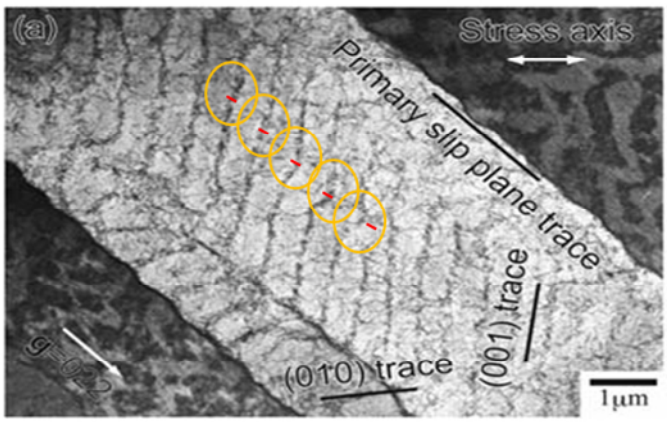

a)

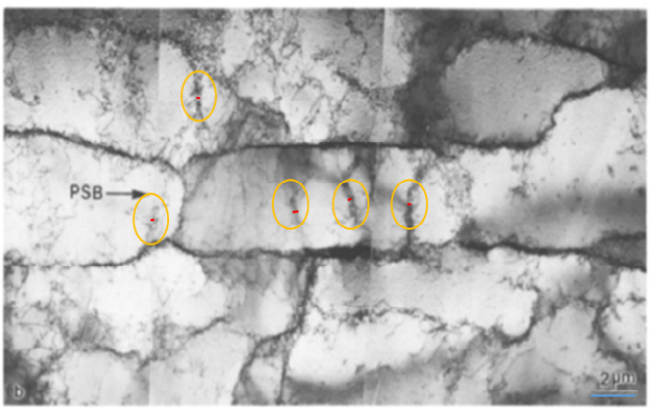

b)

Figure B-1 Persistent slip bands in an aluminium single crystal at 298K [14] and 77K [15]. The highlighted circles show the wall thickness measured using the reference length scale on the Figure.

B.2 Correlation between dislocation cell wall thickness and cell size

Figure B-2, Figure B-3, and Figure B-4 show the dislocation cell substructure in pure aluminium from various sources [16–19] deformed under cyclic loading at 298K and 77K. The cell thickness and cell size are estimated following the reference scale shown on the respective TEM. Since the cell sizes are not constant in each TEM data, therefore we considering quantifying multiple cell sizes in each data to account for uncertainty as shown in Figures below. The quantitative data is shown in Figure 3-8.

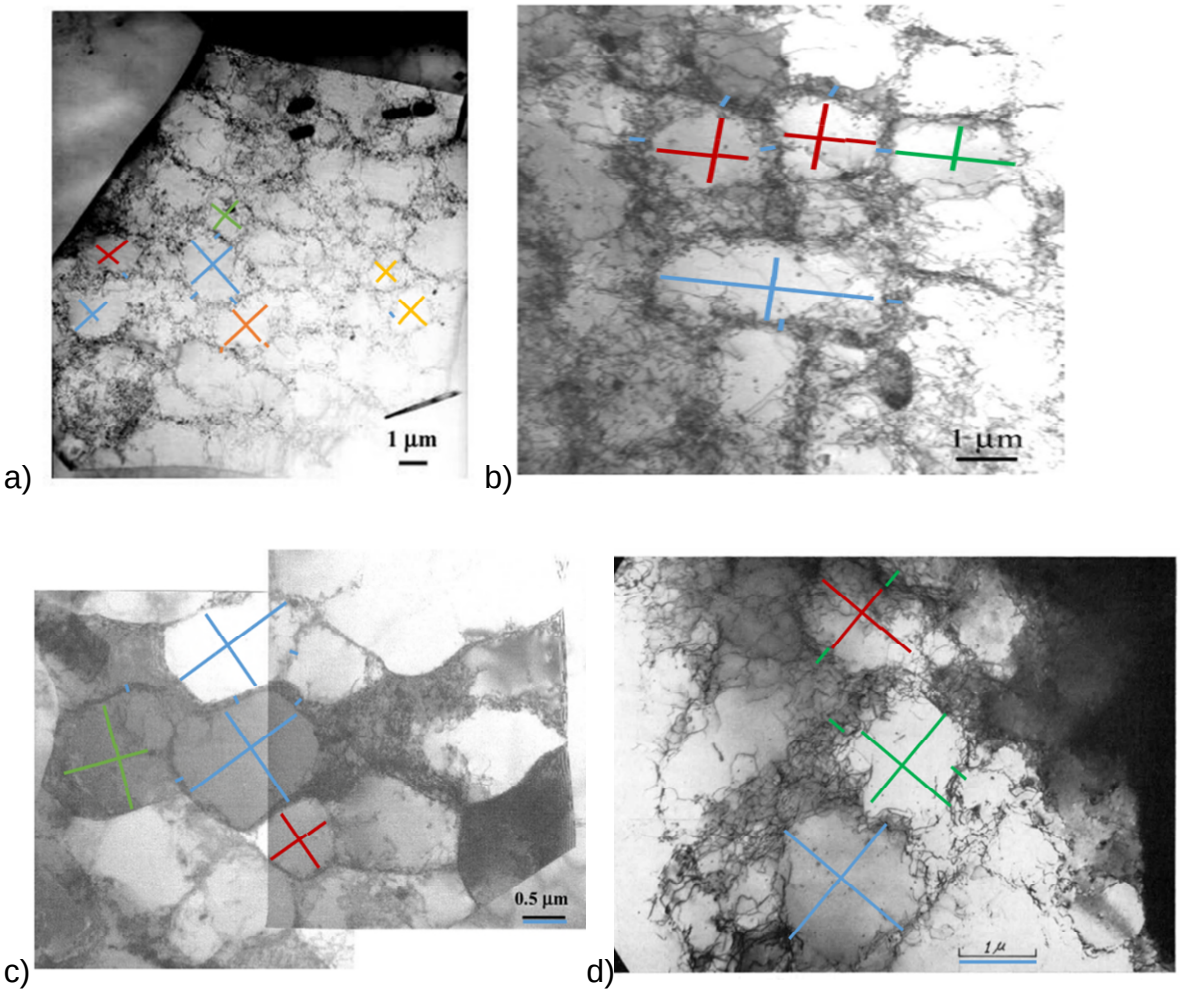

Figure B-2 Dislocation cell structure in fatigued aluminium at strain amplitude at a) $\frac{\Delta\epsilon_{pl}}{2} = 0.0184\ \%$ b) $\frac{\Delta\epsilon_{pl}}{2} = 0.0625\ \%$ c) $\frac{\Delta\epsilon_{pl}}{2} = 0.26\ \%$ d) $\frac{\Delta\epsilon_{pl}}{2} = 0.725\ \%$ at 298K [16].

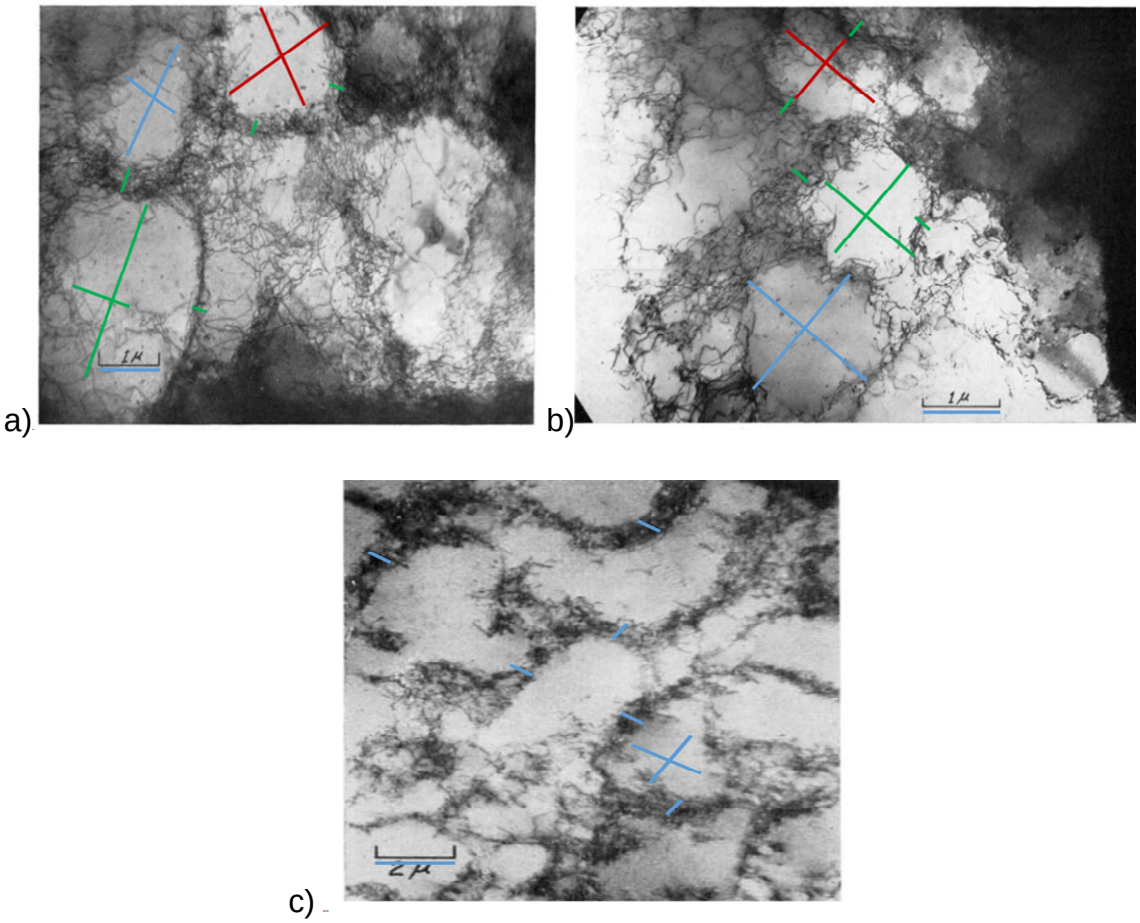

Figure B-3 Dislocation cell structure in pure aluminium under cycling loading at a,b) $\Delta\epsilon = 10\ \%$, T=78 K [17] c) $\Delta\epsilon = 0.2\ \%$, T=78 K [18].

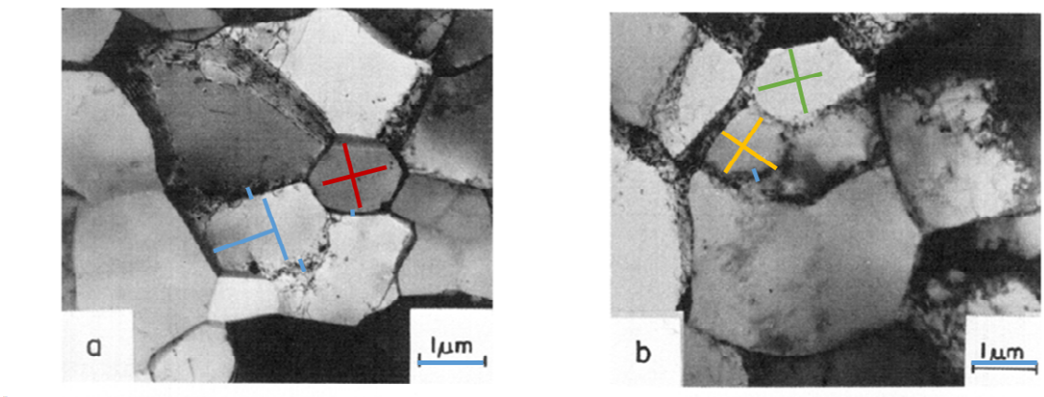

Figure B-4 Dislocation cell structure developed in 99.8% pure aluminium under cyclic loading at $\Delta\epsilon_{pl} = 1\%$, T=298 K [19] a) extruded hard b) extruded soft. The cell size and thickness are measures with reference to the scale given in the figure.

Appendix C

C.1 Details of grain size and orientation

Average grain dia (μm)	Euler angles (radians)			Average grain dia (μm)	Euler angles (radians)		
	φ_1	φ	φ_2		φ_1	φ	φ_2
48.5718	4.0458	1.7869	0.3356	44.7747	4.0937	0.7571	5.7686
29.173	6.0678	1.0619	3.0329	42.4314	5.3	2.3835	3.0686
46.8956	2.1574	1.2566	1.3489	53.682	4.6607	1.3553	2.1387
44.1304	2.7358	1.7861	3.5735	53.682	1.5776	1.4737	6.0556
41.7121	4.5598	2.2945	6.0223	51.8531	3.6901	2.3543	0.2725
48.3004	2.327	2.569	5.9221	54.1203	5.5071	1.1473	0.7906
44.1304	5.7805	1.4147	5.6074	50.6411	6.0452	2.6632	1.0074
19.6949	2.1975	0.8027	5.2774	29.173	3.2743	1.7072	4.6522
49.1056	4.8225	1.5239	1.1716	50.1397	0.34565	2.3083	4.0079
44.7747	3.9768	0.6078	5.3259	45.0901	2.8374	2.0119	1.4162
55.3941	0.8054	1.0899	0.8862	44.4549	1.8546	1.8772	0.4868
52.7834	1.3906	2.5423	2.7857	46.3093	5.5192	1.1499	6.1738
51.8531	4.0546	1.5405	2.5831	52.7834	5.7998	0.6456	2.1072
45.7078	0.01399	2.8227	4.817	56.4126	3.8835	1.3995	2.6985
47.1833	3.6861	1.2803	4.815	47.4675	0.77552	1.6114	0.83863
51.8531	2.282	1.4458	2.4707	57.7796	5.3293	1.8082	0.90509
45.401	4.4291	0.91516	3.2179	52.0888	4.3959	0.96316	0.39122
48.8402	3.7458	0.5361	2.5262	59.0847	6.2814	2.6194	4.6018

48.3004	4.3025	1.6119	3.0332	55.1859	1.4101	1.9639	1.3171
48.5718	0.893	2.1378	5.3688	48.8402	5.5715	0.51679	5.0351
50.3917	2.0956	0.98108	1.0798	48.026	0.9109	2.2299	3.5058
47.1833	2.0227	2.3135	5.2229	48.5718	5.5787	2.0268	2.1457
52.5539	1.7612	2.4962	4.9264	52.5539	2.9669	2.3143	6.1269
50.3917	5.3633	1.2474	2.4227	47.7484	0.060493	1.7811	5.5761
57.0065	1.6557	0.80177	5.887	57.7796	4.6126	2.1031	4.367
58.9018	3.2679	0.79769	1.9713	41.3429	0.13446	2.6395	3.8901
29.173	4.0458	1.7869	0.33568	40.967	2.9122	2.0363	0.92892

References

1. Varshni Y.P. Temperature dependence of the elastic constants. Physical Review B. 1970; 2(10): 3952–3958. http://dx.doi.org/10.1103/PhysRevB.2.3952

2. Ledbetter H.M. and Naimon E.R. Relationship between single-crystal and polycrystal elastic constants. Journal of Applied Physics. 1974; 45(1): 66–69. http://dx.doi.org/ org/10.1063/1.1663019

3. Kocks U.F.,Argon A.S. and Ashby M.F. Thermodynamics and kinetics of slip. Progress in Materials Science. Pergamon Press; 1975. 291 p.

4. Ledbetter H.M. Stainless-steel elastic constants at low temperatures. Journal of Applied Physics. 1981. pp. 1587–1589. http://dx.doi.org/ org/10.1063/1.329644

5. Frost H.J. and Ashby M.F. Deformation mechanisms maps. Pergamon Press; 1982. 44–48 p.

6. Lindgren L.E., Hao Q. and Wedberg D. Improved and simplified dislocation density based plasticity model for AISI 316 L. Mechanics of Materials. Elsevier Ltd; 2017; 108: 68–76. http://dx.doi.org/ org/10.1016/j.mechmat.2017.03.007

7. National Bureau of Standards, Low temperature mechanical properties of copper and selected copper alloys, Report. United States Department of Commerce. 1959. Online available : https://nvlpubs.nist.gov/nistpubs/Legacy/MONO/nbsmonograph101.pdf.

8. Gault C., Dauger A. and Boch P. Variations of the elastic constants of aluminium–magnesium single crystals with Guinier-Preston zones. Physica Status Solidi (a). 1977; 43(2): 625–632. http://dx.doi.org/ org/10.1002/pssa.2210430233

9. Mukherjee AK., Mote J.D. and Dorn J.E. Strain hardening of single aluminum crystals during polyslip. Transactions of AIME. Berkeley, California; 1965.

10. Yao Z., Schäublin R., Spätig P. and Victoria M. The tensile properties of irradiated Ni single crystals and their temperature dependence. Philosophical Magazine. 2005; 85: 745–755. http://dx.doi.org/ org/10.1080/14786430412331319947

11. Bullen F.P. and Cousland S.M. The temperature dependence of the flow stress of copper single crystals. Physica Status Solidi (B). 1968; 27(2): 501–512. http://dx.doi.org/ org/10.1002/pssb.19680270205

12. Wille T.H., Gieseke W. and Schwink C.H. Quantitative analysis of solution hardening in selected copper alloys. Acta Metallurgica. 1987; 35(11): 2679–2693. http://dx.doi.org/ org/10.1016/0001-6160(87)90267-7

13. Abraham D.P. and Altstetter C.J. The effect of hydrogen on the yield and flow stress of an austenitic stainless steel. Metallurgical and Materials Transactions A. 1995; 26(11): 2849–2858. http://dx.doi.org/ org/10.1007/BF02669643

14. Zhai T., Martin J.W., Briggs G.A.D. and Road P. Fatigue damage at room temperature aluminium single crystals- II. TEM. Acta Metallurgica. 1996; 44(5): 1729–1739. https://doi.org/10.1016/1359-6454(95)00330-4.

15. Nakanishi Y., Tanaka H., Fujii T., Onaka S. and Kato M. Low-temperature fatigue behaviour and development of dislocation structure in aluminium single crystals with single-slip orientation. Philosophical Magazine. 2013; 93(21): 2759–2768. http://dx.doi.org/ org/10.1080/14786435.2013.786193

16. El-Madhoun Y., Mohamed A. and Bassim M.N. Cyclic stress-strain response and dislocation structures in polycrystalline aluminum. Materials Science and Engineering A. 2003; 359(1–2): 220–227. http://dx.doi.org/ org/10.1016/S0921-5093(03)00347-2

17. Feltner C.E. Dislocation arrangements in aluminum deformed by repeated tensile stresses. Acta Metallurgica. 1963; 11(7): 817–828. http://dx.doi.org/org/10.1016/0001-6160(63)90021-X

18. Feltner C.E. Dislocation debris in aluminium fatigued at 78°k. Philosophical Magazine. 1963; 8(96): 2121–2124. http://dx.doi.org/org/10.1080/14786436308209107

19. Kayali E.S. and Plumtree A. Stress-substructure relationships in cyclically and monotonically deformed wavy slip mode metals. Metallurgical Transactions A. June 1982; 13(6): 1033–1041. http://dx.doi.org/org/10.1007/BF02643400

Publications

1- Ashraf F. and Castelluccio G.M. Estimation of Dislocation Glide Barrier in FCC Metals and Alloys, Materials Science and Engineering A. 2020 (Submitted)

2- Ashraf F. and Castelluccio G.M. Unravelling the effect of number of cycles on mesoscale dislocation substructures under cyclic deformation. Materials Science and Engineering A. 2021 (In preparation)

3- Ashraf F. Cini A., and Castelluccio G.M. Coupling microstructure and geometric gradients independently to estimate transgranular fatigue life in pure Al. International Journal of Fatigue. 2021 (In preparation)

4- Ashraf F., Cini A., and Castelluccio, G.M. Coupling geometric and microstructure gradients in fatigue crack formation. (2020). TESConf 2020 - 9th International Conference on Through-life Engineering Services. Cranfield University UK

5- Ashraf F., Cini A., and Castelluccio, G.M. Decoupling geometric and microstructural gradients in fatigue crack formation (2021). Fatigue 2021 Cambridge University. UK. (Under review)